

**PL-TR-96-2032**

# **ON THE MODELLING OF SPACE PLASMA DYNAMICS AND STRUCTURE**

**Jay Albert  
Stephen Anderson  
Michael Silevitch  
Elena Villalon**

**Northeastern University  
360 Huntington Avenue  
Boston, MA 02115**

**15 November 1995**

**Final Report  
1 December 1992-30 November 1994**

**APPROVED FOR PUBLIC RELEASE; DISTRIBUTION UNLIMITED**

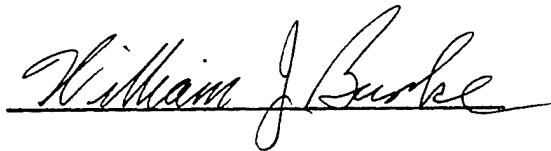


**PHILLIPS LABORATORY  
Directorate of Geophysics  
AIR FORCE MATERIEL COMMAND  
HANSCOM AFB, MA 01731-3010**

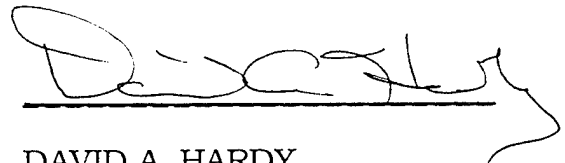
**19960227 094**

**DTIC QUALITY INSPECTED 1**

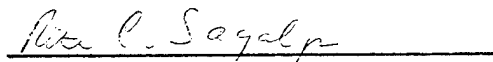
"This technical report has been reviewed and is approved for publication."



WILLIAM J. BURKE  
Contract Manager



DAVID A. HARDY  
Branch Chief



RITA C. SAGALYN  
Division Director

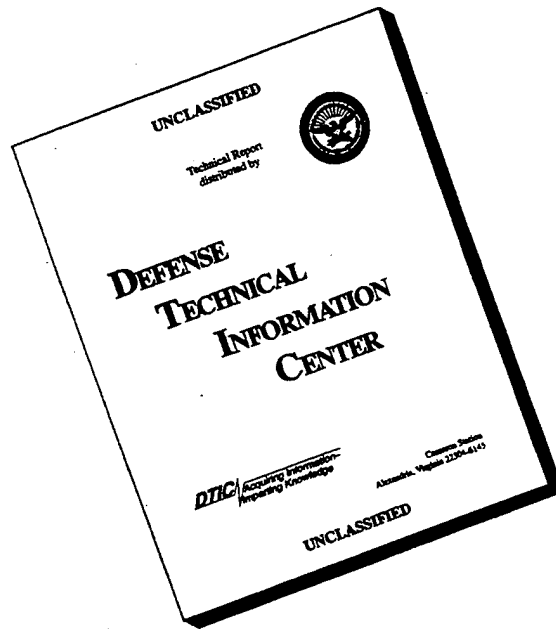
This report has been reviewed by the ESC Public Affairs Office (PA) and is releasable to the National Technical Information Service (NTIS).

Qualified requestors may obtain additional copies from the Defense Technical Information Center.

If your address has changed, or if you wish to be removed from the mailing list, or if the addressee is no longer employed by your organization, please notify PL/TSI, Hanscom AFB, MA 01731-5000. This will assist us in maintaining a current mailing list.

Do not return copies of this report unless contractual obligations or notices on a specific document requires that it be returned.

# DISCLAIMER NOTICE



**THIS DOCUMENT IS BEST QUALITY AVAILABLE. THE COPY FURNISHED TO DTIC CONTAINED A SIGNIFICANT NUMBER OF PAGES WHICH DO NOT REPRODUCE LEGIBLY.**

REPORT DOCUMENTATION PAGE			Form Approved OMB No. 0704-0188	
Public reporting burden for this collection of information is estimated to average 1 hour per response, including the time for reviewing instructions, searching existing data sources, gathering and maintaining the data needed, and completing and reviewing the collection of information. Send comments regarding this burden estimate or any other aspect of this collection of information, including suggestions for reducing this burden, to Washington Headquarters Services, Directorate for Information Operations and Reports, 1215 Jefferson Davis Highway, Suite 1204, Arlington, VA 22202-4302, and to the Office of Management and Budget, Paperwork Reduction Project (0704-0188), Washington, DC 20503.				
1. AGENCY USE ONLY (Leave blank)		2. REPORT DATE 15 November 1995	3. REPORT TYPE AND DATES COVERED Final (1 December 1992-30 November 1994)	
4. TITLE AND SUBTITLE On the Modelling of Space Plasma Dynamics and Structure			5. FUNDING NUMBERS PE 62101F PR 2311 TA G6 WU NU	
6. AUTHOR(S) Jay Albert Stephen Anderson Michael Silevitch Elena Villalon			Contract F19628-92-K-0007	
7. PERFORMING ORGANIZATION NAME(S) AND ADDRESS(ES) Northeastern University 360 Huntington Avenue Boston, MA 02115			8. PERFORMING ORGANIZATION REPORT NUMBER	
9. SPONSORING / MONITORING AGENCY NAME(S) AND ADDRESS(ES) Phillips Laboratory 29 Randolph Road Hanscom AFB, MA 01731-3010  Contract Manager: William Burke/GPSG			10. SPONSORING / MONITORING AGENCY REPORT NUMBER  PL-TR-96-2032	
11. SUPPLEMENTARY NOTES				
12a. DISTRIBUTION / AVAILABILITY STATEMENT  Approved for public release; distribution unlimited			12b. DISTRIBUTION CODE	
13. ABSTRACT (Maximum 200 words) The research described in this report was focused into two related areas. These were:  (A) A study of nonadiabatic particle orbits and the electrodynamic structure of the coupled magnetosphere-ionosphere auroral arc system.  (B) An examination of electron acceleration and pitch-angle scattering due to wave-particle interactions in the ionosphere and radiation belts.				
14. SUBJECT TERMS Radiation belts Auroral arcs Wave-particle interactions			15. NUMBER OF PAGES 150	
			16. PRICE CODE	
17. SECURITY CLASSIFICATION OF REPORT Unclassified	18. SECURITY CLASSIFICATION OF THIS PAGE Unclassified	19. SECURITY CLASSIFICATION OF ABSTRACT Unclassified	20. LIMITATION OF ABSTRACT SAR	



## CONTENTS

Introduction	1
Description of Research	1
Publications:	
$O^-$ Phase Bunching and Auroral Arc Structure	5
Single Ion Dynamics and Multiscale Phenomena	15
Particle Dynamics in a Spatially Varying Electric Field	19
Test Particle Motion in the Cyclotron Resonance Regime	30
Cyclotron Resonance in an Inhomogeneous Magnetic Field	49
Quasi-Linear Pitch Angle Diffusion Coefficients: Retaining High Harmonics	56
Proton-Whistler Interactions in the Radiation Belts	61
Whistler Interactions With Energetic Protons	72
Proton Diffusion by Plasmaspheric Whistler Waves	84
Proton Whistler Interactions Near the Equator in the Radiation Belts	96
Diffusion of Radiation Belt Protons by Whistler Waves	109
Whistler Wave Interactions: Sources for Diffuse Aurora Electron Precipitation?	121
Pitch Angle Scattering of Diffuse Auroral Electrons by Whistler Mode Waves	129
Interaction of Ring Current and Radiation Belt Protons With Ducted Plasmaspheric Hiss. 2. Time Evolution of the Distribution Function	138

## Introduction

This document is a final report describing the research activities performed under the contract F19628-K-92-0007, "*On the Modelling of Space Plasma Dynamics and Structure.*" The research was focused into two related areas. These were:

- (A) A study of nonadiabatic particle orbits and the electrodynamic structure of the coupled magnetosphere-ionosphere auroral arc system.
- (B) An examination of electron acceleration and pitch-angle scattering due to wave-particle interactions in the ionosphere and radiation belts.

In the next section we present a more detailed description of the two research areas. Following that are copies of the refereed publications which resulted from the research investigations.

## Description of Research

In this section we present a more detailed synopsis of the research areas which were investigated during the period of the contract.

- (A) A study of nonadiabatic particle orbits and the electrodynamic structure of the coupled magnetosphere-ionosphere auroral arc system.

In this area we have focused on the development of a self-consistent model of an auroral arc system. This includes elements such as the structure of the magnetospheric generator mechanism, the role of heavy ions such as oxygen in determining the arc structure, and the interplay between the large scale background magnetospheric electric and magnetic fields and the small scale auroral arcs embedded within them.

It has long been recognized that there is a coupling between microscopic single ion dynamics, as defined by the ion gyroradius, and macroscopic MHD phenomena. Two obvious examples are kinetic Alfvén waves and the ion tearing mode. Another important example is the effect of the large scale electric field variation near the Harang discontinuity on single ions as they drift earthward from the magnetotail. We found that under substorm growth phase conditions, single oxygen ion trajectories were modified and caused macroscopic density striations. Current conservation of the associated inertial currents implied a connection between the striations and auroral arc formation. This result is of importance because it provides a natural mechanism for the formation of thin ordered structures (the arcs) from a uniform source of plasma flowing in from the geotail region. This work was published in the *Journal of Geophysical Research* and is reproduced in this report. We have extended the above analysis by examining the regions of strong curvature inherent in the large scale magnetospheric electric fields within the Harang discontinuity region. It

was found that for sufficiently strong curvature in the earthward electric field, the heavy ions became untrapped. Thus there are situations which invalidate even a nonideal MHD theory which treats finite orbit effects in a perturbative manner. It was recently shown that these heavy ions can contribute to substorm onset [AGU Geophysical Monograph 93; JGR 1995 (both reprinted in this report)].

In addition to this work we have also developed the theory that parallel auroral arc structure is determined by resonant kinetic Alfvén waves bouncing from pole to pole. Because they do not travel exactly along the magnetic field, but deviate slightly, they bounce off the ionosphere in slightly different positions with each bounce, giving rise naturally to the observed arc spacing and resonant frequencies. The results have been expressed in terms of a Green's function solution for the incoming and outgoing fluctuating magnetic fields.

Our current research is focused on the effects caused by the variation of the magnetic fields in the vicinity of the magnetospheric auroral arc structure. These fields can arise from two sources: the large scale background field and the self-consistent fields generated by the currents within the arc itself. Although our work is still in its preliminary stages, we have already determined that the constraints imposed on the system by the large scale field can help provide an explanation for the limited spatial region that is associated with auroral arc formation. The small scale fields will be integral to the development of a self-consistent theory of the magnetospheric arc generator.

- (B) An examination of electron acceleration and pitch-angle scattering due to wave-particle interactions in the ionosphere and magnetosphere.

In this area we have studied the following problems:

- (1) *The interaction of a relativistic test particle with an electromagnetic wave in a spatially varying magnetic field.* Observations of proton pitch-angle scattering apparently induced by artificially produced VLF waves motivated this study of a ubiquitous phenomenon. Under a previous contract, we had studied cyclotron-resonant behavior with the simplifying assumption of constant background magnetic field, which determines the particle's cyclotron frequency. Significant changes in energy and pitch angle were found to occur when the Doppler-shifted wave frequency was a multiple of the cyclotron frequency. Here, we considered the complication that as a particle moves along a field line, the cyclotron frequency changes, so that the particle enters, experiences, and leaves distinct regions of resonance. This time-dependent interaction was shown to have two distinct regimes, depending on the relative strength of the magnetic field inhomogeneity. In the weak regime, the effect of each resonance is proportional to the square root of the wave amplitude, and individual resonances combine additively. In the strong regime, the effect of each resonance is proportional to the wave amplitude, and individual resonances combine independently, giving a random walk (diffusion) in energy and pitch angle. This work resulted in a paper published in *The Journal of Geophysical Research*.

- (2) *The quasilinear interaction of radiation belt electrons with a turbulent spectrum of whistler waves (hiss).* The prevailing theory of particle-hiss interaction was examined, and it was found that the corresponding numerical calculations in the literature were inadequate; only 5 harmonic interactions were considered in the evaluation of the pitch-angle diffusion coefficients, which is insufficient for electrons with energy above 500 keV. Efficient algorithms were developed, based on upper bounds, and the calculations were redone keeping up to 100 harmonics. The diffusion coefficients were naturally increased, and the corresponding particle flux distribution functions were decreased in the outer zone. This work resulted in a paper published in *The Journal of Geophysical Research*.
- (3) *The response of outer zone electrons and protons to a model of the sudden storm commencement (SSC) of March 24, 1991.* An explicit model for the pulse profile, developed by the group at Dartmouth, has been used in test particle simulations to demonstrate the rapid injection and energization of electrons and protons to form the "second belt." Analytical work on the resulting guiding center equations of motion have yielded insights into the physical mechanism, and indicate when such pulses are likely to be effective, and for which particles. This work has been presented as an AGU meeting, and is still in progress.
- (4) *Proton radiation belt structure and evolution as observed by CRRES.* The quiet and active models derived from Protel observations have been used to study flux and phase space density profiles parameterized by constant first adiabatic invariant. The steady-state diffusion model has been shown not to be a good description even for the quiet, pre-storm period. Adjustment of parameters, variation of boundary fluxes, even imposition of *ad hoc* wave-particle effects have been considered and rejected as explanations for the discrepancy. On the other hand the hypothesis of a drastic, non-adiabatic disturbance prior to the launch of CRRES, followed by conventional diffusive relaxation during the first half of the CRRES mission, is a plausible and consistent scenario. This conclusion follow from comparing observed time variation of the data with explicitly evaluated diffusion and loss terms prescribed by diffusion theory. Even so, detailed agreement is achieved only for energy below about 20 MeV and L less than about 2.5, beyond which the data is too variable to evaluate the derivatives reliably. Progress on this work has been presented at AGU meetings, the GEM meeting (Snowmass, 1994), the Workshop on Radiation Belts (Brussels, 1995), and is being written up for publication in *JGR*.
- (5) *A study of the interaction of protons and whistler waves near the quasi-electrostatic limit in equatorial regions of the plasmasphere.* The interaction of protons with quasi-electrostatic whistler waves were investigated using a test particle Hamiltonian formalism, and quasilinear diffusion theory. A number of experimental observations [Kovrazhkin et al., 1983, 1984; Koons, 1975, 1977] have shown that VLF transmissions pulses from the ground can precipitate 80 to 500 keV protons into the ionosphere. The predominant feature of the whistler proton interaction is the crossing of multiple harmonics of the proton gyrofrequency near equatorial regions of the plasmasphere. The wave frequency spectrum is coherent, and varies as a function of the distance

along the field line, thus the inhomogeneity of the magnetic field is compensated by the frequency variation. This way proton whistler interactions satisfy the conditions for second-order resonances for all the gyroharmonics. The combined contributions of all the harmonics allow the protons which are near the loss cone to diffuse toward smaller pitch angles. The quasilinear diffusion coefficients in energy, cross energy/pitch angle, and pitch angle are obtained for second-order resonant interactions.

- (6) *The interaction of ring current and radiation belt protons with ducted plasmaspheric hiss.* We have also studied the interaction of ring current and radiation belt protons with ducted plasmaspheric hiss [Kozyra et al., 1995]. The evolution of the bounce-averaged ring current/radiation belt proton distribution is obtained for multiple harmonic resonances crossing with the plasmaspheric hiss. Because the wave spectrum is incoherent, only first-order resonances contribute. The interaction with the electrons maintains the level of the waves, thus the energy is transferred between energetic electrons and protons using the hiss as an intermediary. The similarity between the distributions observed by the OGO 5 satellite, and those resulting from the simulations raises the possibility that interaction with plasmaspheric hiss may play a role in forming and maintaining the characteristic zones of anisotropic proton precipitation in the subauroral ionosphere.
- (7) *Pitch angle scattering of low energy electrons by whistler mode waves in equatorial regions of the plasmasheet.* The interaction of oblique whistler waves and electrons of energy below 10 keV, to describe diffuse auroral precipitation. Whistler waves of large enough amplitude have been observed in the outer magnetosphere. Figure 3 of Burke et al. [1995] gives an example of these waves as observed by the CRRES satellite. Experimental observations [Johnstone, et al., 1993], show that the low energy electrons ( $< 10$  keV) are precipitated by the whistler waves whose frequencies are close to the electron cyclotron frequency. We investigated a theoretical model to explain the experimental results. Second-order resonant interactions are shown to be very efficient in precipitating the electrons toward the atmospheric loss cone. The frequency spectrum is assumed to be coherent as present in chorus emissions, and the waves propagate at large angles with respect to the geomagnetic field so that they are near the quasi-electrostatic limit.
- (8) *The generation of whistler chorus outside the plasmasphere.* The generation of chorus and triggered emissions in the magnetosphere through resonant first harmonic interactions with energetic electrons. The mechanism of dynamical spectrum formation inside a chorus element is closely connected with the triggering emission problem [Trakhtengerts, 1994]. The basic theory for triggered emissions was laid out by Helliwell, [1967]. It is well known that chorus emissions are generated in the plasmasheet from monochromatic wavelets in the underlying hiss [Hattori et al., 1991]. Presently we are investigating the non-linear current that result from second-order resonant energetic electrons, and that generates the chorus. When these emissions propagate at large angles then they interact coherently with the low energy electrons ( $< 10$  keV) that form the diffuse aurora.

## O<sup>+</sup> phase bunching and auroral arc structure

Paul L. Rothwell

Geophysics Research Directorate, Phillips Laboratory, Hanscom Air Force Base, Bedford, Massachusetts

Michael B. Silevitch

Center for Electromagnetics Research, Northeastern University, Boston, Massachusetts

Lars P. Block and Carl-Gunne Fälthammar

Department of Plasma Physics, Alfvén Laboratory, Royal Institute of Technology, Stockholm, Sweden

**Abstract.** The equations of motion are solved for ions moving in a model electric field that corresponds to the nightside equatorial region of the magnetosphere. The model represents the poleward region of the Harang discontinuity mapped to the magnetosphere. Within this region the model electric field has a constant earthward gradient superimposed on a constant dawn-to-dusk electric field. In combination with the earthward drift motion due to the dawn-to-dusk field, the electric field gradient introduces an earthward inertia drift, which is proportional to the ion mass and therefore faster for O<sup>+</sup> ions than for H<sup>+</sup> ions or electrons. It is also found that the entry of the ions into the gradient region causes phase bunching and as a result ion density striations form. The striations are enhanced for more abrupt changes in the electric field gradient, a weaker magnetic field, a stronger cross-tail electric field and colder O<sup>+</sup> ions. The first two conditions apply during the growth phase of a substorm. Using the Tsyanenko (1987) model a minimum electric field gradient value of  $1 \times 10^{-9}$  V/m<sup>2</sup> ((1 mV/m)/1000 km) at  $L = 6-7$  is found. Charge neutrality requires coupling with the ionosphere through electrons moving along magnetic field lines, and such electrons may be the cause of multiple auroral arcs.

## Introduction

In an electric field, such as shown in the bottom panel of Figure 1, plasma sheet O<sup>+</sup> ions that are  $E \times B$  drifting toward the Earth (region A) encounter a weak, positive electric field gradient (region B) in the Harang discontinuity region (HDR). We concentrate on the ion injection into and the dynamics within region B as labeled in Figure 1. The effect of the full HDR, including the field reversal region, on the ion dynamics will be treated in a future paper. It is found that variations in electric field gradients can dramatically change the shape of the ion orbits as seen from Figure 2. In the presence of a finite electric field gradient we will show that single ion effects can be important over much larger distances than the ion gyroradius. It is also found that a velocity distribution that is isotropic in the plane perpendicular to the magnetic field in a region with zero electric field gradient will become anisotropic upon entering a region with a nonzero gradient. This mechanism is called phase bunching. The net effect is that the ion density, which was initially uniform, becomes striated when the earthward electric field gradient is sufficiently large.

The factors that enhance the presence of O<sup>+</sup> density striations are also associated with substorms. They are (1) an intensification of the HDR [Erickson *et al.*, 1991] (i.e., steeper electric field gradients); (2) equatorial enhancement of ionospheric O<sup>+</sup> [Cladis and Francis, 1992; Daglis *et al.*,

1990]; (3) an enhancement of the cross-tail electric field; and (4) a local weakening of the magnetic field.

We address two main questions in this paper. (1) Can the stretching of magnetic field lines in the midnight sector and the estimates of the electric field gradients be consistent with a derived criterion for striation formation? (2) If these striations do occur what are the implications, if any, for auroral arc structure?

The paper is organized as follows. First, we analytically solve the equations of motion for a constant, earthward electric field gradient and a constant east-west electric field as inferred from Marklund [1984]. Second, phase bunching, and the resulting spatial striation mechanism, is defined and quantified. Third, a Monte Carlo calculation is carried out for a Maxwellian velocity distribution in order to show that phase bunching is not averaged out at realistic ion temperatures. Finally, we show that magnetic field line stretching and an enhanced cross-tail electric field lowers the minimum value of the electric field gradient at which striations will occur. Implications for auroral arc structure are then discussed.

## The Equations

Cole [1976] originally treated single-ion motion in a constant electric field gradient. In his model the electric field and gradient only had components in the earthward ( $x$ ) direction. Because of the unidirectional nature of the electric field  $E_x$  the ions drifted solely in the eastward ( $-y$ ) direction with a drift speed given by

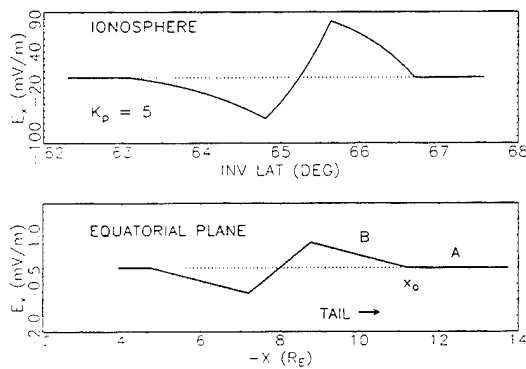


**Figure 1.** A simplified Harang discontinuity model as seen in the (upper) ionosphere and the (bottom) equatorial plane. The upper panel was obtained from the lower panel by mapping the electric field in invariant latitude using the *Tsyganenko* [1987] model,  $K_p = 5$ , at local midnight. The letters A and B denote the regions of interest for the present paper. It is interesting to note the similarity between these results and the observations of *Maynard* [1974].

$$V_{dy} = -\frac{\omega^2 E_0}{\Omega^2 B} + V_{y0} \left(1 - \frac{\omega^2}{\Omega^2}\right) \quad (1)$$

where

$$\Omega^2 = \omega^2 - \frac{e}{M} \frac{dE_x}{dx} \quad (2)$$

$E_0$  is the electric field value at the initial ion position,  $e$  is the electronic charge,  $B$  is the magnetic field value,  $V_{y0}$  is the  $y$  component of the initial velocity, and  $\omega = eB/M$  is the ion magnetic gyrofrequency.

Therefore in a region of a positive  $E$  field gradient the effective drift velocity exceeds the usual  $E/B$  value and for a negative gradient it is less. Note in (2) that the first term on the right-hand side varies as  $M^{-2}$ , while the second term varies as  $M^{-1}$ . Heavy ions therefore are more efficiently affected by an electric field gradient. This is the source of the preferential decoupling of the  $O^+$  ions relative to protons ( $H^+$ ) that was mentioned above. *Lysak* [1981] and *Yang and Kan* [1983] have suggested that the enhanced ion drift velocity as given by (2) is responsible for ion conics in narrow arc structures where one would expect large electric field gradients.

In this paper we extend *Cole's* analysis to include an  $E_y$  component of the electric field. The equations of motion in a two-dimensional electric field are given by

$$\begin{aligned} \frac{dV_x}{dt} &= \frac{e}{M} \{E_x[x(t)] + V_y B\} \\ \frac{dV_y}{dt} &= \frac{e}{M} (E_y - V_x B) \end{aligned} \quad (3)$$

These equations can easily be recast as a single second-order inhomogeneous differential equation:

$$\frac{d^2 V_x}{dt^2} + \left( \omega^2 - \frac{e}{M} \frac{dE_x}{dx} \right) V_x = \frac{\omega^2 E_y}{B} \quad (4)$$

Equation (4) represents a harmonic oscillator with a frequency that is modified by the presence of an  $E$  field gradient. Its solution is

$$\begin{aligned} V_x(t) &= \frac{\omega^2 E_y}{\Omega^2 B} + \left( V_{x0} - \frac{\omega^2 E_y}{\Omega^2 B} \right) \cos(\Omega t) \\ &+ \frac{\omega}{\Omega} \left( V_{y0} + \frac{E_0}{B} \right) \sin(\Omega t) \end{aligned} \quad (5)$$

where  $V_{x0}$  and  $V_{y0}$  are determined by the initial conditions at  $t = 0$ .  $E_0$  is the value of the  $x$  component of the electric field for  $x \leq x_0$ , which in the present instance is zero. It is assumed that  $dE_x/dx > 0$  only for  $x > x_0$ . The subscript  $B$  will be used to denote parameters defined in this region. The letter  $A$  denotes the region  $x < x_0$ .  $E_y$  is the cross-tail electric field which is assumed to be constant. It is important to note that positive  $E$  field gradients demagnetize the particle while negative  $E$  field gradients simulate a more intense magnetic field. If  $\Omega^2 < 0$  [Cole, 1976], the particle is exponentially accelerated. If  $\Omega^2 = 0$ , then  $V_x$  increases quadratically with time. The  $x$  component of the velocity for the case  $\Omega^2 > 0$  is given by (5). Equation (6) is the expression for the  $y$  component of the velocity.

$$\begin{aligned} V_y(t) &= V_{y0} - \frac{\omega^2}{\Omega^2} \left( V_{y0} + \frac{E_0}{B} \right) [1 - \cos(\Omega t)] \\ &- \frac{\omega}{\Omega} \left( V_{x0} - \frac{\omega^2 E_y}{\Omega^2 B} \right) \sin(\Omega t) - \frac{\omega^2 E_y}{\Omega^2 B^2} \frac{dE_x}{dx} t \end{aligned} \quad (6)$$

Figure 2 illustrates the relevant phase angles for an ion  $E \times B$  drifting toward the Earth. As the ion exits region A it may cross the boundary ( $x = x_0$ ) more than once. Therefore care must be taken that the final ion crossing is chosen. Note

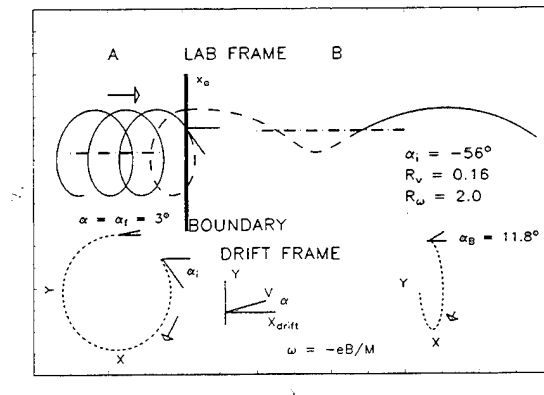


**Figure 2.** Ion kinematics in both the (top) laboratory and the (bottom) drift reference frames. The orbit in the laboratory frame is to be interpreted in  $V_x$  versus  $X$  coordinates, while those in the drift frames are in terms of  $Y$  versus  $X$ .  $O^+$  ions  $E \times B$  drift toward the Earth (left to right in the figure). In region A the electric field gradient is zero. At the boundary (thick vertical line) the gradient changes discontinuously to a constant value in region B which has a profound effect on the ion orbit. The ion may undergo multiple boundary crossings and care must be taken in choosing the appropriate initial conditions. In this case the ion first crosses the boundary at an angle  $\alpha_i$  equal to  $-56^\circ$  in the drift frame of region A while exiting at an angle of  $3^\circ$ . It is the stretching out of the ion orbit as seen in region B (top portion of figure) that leads to ion density striations. The bottom part of the figure denotes the ion orbit in the two drift frames.

that  $\alpha$  and  $\alpha_B$  are defined in the respective drift frames of regions A and B. In Figure 2 we have chosen  $\alpha = 3^\circ$ . The corresponding phase angle  $\alpha_B$  in the region B drift frame is  $11.8^\circ$ . This difference is discussed in detail below. The components of the initial velocity can be written:

$$\begin{aligned} V_{x0} &= V \cos(\alpha) + \frac{E_y}{B} \\ V_{y0} &= V \sin(\alpha) - \frac{E_0}{B} \end{aligned} \quad (7)$$

where  $V$  is the ion gyrovelocity in the zero gradient region (region A) and  $\alpha$  is the phase angle of  $V$  relative to the  $x$  axis at  $x = x_0$ . We now assume that (5) and (6) for region B can be expressed in the following form:

$$\begin{aligned} V_x(t) &= V_{dx} + V_B \cos(\Omega t - \alpha_B) \\ V_y(t) &= V_{dy}(t) - V_B \frac{\omega}{\Omega} \sin(\Omega t - \alpha_B) \end{aligned} \quad (8)$$

where  $V_{dx}$  and  $V_{dy}(t)$  are the drift terms from (5) and (6), respectively. The coefficients of the trigonometric terms in (8) correspond to an elliptical polarization of the velocity vector in the drift frame [Cole, 1976]. Expanding the trigonometric functions in (8) the usual way and equating the results to (5) and (6) with the initial conditions as defined in (7), we find the results shown in (9) that hold for all  $t \geq 0$ . It is possible to show that at  $t = 0$ , (8) reduces to (7) if the appropriate drift velocities are used together with the relations shown in (9).

$$V_B \cos(\alpha_B) = V \cos(\alpha) + \left(1 - \frac{\omega^2}{\Omega^2}\right) \frac{E_y}{B} \quad (9a)$$

$$V_B \sin(\alpha_B) = \frac{\omega}{\Omega} V \sin(\alpha) \quad (9b)$$

### Phase Bunching

First, we note that the two expressions in (9) can be combined as

$$\tan(\alpha_B) = \frac{\frac{\omega}{\Omega} \sin(\alpha)}{\cos(\alpha) - \frac{E_y}{BV} \left(\frac{\omega^2}{\Omega^2} - 1\right)} \quad (10)$$

Equation (9a) represents the continuation of the  $x$  component of the velocity in the laboratory frame; i.e.,  $V_{xB}(\text{lab}) = V_{xA}(\text{lab})$  at  $t = 0$ . The  $x$  component of the drift velocity in region B is  $(\omega/\Omega)^2$  times that in region A. Therefore the  $x$  component of the gyration velocity as seen at the boundary from the drift frame of region B is less than that in region A. In fact, if the relative drift velocity between regions B and A is sufficiently large then all ions entering region B are seen as moving tailward in the region B drift frame. (They have a phase angle  $\pi/2 < \alpha_B < 3\pi/2$ .) This is the source of phase bunching and the resulting density striations. We will now quantify these statements.

Figure 3a is a plot of (10) for various values of  $R_\omega = \omega/\Omega$ , the ratio of the gyrofrequency in region A to that in region B.

The relationship between  $R_\omega$  and the corresponding electric field gradient is given by

$$\frac{e}{M} \frac{dE_x}{dx} = \omega^2 \frac{(R_\omega^2 - 1)}{R_\omega^2} \quad (11)$$

Note the quadratic dependence on the magnetic field value. Figure 3b is a similar plot for various values of  $R_v = E_y/(BV)$ , the ratio of the drift speed to the gyrovelocity in region A. The case  $R_\omega = 1$  in Figure 3a is the zero gradient condition and corresponds to an identity mapping of  $\alpha$  onto  $\alpha_B$ . As  $R_\omega$  increases one sees that the ions tend to cluster around  $\alpha_B = \mp\pi$  or the tailward direction. The clustered ions tend to gyrate in phase and form density striations as discussed below.

In Figure 3a we use for realism an  $O^+$  energy of 2 keV, a  $B$  field value of 40 nT and a value for the cross-tail electric field of 1 mV/m. These values correspond to  $R_v = 0.16$ . As  $R_v$  increases (drift speed in region A enhanced relative to gyrovelocity) phase bunching is enhanced as seen in Figure 3b. On the other hand, at higher ion energies  $R_v$  decreases and, hence, phase bunching (i.e., density striations) is smeared out. Note, however, that even for the infinite gyrovelocity case ( $R_v = 0$ ) there is a residual phase bunching effect. Therefore a more taillike configuration (lower  $B$  field values), colder ions and enhanced values of  $E_y$  all intensify the density striations.

We will now discuss the dependence of the gyrovelocity in region B on the phase angle  $\alpha$ . This dependence arises because of the difference in the drift speed components in the two regions as seen from (9). We define the difference in the earthward drift velocity in the following:

$$\Delta V_{dx} = \left(\frac{\omega^2}{\Omega^2} - 1\right) \frac{E_y}{B} \quad (12)$$

Then the gyrovelocity in region B is determined from (9) as

$$V_B^2 = [V \cos(\alpha) - \Delta V_{dx}]^2 + V^2 \frac{\omega^2}{\Omega^2} \sin^2(\alpha) \quad (13)$$

Figures 4a and 4b show a plot of (13) for two different sets of input parameters. The  $R_\omega = 1$  case is not shown since the velocity ratio is then one for all  $\alpha$ . Note from Figure 4a that as  $R_\omega$  increases  $V_B$  also increases which reflects the complex mixture of gyrovelocity and drift velocity in region B. This implies that oxygen ions will generally have a higher gyrovelocity in a region with a sufficiently large positive electric field gradient. Figure 4b shows the variation of  $V_B$  as a function of  $R_v$ . The rather dramatic behavior of these curves near  $\alpha = 0$  can easily be understood by examining the first term on the right-hand side of (13).  $V_B$  approaches zero at  $\alpha = 0$  when  $V = \Delta V_{dx}$ . Recall that  $\alpha$  is the exit phase angle at the boundary. The kinematics of the boundary crossing, as shown in Figure 2, restrict the values of  $\alpha$  to a finite range around  $\alpha = 0$  in Figures 3 and 4. Because of the clockwise nature of the gyromotion and the value of  $R_v$  defined above the ions initially intersect the boundary over a limited range of angles. If the initial phase angle is too negative the ion will reenter region A and will finally exit at a more positive angle (see Figure 2). This effect limits the range of  $\alpha$ .

As an example, we note that for  $\alpha = 0^\circ$  we have  $V_B$  as defined in the following:



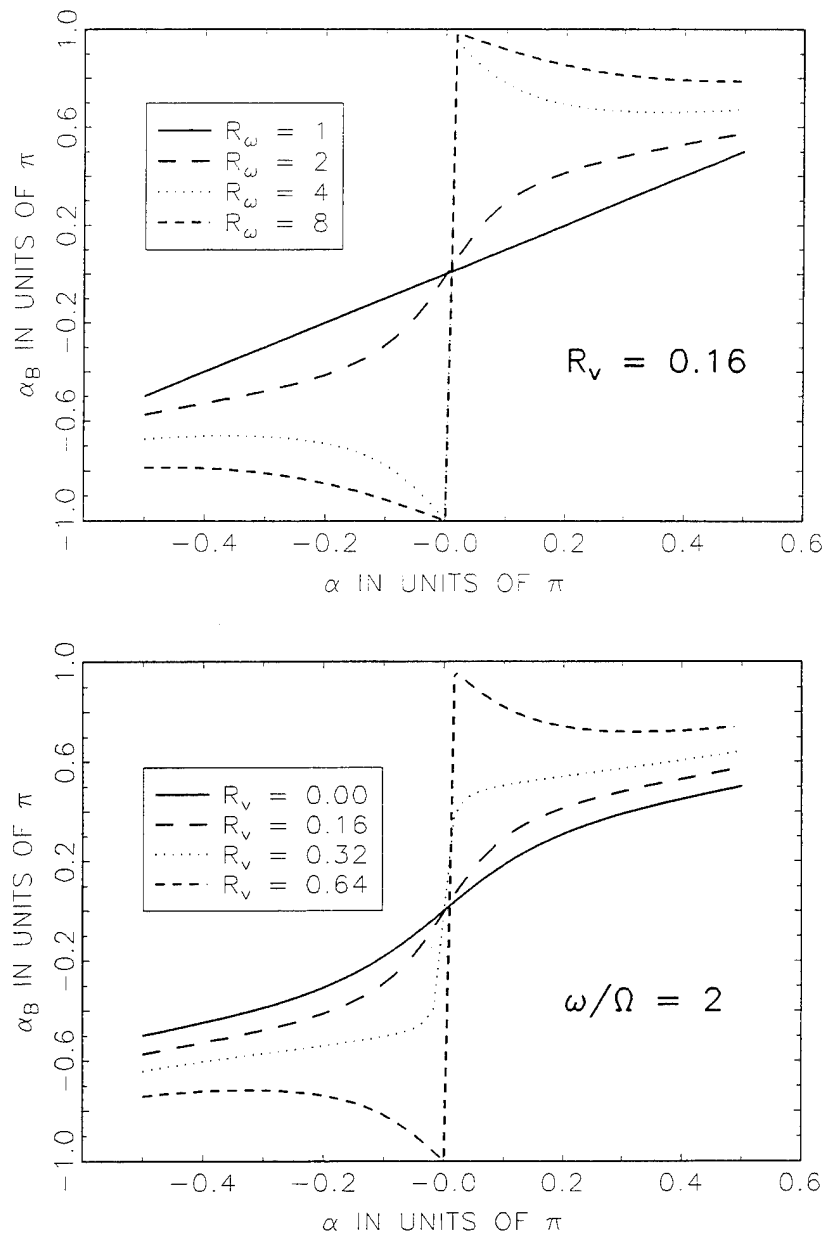


**Figure 3.** These are plots of equation (10). The phase angle  $\alpha$  is the angle of the gyrovelocity with the  $x$  axis at the boundary between the region of zero electric field gradient (region A) and the finite gradient region (region B). The parameter  $\alpha_B$  is the corresponding phase angle in region B. It should be noted that only a relatively narrow range of  $\alpha$  is relevant due to the way in which the ions cross the boundary. (a) The phase angle  $\alpha_B$  versus  $\alpha$  for various values of  $R_\omega = \omega/\Omega$ , the ratio of the ion gyrofrequencies in region A and B, respectively. Note for the tendency of the ions to bunch in the tailward ( $-X$ ) direction as the value of the gradient increases. This is ion phase bunching. (b) The phase angle  $\alpha_B$  versus  $\alpha$  for various values  $R_v = E_y/(VB)$ , the ratio of drift speed to gyrovelocity in region A.

$$V_B = |V - \Delta V_{dx}| \quad (14)$$

This is simply the entering ion velocity as seen in the region B drift frame. As pointed out previously when the associated drift velocity is sufficiently large, the entering ions will be perceived as traveling tailward in this drift frame. This is the case when  $|V_B/V| > 1$  as seen from (12) and (10). Ions entering region B with zero phase angle will have  $\alpha_B > 90^\circ$  if the difference in the drift speeds is greater than the gyrovelocity in region A.

#### Elliptical Polarization

Let us for the moment look at the implications of elliptical polarization in region B. Elliptical polarization implies that the velocity components satisfy the equation for an ellipse. From (8) we obtain

$$\frac{[V_x - V_{dx}]^2}{a^2} + \frac{[V_y - V_{dy}]^2}{b^2} = 1 \quad (15)$$

where

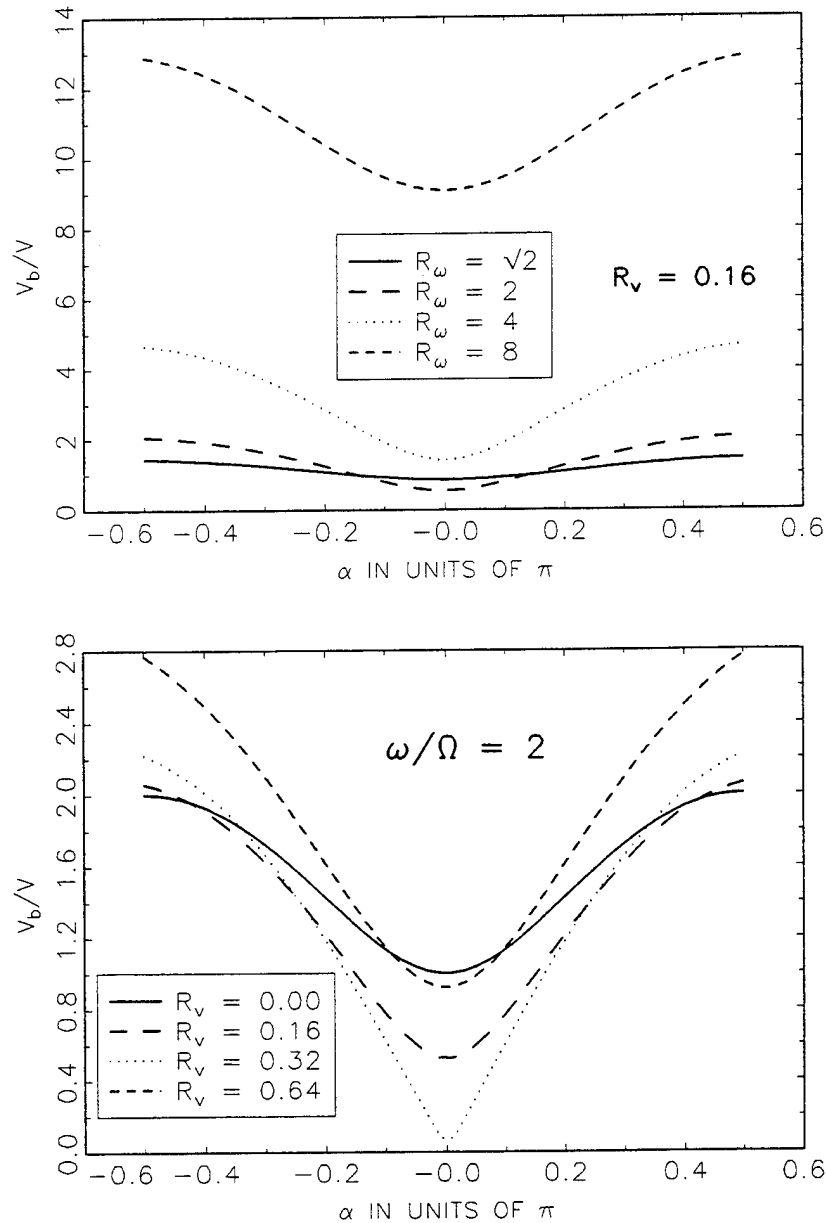


**Figure 4.** These are plots of equation (13).  $V_B$  is the gyrovelocity in region B. Note that both the drift velocity and the gyrovelocity can be greater in region B. This energy comes from the radial electrostatic potential which is sustained by the large-scale plasma flows that create the Harang discontinuity.

$$a = V_B \quad b = V_B \frac{\omega}{\Omega}$$

Elliptical polarization implies that the gyrovelocity amplitude in the  $x$  and  $y$  directions are not equal. That is, ion detectors should measure a higher average kinetic energy in the  $\pm y$  direction that is  $R_\omega^2$  times that in the  $\pm x$  direction. This could provide a way of determining large-scale electric field gradients through (11).

### Numerical Methods

Equations (3) were numerically integrated using a fourth-order Runge-Kutta technique as described by Press *et al.* [1986]. The ions were initialized in uniform increments of  $x$  over the interval  $(2\pi/\omega)(E_y/B)$  some tens of gyroradii in

front of the boundary. A sufficient number of phase angles were sampled in order to obtain reasonable statistics. The total energy at each integration step was also calculated and compared with the initial total energy. The time step was adjusted to keep the fractional difference to be less than 5 significant figures. At each integration step each ion was binned according to its  $x$  position and the appropriate counter incremented by one. A running total was maintained for each bin which represented the relative ion number density as a function of  $x$ .

### Results

#### Density Striations

We first choose a lower ion energy (200 eV) in order to highlight the striation effect. Three hundred ions were traced

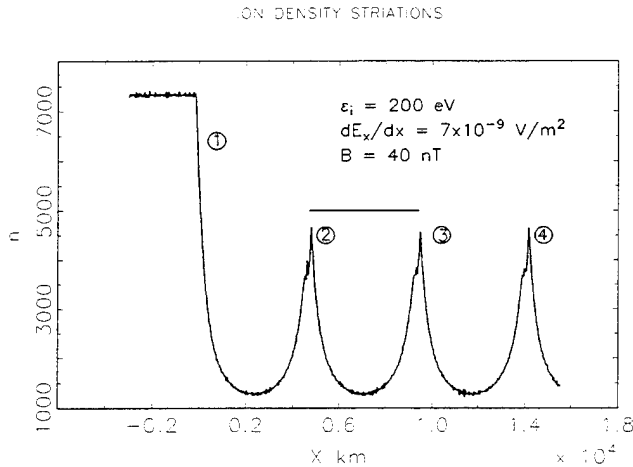


**Figure 5.** This is the relative density of an ensemble of  $O^+$  ions as they were numerically traced through regions A and B. In all cases,  $E_y = 1$  mV/m except where noted differently. Positive  $X$  points earthward. Note in region A there is a constant density as expected. The density decreases at the boundary due to the enhanced earthward drift speed in region B. Striations form in region B due to the phase bunching effect. The solid line denotes the distance an  $O^+$  ion travels during one period  $2\pi/\Omega$ , which matches the peak separation very well.

and their positions noted as described above. The solid line in Figure 5 represents the distance between striation maxima which is equivalent to the distance that an ion travels in one gyroperiod in region B. This distance  $d$  is defined by

$$d = \frac{2\pi}{\Omega} R_\omega^2 \frac{E_y}{B}. \quad (16)$$

In Figure 5,  $d = 4718$  km where in this case  $R_\omega = 1.93$ ,  $E_y = 1$  mV/m, and  $R_v = 0.51$ . The chosen  $B$  field value of 40 nT is consistent with the *Tsyganenko* [1987] model for  $L = 6$  and  $Kp = 4$ . Note the excellent agreement with the theoretical estimate for the distance between the density peaks. This distance is sensitive to the value of the electric field gradient and can substantially increase for even a relatively minor steepening of the gradient. The gradient varies, of course, inversely with the scale size of the electric field variation, so that there can be no positive correlation of this scale size with the spacing between density peaks. In region A we note a constant ion density consistent with a steady  $E \times B$  drift. The rapid drop in ion density at the boundary (labeled 1) in Figure 5 is due to the enhanced drift velocity in region B. This was checked by numerically determining the average density in region B and noting that its ratio to the density in region A was equal to  $1/R_\omega^2$ . The "test" electrons are drifting at the same ( $E_y/B$ ) speed in both regions. In order to maintain charge neutrality in a self-consistent manner in region B there must be a comparable loss of electrons to the ionosphere at the boundary. This would produce a narrow arc that is the ionospheric demarcation of the polar boundary between regions A and B. In geophysical terms we speculate that this poleward arc (number 1 in Figure 5) is the ionospheric signature of where the electric fields associated with the HDR start to affect the  $O^+$  ion dynamics in the equatorial plane. The striations,

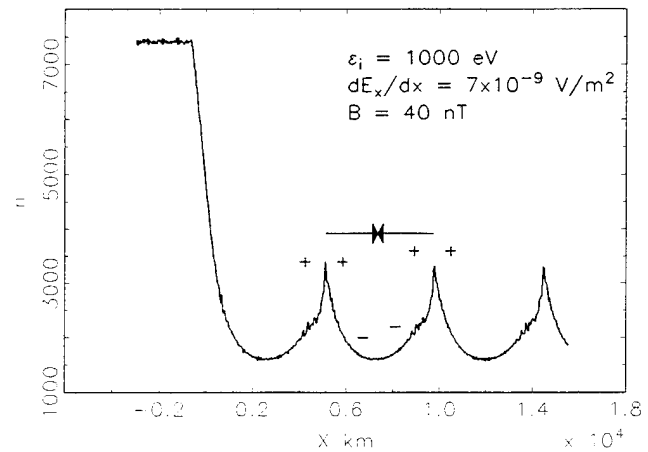


**Figure 6.** Same as for the previous figure but with the  $O^+$  ion energy increased to 1 keV. Note the decrease in the peak/valley ratio in comparison with Figure 5. The plus and minus signs denote a possible charge imbalance if field-aligned electrons cannot fully neutralize the ion density striations. The arrows denote the resulting electric field structure. Note the similarity to that expected from U-shaped field-aligned potential drops.

labeled 2, 3 and 4, could produce multiple arcs poleward of the Harang discontinuity if region B is sufficiently extended and  $O^+$  ions are plentiful in the plasma sheet.

We now change the initial gyro-energy. Figure 6 shows the results for  $O^+$  ions with a 1 keV initial energy. The distance between the density peaks is unchanged in comparison with Figure 6 (200 eV) but the ratio between the peak height to valley decreases from  $R_p = 3.6$  to 2.1 as the energy increased. The average density in region B (Figure 6) is essentially the same for Figure 5. This demonstrates that phase bunching is less pronounced at higher initial gyrovelocities as one would expect from the above discussion regarding Figure 3b.

Finite temperatures also tend to decrease  $R_p$  as seen in Figure 7. The ions are sequentially initialized in  $\Delta x$  as before, but the velocity components are independently chosen according to a Maxwellian distribution. This, no doubt, contributes to the noise seen in Figure 7. Note that  $R_p = 1.6$  in comparison to 2.1 for the monoenergetic case. We also conclude that the density striations are diminished at higher ion temperatures but are enhanced by larger electric field gradients in region B. This increases the difference in drift speed between regions A and B which is the source of the striations. A difference in drift speeds implies a difference in electric field gradients between the two regions and, therefore, it is not necessary that the electric field gradient in region A be zero.

In the present instance where  $B = 40$  nT and  $E_y = 1$  mV/m, the equatorial distance between striations varies between 667 and 4722 km for  $dE/dx$  in the range of  $0.1$ – $7.0 \times 10^{-9}$  V/m². Using a mapping factor of 0.016 based on the *Tsyganenko* [1987] magnetic field model these distances correspond to 10.7–75 km in the ionosphere.

#### Finite Boundary Effects

Up to now we have treated the boundary between regions A and B as a discontinuous change in the electric field

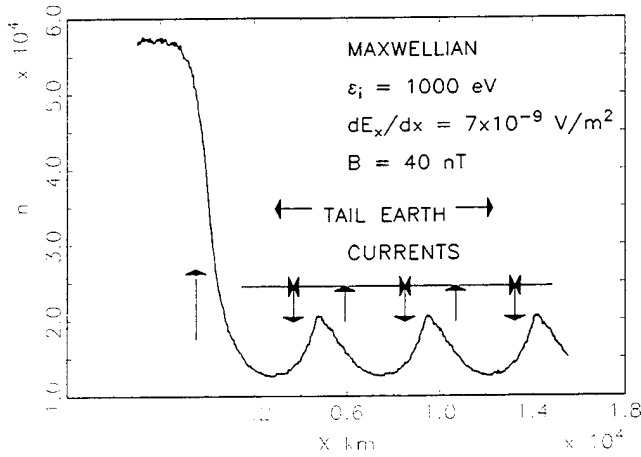


**Figure 7.** Same as Figure 6 but with the  $O^+$  ions initialized by a Maxwellian velocity distribution with a temperature of 1 keV. There is slightly more noise in region A due to the finite number of sampled ions. Also, the ion density peaks are broader and the peak/valley ratio is further decreased. The expected currents generated by the density striations are also shown. The vertical arrows denote field-aligned currents. See text.

gradient. The effects of a finite boundary region on  $R_p$  will now be investigated. This is done by using a smoothing of the boundary based upon an "error" function. The function is modified such that in nondimensional units,  $\xi = x/(\lambda R_c)$ , it goes to zero at  $-1.5$  and to  $+1.0$  at  $+1.5$  and is denoted by  $f(\xi)$ .  $R_c$  is the ion gyroradius as defined in region A. The boundary thickness  $T$  is equal to  $3\lambda R_c$ . By scaling the boundary at different multiples ( $\lambda$ ) of the ion gyroradius we can investigate the effect of varying the boundary thickness ( $T$ ). The electric field gradient is then defined by

$$\frac{dE}{dx}(x) = f\left(\frac{x}{\lambda R_c}\right) \left(\frac{dE}{dx}\right)_0 \quad (17)$$

where  $(dE/dx)_0$  is the constant value in region B. Inside the boundary where  $f(\xi)$  is changing we calculate the electric field by integrating (17). The calculations were made with  $(dE/dx)_0 = 7 \times 10^{-9}$  V/m<sup>2</sup>. Figure 8 shows the results for 200-eV and 1-keV ions. Each symbol represents a complete run such as shown in Figure 6 from which  $R_p$  is estimated. Note that  $R_p$  decreases as the boundary thickness is increased. The gyroradius of a 200 eV  $O^+$  ion is 205 km and that of a 1 keV  $O^+$  ion is 458 km in a 40-nT magnetic field. This means from Figure 8 that if the transition (boundary) region is less than  $R_E/3$  then 1 keV  $O^+$  ions will strongly striate. Even if the boundary thickness is of the order  $1R_E$ , 20% enhancements are possible. We conclude that higher ion temperatures and finite boundary effects can diminish, but not eliminate the density striations.

## Discussion

Density striations have been observed in barium releases when the injection velocity exceeds the expansion speed of the cloud [Bernhardt et al., 1993]. In that case, striations are spaced by the component of the injection speed perpendicular to  $B$  times the ion gyroperiod. These results agree with

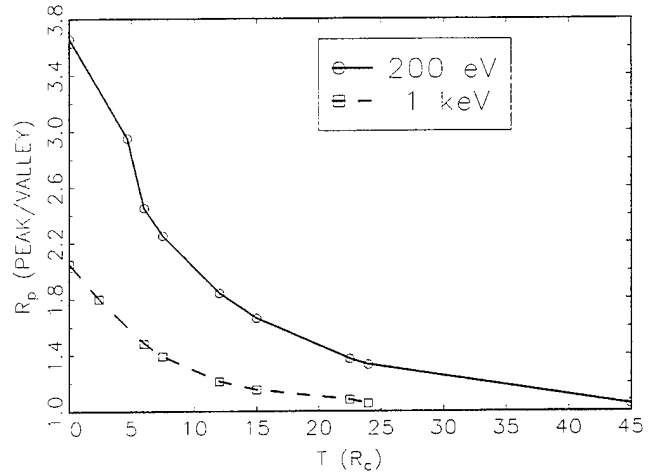


**Figure 8.** Clearly, the transition between region A and B is not physically discontinuous as assumed in the analytic treatment. Therefore we have varied the size of this boundary and parameterized it in terms of the  $O^+$  gyroradius  $R_c$  in region A. See text for more details. One sees that the peak/valley ratio  $R_p$  asymptotically decreases as the boundary is made thicker but it does not disappear. There is a residual density striation that we believe could support a field-aligned potential drop.

our work if one replaces the injection speed component by the enhanced drift speed in region B.

## Existence Criteria

We have shown that heavy ions when entering a region where a positive electric field gradient is present (e.g., near the Harang discontinuity) may produce density striations parallel to the  $y$  axis. Are the required variations in the electric field gradients reasonable and how important, if at all, is this effect for auroral arc structure? In order to answer the first question we define the conditions for the existence of significant striations to be when the difference in the  $x$  drift velocity between regions A and B exceeds the thermal speed  $V$ . This is the condition for all the ions to be seen in the tailward direction from the region B drift frame (ion phase bunching—See equation (9)). An analytical expression for this condition is

$$\Delta V_{dx} = \left( \frac{\omega^2}{\Omega^2} - 1 \right) \frac{E_y}{B} \geq V \quad (18a)$$

This leads to a conservative definition of the minimum value of the required discontinuity in the electric field gradient as a function of  $E_y$ ,  $B$ , and  $V$  as

$$\frac{e}{M} \left( \frac{dE_x}{dx} \right)_{\min} \geq \frac{\omega^2}{(R_v + 1)} \quad (18b)$$

The maximum value of the electric field gradient is defined by the condition  $\Omega^2 = 0$  (equation (2)). It is given by

$$\left( \frac{dE_x}{dx} \right)_{\max} = \frac{e}{M} B^2 \quad (19)$$

A higher value of  $E_y$  and/or a lower ion temperature (larger  $R_v$ ) for a given  $B$  value will lower the minimum  $E$

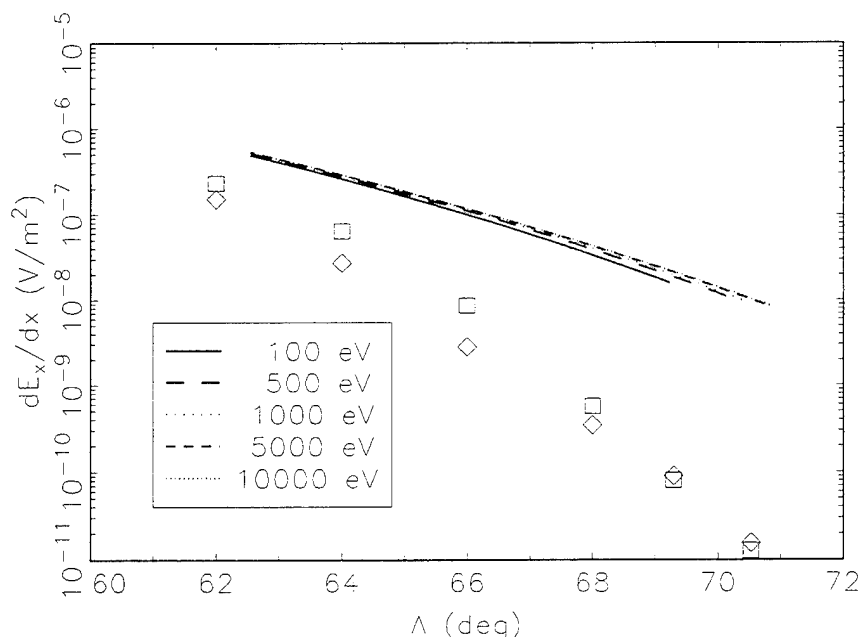


**Figure 9.** Ion density striations should exist in the near-Earth magnetosphere under disturbed conditions. The lines represent the minimum gradient required for striations to occur using a dipole magnetic field. The different lines represent different ion energies as shown in the legend. The horizontal axis is in units of invariant latitude. The squares and diamonds represent the effect of magnetic field line stretching for  $Kp = 4$  and  $5$ , respectively, according to the *Tsyganenko* [1987] model for which an  $O^+$  ion energy of  $10$  keV has been used. Clearly, the distortion of the field lines significantly lowers the threshold and will go even lower if the ion energy decreases and/or  $E_y$  increases. See text. Here we used  $E_y = 1$  mV/m.

field gradient step required to produce significant ion density striations. Lower values of  $E_y$  and/or a higher ion temperature (smaller  $R_v$ ) causes (18b) to asymptotically approach (19). The interval of gradient steps over which striations are expected is found by subtracting (18b) from (19). The result is

$$\Delta \frac{e}{M} \frac{dE_x}{dx} = \frac{R_v \omega^2}{R_v + 1} \quad (20)$$

We see that the gradient interval is larger and the minimum threshold smaller for a higher cross-tail electric field and colder ions. This is the geophysical criteria for creating the density striations. It is interesting to note that *Mozer et al.* [1980] measured electric field gradients that satisfied (19). We refer the reader to *Mozer et al.* [1980] for a comprehensive treatment of magnetospheric electric fields.

#### Stretching of Magnetic Field Lines

The curves in Figure 9 represent (18b) plotted as a function of invariant latitude,  $\Lambda$ , for a dipole magnetic field at various incident ion energies and with  $E_y = 1$  mV/m. Finite energy effects are seen to be quite weak and the required minimum value of the gradient is about  $1 \times 10^{-7}$  V/m<sup>2</sup> ((1 mV/m)/10 km) at  $\Lambda = 66^\circ$ . This value appears to be too high to be physically reasonable. Therefore we maintain that in the dipole approximation density striations do not occur. However, if the same calculation is carried out with the *Tsyganenko* [1987] model for  $Kp = 4$  (squares),  $5$  (diamonds) we see that the threshold is significantly reduced. This is due to the stretching of the magnetic field lines during disturbed periods. The *Tsyganenko* calculations were carried out with the ion temperature set at  $10$  keV. Lower ion

temperatures, enhanced field line stretching, and a higher value of  $E_y$  would lower the threshold even further. An electric field gradient of  $1 \times 10^{-9}$  V/m<sup>2</sup> ((1 mV/m)/1000 km) appears physically obtainable. For example, a  $40$ -nT magnetic field reduces the above value for the gradient minimum to  $9.6 \times 10^{-9}$  V/m<sup>2</sup>. This leads us to conclude that under disturbed conditions density striations probably exist.

During the growth phase of a substorm, ionospheric oxygen seeds the central plasma sheet [*Daglis et al.*, 1990; *Cladis and Francis*, 1992] which provides a striation source. Using data from the equatorial SCATHA satellite, *Mullen and Gussenhoven* [1983] note that during periods of high magnetic activity, the  $O^+$  concentration may increase more than a factor of  $4$ , replacing  $H^+$  as the main constituent in the near-Earth plasma sheet.

#### Auroral Arcs

Our model provides a possible magnetospheric driver for auroral arc formation. The density striations through charge separation and current divergence can create equatorial voltage or current sources which can be used as inputs for arc models [*Lysak*, 1990; *Chiu et al.*, 1981; *Chiu and Cornwall*, 1980].

This returns us to the second question of the introduction regarding striations and auroral arc structure. We now turn to Figure 6 and address charge neutrality. The electron motion is characterized in the  $x$  direction by a uniform  $E_y/B$  drift which, in the absence of time-dependent or field-aligned sources, yields a constant electron density as a function of  $x$ . Therefore the ion density variations must be neutralized either by the generation of very intense electric fields that demagnetize the electrons and allow them to join the ions or

else charge neutrality is maintained by electrons moving parallel to  $B$ . Since the latter is far more probable, we expect that in the regions of ion density enhancements there are upward flowing electrons, while in the regions of ion depletion we expect downward flowing electrons. It is interesting to note that if charge neutrality is not strictly obeyed then small-scale reversed electric field structures consistent with field-aligned potential drops could develop in the regions of ion depletion. These smaller-scale variations in the electric field would be superimposed on the larger-scale gradient. Larger-scale variations are considered to be much larger than the  $O^+$  gyroradius while smaller-scale variations are on the same order. This idea is highlighted in Figure 6 by the plus and minus signs representing the charge imbalance and the reversed arrows that denote the expected electric fields resulting from such a charge imbalance. It should be noted that a much weaker electric field gradient could still produce small deviations from charge neutrality with measurable electric fields. In the present case we have assumed that the electric field gradients are created by large-scale plasma flows as observed by Heppner and Maynard [1987] and as modeled by Erickson *et al.* [1991]. We therefore expect that the smaller-scale variations can be treated as perturbations. The test particle approach presented here gives zero-order results that could lead to a self-consistent description.

For the sake of discussion we will presently assume that striations do lead to a valid description of periodic auroral arcs and interpret the results in terms of our earlier work [Rothwell *et al.*, 1991]. Recall that we developed a two-component circuit for describing the current wedge representation of an auroral arc. For consistency it was necessary to close the north-south ionospheric current in the arc by an earthward inertia current in the equatorial plane which is given by

$$J_x = K_m \frac{\partial E_x}{\partial x} \quad (21)$$

$$K_m = \frac{\rho d_{\parallel} E_y}{B^3}$$

where  $\rho$  is the mass density and  $d_{\parallel}$  is the integration height along the magnetic field in the equatorial plane. Note that the time-average of (5) also leads to an average inertial current which is identical to (21) times  $R_{\omega}^2$ . Since the particle density is inversely proportional to the  $x$  component of the particle velocity, we see that the ions have a maximum velocity in regions of ion depletion and a minimum velocity in regions of ion enhancement. Electrons drift at a constant speed and have a number density only slightly different from that of the ions. In the regions of ion depletion therefore we expect enhanced earthward currents while near the ion density peaks we expect tailward currents (see Figure 7). The divergence of these currents requires field-aligned currents as shown. There is therefore a close analogy between our previous finite element circuit model [Rothwell *et al.*, 1991] and the test particle analysis presented here. Finally, we note that at the Harang discontinuity itself there is a rapid electric field reversal that may momentarily trap and stochastically heat and accelerate the  $O^+$  ions in the manner described by Rothwell *et al.* [1992].

In summary, the nonadiabatic behavior of even cold  $O^+$  ions in contrast with the expected adiabatic behavior of  $H^+$  and electrons near the HDR could be a source for auroral arc

structure. The electric field gradient preferentially decouples the  $O^+$  ions from the magnetic field, weakening the westward gradient-curvature drift that strongly affects the  $H^+$  ions. The  $O^+$  ions then periodically bunch along the direction of the electric gradient (perpendicular to the Harang discontinuity) which results in density striations that are almost parallel to the east-west direction. This would explain the usual arc elongation in that direction. The  $O^+$  ions then generate an enhanced inertial current that is perpendicular to the striations. This equatorial current is in the right direction to close the current wedge as proposed by Rothwell *et al.* [1991]. Other features to recommend this approach is its explicit dependence on the  $O^+$  population [Daglis *et al.*, 1990; Cladis and Francis, 1992] and on the stretching of the magnetic field lines. Both features are closely connected with the substorm process.

**Acknowledgments.** We are grateful to Michael Heinemann and Jay Albert for interesting and fruitful discussions on this subject. One of us (M.B.S.) would like to acknowledge support from Air Force contract F19628-92-K-0007.

The Editor thanks M. A. Temerin and another referee for their assistance in evaluating this manuscript.

## References

- Bernhardt, P. A., J. D. Huba, M. B. Pomgratz, D. J. Simmons, and J. H. Wolcott, Plasma irregularities caused by cycloidal bunching of the CRESS G-2 barium release, *J. Geophys. Res.*, 1613–1627, 1993.
- Chiu, Y. T., and J. M. Cornwall, Electrostatic model of the quiet auroral arc, *J. Geophys. Res.*, 85, 543–556, 1980.
- Chiu, Y. T., A. L. Newman, and J. M. Cornwall, On the structures and mapping of auroral electrostatic potentials, *J. Geophys. Res.*, 86, 10029–10037, 1981.
- Cladis, J. B., and W. E. Francis, Distribution in the magnetotail of  $O^+$  ions from cusp/cleft ionosphere: a possible substorm trigger, *J. Geophys. Res.*, 97, 123–130, 1992.
- Cole, K. D., Effects of crossed magnetic and (spatially dependent) electric fields on charged particle motion, *Planet. Space Sci.*, 24, 515–518, 1976.
- Daglis, A., E. T. Sarris, and G. Kremser, Indications for ionospheric participation in the substorm process from AMPTE/CCE observations, *Geophys. Res. Lett.*, 17, 57–60, 1990.
- Erickson, G. M., R. W. Spiro, and R. A. Wolf, The physics of the Harang discontinuity, *J. Geophys. Res.*, 96, 1633–1645, 1991.
- Heppner, J. P., and N. C. Maynard, High latitude electric field models, *J. Geophys. Res.*, 92, 4467–4490, 1987.
- Lysak, R. L., Electron and ion acceleration by strong electrostatic turbulence, in *Physics of Auroral Arc Formation*, *Geophys. Monogr. Ser.*, vol. 25, S.-I. Akasofu and J. R. Kan, editors, pp. 444–450, AGU, Washington, D. C., 1981.
- Lysak, R. L., Electrodynamical coupling of the magnetosphere and the ionosphere, *Space Sci. Rev.*, 52, 33–87, 1990.
- Marklund, G., Auroral arc classification scheme based on the observed arc-associated electric field pattern, *Planet. Space Sci.*, 32, 193–211, 1984.
- Maynard, N. C., Electric field measurements across the Harang discontinuity, *J. Geophys. Res.*, 79, 4620–4631, 1974.
- Mozer, F. S., C. A. Cattell, M. K. Hudson, R. L. Lysak, M. Temerin, and R. B. Torbert, Satellite measurements and theories of auroral particle acceleration, *Space Sci. Rev.*, 27, 155, 1980.
- Mullen, E. G., and M. S. Gussenhoven, SCATHA environmental atlas, *Tech. Rep. AFGL TR-830002*, Air Force Geophys. Lab., Bedford, Mass., 1983.
- Press, W. H., B. P. Flannery, S. A. Teukolsky, and W. T. Vetterling, *Numerical Recipes*, University of Cambridge, New York, 1986.
- Rothwell, P. L., M. B. Silevitch, L. P. Block, and C.-G. Fälthammar, Prebreakup arcs: A comparison between theory and experiment, *J. Geophys. Res.*, 96, 13,967–13,975, 1991.
- Rothwell, P. L., M. B. Silevitch, L. P. Block, and C.-G. Fältham-

- mar, Acceleration and stochastic heating of ions drifting through an auroral arc, *J. Geophys. Res.*, 97, 19,333–19,339, 1992.
- Tsyganenko, N. A., Global quantitative models of the geometric field in the cislunar magnetosphere for different disturbance levels, *Planet. Space Sci.*, 35, 1347–1358, 1987.
- Yang, W. H., and J. R. Kan, Generation of conic ions by auroral electric fields, *J. Geophys. Res.*, 88, 465–468, 1983.
- P. L. Rothwell, Geophysics Research Directorate, Phillips Laboratory, 29 Randolph Road, Hanscom Air Force Base, MA 01731-3010.
- M. B. Silevitch, Center for Electromagnetics Research, Northeastern University, Boston, MA 02115. (e-mail: msilevit@lynx.neu.edu)

---

L. P. Block and C.-G. Fälthammar, Department of Plasma Physics, Alfvén Laboratory, Royal Institute of Technology, S 100 44 Stockholm 70, Sweden. (e-mail: SPAN.plafys::falthammar)

(Received February 26, 1993; revised August 25, 1993; accepted September 3, 1993.)

# Single Ion Dynamics and Multiscale Phenomena

P. L. Rothwell

*Geophysics Research Directorate, Phillips Laboratory, Hanscom AFB, Bedford, Massachusetts*

M. B. Silevitch

*Center for Electromagnetics Research, Northeastern University, Boston, Massachusetts*

Lars P. Block and Carl-Gunne Fälthammer

*Division of Plasma Physics, Alfvén Laboratory, Royal Institute of Technology, Stockholm, Sweden*

The magnetosphere is populated by hot, tenuous plasma. Therefore, it is expected that at times electric fields will dominate the single ion dynamics which invalidates the usual fluid MHD description. We have found two such examples which we review in this paper. (1) The effect of a large scale electric field gradient on the single ion dynamics which leads to density striations and possible auroral arc formation. (2) Large spatial variations of the electric field on the scale of the ion gyro radius which causes chaotic untrapping of  $O^+$  ions to occur.

## 1. INTRODUCTION

In this paper we review the interplay between micro and meso-scale phenomena that we have found and highlight the conditions underwhich an MHD approach is not valid. This is done by examining single ion dynamics in a spatially varying electric field. For example, we examined [Rothwell et al. 1994] the effect of the electric field variation near the equatorial Harang discontinuity on single ions as they drift earthward from the magnetotail. We found that under substorm growth phase conditions single ion trajectories were modified and caused macroscopic density striations if the electric field gradient is sufficiently strong. Conservation of the associated inertial current implied a connection between the striations and auroral arcs. Similarly if the electric field has a sufficiently large second derivative in the electric field then the ion gyro orbits become very distorted with the gyro velocity being highly variable over a gyro orbit. The problem is analogous to that of a finite

pendulum. Just as a finite pendulum if driven sufficiently hard will pass from an oscillating mode to a rotating one a gyrating ion will become unmagnetized if the second derivative of the electric field is sufficiently large. This can cause heavy ions to become chaotically untrapped [Rothwell et al., 1995]. In this paper we briefly review this work with emphasis on the physical concepts.

## 2. TWO EXAMPLES OF MULTISCALE PHENOMENA

**Constant First Derivative in  $E_x$ .** We begin by looking at the simple case of a constant electric field gradient. The equations of motion [Cole 1976] are given by

$$\begin{aligned}\frac{dV_x}{dt} &= \frac{e}{M}(E_x(x(t)) + V_y B) \\ \frac{dV_y}{dt} &= -\frac{e}{M}V_x B\end{aligned}\tag{1}$$

which can be combined into a single equation

$$\frac{d^2 V_x}{dt^2} + (\omega^2 - \frac{e}{M} \frac{dE_x}{dx}) V_x = 0\tag{2}$$



GAUSS Thu May 18 10:39:39 1995

## ION DENSITY STRIATIONS

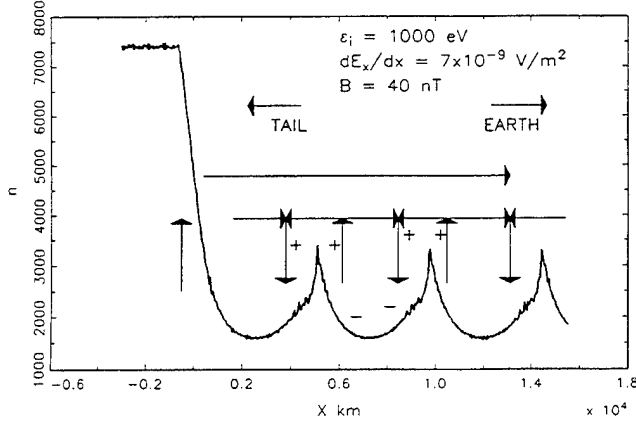


Fig. 1. A computer simulation of  $O^+$  ions ExB drifting towards the earth and encountering an electric field gradient at  $x=0$ . Phase bunching causes density striations to form in the gradient region which could be a source of multiple auroral arcs.

where we define the gyro-frequency to be

$$\Omega^2 = \omega^2 - \frac{e}{M} \frac{dE_x}{dx} \quad (3)$$

The main effect of a spatial gradient in  $E_x$  is to modify the gyrofrequency. The symbol  $\omega$  denotes the gyrofrequency  $eB/M$ . It is immediately seen that if  $\Omega^2 < 0$  then  $V_x$  has an exponential rather than an oscillatory solution. That is, if the electric field gradient is too steep the ions become locally untrapped. This effect becomes significant in regions of the magnetosphere where the magnetic field is weak and the electric field gradient is strong. One such region is the equatorial Harang discontinuity. For example, (3) predicts that  $O^+$  ions will become untrapped in a  $40\gamma$  magnetic field if  $dE_x/dx > 9.6 \times 10^{-9} \text{ V/m}^2$ .

The next questions to ask relates to what happens when an ensemble of  $O^+$  ions EXB drift from the magnetotail into a region of significant earthward (positive) electric field gradient. It has been noted by Daglis et al. [1991] and others that during active periods there is an efficient transport of ionospheric  $O^+$  to the plasma sheet. What effect does this global transport have interfacing with the mesoscale electric field structure of the Harang discontinuity? How does this interfacing create micro-scale structure and do the different processes acting at different scales reach some form of equilibrium?

**Density Striations.** Oxygen ions injected into the plasma sheet drift earthward due to a cross-tail electric field  $E_y$ . The solution to (1) with an  $E_y$  term was reported by Rothwell et al. [1994]. The earthward drift velocity  $V_{xd}$  in the region of finite  $dE_x/dx$  becomes

$$V_{xd} = \frac{\omega^2}{\Omega^2} \frac{E_y}{B} \quad (4)$$

so that if  $dE_x/dx$  is positive then  $V_{xd} > E_y/B$ . Earthward drifting ions that encounter a region of  $dE_x/dx > 0$  acquires a higher drift velocity than they had outside the region. Before encountering the E-field gradient the ions are uniformly distributed in phase angle in the  $E_y/B$  drift frame. Upon encountering the gradient region the ions acquire a faster drift velocity. The acceleration of the drift frame imparts a negative velocity component in that frame to each ion. This causes the ions to bunch in phase in the tailward direction. They then gyrate as a group. Where the ions have their turning points in the gradient region, density enhancements or striations form [Rothwell et al. 1994].

Figure 1 illustrates the effect using a computer simulation. Monoenergetic 1 keV ions are injected tailward of the gradient region which begins at  $x=0$ . The increase in the ion drift velocity in the gradient region causes the density  $n$  to drop from its previous value which requires an upward field aligned current near  $x=0$  to maintain charge quasi-neutrality. The long horizontal arrow denotes an earthward inertial current  $J_x$  which is the continuation of this upward current in the magnetosphere. In this picture the current  $J_x$  closes on the earthward side of the Harang discontinuity to the ionosphere, creating a macroscopic radial current system between the ionosphere and the equatorial plane.

The presence of density striations modulates the earthward inertial current  $J_x$  and is denoted by the shorter arrows in Figure 1. The modulation creates a series of smaller current wedges that are related to the multiple arcs which are symbolized by the upward pointing arrows. Physical insight can be gained by deriving an expression for  $J_x$ . We assume a coordinate system such that positive  $x$  is earthward,  $y$  points westward and  $z$  is parallel to  $B$ , the magnetic field. We also assume that the number flux of ions is conserved as they drift earthward. This means that the earthward ion flux  $F_i$  in the electric field gradient region is the same as outside (i.e.  $F_i = N_0 E_y/B$  where  $N_0$  is the ambient ion number density in the plasma sheet). However, in the gradient region the ions are drifting faster than the electrons according to (4). Therefore, the average ion density in the gradient region is  $N_0/(\omega^2/\Omega^2)$ . Charge neutrality requires that the electron number density is the same as the ion number density. This can only be achieved by a magnetic-field-aligned electron flux at the onset of the gradient region. The electron flux in the gradient region is  $F_e = N_0(\Omega^2/\omega^2)(E_y/B)$ . The net electric current is equal to  $e(F_i - F_e)$  which can by using (3) be written as

$$J_x = \left( \frac{\rho_o E_y}{B} \right) \frac{1}{B^2} \frac{dE_x}{dx} \quad (5)$$

$$J_x = \frac{\omega^2}{\Omega^2} \frac{\rho_o E_y}{B^3} \frac{dE_x}{dx}$$

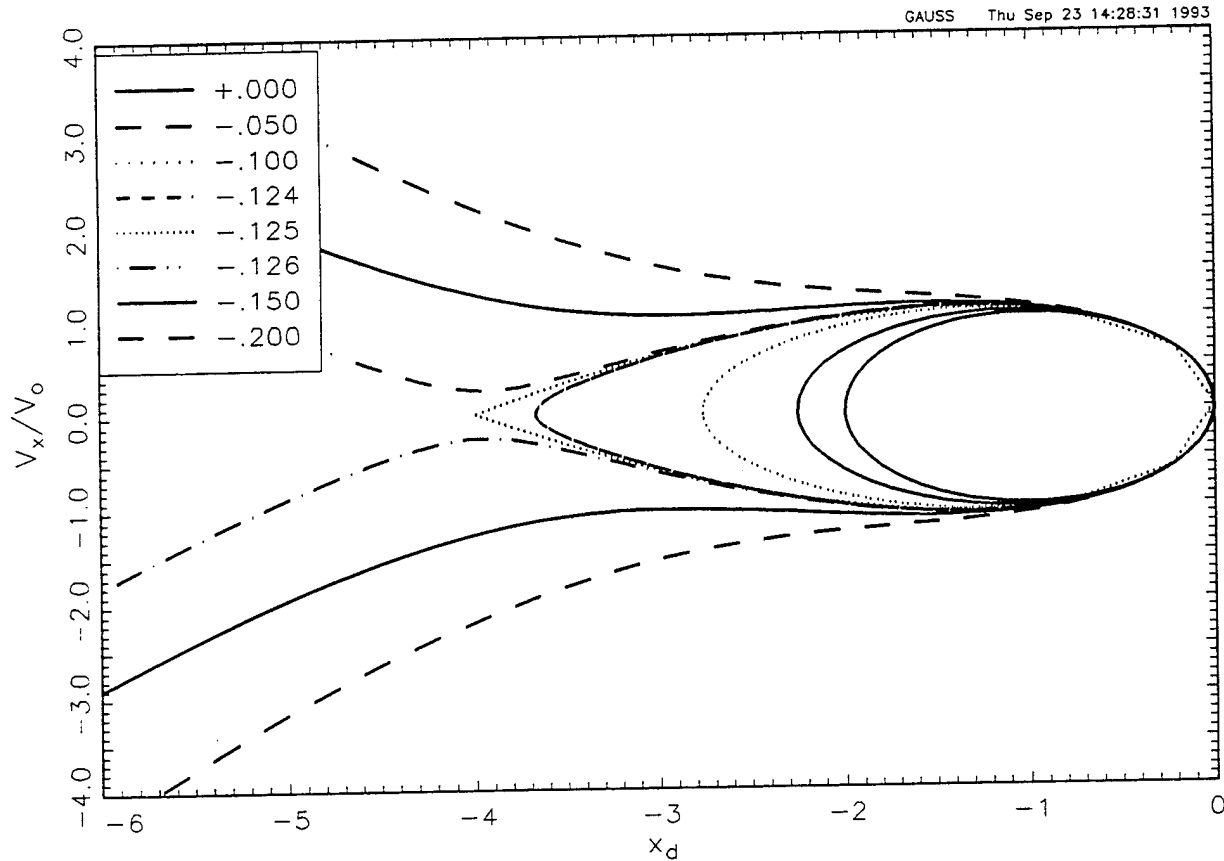


Fig. 2. Orbit shapes for negative  $d^2E/dx^2$  and for  $\alpha_0 = \pi/2$ . Note that the transition to open (untrapped) orbits for  $A_d \leq -1/8$  where  $A_d$  is a dimensionless representation of  $d^2E/dx^2$ .  $x_d = -4$  is a critical point and is located at twice the ion gyro-diameter corresponding to the  $d^2E/dx^2 = 0$  orbit. Similarly untrapping occurs for  $\alpha_0 = +\pi/2$ ,  $x_d = +4$  when  $A_d \geq +1/8$ .

The symbol  $\rho$  denotes mass density in the gradient region and  $\rho_0$  refers to the mass density in the gradient-free region. The mass flux inside the bracket will be constant if the ions are conserved as they drift earthward. In this case  $J_x$  varies as  $B^2$  rather than  $B^3$ .

The principle of quasi-neutrality requires that locally  $N_e(x) \approx N_i(x)$ . The electrons have an earthward flux  $F_e = N_e(x)E_y/B$  where  $N_e(x)$  approximates the local number density of the ions which is spatially dependent due to phase bunching. Satisfaction of the quasi-neutrality principle requires that electrons are free to move along magnetic field lines between the ionosphere and magnetosphere. In other words, the presence of density striations implies magnetospheric-ionospheric coupling and the formation of periodic auroral structures. Density striations and the principle of charge quasi-neutrality lead to perturbations in the earthward inertial current  $J_x$  (Figure 1) associated with the gradient region. Note that in regions of density enhancement the perturbation in  $J_x$  is tailward and in regions of density depletion it is earthward. This requires a downward field-aligned current where the density

is increasing and an upward field-aligned current where the density is decreasing. Since upward field-aligned currents are carried in part by precipitating electrons this is where we locate the auroral arcs in this model. Reference is made to Rothwell et al. [1994] for more details. This is an example of how the meso-scale properties of the electric field modifies the micro-scale orbital characteristics of the single ions so as to produce unexpected micro-scale structure that may have geophysical significance.

For example, periodic arc structures spaced 35 km apart in the ionosphere correspond to magnetospheric density striations spaced approximately  $2 \times 10^6$  apart at the equator. A simple calculation shows that the required electric field gradient in the equatorial plane is  $5 \times 10^{-9}$  V/m<sup>2</sup>. This assumes  $E_y = 1 \times 10^{-3}$  V/m and  $B = 40$  nT.

**Constant Second Derivative in  $E_x$ .** We now look at how electric field structure on the scale size of an ion gyroradius can modify the gyro motion. The effect of a second spatial derivative

of  $E_x$  will now be considered. The presence of a constant second derivative in  $E_x$  can be examined by expanding the first derivative about the initial position  $x_0$  of the ion.

$$\frac{dE_x}{dx} = \frac{dE_x}{dx} \Big|_{x=x_0} + \frac{d^2E_x}{dx^2}(x-x_0) \quad (6)$$

Then equation (1) can be rewritten as

$$\frac{d^2V_x}{dt^2} + \Omega_0^2 V_x - \frac{e}{M} \frac{d^2E_x}{dx^2}(x-x_0) V_x = 0 \quad (7)$$

where  $\Omega_0$  is the gyro-frequency as defined in equation (3) with  $dE_x/dx = dE_x/dx|_{x=x_0}$ . This is to be distinguished from the gyro-frequency  $\Omega$  which reflects a constant second derivative in  $E_x$ . Equation (7) can be easily integrated by noting that  $V_x = dx/dt$  in the second and third terms. A subsequent integration is also trivial after the previous result is multiplied by  $V_x$ . The final result is cast into the following form.

$$\left(\frac{dx}{dt}\right)^2 = A_d(x_d - a_d)(x_d - b_d)(x_d - c_d) \quad (8)$$

where the subscript 'd' refers to dimensionless quantities.

Equation (8) is solved in terms of Jacobian Elliptic functions [Byrd and Friedman 1971]. The key point is that the usual concept of uniform circular gyration about the magnetic field line is not true in this case. The orbits are highly distorted by the electric field structure and the orbital speed is highly variable. Figure 2 shows the solutions to (8) for large, negative  $d^2E_x/dx^2$ . If the second derivative in  $E_x$  is sufficiently large the ions can become locally untrapped. There is a critical point at  $A_d = -1/8$ , where  $A_d$  is proportional to  $d^2E/dx^2$ . It is found that the untrapping criterion is dependent on the initial azimuthal phase angle of the ion and the sign of the second derivative. This untrapping criterion will be satisfied for 5 keV  $O^+$  ions in a 40 nT magnetic field if  $|d^2E/dx^2| \geq 40$  (mV/m)/ $R_E^2$ .

### 3. DISCUSSION AND CONCLUSIONS

Multi-scale phenomena has been shown for the two cases considered. In the first case a large scale electric field gradient

was shown to produce a set of nested current systems between the ionosphere and the magnetosphere. Presently, we are investigating the self-consistency of the structure shown in Figure 1. That is, the upward current regions are associated with field-aligned potential drops. The question is whether the equatorial electric fields associated with these currents are sufficiently strong as to scatter the ions and, thereby, destroy the striations. The result depends on the auroral arc model used. In the second case small scale electric field structure strongly affected the orbital dynamics of trapped ions. In both examples that were considered the unifying idea is that when (3) becomes small or negative then finite orbit effects become important. Another important example that depends on this concept is the stochastic heating of ions [Rothwell et al. 1992].

A negative value of (3) implies that in the x-direction the ion's increase in momentum due to the electric field gradient is larger than the ion's decrease in momentum due to the magnetic field. This is the physical basis of untrapping.

### 4. REFERENCES

- Byrd, P. F., and M. D. Friedman, *Handbook of Elliptic Integrals for Engineers and Scientists, 2nd edition, revised*, Springer-Verlag Publ., New York, 1971.
- Cole, K. D., Effects of crossed magnetic and (spatially dependent) electric fields on charged particle motion, *Planet. Space Sci.*, 24, 515-518, 1976.
- Daglis, I. A., E. T. Sarris, and G. Kremser, Ionospheric contribution to the cross-tail current during the substorm growth phase, *J. Atmos. Terr. Phys.*, 53, 1091-1098, 1991.
- Rothwell, P. L., M. B. Silevitch, L. P. Block, and C.-G. Fälthammar, Acceleration and stochastic heating of ions drifting through an auroral arc, *J. Geophys. Res.*, 97, 19,133-19,339, 1992.
- Rothwell, Paul L., Michael B. Silevitch, Lars P. Block, and Carl-Gunne Fälthammar,  $O^+$  phase bunching and auroral arc structure, *J. Geophys. Res.*, 99, 2461-2470, 1994.
- Rothwell, Paul L., Michael B. Silevitch, Lars P. Block, and Carl-Gunne Fälthammar, Particle dynamics in a spatially varying electric field, accepted for publication in *J. Geophys. Res.*, 1995.

## Particle dynamics in a spatially varying electric field

Paul L. Rothwell

Geophysics Research Directorate, Phillips Laboratory, Hanscom Air Force Base, Bedford, Massachusetts

Michael B. Silevitch

Center for Electromagnetics Research, Northeastern University, Boston, Massachusetts

Lars P. Block and Carl-Gunne Fälthammar

Division of Plasma Physics, Alfvén Laboratory, Royal Institute of Technology, Stockholm, Sweden

**Abstract.** For an MHD description of a plasma a distinct separation between the macroscopic and microscopic spatial and temporal scales is assumed. In this paper we solve the particle dynamics with finite first and second spatial derivatives in the electric field. We find that (1) MHD (ideal and nonideal) becomes invalid for a sufficiently strong constant electric field gradient perpendicular to the magnetic field; (2) a sufficiently large second derivative in the electric field can cause heavy ions to become chaotically untrapped; (3) for an electric field with a constant gradient the ion drift velocity is equal to  $(\mathbf{E} \times \mathbf{B})/B^2$  as long as the orbit-averaged value of  $\mathbf{E}$  is used. There are no finite currents associated with the ion drift for such an electric field; (4) perturbation technique gives a poor approximation to the ion drift velocity even for values of the second derivative that may well occur in the magnetosphere. Results 1 and 2 provide necessary criteria for the applicability of magnetospheric MHD models of spatially varying electric fields. They also predict an asymmetry in the heavy ion fluxes, a feature that could be useful in inferring magnetospheric electric field structure. We illustrate these results by application to the Harang discontinuity. It is found that if the interplanetary magnetic field swings northward under substorm growth conditions the orbits of the equatorial  $O^+$  may dramatically change due to result 2. This effect may contribute to the substorm onset process.

### 1. Introduction

It has long been recognized that there is a coupling between the microscopic single-ion dynamics as defined by the ion gyroradius and macroscopic MHD phenomena. Two obvious examples are the kinetic Alfvén wave [Hasegawa, 1976; Goertz, 1984] and the ion tearing mode [Galeev and Zelenyi, 1976]. More recently, we showed that the chaotic behavior of single-ion trajectories may cause macroscopic heating and acceleration as they drift through an auroral arc [Rothwell *et al.*, 1992]. Another important example is the effect of the electric field variation near the Harang discontinuity on single ions as they drift earthward from the magnetotail. We found [Rothwell *et al.*, 1994] that under substorm growth phase conditions, single-ion trajectories were modified and caused macroscopic density striations. Current conservation of the associated inertial current implied a connection between the striations and auroral arcs.

In this paper we examine single-ion dynamics in a spatially varying one-dimensional electric field  $E_x(x)$  which is perpendicular to a magnetic field  $B = B_z$ . We analytically solve and numerically analyze single-ion motion in a magnetic field when

the first and second spatial derivatives of a coexisting electric field are significant. The single-ion dynamics for a constant one-component electric field gradient have been previously treated by Cole [1976]. Cole argued that the ion drift velocity in the  $-y$  direction was greater than  $-E_x(x)/B$  and therefore a current in that direction was present. Here we show that for a one-dimensional electric field there is no drift current. In section 2 we treat the ion dynamics for a constant electric field gradient. We also show in section 2 that the ion drift velocity is still equal to  $-E_x(x)/B$  if the value of the electric field at the center of the ion gyro-orbit is used. In sections 3 and 4 we treat the more general case of a constant second derivative in  $E_x$ . Exact solutions are found in terms of Jacobian elliptic functions (JEF). The orbit shape can become severely distorted by the electric field, and the concept of a particle uniformly rotating about  $\mathbf{B}$  in a circular path is no longer sound. For sufficiently large values of the second derivative in  $E_x$  the ions become untrapped. There are therefore situations in which even a nonideal MHD that treats finite orbit effects in a perturbative manner is not valid. Also, our results provide criteria for the applicability of magnetospheric MHD models for spatially varying electric fields in the magnetosphere. In section 5 these results are applied to the Harang discontinuity for the case when the interplanetary magnetic field swings northward. It is argued that the change in orbital characteristics of the ions in that part of the Harang where the electric field has sufficient curvature may contribute to substorm onsets. Conclusions and a short discussion are contained in section 6.

Copyright 1995 by the American Geophysical Union.

Paper number 95JA00627.  
0148-0227/95/95JA-00627\$05.00

## 2. A Constant First Derivative of $E_x$

We choose a coordinate system such that the  $z$  axis is parallel to the magnetic field  $\mathbf{B}$ . In addition to  $\mathbf{B}$  there is an electric field in the  $x$  direction with a constant gradient. The equations of motion [Cole, 1976] are given by

$$\begin{aligned} \frac{dV_x}{dt} &= \frac{e}{M} (E_x(x(t)) + V_y B) \\ \frac{dV_y}{dt} &= -\frac{e}{M} V_x B \end{aligned} \quad (1)$$

which can be combined into a single equation:

$$\frac{d^2 V_x}{dt^2} + (\omega^2 - \frac{e}{M} \frac{dE_x}{dx}) V_x = 0 \quad (2)$$

The solutions for  $V_x(t)$  and  $V_y(t)$  are

$$\begin{aligned} V_x(t) &= V_{x0} \cos(\Omega t) + \dots \\ &\dots + \frac{\omega}{\Omega} (V_{y0} + \frac{E_x(x_0)}{B}) \sin(\Omega t) \end{aligned} \quad (3)$$

$$\begin{aligned} V_y(t) &= V_{y0} - \frac{\omega^2}{\Omega^2} (V_{y0} + \frac{E_x(x_0)}{B}) \dots X \\ &\dots (1 - \cos(\Omega t)) - \frac{\omega}{\Omega} V_{x0} \sin(\Omega t) \end{aligned} \quad (4)$$

$$\Omega^2 = \omega^2 - \frac{e}{M} \frac{dE_x}{dx} \quad (5)$$

where  $x_0$  is the initial position of the ion and  $V_{x0}$  and  $V_{y0}$  are the velocity components at  $t=0$ .  $E_x(x_0)$  is the value of  $E_x(x(t))$  at  $t=0$ . The coordinate origin ( $x=0$ ) is assumed to be located at the gyrocenter. Note that  $E_x(x_0)$  is different for each initial position along the trajectory as defined by (3) and (4). In addition, (2) will only describe trapped orbits if  $\Omega^2 > 0$  or  $dE_x/dx < (e/M)B^2$ ; otherwise, the ions are exponentially accelerated by the electric field. For  $0 < dE_x/dx < (e/M)B^2$ ,  $\omega^2/\Omega^2 > 1$ , and for  $dE_x/dx < 0$ ,  $\omega^2/\Omega^2 < 1$ . Equations (3) and (4) represent an elliptical gyration plus a constant drift in the  $-y$  direction. The drift velocity  $V_{yd}$  is given by

$$V_{yd} = V_{y0} - \frac{\omega^2}{\Omega^2} (V_{y0} + \frac{E_x(x_0)}{B}) \quad (6)$$

Cole [1976] assigned a purely gyrating component to the initial velocity  $V_{y0}$  which averaged to zero for Maxwellian distributions.

In that case the ion drift speed equals  $-(E_x(x_0)/B)(\omega^2/\Omega^2)$ , and a net current is implied since the electrons were assumed to have a drift speed equal to  $-E_x(x_0)/B$ . On the other hand, the orbit average of (1) implies that

$$V_{yd} = -\frac{\langle E_x \rangle}{B} \quad (7)$$

where the angle brackets denote the orbit average. Since one can identify an electron located at  $E_x(x) = \langle E_x \rangle$  for each ion, (7) implies zero net current. There is serious disagreement between the two results. The point is that  $V_{y0}$  does not consist solely of a gyrating component. The ion at  $t=0$  has an additional velocity in the  $-y$  direction. We have

$$V_{y0} = V_o \sin(\alpha_o) - \frac{E_x(x_o)}{B} \quad (8)$$

where  $\alpha_o$  is the initial phase angle relative to the positive  $x$  axis. Note that the phase angle average of (8) is consistent with (7).

It will now be shown that (8) leads to  $\langle E_x \rangle = E_x(0)$  for the case of a constant first derivative in  $E_x$  where  $x=0$  corresponds to the gyrocenter. Inserting (8) into (6), we find

$$V_{yd} = -\frac{E_x(x_o)}{B} - \frac{\omega}{B} \frac{dE_x}{dx} \frac{V_o \sin(\alpha_o)}{\Omega^2} \quad (9)$$

Substituting (8) into (3) and (4), we rewrite (3) and (4) in the form

$$\begin{aligned} V_x(t) &= V_a \cos(\Omega t - \alpha_a) \\ V_y(t) &= V_{yd} - \frac{\omega}{\Omega} V_a \sin(\Omega t - \alpha_a) \end{aligned} \quad (10)$$

where  $\alpha_a$  and  $V_a$  are defined by

$$\begin{aligned} V_a \cos(\alpha_a) &= V_o \cos(\alpha_o) \\ V_a \sin(\alpha_a) &= \frac{\omega}{\Omega} V_o \sin(\alpha_o) \\ \tan(\alpha_a) &= \frac{\omega}{\Omega} \tan(\alpha_o) \\ V_a &= V_o [\cos(\alpha_o)^2 + (\frac{\omega}{\Omega})^2 \sin(\alpha_o)^2]^{1/2} \end{aligned} \quad (11)$$

This transformation allows us to recast the problem in terms of a particle with a constant gyration velocity  $V_a$  following an elliptical path. We will shortly show that  $V_a$  is a constant of the motion. Note that  $V_o = V_o(\alpha_o)$  due to the variation of the electro-

static potential with  $x$ . That is, different initial phase angles correspond to different values of  $x_0$  and hence different values of  $V_0$ . Equation (10) can be integrated directly to give

$$\begin{aligned} x(t) &= x_0 + \frac{V_a}{\Omega} \sin(\Omega t - \alpha_0) + \frac{V_a}{\Omega} \sin(\alpha_0) \\ y(t) &= y_0 + V_{yd} t + \frac{\omega}{\Omega^2} V_a \cos(\Omega t - \alpha_0) - \\ &\quad - \frac{\omega}{\Omega^2} V_a \cos(\alpha_0) \end{aligned} \quad (12)$$

Note that the conditions  $\langle x \rangle = 0$  and  $\langle y \rangle = V_{yd} t$  imply that

$$\begin{aligned} x_0 &= -\frac{V_a}{\Omega} \sin(\alpha_0) = -\frac{\omega V_0}{\Omega^2} \sin(\alpha_0) \\ y_0 &= \frac{\omega}{\Omega^2} V_a \cos(\alpha_0) = \frac{\omega V_0}{\Omega^2} \cos(\alpha_0) \end{aligned} \quad (13)$$

Equation (13) describes an ellipse, not a circle, since  $V_a$  is constant. This ellipse is equivalent to that described by (12). In performing a numerical simulation, (13) ensures that ions initiated at different phase angles will be loaded onto the same trajectory.

The ellipse described by (10) has a semimajor axis equal to  $(\omega V_0)/\Omega$  along  $V_y$  and a semiminor axis along  $V_x$  equal to  $V_0$ . Therefore the eccentricity  $\epsilon$  of the ellipse is given by

$$\begin{aligned} \epsilon &= \frac{(\omega^2 - \Omega^2)^{1/2}}{\omega} \\ &= \frac{(e \frac{dE}{M dx})^{1/2}}{\omega} \end{aligned} \quad (14)$$

which of course also holds for the orbit in  $x, y$  coordinates (12).

The total energy is given by

$$\begin{aligned} U_{tot} &= \frac{1}{2} M (V_x(t)^2 + V_y(t)^2) - \\ &\quad - e E_x(x=0) x(t) - \frac{e}{2} \frac{dE}{dx} x(t)^2 = \\ &\quad = \frac{1}{2} M V_a^2 + \frac{1}{2} M V_{yd}^2 \end{aligned} \quad (15)$$

where (5), (10), and (12) have been used. There is a clear division between the orbital and drift energies. Since each value of  $U_{tot}$  defines a specific ion trajectory,  $V_a$  is constant and  $V_0$  can be determined for each value of  $\alpha_0$  through (11).

We now return to the drift velocity and find that by inserting (13) into (9),  $V_{yd}$  now becomes

$$\begin{aligned} V_{yd} &= \frac{-E_x(x_0) + \frac{dE_x}{dx} x_0}{B} \\ &= -\frac{E_x(0)}{B} \end{aligned} \quad (16)$$

which is what we set out to prove. In other words, for  $V_{yd}$  one must use the value of the electric field at the orbit center, not the value at the initial ion position. Then the drift velocity is phase independent and is given by the usual expression. This is true for each ion, and therefore the particle distributions do not modify the drift velocity in contrast to the results of Cole [1976].

The MHD approximation is valid when the associated spatial and temporal scales are much larger than the ion gyroradius and gyroperiod [Krall and Trivelpiece, 1973]. However, in this section we see that the gyroperiod (equation (5)) and therefore the spatial extent of the ion trajectory (equation (12)) approach infinity as  $dE_x/dx \rightarrow (e/M)B^2$ . For an  $O^+$  ion in a 40 $\gamma$  magnetic field,  $(e/M)B^2 = 9.6 \times 10^{-9}$  V/m<sup>2</sup>, which is consistent with expected values near the equatorial Harang discontinuity. Therefore the MHD approximation may not be valid near the Harang discontinuity and inside auroral arcs if the electric field gradient is sufficiently large. It should be pointed out that Mozer *et al.* [1980] have measured electric field gradients that have exceeded this criterion.

### 3. A Constant Second Derivative in $E_x$

We now consider the case where the second derivative of  $E_x$  rather than  $E_x$  or  $dE_x/dx$  is considered constant over the ion orbit. Note that we defined  $z$  as parallel to  $B$  so that the ions' sense of gyration in terms of  $d^2E/dx^2$  is well-defined. In the  $x, y$  plane ions gyrate in a clockwise manner. The presence of a constant second derivative in  $E_x$  can be examined by expanding the first derivative about the initial position  $x_0$  of the ion.

$$\frac{dE_x}{dx} = \frac{dE_x}{dx} \Big|_{x=x_0} + \frac{d^2E_x}{dx^2} (x - x_0) \quad (17)$$

Then (2) can be rewritten as

$$\frac{d^2V_x}{dt^2} + \Omega_0^2 V_x - \frac{e}{M} \frac{d^2E_x}{dx^2} (x - x_0) V_x = 0 \quad (18)$$

where  $\Omega_0$  is the gyrofrequency as defined in (5) with  $dE_x/dx = dE_x/dx|_{x=x_0}$ . This is to be distinguished from the gyrofrequency  $\Omega$  which reflects a constant second derivative in  $E_x$ . Each term in (18) is a perfect differential of  $x$  with respect to time since  $V_x = dx/dt$ . Integrating once, we obtain

$$\begin{aligned} \frac{d^2x}{dt^2} + \Omega_0^2 (x - x_0) &= \\ \frac{dV_x}{dt} \Big|_{t=0} + \frac{e}{2M} \frac{d^2E_x}{dx^2} (x - x_0)^2 & \end{aligned} \quad (19)$$

where  $dV_x/dt|_{t=0}$  is given by

$$\begin{aligned} \frac{dV_x}{dt}|_{t=0} &= \omega \left( \frac{E_o}{B} + V_{yo} \right) \\ &= \omega V_o \sin(\alpha_o) \end{aligned} \quad (20)$$

Equations (1) and (8) have been used and  $E_o = E_x(x_o)$ . Multiplying (19) by  $dx/dt$  we can integrate again with the result

$$\begin{aligned} \left( \frac{dx}{dt} \right)^2 &= (x - x_o) [-\Omega_o^2 (x - x_o) + \dots \\ &\dots + 2\omega V_o \sin(\alpha_o) + A(x - x_o)^2] + \dots \\ &\dots + V_o^2 \cos^2(\alpha_o) \\ A &= \frac{1}{3} \frac{\omega}{B} \frac{d^2 E}{dx^2} \end{aligned} \quad (21)$$

If we choose the initial position  $x_o$  to be a turning point, then  $dx/dt = 0$ . This automatically finds one of the roots of the cubic and reduces the problem of finding the other roots to a quadratic equation in  $x - x_o$ . Note that only one of the two roots of the quadratic can be associated with a physical turning point since the other turning point has already been chosen to be a root. If  $x_o$  is not identified with one of the turning points then a much more complicated cubic equation must be solved. We leave the general solution for future work. In order to compare the present analysis to the simpler case described in section 2 we set  $\alpha_o = -\pi/2$  in (11) and insert the results in (12). We find that the initial turning point in  $x$  is located a distance  $\omega^2 R_c / \Omega_o^2$  from the orbit center rather than  $R_c = V_o / \omega$ . This is the rationale for normalizing the  $x$  coordinate as shown in (22).

Before solving the quadratic associated with (21) we reduce (21) to a dimensionless form according to the following normalization:

$$\begin{aligned} x_d &= \frac{x \Omega_o^2}{\omega^2 R_c}, \quad R_c = \frac{V_o}{\omega}, \quad \omega_d = \frac{\omega}{\Omega_o} \\ \tau &= \Omega_o t, \quad V_d = \frac{\Omega_o}{\omega}, \quad A_d = \frac{\omega^2 R_c A}{\Omega_o^4} \end{aligned} \quad (22)$$

where the subscript  $d$  denotes dimensionless quantities. Note that  $\omega_d V_d = 1$  in this set of units. Equation (21) can then be rewritten as

$$\begin{aligned} \left( \frac{dx_d}{d\tau} \right)^2 &= (x_d - x_{od}) [-(x_d - x_{od}) \pm 2 \\ &\dots + A_d (x_d - x_{od})^2] \end{aligned} \quad (23)$$

where  $x_{od}$  is the initial location written in dimensionless form and the sign in front of the 2 is associated with  $\alpha_o = \pm\pi/2$ . The roots of the right-hand side of this equation now depend only on the value of  $A_d$  and are given by

$$x_{d\pm} = \frac{1 \pm (1 + 8A_d)^{1/2}}{2A_d} + x_{od} \quad (24)$$

The sign inside the radical is chosen consistent with  $\alpha_o = \pm\pi/2$ . Since  $x_{od}$  is defined to be one turning point, only one root of (24) can correspond to the other turning point. This brackets the allowed values of  $x$  between the relevant roots. The third root modifies the orbit shape through the JEF as shown below. Equation (24) has a set of two solutions for each turning point. Equation (23) can now be written as

$$\begin{aligned} \left( \frac{dx_d}{d\tau} \right)^2 &= A_d (x_d - x_{od}) (x_d - x_{d+}) \\ &\quad (x_d - x_{d-}) \\ &= A_d (x_d - a_d) (x_d - b_d) (x_d - c_d) \end{aligned} \quad (25)$$

It should be pointed out that the proper mapping of the roots of (25) to the turning points implies that (25) is never negative for physical orbits. The roots  $\{x_{od}, x_{d+}, x_{d-}\}$  are defined in terms of  $\{a_d, b_d, c_d\}$ , the nomenclature of *Byrd and Friedman* [1971]. Equation (25) is then in a form that can be solved using JEFs. For example, we have three distinct solutions for  $\alpha_o = -\pi/2$  based on the value of  $A_d$ . They are for  $A_d > 0$ ,  $a_d = x_{d+}$ ,  $b_d = x_{od}$ ,  $c_d = x_{d-}$ ,  $c_d < x_{od} < b_d < a_d$ , (case I);  $-1/8 \leq A_d < 0$ ,  $a = x_o$ ,  $b_d = x_{d-}$ ,  $c_d = x_{d+}$ ,  $c_d < b_d \leq x_{od} < a_d$ , case II; and  $A_d \leq -1/8$  case III. Similar solutions for  $\alpha_o = +\pi/2$  can be obtained by a simple transformation as described in the appendix. Case II differs from case I in that the order of the roots changes as the second derivative in  $E_x$  changes from a positive to a negative value. This change corresponds to another distinct solution in terms of the JEFs. Case III corresponds to the situation when the only turning point is the one chosen at the initial position  $x_o$ . The other two roots are complex conjugate and therefore not physically accessible. The particle is untrapped. The solutions are obtained on pages 72, 79, and 93 of *Byrd and Friedman* [1971] and are presented in the appendix.

We now perform a consistency check of our solutions. The orbit average of (1) immediately gives

$$\begin{aligned} \langle V_x \rangle &= 0 \\ \langle V_y \rangle &= - \frac{\langle E_x \rangle}{B} \end{aligned} \quad (26)$$

where the angle brackets denote orbit-averaged quantities. Within every ion orbit there is a point where  $E_x = \langle E_x \rangle$  and, therefore, an electron that has the same drift speed. A one-dimensional electric field cannot give rise to inertial currents. In other words the current density  $j$  is

$$j = ne \left( V_{yd} + \frac{\langle E_x \rangle}{B} \right) = 0 \quad (27)$$

where  $n$  is the ion number density. This result can be used as an overall consistency check of our analysis.

The average electric field is given by

$$\begin{aligned} \langle E_x \rangle = E_o + \langle (x - x_o) \rangle \frac{dE_x}{dx} \Big|_{x=x_o} + \dots \\ + \frac{\langle (x - x_o)^2 \rangle}{2} \frac{d^2 E_x}{dx^2} \end{aligned} \quad (28)$$

which is found by integrating the appropriate expressions as given by (A1) and (A7) for  $x - x_o$  and  $(x - x_o)^2$ . For case I (equation (A1)) we have

$$\begin{aligned} \langle E_x \rangle = E_o + (c - b) \frac{dE_x}{dx} \Big|_o \left[ 1 - \frac{(K - E)}{k^2 K} \right] \\ + \frac{(c - b)^2}{2} \frac{d^2 E_x}{dx^2} \left[ 1 + \dots \right. \\ \left. + \frac{2(K - E) - k^2(5K - 4E)}{3k^4 K} \right] \end{aligned} \quad (29)$$

and for case II (equation (A7))

$$\begin{aligned} \langle E_x \rangle = E_o + (b - a) \frac{dE_x}{dx} \Big|_o \left( \frac{K - E}{k^2 K} \right) \\ + \frac{(b - a)^2}{2} \frac{d^2 E_x}{dx^2} \left[ \frac{(2 + k^2)K - 2(1 + k^2)E}{3k^4 K} \right] \end{aligned} \quad (30)$$

We find that (27) is identically zero for both cases I and II upon substituting the appropriate expressions for  $V_{y0}$ ,  $b$ ,  $c$  and  $k^2$  into (28), (29), and (30).  $K$  is the complete elliptical integral of the first kind while  $E$  is the complete elliptical integral of the second kind.

Any given orbit should be independent of the initial starting point. For example, we start at one turning point where the distance between turning points is defined by the upper/lower set of signs in (24). One can show by properly defining the relation between the orbital and drift speeds at the two turning points that (24) is invariant as to which turning point we initially choose. In the next section we will examine in detail the properties of the solutions presented here.

## 4. Results

Figure 1 is a plot of the right-hand side of (23) as a function of the dimensionless coordinate  $x_d$  with the turning point  $x_{od}$  set to zero. The legend corresponds to various values of  $A_d$  (the dimensionless form of  $d^2 E_x / dx^2$ ). Note that regions I-III correspond to cases I-III as described above. Note also that the turning points associated with  $\alpha_o = -\pi/2$  are plotted only for  $x_d < 0$ , while the turning points associated with  $\alpha_o = +\pi/2$  are only plotted for  $x_d > 0$ . This is consistent with the clockwise gyration

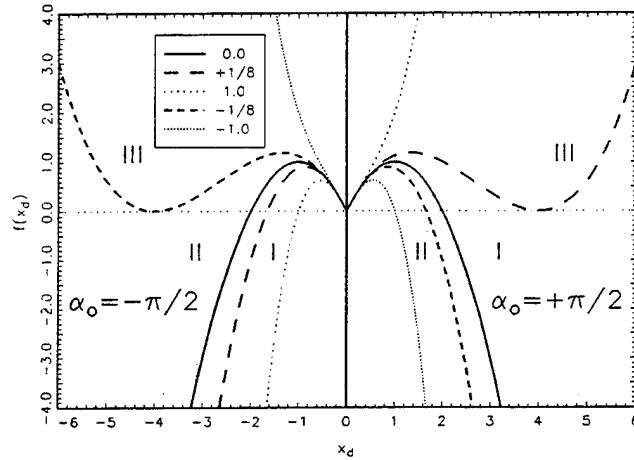


**Figure 1.** The right-hand side of (23) plotted in dimensionless coordinates for  $\alpha_o = \pm\pi/2$  ( $x_{od} = 0$ ). Regions I, II, and III correspond to different solutions of (23) (see appendix). The right-hand side is restricted to  $\alpha_o = +\pi/2$ , while the left-hand side is restricted to  $\alpha_o = -\pi/2$ , consistent with the clockwise rotation of the ion. The legend refers to various values of  $d^2 E_x / dx^2$  expressed in terms of the dimensionless quantity  $A_d$  as defined in (22). This definition holds for subsequent figures unless specifically stated otherwise. For  $A_d \geq +1/8$  ( $\alpha_o = +\pi/2$ ) or  $A_d \leq -1/8$  ( $\alpha_o = -\pi/2$ ) there is one real root and two complex conjugate roots. This means there is only one turning point and the corresponding ion is untrapped.

of the ions. The nonphysical roots have not been plotted. Consider the solid line that crosses the  $f(x_d) = 0$  axis at  $-2.0$  ( $A_d = 0.0$ ). The continuation (not plotted in Figure 1) of this curve for  $x_d > 0$  implies a root at  $a = x_{y+} = +\infty$ . This causes  $k^2 \rightarrow 0$  from (A1) and the elliptic functions in this case to reduce to the trigonometric functions. Therefore the usual sinusoidal gyromotion is a special limiting case of the third root being at infinity. Note that the third root does not correspond to a physical turning point of the orbit. It influences the shape of the orbit as determined by the JEFs. For case I ( $\alpha_o = -\pi/2$ ,  $A_d \sim d^2 E_x / dx^2 > 0$ ) and case II ( $\alpha_o = +\pi/2$ ,  $A_d \sim d^2 E_x / dx^2 < 0$ ) the orbit size decreases as  $|A_d|^{(-1/2)}$  in the limit of  $|A_d| \rightarrow +\infty$ ,  $k^2 \rightarrow 1/2$ . Similar comments apply to case II ( $\alpha_o = +\pi/2$ ) for negative  $A_d$ .

For case I ( $\alpha_o = +\pi/2$ ,  $A_d \sim d^2 E_x / dx^2 > 0$ ) and case II ( $\alpha_o = -\pi/2$ ,  $A_d \sim d^2 E_x / dx^2 < 0$ ) there are closed orbits for  $0 \leq |A| \leq 1/8$  ( $|A| = \Omega_e^4 / (8\omega V_o)$ ) (Figure 1). At  $|A_d| = 1/8$  the two roots merge, and the ion is marginally trapped. At larger absolute values of  $A_d$  the ion does not execute a closed orbit. Note that the critical point at which untrapping takes place is located at exactly twice the gyrodiameter of the  $A_d = 0$  orbit as described in section 2. i.e.,  $|x_d - x_o| = 4(\omega / \Omega_e)^2 R_e$ . Another interesting feature of this critical point is that at this location  $k^2 \rightarrow 1$  which means that the gyroperiod is infinitely long when untrapping takes place since  $K(k^2=1) = \infty$ . This critical point is equivalent to a hyperbolic fixed point as described, for example, by Rothwell et al. [1992], and gives rise to chaotic-type behavior. This feature will be discussed in more detail below.

The JEFs were evaluated using the codes published by Press et al. [1986]. The analytical results presented in section 3 and the appendix were found to be in precise agreement with a Runge-



Kutta numerical integration [Press *et al.*, 1986] of (1). The ions gyrate in a clockwise fashion looking into the plane of the paper so that at  $x_{od} = 0$   $\alpha_o = -\pi/2$  corresponds to the rightmost turning point and  $\alpha_o = +\pi/2$  to the leftmost turning point. As previously shown, the orbit size depends on the value of  $dE_x/dx$  at the initial turning point. In (22) we rescaled the  $x$  and  $t$  coordinates in order to remove this dependence in the  $x$  and  $V_x$  variables.

### Case I ( $A_d > 0$ , $\alpha_o = -\pi/2$ )

Figure 2 shows the ion dynamics in  $x_d, V_{xd}$  coordinates ( $V_{xd} = (\Omega_o/\omega)(V_x/V_o)$ , see (22)). (Recall that the subscript  $d$  denotes dimensionless quantities. The quantity  $V_{yd}$  denotes the drift velocity in the  $y$  direction, while  $V_{yd}$  is its dimensionless form.) The legend box denotes the value of  $A_d$  corresponding to the different curves. The large circle is the gyro-orbit corresponding to  $A_d (d^2E/dx^2) = 0$ . Note that as the value of  $A_d$  increases the orbit becomes smaller and asymmetric. In particular, the maximum orbital velocity becomes progressively smaller which implies that the drift velocity must become progressively larger. This is easily seen from (A6). For small values of  $b$  and  $c$ ,  $V_{yd}$  approaches  $-V_o E_d/B$ . ( $E_o = E_x(b)$ , the value of the electric field at the initial ion position.) Therefore the presence of a finite second derivative in the electric field makes the ion drift velocity dependent on the ion gyration velocity. As  $A_d$  increases in value, the orbit becomes more elongated in the  $y$  direction and shortened in the  $x$  direction reflecting the enhanced drift in the  $-y$  direction. Similar results for case II,  $\alpha_o = +\pi/2$ , are easily obtained by setting  $A_d \rightarrow -A_d$ ,  $x_d \rightarrow -x_d$  and  $y \rightarrow -y$  in Figure 2.

### Cases II and III ( $A_d < 0$ , $\alpha_o = -\pi/2$ )

In Figure 3 the  $A_d = 0$  case is the solid curve farthest to the right. As  $A_d$  becomes progressively more negative, the orbit size becomes larger until at  $A_d = -1/8$  ( $-0.125$ ) the ion is no longer trapped. This occurs when the distance between the turning points along the  $x$  axis is equal to  $4\omega V_o/\Omega_o^2$ . As mentioned, this critical point is associated with an infinite period and chaotic

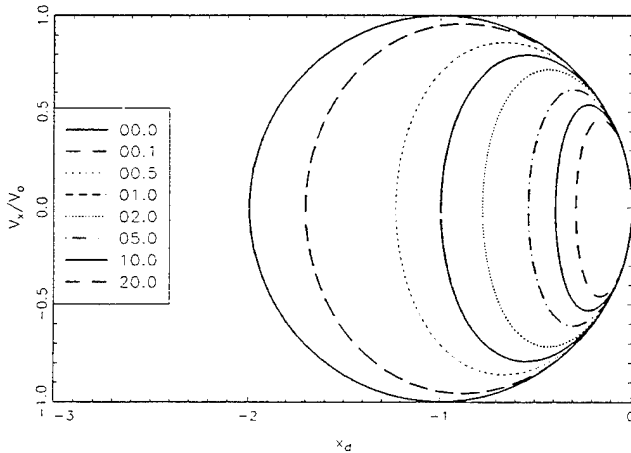


**Figure 2.** The change in orbital shape as the second derivative of  $E_x$  becomes more positive for  $\alpha_o = -\pi/2$ . Note that all ions were initiated at  $x_d = 0$ ,  $y_d = 0$ ,  $V_{xd} = 0$  and  $V_{yd} = -1$ . As  $d^2E_x/dx^2$  becomes more positive, the maximum  $x$  velocity becomes less and the drift in the  $y$  direction is enhanced. Analogous results hold for  $\alpha_o = +\pi/2$  and  $d^2E_x/dx^2 < 0$ .

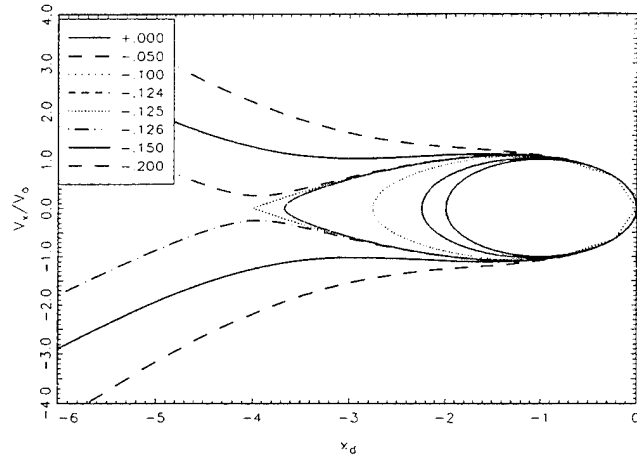


**Figure 3.** Orbit shapes for negative  $d^2E_x/dx^2$  and for  $\alpha_o = -\pi/2$ . Note that the transition to open (untrapped) orbits for  $A_d \leq -1/8$ . The critical point  $x_d = -4$  is located at twice the ion gyro diameter corresponding to the  $d^2E_x/dx^2 = 0$  orbit. Similarly, untrapping occurs for  $\alpha_o = +\pi/2$ , and  $x_d = +4$  when  $A_d \geq +1/8$ .

effects. Note the radically different orbit shapes for very small changes in  $A_d$ . Chaotic behavior is clearly evident in Figure 4 which is an  $x, y$  plot of the ion trajectory. The small egg-shaped curve (solid line) is the  $A_d = 0$  case. As the second derivative in  $E_x$  becomes more negative, the ion drifts progressively faster in the  $+y$  direction. When  $A_d$  approximates  $-1/8$  the ion is drifting parallel to the  $+y$  axis at a speed which can be obtained from (A9).

$$V_{yd} = V_o \left( 4 \frac{\omega^2}{\Omega_o^2} - 1 \right) - \frac{E_o}{B} \quad (31)$$

Similar comments can be made for cases I and III for  $\alpha_o = +\pi/2$  and  $A_d = +1/8$ . Note in the latter case, however, that the ion is traveling in the  $-y$  direction as  $A_d$  approximates  $+1/8$ . Chaotic untrapping is phase angle dependent.

We now want to plot  $V_y$  versus  $V_x$  in a nondimensional manner for cases I and II ( $\alpha_o = -\pi/2$ ). In this way, physical insight will be succinctly obtained regarding the drift velocity by removing the  $dE_x/dx|_{x=x_o}$  dependence. This is done by transforming to a drift frame that is moving with a velocity  $-E_x(0)/B$  where

$$E_x(0) = E_o - \frac{\omega^2}{\Omega^2} R_c \frac{dE_x}{dx} \Big|_{x=x_o} \quad (32)$$

Again,  $E_o = E_x(x = x_o)$  and  $E_x(0)$  is the electric field at the gyrocenter of a particle that starts at  $x = x_o$  in a constant gradient electric field. In section 2 we showed (equation (16)) for the constant gradient case that the particle drift velocity is equal to  $-E_x(0)/B$ . We transform (A16) and (A17) to the drift frame of the constant gradient electric field by adding  $E_x(0)/B$  to both equations. These equations then become only a function of  $A_d$ , the nondimensional form of the second derivative of  $E_x$ . In this way a single set of universal curves can be generated which hold for all values of  $dE_x/dx|_{x=x_o}$ .

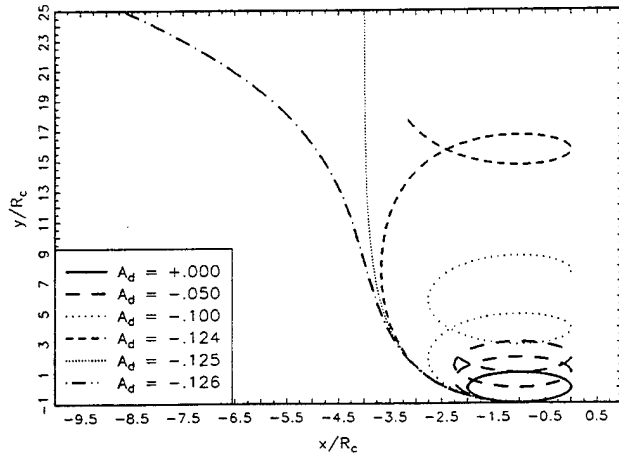


**Figure 4.** The orbit characteristics near the critical point shown in Figure 3.

This gives for case I ( $\alpha_0 = -\pi/2$ )

$$V_y = -1 + (b_d - c_d) \operatorname{cn}^2(u) \quad (33)$$

and for Case II ( $\alpha_0 = \pi/2$ ) we have

$$V_y = -1 + (a_d - b_d) \operatorname{sn}^2(u) \quad (34)$$

where  $V_y$  in (33) and (34) is made dimensionless by dividing through by  $(\omega/\Omega_0)^2 V_0$ . The dimensionless quantities  $a_d$ ,  $b_d$ , and  $c_d$  are formed by dividing  $a$ ,  $b$  and  $c$  by  $(\omega/\Omega_0)^2 R_c$  consistent with (22). The results are shown in Figure 5. Note the onion-shaped orbits and that the ion drift velocity becomes progressively more negative as the second derivative of  $E_x$  becomes more positive. Solutions for ( $\alpha_0 = +\pi/2$ ) are obtained from Figure 5 by the transformation  $A_d \rightarrow -A_d$ ,  $V_{yd} \rightarrow -V_{yd}$  (appendix).

The drift velocities for cases I and II ( $\alpha_0 = \pm\pi/2$ ) as given by equations (A6) and (A9) are now renormalized in a similar fashion. The result is denoted by  $V_{ydr}$  and is shown in Figure 6. The solid line is  $V_{ydr}$  as calculated from the JEF, and the small squares denote  $V_{ydr}$  as obtained by a direct numerical integration of (1). Here both  $x_{od}$  and  $dE/dx|_{x=x_{od}}$  equal zero. The results for cases I and II ( $\alpha_0 = \pm\pi/2$ ) are found by the usual transformation. Therefore a positive value of  $d^2E/dx^2$  causes negative  $y$  ion drift, while a negative value of  $d^2E/dx^2$  causes positive  $y$  ion drift in the chosen drift frame. If (31) is normalized as described above, one finds that  $V_{ydr} = \mp 3$  for  $\alpha_0 = \pm\pi/2$  at the critical points where  $A_d = \pm 1/8$ .

Near  $A_d = 0$  the drift speed is a highly nonlinear function of the second derivative of  $E_x$ . However, most present treatments [e.g., Chen, 1990] use a perturbation expansion that neglects the first derivative of  $E_x$ . The usual expression is given by

$$V_{ydr}^p = -\frac{1}{4} \frac{R_c^2}{B} \frac{d^2 E_x}{dx^2} \quad (35)$$

where the superscript  $p$  denotes a perturbation expansion result.

The renormalized expression for (35) using (22) is  $V_{ydr}^p = -3A_d/4$  which is plotted as a dotted line in Figure 6. (Note that since  $dE_x/dx|_{x=x_0}$  implicitly equals zero in (35),  $\Omega_0 = \omega$  in carrying out the renormalization.)  $V_{ydr}^p$  is seen to be a fairly good approximation of  $V_{ydr}$  for small positive values of  $A_d$ , but a very poor approximation for negative values of  $A_d$ . The poor agreement is due to the untrapping of the ions at  $A_d = -0.125$  which is a highly nonlinear effect and therefore not amenable to perturbation techniques. For large positive values of  $A_d$  the ion drift velocity approaches  $-V_0(\omega/\Omega)^2$  for ions with  $\alpha_0 = -\pi/2$ . For large negative values of  $A_d$  and  $\alpha_0 = +\pi/2$  the ion drift velocity approaches  $+V_0(\omega/\Omega)^2$ . Therefore ion drift along  $+y$  is associated with negative  $A_d$ , while ion drift along  $-y$  is associated with positive  $A_d$ . The ion drift velocity is independent of the gyrovelocity only in the limit that  $A_d$  becomes very small.

#### Limit as $A(d^2E/dx^2) \rightarrow 0$

The limit of  $V_{ydr}$  as  $A \rightarrow 0$  can be obtained by looking at the limits of  $K$  and  $E$  as  $k^2 \rightarrow 0$ . The expansion of the elliptic functions  $K$  and  $E$  near  $k^2 = 0$  is given by Byrd and Friedman [1971, pp. 298-299]. Inserting these expansions into either (A6) or (A9), we find the following expression for  $V_{ydr}$

$$\begin{aligned} V_{ydr} = V_{ydr0} - \frac{3}{4} \left( \frac{\omega}{\Omega_0} \right)^6 \frac{R_c^2}{B} \frac{d^2 E_x}{dx^2} + \dots \\ + \frac{13}{12} \frac{\omega^9}{\Omega_0^{10}} \frac{R_c^3}{B^2} (d^2 E_x / dx^2)^2 + \dots \\ + O(d^2 E_x / dx^2) \end{aligned} \quad (36)$$

where  $V_{ydr0}$  is the drift velocity in the limit as the second derivative goes to zero and as given in (16). There are significant differences between (36) and (35). The coefficient of the linear term in (36) is 3 times that in (35), and it is evident that the first

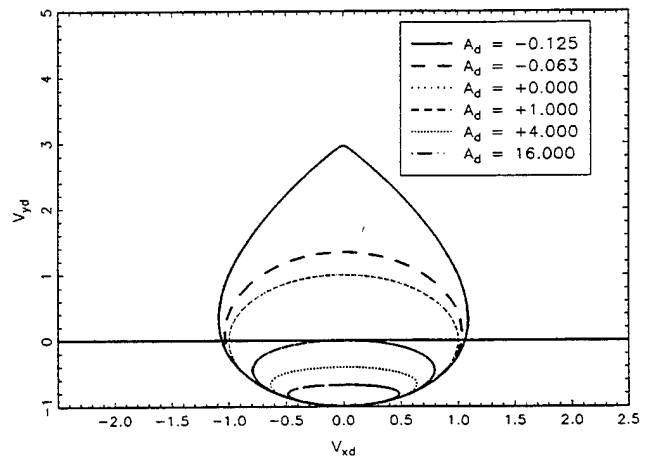


**Figure 5.**  $V_{ydr}$  versus  $V_{xdr}$  for trapped orbits ( $\alpha_0 = -\pi/2$ ) including drift effects. Subscript  $d$  denotes dimensionless. Note that the concept of a particle uniformly gyrating about the magnetic field is not physically valid if  $d^2E_x/dx^2 \neq 0$ . Results for  $\alpha_0 = +\pi/2$  are easily obtained by the transformation  $A_d \rightarrow -A_d$  and  $V_{ydr} \rightarrow -V_{ydr}$ .

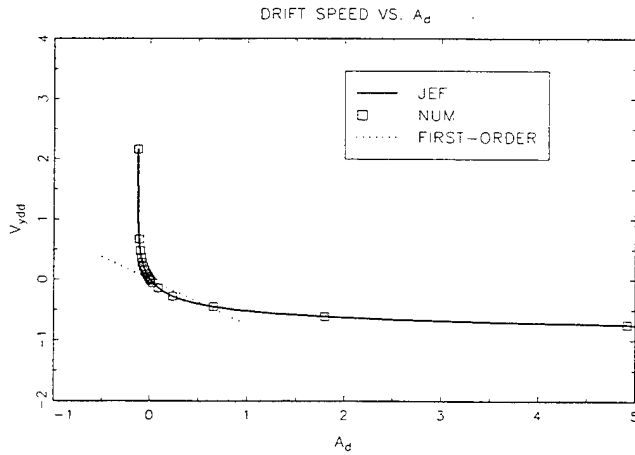


**Figure 6.** The dimensionless drift velocity in the  $y$  direction as a function of the dimensionless form of  $d^2E_x/dx^2$ . This is for the  $\alpha_o = \pi/2$  case. The solid line represents the calculated values from evaluating the Jacobian elliptic functions. The squares are obtained by numerically integrating (1) and determining the drift velocity by the successive  $y$  displacements at constant orbital phase. The dotted line is the result of first-order perturbation theory. Because of the presence of the critical point the perturbation result is a very poor approximation. Results for the  $\alpha_o = +\pi/2$  are obtained as in Figure 5.

derivative of  $E_x$  through its modification of the gyrofrequency has a substantial impact on the drift velocity, a fact which is usually ignored. We emphasize therefore that (35) should be used with caution.

### Physics of Chaotic Untrapping

Chaotic untrapping of heavy ions occurs when the second turning point is in a region where the first derivative of the electric field is more positive. This situation exists for  $A_d > 1/8$  ( $\alpha_o = +\pi/2$ ) and for  $A_d < -1/8$  ( $\alpha_o = -\pi/2$ ) and is analogous to the results given in section 2. Recall that the orbital speed is not constant over the orbit path. Using the condition ( $A_d = \pm 1/8$ ) and the direct integration of (1) for  $V_y$  (equation (A5)) we find that the gyrospeed is zero at the second turning point when untrapping occurs. All the kinetic energy at the second turning point is contained in the drift speed which leads to untrapping (Figure 4). It should be noted that the second turning point is located in a region where  $dE/dx > 0$  such that  $\Omega_o^2$  would be  $< 0$  if that turning point was chosen to be  $x_o$ . The results in this section will now be applied to the magnetosphere.

### 5. Application to Space Physics

The main application of this work to space physics is to help delineate those regions of the magnetosphere where ideal and nonideal MHD break down. *Mozier et al.* [1980] have, for example, measured electric field gradients that exceed the untrapping criterion (section 2). The present work shows that finite orbit effects are not always slowly varying functions of the first and second derivatives in the electric field. There are regions where small changes in these quantities can cause dramatic changes in orbital trajectories. It is in these regions that

perturbative techniques, such as those used in nonideal MHD, are of little use. This is also the case in theories where the ion drift velocity depends on the second derivative of  $E$ . We have shown that one must perform orbit averaging over the exact orbit to obtain the right result. In this case, perturbation theory explicitly fails.

Although we have not solved the particle orbits for all phase angles, we can still draw some conclusions. Consider a satellite which can detect the azimuthal phase angle distribution of heavy ions. The results presented here suggest an east-west asymmetry in the detected ion fluxes. This asymmetry arises from the particle loss due to the open orbits. For positive  $d^2E_x/dx^2$  and for positive  $x$  pointing earthward we expect higher fluxes from the west than the east. The reverse is expected if  $d^2E_x/dx^2$  is negative. The feasibility of this feature as a tool for defining magnetospheric electric field structures needs further study.

Large-scale magnetospheric electric field structures are expected near the Harang discontinuity from the mapping of low-altitude measurements [Maynard, 1974; Rothwell et al. 1994]. These structures have a region where the second derivative is finite. It has been well established [e.g., Daglis et al., 1991] that the  $O^+$  ion population is enhanced in the plasma sheet during active periods. The question arises whether the condition for chaotic untrapping of these ions can be satisfied for reasonable values in the relevant geophysical parameters.

We model the region with a negative second derivative in  $E_x$  by a Gaussian which, of course, has a nonconstant second derivative. Figures 7a and 7b show the results of numerically integrating (1) at different initial locations for a zero cross-tail electric field ( $E_{ye} = 0$ ). Figures 7a and 7b should be viewed as snapshots in time as the normally earthward drifting ions stop drifting as a result of  $E_{ye} \rightarrow 0$ . When  $B \geq 40$  nT (Figure 7a), the  $O^+$  ion orbits are dominated by the magnetic field. On the other hand, when  $B$  drops to 10 nT, some of the ion gyroradii increase dramatically (Figure 7b) consistent with Figure 3. The presence of the second derivative in  $E_x$  becomes important.

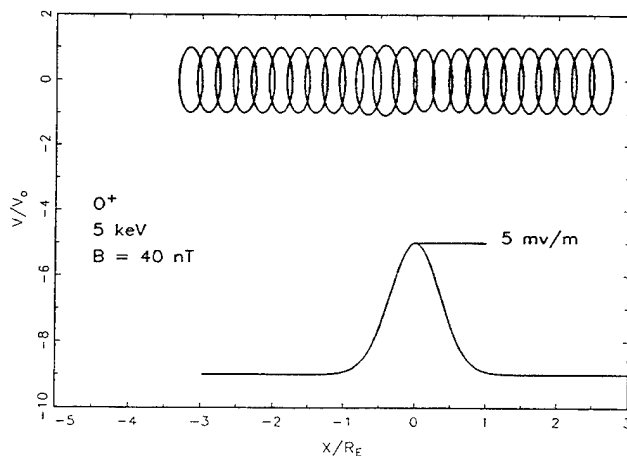


**Figure 7a.** The region near the Harang discontinuity partly replaced by a Gaussian-shaped electric field profile. We assume that the cross-tail electric field  $E_{ye}$  is zero due to the interplanetary magnetic field swinging northward, and the orbits shown are executed by the ions at different  $x$  locations. Note that if  $B = 40$  nT, the orbital distortion is insignificant.

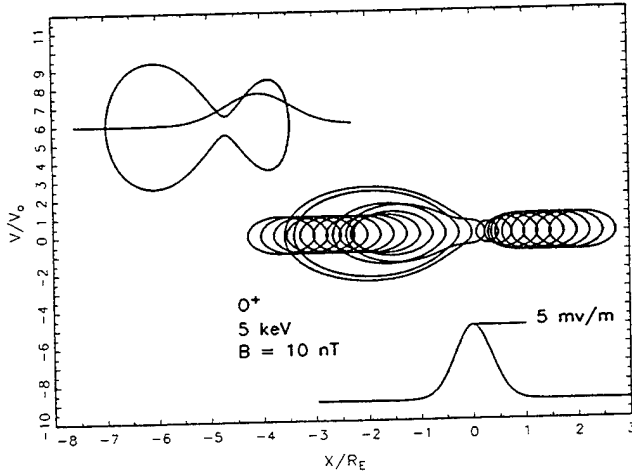


**Figure 7b.** Same as Figure 7a except  $B=10$  nT. Note that there are now some ions whose orbits become much larger than expected by weakening the  $B$  field. In fact, "bow tie" shaped orbits, such as that shown in the upper left-hand corner, approach the critical point described in the text and have very long periods. The Gaussian-shaped electric field is also shown with the bow tie to show where these orbits are most likely to occur.

At the Gaussian peak (where  $\Omega_o = \omega$ ) the condition for untrapping according to our analysis is

$$\left. \frac{d^2 E}{dx^2} \right|_{x=0} = -\frac{4E_x(MAX)}{R_E^2} \leq -\frac{3}{8} \frac{e}{M} \frac{B^2}{R_c} \quad (37)$$

where  $R_E = 6.37 \times 10^6$  m. This condition is not satisfied for Figure 7a but is satisfied for Figure 7b consistent with the right-hand side of (37) varying as  $B^3$ .

Not only do the ion gyroradii increase, but the gyroperiods increase as well from the above analysis. For example, in the upper left-hand portion of Figure 7b we show a specific ion orbit that is close to being split. We plot the "bowtie" shape of the ion orbit superimposed on the Gaussian structure of the electric field. This orbit was obtained by numerical integration of (1). Note that it approximates the critical orbits shown in Figure 3. For the latter case it was pointed out that at the critical point the orbit period approached infinity. For the bowtie shaped orbit shown, the orbit period is 2.6 times the normal gyroperiod ( $2\pi/\omega$ ). This indicates that  $O^+$  ions can shift resonance and absorb energy from a broad spectrum of lower-frequency waves as the magnetic field lines stretch. The absorption of Pi 2 pulsations by the magnetospheric  $O^+$  ions, for example, could lead to ion heating and eventual untrapping. Similar arguments hold in the presence of a field line resonance [Samson *et al.*, 1992]. Therefore it is quite possible that the finite orbit effects determined here play a role in the substorm process.

## 6. Conclusions and Discussion

In MHD it is assumed that a distinct separation between the macroscopic and microscopic spatial and temporal scales exists. In this paper we examined particle dynamics with finite first and second spatial derivatives in the electric field. We find that (1)

even nonideal MHD will be invalid even for the simple case of a constant electric field gradient perpendicular to a magnetic field if  $dE_x/dx \geq eB^2/M$  and that (2) a sufficiently large second derivative in the electric field  $\geq |(3eB^2)/(8MR_c)|$  can cause heavy ions to become chaotically untrapped. The first condition will be satisfied for  $O^+$  ions in a 40 nT magnetic field if  $dE_x/dx$  exceeds  $1 \times 10^{-8}$  V/m<sup>2</sup>. The second condition will be satisfied for 5 keV  $O^+$  ions in a 40 nT magnetic field if  $|d^2E_x/dx^2| \geq 3.4 \times 10^{-15}$  V/m<sup>3</sup>. It is suggested that large-scale magnetospheric models be modified to flag those portions of the magnetosphere where conditions (1) and (2) are satisfied. It is in these regions that finite orbit effects have to be carefully investigated. One such region is the Harang discontinuity.

An important conclusion of this work is that the presence of a finite  $d^2E_x/dx^2$  could create an asymmetry in the heavy ion fluxes. The heavy ions such as  $O^+$  might therefore be useful as a probe of the large-scale electric field structure in the magnetosphere. More research is needed to ascertain the practicality of this suggestion.

## 7. Appendix

The interested reader is referred to Byrd and Friedman [1971] and Cayley [1961] for more details about elliptic functions. We will now solve (25) for the three cases.

### Initial Phase Angle Equals $-\pi/2$ : Case I

For this case  $A_d > 0$ ,  $a_d = x_{d+}$ ,  $b = x_o$ ,  $c_d = x_d$ ,  $c_d < x_d \leq b_d < a_d$ . The solution is given by [Byrd and Friedman, 1971, p.72]. In dimensional units the solution is

$$\begin{aligned} x &= c + (b-c)sn^2(u) \\ k^2 &= \frac{b-c}{a-c} \\ u &= \frac{\Omega t}{2} + K \end{aligned} \quad (A1)$$

Equation (A1) is a solution such that  $u=0$  corresponds to turning point  $c$  ( $c < b$ ,  $sn(0)=0$ ). By adding  $K$  the  $t=0$  particle position is at turning point  $b$  ( $sn(K)=1$ ) consistent with our original assumption. The derivative of (A1) with respect to  $t$  yields the following equation:

$$\left( \frac{dx}{dt} \right)^2 = \Omega^2 (b-c)^2 sn^2(u) cn^2(u) dn^2(u) \quad (A2)$$

Equation (A1) can be used to construct the following relationships.

$$\begin{aligned} (x-c) &= (b-c)sn^2(u) \\ (b-x) &= (b-c)cn^2(u) \\ (a-x) &= \frac{(b-c)}{k^2} dn^2(u) \end{aligned} \quad (A3)$$

Equation (A3) follows from the definition of  $k^2$  (A1) and the identities  $sn^2(u) + cn^2(u) = 1$  and  $k^2 sn^2(u) + dn^2(u) = 1$ . The substitution of (A3) into (A2) will yield an expression equivalent to

(25) if the coefficient of the  $x^3$  term is the same. This automatically gives us an expression for the generalized frequency  $\Omega$  as a function of the second derivative in  $E_x$ .

$$\begin{aligned}\frac{k^2 \Omega^2}{b-c} &= A \\ \Omega^2 &= A(a-c) \\ \Omega^2 &= [\Omega_o^4 + 8\omega A V]^{1/2}\end{aligned}\quad (\text{A4})$$

The gyroperiod by definition is  $T_p = 4 K/\Omega$ , where  $K=K(k^2)$  the complete elliptic integral of the first kind. Note that as  $A \rightarrow 0$ ,  $k^2 \rightarrow 0$ ,  $\Omega \rightarrow \Omega_o$ , and  $T_p \rightarrow 2 \pi/\Omega_o$ .

Now we calculate the drift velocity. From the second equation of (1) we have

$$\begin{aligned}V_y &= V_{yo} - \omega(x-b) \\ V_y &= V_{yo} + \omega(b-c) cn^2(u)\end{aligned}\quad (\text{A5})$$

The symbol  $V_{yo}$  denotes the initial velocity taken at point  $x_0 = b$ . The orbit average of (A5) is

$$V_{yd} = -V_o - \frac{E_x(b)}{B} - \omega(b-c) \left( \frac{K-E}{k^2 K} - 1 \right) \quad (\text{A6})$$

where (8) has been used with  $\alpha_o = \pi/2$ .  $K$  and  $E$  are the complete elliptic integrals of the first and second kind.

### Case II

For this case  $-1/8 \leq A_d < 0$ ,  $a = x_o$ ,  $b_d = x_d$ ,  $c_d = x_d$ ,  $c_d < b_d \leq x_d < a_d$ . The solution is given by *Byrd and Friedman* [1971, p.79].

$$\begin{aligned}x &= a - (a-b) sn^2(u) \\ k^2 &= \frac{a-b}{a-c}\end{aligned}\quad (\text{A7})$$

the gyrofrequency in dimensional form is found to be

$$\Omega^2 = \frac{\Omega_o^2 + (\Omega_o^4 + 8 A \omega V_o)^{1/2}}{2} \quad (\text{A8})$$

Note that both (A8) and (A4) go to  $\Omega_o$  as  $A$  goes to zero from both negative and positive values, respectively. The drift velocity is again calculated as before except that for this case, the  $t=0$  point is at turning point  $a$ .

$$V_{yd} = -V_o - \frac{E_o}{B} - \omega(b-a) \left( \frac{K-E}{k^2 K} \right) \quad (\text{A9})$$

### Case III

In this case  $A_d \leq -1/8$  which makes the roots shown in (24) to be complex conjugate and the corresponding orbits not closed.

The particle is not trapped. We take  $a$  as our initial position and consider  $b$  and  $c$  to be the complex roots. The solution is given by *Byrd and Friedman* [1971, p.93].

$$\begin{aligned}b_1 &= \frac{b+c}{2} & a_1^2 &= -\frac{(b-c)^2}{4} \\ \gamma^2 &= (b_1 - a)^2 + a_1^2 & k^2 &= \frac{\gamma - b_1 + a}{2\gamma} \\ cn(u) &= \frac{a - \gamma - x}{a + \gamma - x}\end{aligned}\quad (\text{A10})$$

In terms of the problem at hand these parameters take the following form.

$$\begin{aligned}b_1 &= a + \frac{\Omega_o^2}{2A} & a_1^2 &= \frac{8|A|\omega V_o - \Omega_o^4}{4A^2} \\ \gamma^2 &= \frac{2\omega V_o}{|A|} & k^2 &= \frac{1}{2} \left[ 1 + \frac{\Omega_o^2}{\sqrt{8\omega V_o |A|}} \right] \\ a - x &= \gamma \frac{(1 + cn(u))}{(1 - cn(u))}\end{aligned}\quad (\text{A11})$$

Note that the  $u=0$  point corresponds to  $x = -\infty$  and that  $x_o = a$  (the initial ion position) corresponds to  $u=2K$  where  $cn=-1$  (Figure 3). This fact is important in carrying out the numerical computations. The frequency  $\Omega$  in case III is given by

$$\Omega = [2\omega |A| V_o]^{1/4} \quad (\text{A12})$$

At  $A = -\Omega_o^4/(8\omega V_o)$  both (A12) and (A8) reduce to  $\Omega = \Omega_o/2^{1/2}$ .

The corresponding expressions for the  $x$  component of the velocity ( $V_x = dx/dt$ ) for the three cases are as follows:

Case I

$$V_x = (b-c) \Omega_I sn(u) cn(u) dn(u) \quad (\text{A13})$$

Case II

$$V_x = -(a-b) \Omega_{II} sn(u) cn(u) dn(u) \quad (\text{A14})$$

Case III

$$V_x = \frac{2\gamma \Omega_{III}}{(1 - cn(u))^2} sn(u) dn(u) \quad (\text{A15})$$

The subscript on  $\Omega$  is to alert the reader that the expression for each case must be used.

The  $y$  component of the velocity for the three cases are the following:

Case I, the initial location is at turning point  $b$ .

$$V_y = -V_o - \frac{E_o}{B} + \omega(b-c) cn^2 u \quad (\text{A16})$$

Case II, the initial location is at turning point  $a$ .

$$V_y = -V_o - \frac{E_o}{B} + \omega(a-b)sn^2u \quad (A17)$$

Case III, the initial location is at turning point  $a$  and  $u \rightarrow 2K+u$ .

$$V_y = -V_o - \frac{E_o}{B} + \omega\gamma \frac{(1+cnu)}{(1-cnu)} \quad (A18)$$

### Initial Phase Angle Equals $+\pi/2$

It should be noted that another class of solutions exist for which  $\alpha_o = +\pi/2$ . In that case, (24) becomes

$$x_{dt} = \frac{1 \pm (1 - 8A_d)^{1/2}}{2A_d} + b_d \quad (A19)$$

such that the relation

$$(x_{dt} - x_{od})|_{Ad, \alpha_o = -\pi/2} = - (x_{dt} - x_{od})|_{-Ad, \alpha_o = +\pi/2} \quad (A20)$$

holds. Equation (A20) states that by reversing the direction of the initial velocity and the sign of the second derivative of the electric field the roots of the cubic are reflected about  $x_{od}$ , the initial position of particle (also one of the roots). One then orders the roots as  $a > b > c$  according to the nomenclature of Byrd and Friedman [1971]. After reflection about  $x_{od}$ , case I maps into case II and vice versa (Figure 1).

This has been verified by numerical integration of (1). Case III remains essentially invariant under (A20). The results are the same as (A11) if one replaces  $a-x$  by  $x-a$  and sets  $u=0$  at  $x=+\infty$ . The key point, however, is that the complex roots (open orbits) occur for positive  $A_d > +1/8$  ( $\alpha_o = +\pi/2$ ) rather than for negative  $A_d < -1/8$  ( $\alpha_o = -\pi/2$ ). This can produce an asymmetry in the heavy ion fluxes which depends on the sign of  $d^2E_x/dx^2$ . The solutions obtained above for  $\alpha_o = -\pi/2$  also hold for the class of orbits for which  $\alpha_o = +\pi/2$  and therefore will not be repeated in detail.

**Acknowledgements.** One of us (M. B. S.) would like to acknowledge support from Air Force Contract F19628-92-K-007.

The Editor thanks L. M. Zelenyi and J. F. Lemaire for their assistance in evaluating this paper.

### References

Byrd, P. F., and M. D. Friedman, *Handbook of Elliptic Integrals for Engineers and Scientists*, 2nd ed. Springer-Verlag, New York, 1971.

- Cayley, A., *An Elementary Treatise on Elliptic Functions*, 2nd ed., Dover, New York, 1961.
- Chen, F. F., *Introduction to Plasma Physics and Controlled Fusion*, vol. 1, *Plasma Physics*, Plenum, New York, 1990.
- Cole, K. D., Effects of crossed magnetic and (spatially dependent) electric fields on charged particle motion, *Planet. Space Sci.*, 24, 515-518, 1976.
- Daglis, I. A., E. T. Sarris, and G. Kremser, Ionospheric contribution to the cross-tail current during the substorm growth phase, *J. Atmos. Terr. Phys.*, 53, 1091-1098, 1991.
- Galeev, A. A., and L. M. Zeleni, Tearing instabilities in plasma configurations, *Sov. Phys., JETP*, Engl. Transl., 43, 1113-1123, 1976.
- Goertz, C. K., Kinetic Alfvén waves on auroral field lines, *Planet. Space Sci.*, 32, 1387-1392, 1984.
- Hasegawa, A., Particle acceleration by MHD surface wave and formation of aurora, *J. Geophys. Res.*, 81, 5083-5090, 1976.
- Krall, N. A., and A. W. Trivelpiece, *Principles of Plasma Physics*, McGraw-Hill, New York, 1973.
- Maynard, N. C., Electric field measurements across the Harang discontinuity, *J. Geophys. Res.*, 79, 4620-4631, 1974.
- Mozar, F. S., C. A. Cattell, M. K. Hudson, R. L. Lysak, M. Temerin, and R. B. Torbert, Satellite measurements and theories of auroral particle acceleration, *Space Sci. Rev.*, 27, 155-213, 1980.
- Press, W. H., B. P. Flannery, S. A. Teukolsky, and W. T. Vetterling, *Numerical Recipes*, Cambridge University Press, New York, 1986.
- Rothwell, P. L., M. B. Silevitch, L. P. Block, and C.-G. Fälthammar, Acceleration and stochastic heating of ions drifting through an auroral arc, *J. Geophys. Res.*, 97, 19,333-19,339, 1992.
- Rothwell, P. L., M. B. Silevitch, L. P. Block, and C.-G. Fälthammar, O<sup>+</sup> phase bunching and auroral arc structure, *J. Geophys. Res.*, 99, 2461-2470, 1994.
- Samson, J. C., D. D. Wallis, T. J. Hughes, F. Creutzberg, J. M. Ruohoniemi, and R. A. Greenwald, Substorm intensifications and field line resonances in the nightside magnetosphere, *J. Geophys. Res.*, 97, 8495-8518, 1992.

L. P. Block and C.-G. Fälthammar, Division of Plasma Physics, Alfvén Laboratory, Royal Institute of Technology, S 100 44, Stockholm 70, Sweden. (e-mail: playfys:falthammar)

P. L. Rothwell, Geophysics Research Directorate, Phillips Laboratory, 29 Randolph Rd., Bedford, MA 01731.

M. B. Silevitch, Center for Electromagnetics Research, Northeastern University, Boston, MA 02115.

(Received September 13, 1994; revised January 20, 1995; accepted February 17, 1995.)

# Test particle motion in the cyclotron resonance regime

Gregory P. Ginet and Jay M. Albert

*Geophysics Directorate, Phillips Laboratory, Hanscom Air Force Base, Massachusetts 01731*

(Received 20 March 1991; accepted 12 July 1991)

Test particles moving in the field of an electromagnetic wave propagating in a background magnetic field can gain significant energy when the wave parameters and particle energy are such that the cyclotron resonance condition is satisfied. Central to the acceleration process and long time scale periodic behavior is the coherent accumulation over many cyclotron orbits of a small change in energy during each orbit, a result of the circularly polarized component of the wave electric field. Also important is the small change in the relative wave phase during each orbit resulting from relativistic variations of the cyclotron frequency and wave-induced streaming along the background magnetic field. The physical mechanisms underlying cyclotron resonance acceleration are explored using a set of heuristic mapping equations (the PMAP) describing changes in the particle momentum and relative wave phase. More accurate (but less transparent) descriptions of the particle motion are pursued in the context of orbit-averaged Hamiltonian theory. A discrete set of mapping equations for the slowly varying canonical action and angle are derived (the QMAP) but are found to generate inaccurate solutions in certain regions of phase space when the resonance number  $l$  is such that  $|l| = 1$  and the particles are initially cold. These difficulties are avoided by constructing a continuous time orbit-averaged Hamiltonian and solving the resultant canonical equations of motion. Assuming the momentum is small relative to  $mc$  (where  $m$  is the particle mass and  $c$  is the speed of light), details of the distribution of particle trajectories in the action-angle phase space for  $|l| = 1$  and  $|l| = 2$  are presented and criteria for the existence of orbits oscillatory in angle are derived.

## I. INTRODUCTION

When constructing a kinetic-theoretic description of the interaction between an electromagnetic wave and a magnetized plasma, it is important to know the trajectory of test particles in the presence of the electromagnetic wave and background magnetic field. A particularly interesting regime of wave-test particle interaction occurs when the wave frequency  $\omega$  and the particle momentum satisfy the cyclotron resonance condition,

$$\omega - k_z v_z - |l|\Omega \approx 0, \quad (1)$$

where  $\Omega$  is the cyclotron frequency,  $l$  is the resonance number, and  $k_z$  and  $v_z$  are the wave vector and particle velocity, respectively, in the direction of the background magnetic field  $\mathbf{B}_0 = B_0 \mathbf{e}_z$ . In the cyclotron resonance regime, it is possible for test particles to achieve kinetic energies far in excess of the "quiver energy" on time scales of many wave periods, even for relatively small wave amplitudes.<sup>1-7</sup> We define the quiver energy as the maximum energy achieved by a test particle in an electromagnetic wave without a background magnetic field.

In the work of Ginet and Heinemann<sup>6</sup> (hereafter Paper I), a Hamiltonian pseudopotential (HPP) theory was developed and used to predict the maximum kinetic energy  $U_{\max}$  (normalized to the rest mass energy) and acceleration time  $\tau_p$  (normalized to the wave period) resulting from the cyclotron resonance acceleration process in the limit of small wave amplitude. Although the HPP theory proves to be a useful predictive tool, as demonstrated by the extensive comparison of HPP predictions with those obtained from numerical solutions of the full equations of motion given in

Paper I, there are limitations. The HPP theory does not predict any details of the particle trajectory other than the temporal dependence of the kinetic energy and does not provide much physical insight into how the acceleration process actually works.

This paper addresses the details of the cyclotron resonance interaction process that are not covered by the HPP theory. As in Paper I, we restrict ourselves to the regime of small wave amplitude so that particles are not trapped in the troughs of a wave and chaotic motion resulting from overlapping resonances does not occur. In Sec. II, we discuss the physical mechanism underlying the acceleration process in the context of a set of pedagogical mapping equations that describes the change in particle momentum and wave phase from one cyclotron orbit to the next. More accurate (but less transparent) methods for computing details of the cyclotron orbit-averaged particle trajectory based on Hamiltonian theory are presented in Sec. III. At the end of Sec. III, we study in some detail the distribution of particle trajectories in phase space when the momentum is small [ $|\mathbf{p}|/(mc) \ll 1$ ]. A summary of the entire paper is contained in Sec. IV.

## II. THE PHYSICAL MECHANISM

To better understand the physical mechanism responsible for the resonance acceleration process, we develop in this section a mapping of particle momentum and phase from one cyclotron orbit to another. The pedagogical map (PMAP) will be derived from the equations of motion by using estimates of the particle trajectory that are characteristic of the true trajectory yet simple enough to allow us to

piece together the details of the acceleration mechanism. Focusing on the small momentum regime, a reduced version of the PMAP will be obtained that depends only on the perpendicular momentum and relative wave phase. This reduced map will then guide our extended discussion of the acceleration mechanism. For notational convenience, we assume a negatively charged particle in our discussion, though all of the analysis applies equally well to positively charged particles given appropriate sign changes in the trajectory and wave polarizations.

### A. Derivation of the pedagogical map

The equations of motion for the momentum  $\mathbf{p}$  and position  $\mathbf{x}$  of a particle of charge  $q$  and mass  $m$  in a Cartesian coordinate system  $(x, y, z)$  can be written as

$$\frac{d\mathbf{p}}{dt} = q \left( \mathbf{E}_w + \frac{\mathbf{v}}{c} \times (\mathbf{B}_0 + \mathbf{B}_w) \right), \quad (2)$$

$$\frac{d\mathbf{x}}{dt} = \mathbf{v}, \quad (3)$$

where  $\mathbf{p} = \gamma m \mathbf{v}$ ,  $\gamma = \sqrt{1 + |\mathbf{p}|^2 / (mc)^2}$ , and  $\mathbf{B}_0$  is the background magnetic field  $\mathbf{B}_0 = B_0 \mathbf{e}_z$ . The plane wave electric and magnetic fields are taken to be

$$\begin{aligned} \mathbf{E}_w = & E_1 \cos(\mathbf{k} \cdot \mathbf{x} - \omega t) \mathbf{e}_x \\ & - E_2 \sin(\mathbf{k} \cdot \mathbf{x} - \omega t) \mathbf{e}_y - E_3 \cos(\mathbf{k} \cdot \mathbf{x} - \omega t) \mathbf{e}_z, \end{aligned} \quad (4)$$

$$\begin{aligned} \mathbf{B}_w = & B_1 \sin(\mathbf{k} \cdot \mathbf{x} - \omega t) \mathbf{e}_x \\ & + B_2 \cos(\mathbf{k} \cdot \mathbf{x} - \omega t) \mathbf{e}_y - B_3 \sin(\mathbf{k} \cdot \mathbf{x} - \omega t) \mathbf{e}_z, \end{aligned} \quad (5)$$

where  $\omega$  is the wave frequency and  $\mathbf{k} = k_x \mathbf{e}_x + k_z \mathbf{e}_z$  is the wave vector in a coordinate system where  $k_y = 0$  with no loss of generality. The sign convention has been chosen so that if all the wave components are positive then the wave is right-hand circularly polarized. Using the plane wave solution to Faraday's law,

$$\mathbf{B}_w = (c/\omega) \mathbf{k} \times \mathbf{E}_w, \quad (6)$$

the components of the wave magnetic field can be written in terms of the components of the wave electric field,

$$B_1 = \eta_z E_2, \quad (7)$$

$$B_2 = \eta_x E_3 + \eta_x E_1, \quad (8)$$

$$B_3 = \eta_x E_2, \quad (9)$$

where  $\eta_x = ck_x/\omega$ ,  $\eta_z = ck_z/\omega$ , and the index of refraction  $\eta$  is defined as  $\eta = c|\mathbf{k}|/\omega$ .

The wave electric field amplitudes can be expressed as dimensionless quantities  $\epsilon_i$ , where

$$\epsilon_i = |q|E_i/mc\omega, \quad i = 1, 2, 3, \dots \quad (10)$$

The assumption that  $\epsilon \ll 1$ , where  $\epsilon = \max(\epsilon_1, \epsilon_2, \epsilon_3)$ , defines the small wave amplitude approximation. In this limit, the quiver energy is proportional to  $\epsilon^2$  (cf. Appendix A of Paper I).

Numerical solutions of the full equations of motion in the small wave amplitude limit show that the particle motion in the plane perpendicular to  $\mathbf{B}_0$  can be viewed as cyclotron motion with a slowly varying cyclotron radius  $\rho$  and perpen-

dicular momentum  $p_\perp = \sqrt{p_x^2 + p_y^2}$  (e.g., Fig. 2 of Paper I). Thus we are motivated to model the system as a sequence of discrete cyclotron orbits in the perpendicular plane with streaming parallel to the field (i.e.,  $v_z$  is a constant) during each orbit. The dynamics can then be reduced to a map that gives the momentum and position of the particle at a particular phase of the cyclotron orbit in terms of the momentum and position exactly one orbit earlier. We outline the derivation of this pedagogical map (PMAP) below.

Assume that a particle undergoes cyclotron motion in the perpendicular plane and streaming motion parallel to  $\mathbf{B}_0$  with a constant perpendicular and parallel momentum ( $p_\perp, p_{zn}$ ) between times  $t_n$  and  $t_{n+1} = t_n + 2\pi/\Omega_n$ ,  $n = 0, 1, 2, \dots$ . For  $t_n \leq t < t_{n+1}$ , the orbits for a negatively charged particle can be written as

$$\mathbf{p}_\perp = p_\perp \{ \sin[\Omega_n(t - t_n)] \mathbf{e}_x - \cos[\Omega_n(t - t_n)] \mathbf{e}_y \}, \quad (11)$$

$$p_z = p_{zn}, \quad (12)$$

$$x = -\rho_n \cos[\Omega(t - t_n)], \quad (13)$$

$$y = Y - \rho_n \sin[\Omega(t - t_n)], \quad (14)$$

$$z = z_n + v_{zn}(t - t_n), \quad (15)$$

where  $\rho_n = v_\perp/\Omega_n$ ,  $v_\perp = p_\perp/(\gamma_n m)$ ,  $v_{zn} = p_{zn}/(\gamma_n m)$ , and the relativistic cyclotron frequency is defined as

$$\Omega_n = |q|B_0/\gamma_n mc = \omega_c/\gamma_n, \quad (16)$$

with  $\omega_c$  the nonrelativistic cyclotron frequency. In Fig. 1, these orbits are plotted in various slices of  $(\mathbf{x}, \mathbf{p})$  phase space. Since the guiding center in  $x$  is a constant of the motion (Paper I), we have set it equal to zero without any loss of generality. We have also arbitrarily set the  $y$  guiding center  $Y$  equal to zero for illustrative purposes in Fig. 1. The value of  $Y$ , although not constant, is irrelevant since there is no  $y$  dependence in the problem.

At time  $t_{n+1}$ , the particle momentum,  $z$  position, and cyclotron radius are jumped (Fig. 1) by an amount that can be computed by integrating the equations of motion between  $t_n$  and  $t_{n+1}$ , assuming that the wave field is small enough that the particle motion can be reasonably approximated by a cyclotron orbit with streaming parallel to the background field. The  $z$  position variable can be replaced by the relative wave phase variable  $\psi$ , which we define to be

$$\psi = k_z z - \omega t. \quad (17)$$

Noting that the jump in the  $x$  position can be computed from the jump in  $p_\perp$  using the definition of the cyclotron radius  $\rho$ , the equations of motion necessary to compute the jump values can be reduced to three,

$$\begin{aligned} \frac{dp_\perp}{dt'} = & \frac{|q|}{2} \sum_{m=-\infty}^{+\infty} \\ & \times \cos \left( (m\Omega_n + \omega - k_z v_{zn})t' + \frac{m\pi}{2} - \psi_n \right) \\ & \times \left[ \left( E_1 + E_2 - \frac{v_{zn}}{c}(B_1 + B_2) \right) J_{m+1}(k_x \rho_n) \right. \\ & \left. + \left( E_1 - E_2 - \frac{v_{zn}}{c}(B_2 - B_1) \right) J_{m-1}(k_x \rho_n) \right], \end{aligned} \quad (18)$$



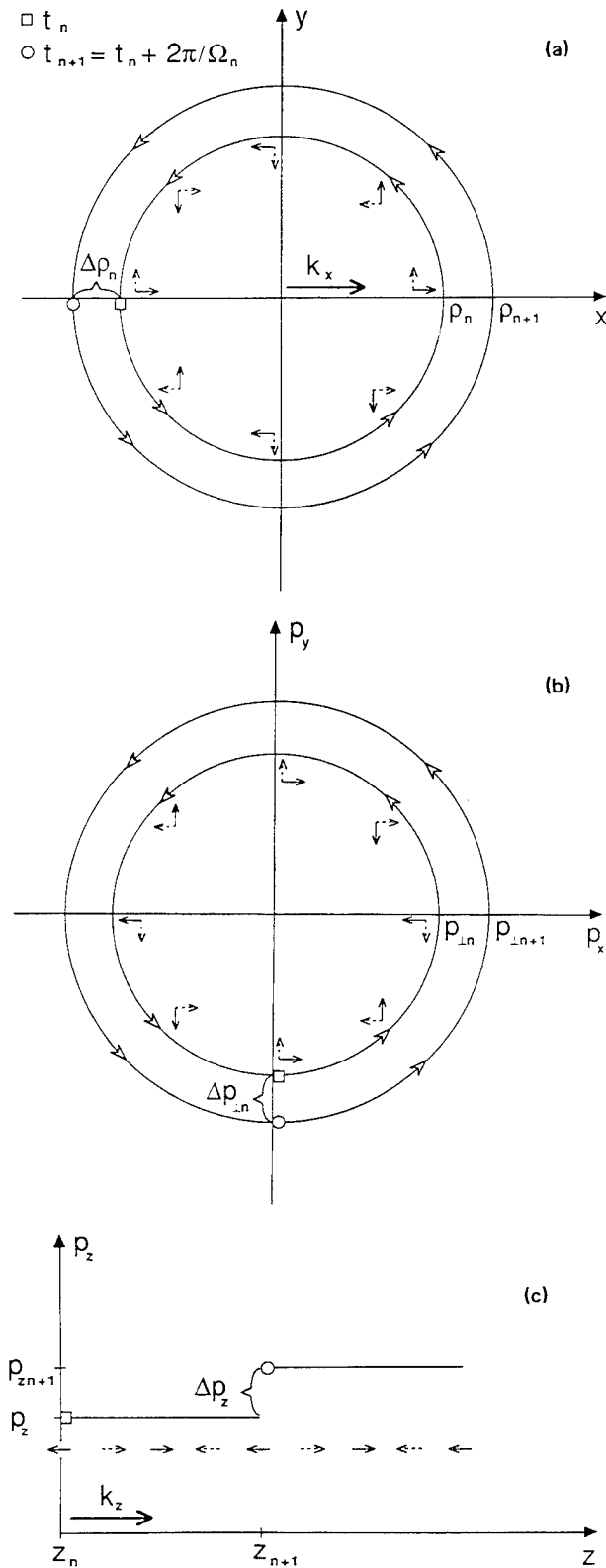


FIG. 1. Phase space trajectories in (a) the  $x$ - $y$  plane, (b) the  $p_x$ - $p_y$  plane, and (c) the  $z$ - $p_z$  plane, which are used for computing the PMAP. The particle begins at  $t_n$  (labeled with a box), completes one orbit, and then is jumped as indicated to begin another orbit at  $t_{n+1}$  (labeled with a circle). Also shown in (a) and (b) are the components of the corotating wave electric field (solid arrows) and magnetic field (dotted arrows) at various points in the orbit for a wave with  $\omega = 2\omega_c$ ,  $\psi_n \pmod{2\pi} = 0$ , and  $|\mathbf{E}_c| = |\mathbf{B}_c|$ . Orientations of the parallel wave electric field (solid arrow) and magnetic field (dashed arrow) at points along the trajectory are shown in (c). Bold face arrows correspond to components of the wave vector  $\mathbf{k}$ .

$$\frac{dp_z}{dt'} = \frac{|q|}{2} \sum_{m=-\infty}^{+\infty} \cos\left((m\Omega_n + \omega - k_z v_{zn})t' + \frac{m\pi}{2} - \psi_n\right) \times \left(2E_3 J_m(k_x \rho_n) + \frac{v_{\perp n}}{c} [(B_1 + B_2) J_{m+1}(k_x \rho_n) - (B_2 - B_1) J_{m-1}(k_x \rho_n)]\right), \quad (19)$$

$$\frac{d\psi}{dt'} = k_z v_{zn} - \omega, \quad (20)$$

where  $t' = t - t_n$  and  $J_m$  represents a Bessel function of integer order  $m$ . These modified equations have been derived from the Cartesian equations of motion [Eqs. (2) and (3)] using the definition of  $p_{\perp}$ , the explicit form for the wave fields [Eqs. (4) and (5)], and the approximate trajectories [Eqs. (11)–(15)] with the appropriate Bessel function expansion.<sup>8</sup> Making the cyclotron resonance approximation [Eq. (1)] with  $l < 0$  for negatively charged particles, the modified equations of motion [Eqs. (18)–(20)] can be integrated over the interval  $t' = [0, 2\pi/\Omega_n]$  to yield

$$\Delta p_{\perp n} = \frac{(-1)^{|l|+1} |q| \pi \cos\left(\psi_n + \frac{|l|\pi}{2}\right)}{\Omega_n} \times \left[ \left(E_1 + E_2 - \frac{p_{\perp n}}{\gamma_n m c} (B_1 + B_2)\right) J_{|l|-1}(k_x \rho_n) + \left(E_1 - E_2 - \frac{p_{\perp n}}{\gamma_n m c} (B_2 - B_1)\right) J_{|l|+1}(k_x \rho_n) \right], \quad (21)$$

$$\Delta p_{zn} = \frac{(-1)^{|l|+1} |q| \pi}{\Omega_n} \times \cos\left(\psi_n + \frac{|l|\pi}{2}\right) \left( -2E_3 J_{|l|}(k_x \rho_n) + \frac{p_{\perp n}}{\gamma_n m c} [(B_1 + B_2) J_{|l|-1}(k_x \rho_n) + (B_2 - B_1) J_{|l|+1}(k_x \rho_n)] \right) \quad (22)$$

$$\Delta \psi_n = 2\pi (k_z p_{zn} / m \omega_c - \omega / \Omega_n). \quad (23)$$

The PMAP is now completely specified: given  $(p_{\perp n}, p_{zn}, \psi_n)$  at time  $t_n$ , the corresponding quantities at  $t_{n+1}$  are given by

$$p_{\perp n+1} = p_{\perp n} + \Delta p_{\perp n}, \quad (24)$$

$$p_{zn+1} = p_{zn} + \Delta p_{zn}, \quad (25)$$

$$\psi_{n+1} = \psi_n + \Delta \psi_n, \quad (26)$$

using Eqs. (21)–(23) for the jump values.

The PMAP will prove to be a useful pedagogical tool for understanding the resonance acceleration process. However, it is not a good computational tool for accurately predicting a particle trajectory over any long period of time. This is largely because the map is not area-preserving in phase space and hence not time-reversal invariant, though the true equations of motion are derivable from a Hamiltonian. After many iterations, the phase space trajectories of the PMAP solutions will drift away from the trajectories of the true solutions.

The PMAP also has difficulties in predicting the initial

phase and initial momentum dependence of the motion, at least when the initial energy is less than or equal to the quiver energy. Our assumption in deriving the PMAP that the particle orbit differs only slightly from a cyclotron orbit could break down when the momentum is at the quiver energy level [ $p/(mc) \leq O(\epsilon)$ ]. If the particle does not complete a reasonable approximation to a cyclotron orbit in the time interval of an unperturbed cyclotron period, then the change in both  $p_{1n}$  and  $p_{zn}$  will not necessarily be as dictated by the PMAP and could be of  $O(\epsilon)$ . This will certainly be the case for the first cyclotron period when starting from cold initial conditions.

In light of these problems, the reader might wonder how we can be confident that the PMAP will be at all useful in understanding the acceleration process. We acquired our confidence from analysis with the PMAP, which yielded the kinetic energy and oscillation period scaling laws for the  $\eta_z \neq 1$  regime derived in Paper I to within a constant factor of order unity. Furthermore, analysis in the limit of parallel propagation ( $\mathbf{k} = k\mathbf{e}_z$ ) with the PMAP can reproduce precisely the asymptotic scaling of energy as a function of time derived from the exact solution of Roberts and Buchsbaum. The derivations of the  $\eta_z \neq 1$  scaling laws from the PMAP are given in the Appendix.

## B. The small momentum limit of the PMAP

The PMAP can be made simpler by assuming that the momentum will be relatively small [ $|\mathbf{p}_n|/(mc) \ll 1, n = 1, 2, 3, \dots$ ], though perhaps much larger than  $O(\epsilon)$ . Having the advantage of knowing what maximum energies are possible (Paper I) we can expect this to be a reasonable approximation in all parameter regimes excepting the case when  $\eta_z \approx 1$ . Even when  $\eta_z \approx 1$ , the small momentum limit of the PMAP will be useful in illustrating how cold initial particles are accelerated through the small momentum regime to eventually achieve energies where  $|\mathbf{p}|/(mc) \sim O(1)$ .

Recalling that  $k_x \rho_n = k_x p_{1n}/(m\omega_c)$ , the Bessel functions in the full PMAP [Eqs. (21)–(23)] can be approximated as<sup>9</sup>

$$J_{|l|}(k_x \rho_n) \approx \frac{1}{2^{|l|}\Gamma(|l|+1)} \left( \eta_x \frac{\omega}{\omega_c} \frac{p_{1n}}{mc} \right)^{|l|} \quad (27)$$

when  $|l| > 1$ . If  $|l| = 0$ , then  $J_{|l|} \approx 1$ . Expanding the relativistic gamma factor and the cyclotron frequency we obtain

$$\gamma_n \approx 1 + p_{1n}^2/2m^2c^2 + p_{zn}^2/2m^2c^2, \quad (28)$$

$$\Omega_n \approx \omega_c (1 - p_{1n}^2/2m^2c^2 - p_{zn}^2/2m^2c^2), \quad (29)$$

and, after some manipulation, we find that to lowest order in  $|\mathbf{p}|/(mc)$  the jump values for the PMAP become

$$\Delta p_{1n} = d_{|l|} (E_1 + E_2) \cos(\psi_n + |l|\pi/2) (p_{1n}/mc)^{|l|-1}, \quad (30)$$

$$\Delta p_{zn} = d_{|l|} (-\eta_x E_3 + B_1 + B_2) \times \cos(\psi_n + |l|\pi/2) (p_{1n}/mc)^{|l|} \quad (31)$$

$$\Delta \psi_n = -2\pi |l| \left( 1 + \frac{p_{1n}^2}{2m^2c^2} + \frac{p_{zn}^2}{2m^2c^2} - \eta_z \frac{p_{zn}}{mc} \right), \quad (32)$$

where  $d_l = |q|\pi/\omega_c$  and

$$d_{|l|} = [(-1)^{|l|-1} |q|\pi/\omega_c 2^{|l|-1} \Gamma(|l|)] \times [\eta_x (\omega/\omega_c)]^{|l|-1}, \quad (33)$$

for  $|l| > 1$ .

Further simplification is possible by noting a convenient relation that follows from the plane wave solution of Faraday's law [Eqs. (7)–(9)],

$$-\eta_x E_3 + B_1 + B_2 = \eta_z (E_1 + E_2). \quad (34)$$

Using this polarization relation, the equation for  $\Delta p_{zn}$  [Eq. (31)] can be rewritten as

$$\Delta p_{zn} = d_{|l|} \eta_z (E_1 + E_2) \cos(\psi_n + |l|\pi/2) (p_{1n}/mc)^{|l|}. \quad (35)$$

Comparing this expression for  $\Delta p_{zn}$  with the mapping equation for  $\Delta p_{1n}$  [Eq. (30)], we find

$$\eta_z \frac{p_{1n}}{mc} \frac{\Delta p_{1n}}{mc} = \frac{\Delta p_{zn}}{mc}. \quad (36)$$

Considering a sequence of orbits, we can sum Eq. (36), beginning at  $n = 0$ , to obtain

$$\eta_z \left( \frac{p_{1n}^2}{2m^2c^2} - \frac{p_{10}^2}{2m^2c^2} \right) = \frac{p_{zn}}{mc} - \frac{p_{z0}}{mc}, \quad (37)$$

where we have assumed  $p_{1n} \Delta p_{1n} \approx \Delta p_{1n}^2/2$ . This relation is the small wave amplitude, small momentum approximation to an exact constant of the motion [cf. Eq. (15) of Paper I].

Using the reduced constant of the motion [Eq. (37)] to replace  $p_{zn}$  in the phase jump equation, we discover to lowest order

$$\Delta \psi_n = -2\pi |l| \left( 1 + (1 - \eta_z^2) \frac{p_{1n}^2}{2m^2c^2} - \eta_z \frac{p_{z0}}{mc} + \eta_z^2 \frac{p_{10}^2}{2m^2c^2} \right), \quad (38)$$

where the quadratic term in  $p_{z0}$  has been dropped since it is much smaller than the term linear in  $p_{z0}$ . The normalized kinetic energy  $U_n = \gamma_n - 1$  can also be approximated using the small momentum expansion [Eq. (28)] and the reduced constant of the motion [Eq. (37)]. We obtain to lowest order in  $\epsilon$ ,

$$U_n = p_{1n}^2/2m^2c^2 + p_{z0}^2/2m^2c^2. \quad (39)$$

Note that the change in kinetic energy is proportional to the change in perpendicular momentum  $\Delta U_n \approx p_{1n} \Delta p_{1n}$ . Thus a discussion of the physical mechanism responsible for the change in momentum will be equally applicable to the change in kinetic energy.

To summarize, the PMAP reduces to two jump equations in the small momentum limit: one for  $\Delta \psi_n$  [Eq. (38)] and another for  $\Delta p_{1n}$  [Eq. (30)]. Values of  $p_{zn}$  are obtained from the reduced constant of the motion [Eq. (37)]. The approximation of small momentum will be valid for small wave amplitudes except when  $\eta_z \approx 1$ , where, after acceleration has taken place,  $p_{1n}/(mc) \sim O(1)$ . We remark that when  $k_x = 0$ , the full version of the PMAP [Eqs. (21)–(23)] is identical to that given in Eqs. (30) and (32) regardless of the value of  $|\mathbf{p}|/(mc)$ .

## C. Discussion of the physical mechanism

Test particles can achieve kinetic energies far in excess of the quiver energy, on times scales of many cyclotron orbits, by coherently accumulating the relatively small changes in kinetic energy that occur during each orbit. The degree to which a particle will gain or lose energy each orbit depends on the value of the relative wave phase, which will vary from orbit to orbit as a function of the energy. In this section, using the PMAP as a guide, we probe the physical effects underlying the change in energy and phase during each cyclotron orbit and how these effects act in concert to produce the long time scale acceleration mechanism. Our discussion will focus on the regime of small momentum describable by the version of the PMAP given in Eqs. (30) and (38).

### 1. The change in energy

The normalized kinetic energy  $U$  of a particle changes in an electromagnetic field according to the relation

$$\frac{dU}{dt} = \frac{q\mathbf{v} \cdot \mathbf{E}}{mc^2}. \quad (40)$$

Our study of the variation of kinetic energy becomes a study of how the particle velocity "lines up with" the wave electric field during the course of a cyclotron orbit. Since the change in kinetic energy  $\Delta U_n$  is proportional to the change in perpendicular momentum  $\Delta p_{\perp n}$  [Eq. (39)] in the small momentum limit, we can use the PMAP expression for  $\Delta p_{\perp n}$  to illustrate the processes responsible for  $\Delta U_n$ .

Examining the expression for  $\Delta p_{\perp n}$  [Eq. (30)], we see that a necessary condition for acceleration is  $E_1 + E_2 \neq 0$ . The reason for this becomes more clear when the wave electric field [Eq. (4)] is written in the following manner:

$$\begin{aligned} \mathbf{E}_w = & [(E_1 + E_2)/2] [\cos(\mathbf{k} \cdot \mathbf{x} - \omega t) \mathbf{e}_x \\ & - \sin(\mathbf{k} \cdot \mathbf{x} - \omega t) \mathbf{e}_y] \\ & + [(E_1 - E_2)/2] [\cos(\mathbf{k} \cdot \mathbf{x} - \omega t) \mathbf{e}_x \\ & + \sin(\mathbf{k} \cdot \mathbf{x} - \omega t) \mathbf{e}_y] \\ & - E_3 \cos(\mathbf{k} \cdot \mathbf{x} - \omega t) \mathbf{e}_z. \end{aligned} \quad (41)$$

The term proportional to  $E_1 + E_2$  represents the electric field component in the plane perpendicular to  $\mathbf{B}_0$  that rotates about  $\mathbf{B}_0$  in the same sense as the particle cyclotron motion. Not surprisingly, it is this component of the electric field (which we term the "corotating component" and denote as  $\mathbf{E}_c$ ) that dictates the energy transfer between the wave and particle via the change in  $p_{\perp n}$ . The corotating wave magnetic field  $\mathbf{B}_c$  can be defined in a similar manner with an amplitude

$$(B_1 + B_2)/2 = [\eta_z(E_1 + E_2) + \eta_x E_3]/2 \quad [\text{Eq. (34)}].$$

The nonzero  $\Delta p_{\perp n}$  arising from the corotating component of the electric field is a result of either of two effects: the corotation effect or the Doppler effect. If  $\omega \approx \omega_c$ , so that  $|I| = 1$  satisfies the resonance condition [Eq. (1)], it is the corotation effect that dominates as follows. When the wave frequency is within  $O(\epsilon)$  of the cyclotron frequency the corotation angle  $\theta$ , defined as the angle between  $\mathbf{p}_\perp$  and  $\mathbf{E}_c$ ,

$$\theta = \arccos\left(\frac{\mathbf{p}_\perp \cdot \mathbf{E}_c}{|\mathbf{p}_\perp| |\mathbf{E}_c|}\right) \quad (42)$$

remains relatively constant during the entire orbit. If the corotating electric field component  $\mathbf{E}_c$  is nonzero, then the integral of  $\mathbf{p}_\perp \cdot \mathbf{E}_c$  will be nonzero and the particle will interact with the wave either gaining or losing energy depending on the value of the corotation angle. Though relatively constant during one orbit,  $\theta$  will vary slightly from orbit to orbit and this slow variation will prove to be a major factor in the acceleration process. We will demonstrate below that  $\theta$  is related to the PMAP phase variable  $\psi_n$  in a simple manner.

If  $\omega \approx |I| \omega_c$  such that  $|I| > 1$  satisfies the cold particle resonance condition, it is the Doppler effect that determines  $\Delta p_{\perp n}$ . The corotating component of the electric field does not maintain a relatively constant angle with respect to  $\mathbf{p}_\perp$  but rotates through an angle of roughly  $2\pi(|I| - 1)$  during the course of an orbit. We illustrate this in the phase space plots of Fig. 1 by showing the directions of the wave electric field vector (solid arrows) and magnetic field vector (dotted arrows) for various points in the PMAP cyclotron orbit for  $|I| = 2$ . Unlike the situation when the corotation effect dominates, the  $x$  dependence of the wave phase (i.e.,  $k_x \neq 0$ ) is essential to the energy gain process. The integral of  $\mathbf{p}_\perp \cdot \mathbf{E}_w$  is dominated by the corotating component of the electric field  $\mathbf{E}_c$  evaluated during that part of the orbit where  $\mathbf{p}_\perp$  is parallel to  $\mathbf{k}$  (the point where  $p_x > 0, p_y = 0$  in Fig. 1). At this point, which we term the "Doppler point," the change of the wave phase with respect to the particle position is slower than at any other point in the orbit. The sign and magnitude of  $\Delta p_{\perp n}$  will depend on the value of the corotation angle at the Doppler point. We denote this angle as  $\theta_{\text{DP}}$ . As with the corotation effect scenario, the value of the  $\theta_{\text{DP}}$  (mod  $2\pi$ ) will change slightly from orbit to orbit according to the change of  $\psi_n$ .

Whether it is the corotation effect or the Doppler effect that is responsible for altering  $p_{\perp n}$ , the sign and magnitude of  $\Delta p_{\perp n}$  will depend on  $\theta_{\text{DP}}$  (in the case of the corotation effect,  $\theta_{\text{DP}}$  is characteristic of the value of  $\theta$  over the entire orbit). To deduce the relation between  $\theta_{\text{DP}}$  and the PMAP phase variable  $\psi_n$ , we first note that the Doppler point is the point one-quarter of the way around the PMAP cyclotron orbit (Fig. 1), which will be reached at the time  $t_{n+1/4} = t_n + \pi/(2\Omega_n)$ . Evaluating the expression for the corotation angle [Eq. (42)] at  $t = t_{n+1/4}$  using the PMAP trajectories [Eqs. (11)–(15)] and the wave field definitions [Eq. (4)], we discover

$$\theta_{\text{DP}} = \mathbf{k} \cdot \mathbf{x}_{n+1/4} - \omega t_{n+1/4}. \quad (43)$$

Since  $x_{n+1/4} = 0$ , this reduces to  $\theta_{\text{DP}} = k_z z_{n+1/4} - \omega t_{n+1/4}$ . Setting  $\Delta\psi_{n+1/4} = \psi_n + \Delta\psi_n/4$ , we can substitute into the PMAP expression for  $\Delta\psi_n$  [Eq. (38)] to arrive at the relation

$$\theta_{\text{DP}} = \psi_n - |I|\pi/2, \quad (44)$$

where we have ignored the small momentum terms. We see that the change in  $\theta_{\text{DP}}$  from one orbit to the next orbit is equivalent to  $\Delta\psi_n$  (mod  $2\pi$ ).

The phase dependence of  $\Delta p_{\perp n}$ , as dictated by the PMAP [Eq. (30)], is contained in the factor

$\cos(\psi_n + |l|\pi/2)$ . Substituting in the expression for the corotation angle at the Doppler point [Eq. (44)], we find

$$\Delta p_{\perp n} \propto (-1)^{|l|} \cos \theta_{DP}. \quad (45)$$

Taking into account the sign of the factor  $a_{|l|}$ ,  $\Delta p_{\perp n}$  is indeed maximized as a function of  $\psi_n$  at exactly the value of  $\psi_n$  that maximizes  $q\mathbf{p}_\perp \cdot \mathbf{E}_c / (|\mathbf{p}_\perp \mathbf{E}_c|)$  at the Doppler point.

It is clear that only the perpendicular component of the particle momentum  $p_{\perp n}$  and the wave electric field component  $\mathbf{E}_w$  are needed to alter the kinetic energy of each cyclotron orbit. If  $|l| > 1$ , there must also exist a nonzero oblique component to the wave vector ( $k_x \neq 0$ ). The parallel momentum  $p_{zn}$  and the wave magnetic field  $\mathbf{B}_w$  cannot be neglected, however, as they play an important role in altering the phase.

## 2. The change in phase

Having established the importance of the Doppler point corotation angle  $\theta_{DP}$  in determining the kinetic energy gain, we consider now the physical mechanisms responsible for the slow variation of  $\theta_{DP}$ , or, equivalently,  $\psi_n$  [Eq. (44)]. The jump in  $\psi_n$  predicted by the PMAP [Eq. (38)] is approximately  $-2\pi|l|$ , indicating that the wave propagates past the particle approximately  $|l|$  phases in a single cyclotron orbit. The small, but essential  $O(\epsilon)$  deviations from an exact  $-2\pi|l|$  phase change are a result of the energy dependence of the cyclotron frequency and the particle's streaming motion along the background magnetic field. These effects are clearly evident in the unapproximated PMAP expression for  $\Delta\psi_n$  [Eq. (23)].

The  $\Delta\psi_n$  equation in the small momentum version of the PMAP [Eq. (38)] contains the energy dependence of the cyclotron frequency in the negative semidefinite term  $-\pi|l| [p_{\perp n}/(mc)]^2$ . As the particle gains energy, the cyclotron frequency decreases and, with a fixed phase velocity  $\omega/k$ , the wave will propagate further past the particle during the increased cyclotron period. Consequently,  $\psi_n$  will decrease slightly more than the nominal value of  $-2\pi|l|$ . Interestingly, the energy dependence of the cyclotron frequency is a relativistic effect and plays a major role in the resonance acceleration process in the apparently nonrelativistic regime of  $|\mathbf{p}|/(mc) \ll 1$ .

The phase  $\psi_n \pmod{2\pi}$  can also be altered by the particle motion along the background magnetic field during the course of the orbit. The streaming component of  $\Delta\psi_n$ , originally proportional to  $p_{zn}$  in the full PMAP [Eq. (23)], reduces to the term

$$2\pi|l| \left( \eta_z^2 \frac{p_{\perp n}}{2m^2c^2} - \eta_z \frac{p_{z0}}{mc} - \eta_z^2 \frac{p_{\perp 0}^2}{2m^2c^2} \right) \quad (46)$$

in the small momentum version of  $\Delta\psi_n$ . Besides the initial streaming terms proportional to  $p_{z0}$  and  $p_{\perp 0}$ , there is an energy-dependent streaming term resulting from the wave interaction. This term is positive semidefinite because the wave interaction always produces a  $p_{zn}$  greater than  $p_{z0}$ , i.e.,  $p_{zn} - p_{z0} \geq 0$  [Eq. (37)]. Assuming for a moment that  $p_{z0} = 0$ , then  $p_{zn} > 0$  so that the particle moves in the same

direction as the wave along  $\mathbf{B}_0$ . Consequently, the wave does not move quite so far past the particle during the course of a cyclotron orbit as would be the case if  $p_{zn} \leq 0$  and  $\psi_n$  will be increased slightly from the nominal value of  $-2\pi|l|$ . If  $p_{z0} > 0$ , the wave-induced streaming is enhanced by the initial streaming. If  $p_{z0} < 0$ , the initial streaming opposes the wave-induced streaming and thus the total streaming part of  $\Delta\psi_n$  will be negative unless the particle energy becomes high enough that the wave-induced streaming dominates.

It is through the non-negligible streaming contribution to  $\Delta\psi_n$  that the motion of the particle in the direction of  $\mathbf{B}_0$  plays a role in the acceleration process. The variation of this motion is determined by the PMAP equation for  $\Delta p_{zn}$  [Eq. (31)] and perhaps a little surprisingly  $\Delta p_{zn}$  is proportional to the corotating component of the wave electric field. A closer examination of the relation between the wave electric and magnetic field polarizations [Eq. (34)] that leads to the simplified form of  $\Delta p_{zn}$  reveals the following picture. If the wave is electrostatic ( $\mathbf{k} \parallel \mathbf{E}_w$ ), then wave magnetic field is zero and the components of the electric field can be written as  $E_2 = 0$ ,  $\eta_x E_3 + \eta_z E_1 = 0$ . The component of the force in the  $z$  direction being proportional only to  $E_3$  can then be expressed in terms of  $E_1$  and hence the corotating component of the wave electric field [Eq. (41)].

If the wave has an electromagnetic component, then  $\Delta p_{zn}$  is determined entirely by the  $(\mathbf{v} \times \mathbf{B}_c)/c$  magnetic force. When averaged over a cyclotron period, the  $z$  component of the electric force is canceled out by the  $(v_x \mathbf{e}_x \times \mathbf{B}_c)/c$  component of the magnetic force leaving the other components of the magnetic force (proportional to  $E_1 + E_2$ ) to push the particle in  $z$ . The one exception would be the case of a wave where  $\eta_x E_3 + \eta_z E_1 = 0$  but  $E_2 \neq 0$  (linearly polarized in the  $y$  direction). In this case, the  $z$  component of the electric force is not canceled out and it is both the electric and magnetic forces that push the particle in  $z$ . We conclude that, for waves that are not purely electrostatic, the magnetic field of the wave cannot be ignored since it determines, to a large extent (if not completely), the motion of the particle parallel to  $\mathbf{B}_0$  and, as we have seen, this is important in determining the variation of  $\psi_n \pmod{2\pi}$  and hence  $p_{\perp n}$ .

## 3. The acceleration scenario for $p_{\perp 0} = p_{z0} = 0$

Our discussion of the cyclotron resonance acceleration process will not be complete until we explain how it is that the momentum and phase changing mechanisms work together to produce large energy gains over many cyclotron orbits. The acceleration scenario will be presented in two parts. First, we consider the case where  $p_{\perp 0} = 0$  (this section). Second, we consider initial momentum such that  $p_{\perp 0} \sim p_{z0} \sim O(\epsilon)$  (Sec. II C 4). We reiterate our earlier comments (Sec. II A) that the PMAP initial momentum will only be within  $O(\epsilon)$  of the true initial momentum. For example,  $p_{z0} = 0$  in the PMAP might correspond to a finite  $p_{z0}$  in reality and vice versa.

The change in phase [Eq. (38)] in the  $p_{\perp 0} = p_{z0} = 0$  limit takes the simple form

$$\Delta\psi_n = -2\pi|l| [1 + (1 - \eta_z^2)(p_{1n}^2/2m^2c^2)]. \quad (47)$$

Though the magnitude of  $\Delta\psi_n \pmod{2\pi}$  depends upon energy, the behavior of  $\psi_n \pmod{2\pi}$  will be monotonic; either monotonic decreasing if  $\eta_z < 1$ , monotonic increasing if  $\eta_z > 1$ , or constant if  $\eta_z = 1$ . When  $\eta_z < 1$ , the phase velocity in the direction of  $\mathbf{B}_0$  is greater than the speed of light and the relativistic cyclotron frequency effect dominates the phase change. Conversely, when  $\eta_z > 1$ , the phase velocity along  $\mathbf{B}_0$  is less than the speed of light and the streaming effect dominates. The phase change effects cancel each other out when  $\eta_z = 1$  leaving  $\psi_n \pmod{2\pi}$  a constant and, as we shall see, this causes singular behavior.

Let us first examine in detail the acceleration scenario for  $|l| = 1$  and then generalize for the scenario for other resonance numbers. When  $|l| = 1$ , the wave frequency is within  $O(\epsilon)$  of the cyclotron frequency and the PMAP equation for the change in perpendicular momentum [Eq. (30)] reduces to

$$\Delta p_{1n} = d_1 (E_1 + E_2) \cos(\psi_n + \pi/2), \quad (48)$$

where  $d_1$  is positive definite. Assume that  $\eta_z > 1$  and  $\psi_0 = \pi + \delta$ , where  $\delta$  is a small number greater than zero ( $\delta/\pi \ll 1$ ). The scenario is illustrated schematically in Fig. 2, where we plot  $\Delta p_{1n}$  as a function of  $\psi_n$  (solid curve). A dot-dashed line below the curve indicates the time history of  $\psi_n$  with a circle denoting the initial and final state of one period within  $O(\epsilon)$ .

Initially,  $\Delta p_{1n} > 0$  causing  $p_{1n}$  to grow and  $\psi_n \pmod{2\pi}$  to increase. The growth of  $p_{1n}$  will continue as long as  $\psi_n$  is in the range  $\pi < \psi_n < 2\pi$  (the "acceleration range") corresponding to the range of corotation angles where  $q\mathbf{p}_1 \cdot \mathbf{E}_c > 0$ . After a finite number of orbits, say  $N$ ,  $\psi_n \pmod{2\pi}$  will reach the value of  $2\pi$  [ $\psi_N \pmod{2\pi} = 0$ ] and  $p_{1n}$  will be a maximum, having accumulated over the  $N$  orbits where  $\Delta p_{1n} > 0$ . Continuing the monotonic increase,  $\psi_n$  will traverse the range  $0 < \psi_n < \pi$  (the "deceleration range") where  $\Delta p_{1n} < 0$  because of the corotation angle being such that  $q\mathbf{p}_1 \cdot \mathbf{E}_c < 0$ . The inverse symmetry of  $\Delta p_{1n}$  about  $\psi_N$  ensures that  $p_{1n}$  will decrease for  $N$  orbits until the initial condition

of  $p_{12N} = 0$  is reached at  $\psi_{2N} = \pi - \delta$ . At this point, one cycle of a periodic process has been completed (give or take the small factor of  $\delta$ ) with a maximum energy from the accumulation process exceeding the quiver energy and a period much longer than a cyclotron period.

If, instead, we were to consider the acceleration scenario for the case where  $\eta_z < 1$ , then  $\psi_n \pmod{2\pi}$  would be monotonically decreasing. The scenario described above would apply given the appropriate choice of initial phase ( $\psi_0 = 2\pi - \delta$ ) and the sign changes for  $\Delta\psi_n$ . Likewise, if we consider different resonance frequencies ( $|l| > 1$ ), the above described scenario will apply given the appropriate choice of  $\psi_0$  and sign of  $\Delta\psi_n$ . The major difference between the acceleration processes at  $|l| = 1$  and  $|l| > 1$  is the relative inefficiency of the Doppler effect in changing the energy compared to the corotation effect. This inefficiency is manifested in the PMAP through the factor of  $(p_{1n}/mc)^{|l|-1}$  in  $\Delta p_{1n}$  [Eq. (30)]. As a result of the less efficient energy gain per orbit  $p_{1n}$  will remain small for a larger number of orbits and  $\psi_n$  will take a larger number of orbits to cover the acceleration and deceleration ranges yielding a longer period for the cyclic process. For  $|l| \gg 3$ , the Doppler effect becomes sufficiently inefficient that maximum energies exceeding the quiver energy are no longer possible.

A less complicated, but more dramatic acceleration scenario exists when  $\eta_z = 1$ . According to the small momentum version of the PMAP,  $\Delta\psi_n = 0$  when  $\eta_z = 1$  [Eq. (38)]. Choosing  $\psi_0$  so that  $\Delta p_{10} > 0$  implies that  $\Delta p_{1n}$  will be greater than zero for all  $n$ , and the particle will accelerate indefinitely. This will be true for arbitrarily large  $p_{1n}$  in the limit  $k_x = 0$ , where the small momentum version of the PMAP becomes equivalent to the full PMAP. If  $k_x \neq 0$ , then the rising  $p_{1n}$  will saturate when  $p_{1n} \sim O(mc)$  because of the effects of higher-order terms not included in the expansions of the relativistic cyclotron frequency and the constant of the motion that were used in deriving the small momentum version of  $\Delta\psi_n$ . Thus, when  $p_{1n} \sim O(mc)$ , the relativistic cyclotron frequency effect no longer cancels out the streaming effect and the phase begins to slip. Such a higher-order effect

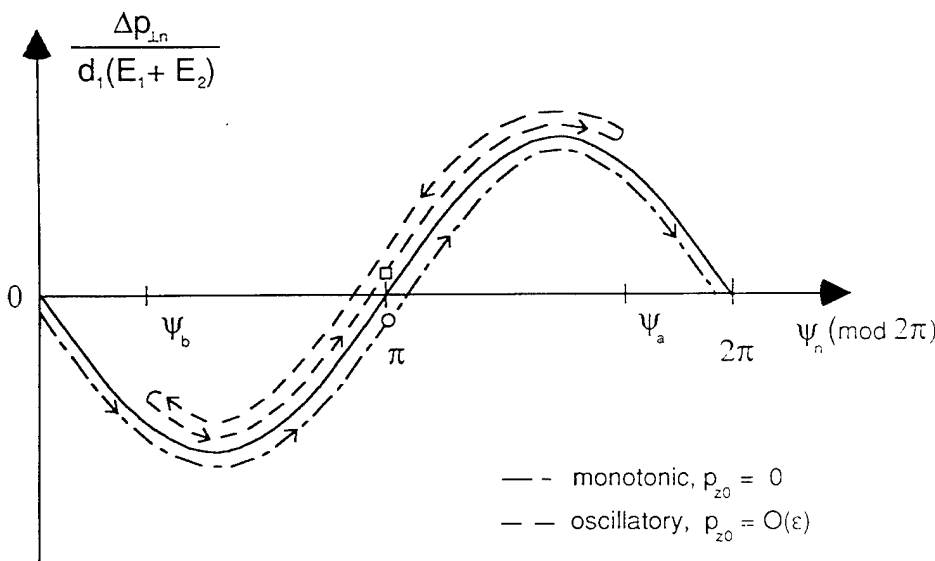


FIG. 2. The change in perpendicular momentum  $\Delta p_{1n}$  as a function of phase  $\psi_n \pmod{2\pi}$  according to the PMAP when  $|l| = 1$  (solid curve). Schematic representations of the time history of  $\psi_n$  are shown for a specific case of  $p_{20} = 0$  (dot-dashed curve) and  $p_{20} \sim O(\epsilon)$  (dashed curve). See the text for a detailed description.

would explain why the maximum energies observed when  $\eta_z = 1$  and  $k_x \neq 0$  are independent of wave amplitude and resonance frequency (Paper I).

The reader may have noted that the descriptions of the acceleration scenarios all depend upon a judicious choice of the initial phase  $\psi_0$ . If  $\psi_0$  is not chosen properly, the PMAP can predict negative values of  $p_{\perp n}$ , an unphysical situation. As we have emphasized, this failure of the PMAP to elucidate the initial phase dependence is a consequence of the cyclotron orbit sometimes failing to be a good approximation to the particle trajectory when  $p_{\perp 0} \leq O(\epsilon)$ .

#### 4. The acceleration scenario for $p_{\perp 0} \sim p_{z0} \sim O(\epsilon)$

Let us consider briefly how the acceleration mechanism works when the initial particle energy is of the order of the quiver energy. When formulated in terms of the PMAP, the predominant changes in the acceleration scenario with respect to the  $p_{\perp 0} = p_{z0} = 0$  case will be due to the effect of the  $p_{z0}$  term in the  $\Delta\psi_n$  relation [Eq. (38)]. This term provides a constant streaming phase change in addition to the phase changes stemming from the energy-dependent streaming and relativistic cyclotron frequency terms. The behavior of  $\psi_n$ , and hence  $p_{\perp n}$ , depends on the relative sign of the  $p_{z0}$  term with respect to the energy-dependent terms that are proportional to  $(1 - \eta_z^2)$ .

If the sign of  $p_{z0}$  is opposite that of  $(1 - \eta_z^2)$ , the acceleration process is little changed from the  $p_{z0} = 0$  scenario. The behavior of  $\psi_n$  is monotonic increasing or decreasing (depending on the value of  $\eta_z$ ), with the background streaming effect simply increasing the rate of change. An increased rate of change means that  $\psi_n$  passes through the acceleration range in fewer orbits. This decreases the sum of  $\Delta p_{\perp n}$  over the acceleration range and, consequently, lowers the maximum energy.

If  $p_{z0}$  has the same sign as  $(1 - \eta_z^2)$ , then the background streaming term contributes to  $\Delta\psi_n$  with a sign opposite to that of the energy-dependent effects. To illustrate how this alters the acceleration scenario, we consider the case where  $|I| = 1$ ,  $\eta_z < 1$ , and  $p_{z0} > 0$ , i.e., a regime where the relativistic cyclotron frequency effect dominates the energy-dependent contribution to  $\Delta\psi_n$ . These parameters lead to the simplified  $\Delta p_{\perp n}$  relation given in Eq. (48). To help guide the reader through the scenario, we display in Fig. 2 a schematic of the time history of  $\psi_n$  on the  $\Delta p_{\perp n}$  vs  $\psi_n$  plot (dashed line above the solid curve) with the square denoting the initial and final states of a long period to within  $O(\epsilon)$ .

Initially, the background streaming dominates the phase change since  $|p_{z0}/mc| \gg |p_{\perp 0}^2/m^2c^2|$  and  $\psi_n$  will increase. Given the appropriate choice of initial phase ( $\psi_0 = \pi + \delta$ ),  $\Delta p_{\perp n}$  will initially be positive and remains positive as long as  $\pi < \psi_n < 2\pi$ . If  $p_{z0}$  is not too large, then the rate of change of  $\psi_n$  will be slow enough to allow  $p_{\perp n}$  to build up to a level that allows the energy-dependent term in  $\Delta\psi_n$  to cancel out and then exceed the background streaming term. Assume that the cancellation of the two terms [ $\Delta\psi_n \pmod{2\pi} = 0$ ] occurs at  $\psi_n = \psi_a$ , where  $\pi < \psi_a < 2\pi$ . The phase will begin to decrease but  $\Delta p_{\perp n}$  remains positive until  $\psi_n = \pi$ , at which point  $p_{\perp n}$  has reached a maxi-

mum. Continuing to decrease,  $\psi_n$  enters the deceleration range ( $0 < \psi_n < \pi$ ), where  $\Delta p_{\perp n} < 0$ . The perpendicular momentum decreases and at the point  $\psi_b = \pi - \psi_a$ , the background streaming term will begin again to dominate  $\Delta\psi_n$ . The phase begins to increase while  $\Delta p_{\perp n}$  remains negative until  $\psi_n = \pi - \delta$  and the cycle is complete.

This acceleration scenario applies equally well to the  $\eta_z > 1$  and  $p_{z0} < 0$  case, provided the appropriate changes in initial phase, acceleration-deceleration ranges, and sign of  $\Delta\psi_n \pmod{2\pi}$  are made. The scenario is similar to the  $p_{z0} = 0$  scenario in that maximum energies much larger than the quiver energy occur with periods of variation much larger than a cyclotron period. In contrast with the  $p_{z0} = 0$  scenario,  $\psi_n$  exhibits oscillatory behavior instead of monotonic behavior. Maximum kinetic energies with an oscillatory  $\psi_n$  can often exceed maximum kinetic energies with a monotonic  $\psi_n$  because an oscillating  $\psi_n$  spends more cyclotron orbits in the acceleration range.

Oscillatory  $\psi_n$  behavior disappears when  $p_{z0}$  exceeds some critical value, say  $p_{zc}$ , and the background streaming propels  $\psi_n$  through the acceleration range before the energy-dependent contributions to  $\Delta\psi_n$  can "shut off" the background streaming. For  $p_{z0} > p_{zc}$ , the phase monotonically changes and the maximum  $p_{\perp n}$  decreases as  $p_{z0}$  increases. Numerical solutions of the full equations of motion have verified that this type of phase behavior occurs with values of  $p_{zc}$  within order unity of those estimated by the PMAP.

As was the case when  $p_{z0} = 0$ , it is not wise to press the PMAP too far since problems with the initial phase and momentum dependence thwart the PMAP predictive power. This becomes obvious when we ask what happens when  $p_{z0} \rightarrow 0$ . Sticking to the oscillatory scenario described in this section for  $p_{z0} \sim O(\epsilon)$ , we would expect that the oscillation period and maximum energy would decrease to zero. But this is not what happens; the initial phase changes to different values so that, when  $p_{z0} \rightarrow 0$ , we have the  $p_{z0} = 0$  acceleration scenario as discussed in Sec. II C 3 with large maximum energies. Let us appreciate the physical intuition that the PMAP has given us and move on to a more complex Hamiltonian analysis that will satisfy our quantitative needs.

### III. REDUCED HAMILTONIAN EQUATIONS OF MOTION

To probe the details of the cyclotron resonance acceleration process that fell through the cracks of the PMAP we turn to a Hamiltonian formulation of the test particle problem. Hamiltonian methods were used in Paper I to derive a pseudopotential function that was able to describe the behavior of the kinetic energy on time scales longer than a cyclotron period. In this section, we extend the Hamiltonian formulation of Paper I to produce reduced equations of motion capable of predicting cyclotron orbit-averaged details of the particle trajectory either analytically or in far less computational time than it would take to compute solutions of the full equations of motion.

In Cartesian coordinates, the Hamiltonian for a test particle in the electromagnetic wave fields described in Sec. II [Eqs. (4) and (5)], is

$$\mathcal{H}(\mathbf{x}, \mathbf{p}; t) = [m^2c^4 + (\mathbf{Pc} - q\mathbf{A})^2]^{1/2}, \quad (49)$$

where the canonical momenta are defined in terms of the physical momenta as  $\mathbf{P} = \mathbf{p} + q\mathbf{A}/c$ . The components of the vector potential can be reduced to

$$A_x = (mc^2/|q|) [ -(\omega_c/\omega)y + \epsilon_1 \sin \beta ], \quad (50)$$

$$A_y = (mc^2\epsilon_2/|q|) \cos \beta, \quad (51)$$

$$A_z = -(mc^2\epsilon_3/|q|) \sin \beta, \quad (52)$$

where  $\epsilon_i$  is given by Eq. (10) and we have introduced the phase variable

$$\beta(x, z, t) = k_x x + k_z z - \omega t. \quad (53)$$

A number of canonical transformations of the Cartesian Hamiltonian must be performed before a sufficiently useful time-independent Hamiltonian and corresponding set of canonical coordinates is produced. We refer the reader to Paper I for details on the sequence of transformations that we employ and will only present here the resultant Hamiltonian and the definitions of the corresponding canonical coordinates in terms of physical coordinates.

The Hamiltonian of interest [Eq. (24) of Paper I] can be written to  $O(\epsilon)$  as

$$H(\xi, \tilde{\phi}, P_\xi, \tilde{I}, P_\mu) = H_0(P_\xi, \tilde{I}, P_\mu) + H_1(\xi, \tilde{\phi}, P_\xi, \tilde{I}, P_\mu), \quad (54)$$

where

$$H_0(P_\xi, \tilde{I}, P_\mu) = Y - P_\xi, \quad (55)$$

$$H_1(\xi, \tilde{\phi}, P_\xi, \tilde{I}, P_\mu) = \frac{1}{2Y} \sum_{n=-\infty}^{\infty} a_n \sin[\xi + s(n-l)\tilde{\phi}], \quad (56)$$

with  $H_0 \sim O(1)$  and  $H_1 \sim O(\epsilon)$ . We have introduced the following quantities into the  $H$  representation:

$$Y(P_\xi, \tilde{I}, P_\mu) = [1 + (2\omega_c/\omega)(\tilde{I} + slP_\xi) + (\eta_z P_\xi - \eta_x P_\mu)^2]^{1/2}, \quad (57)$$

$$a_n(P_\xi, \tilde{I}, P_\mu) = -(\omega_c/\omega)\bar{\rho}[(\epsilon_1 + \epsilon_2)J_{n+1}(\eta_x \bar{\rho}) + (\epsilon_1 - \epsilon_2)J_{n-1}(\eta_x \bar{\rho}) + 2s\epsilon_3(\eta_z P_\xi - \eta_x P_\mu)J_n(\eta_x \bar{\rho})], \quad (58)$$

where

$$\bar{\rho}(P_\xi, \tilde{I}) = [(2\omega/\omega_c)(\tilde{I} + slP_\xi)]^{1/2} \quad (59)$$

and  $s$  is the sign of the charge. Unlike the Paper I representation of  $H$ , we have chosen to use dimensionless canonical variables. In particular, the canonical momenta  $(P_\xi, \tilde{I}, P_\mu)$  are in units normalized to  $\omega/mc^2$  and the Hamiltonian  $H$  is normalized to  $mc^2$ . To maintain the canonical properties of the Hamiltonian system it is necessary to introduce the normalized time variable  $\hat{t} = \omega t$ . In our set of dimensionless variables, derivatives with respect to time are expressed with the independent variable  $\hat{t}$ .

The canonical variables  $(\xi, \tilde{\phi}, P_\xi, \tilde{I}, P_\mu)$  are defined in terms of the physical variables by the relations,

$$\xi = \beta + (\omega/\omega_c)s\eta_x(p_y/mc + s\epsilon_2 \cos \beta) + sl\tilde{\phi}, \quad (60)$$

$$\tilde{\phi} = \arctan\left(\frac{-(p_y/mc + s\epsilon_2 \cos \beta)}{s(p_x/mc + s\epsilon_1 \sin \beta)}\right), \quad (61)$$

$$\mu = k_x x - k_z z - (\omega/\omega_c)s\eta_z(p_y/mc + s\epsilon_2 \cos \beta), \quad (62)$$

$$P_\xi = \frac{1}{\eta^2} \left( \eta_x \frac{p_x}{mc} + \eta_z \frac{p_z}{mc} - \frac{\omega_c}{c} s\eta_x y + s(\eta_x \epsilon_1 - \eta_z \epsilon_3) \sin \beta \right), \quad (63)$$

$$\tilde{I} = \frac{\omega}{2\omega_c} \left[ \left( \frac{p_x}{mc} + s\epsilon_1 \sin \beta \right)^2 + \left( \frac{p_y}{mc} + s\epsilon_2 \cos \beta \right)^2 \right] - slP_\xi, \quad (64)$$

$$P_\mu = \frac{1}{\eta^2} \left( \eta_z \frac{p_x}{mc} - \eta_x \frac{p_z}{mc} - \frac{\omega_c}{c} s\eta_z y + s(\eta_z \epsilon_1 + \eta_x \epsilon_3) \sin \beta \right), \quad (65)$$

with  $\beta(x, z, t)$  given by Eq. (53). Inverting these definitions, we obtain the following expressions for the physical variables as functions of the canonical variables:

$$x = (c/\omega\eta^2)(\eta_z \mu + \eta_x \xi - sl\eta_x \tilde{\phi} + \eta_x \hat{t} + s\eta^2 \bar{\rho} \sin \tilde{\phi}), \quad (66)$$

$$y = (c/\omega) [ -s(\omega/\omega_c)(\eta_x P_\xi + \eta_z P_\mu) + \bar{\rho} \cos \tilde{\phi} ], \quad (67)$$

$$z = (c/\omega\eta^2)(\eta_z \xi - \eta_x \mu - sl\eta_z \tilde{\phi} + \eta_z \hat{t}), \quad (68)$$

$$p_x/mc = (s\omega_c/\omega)\bar{\rho} \cos \tilde{\phi} - s\epsilon_1 \sin(\xi - sl\tilde{\phi} + s\eta_x \bar{\rho} \sin \tilde{\phi}), \quad (69)$$

$$p_y/mc = -(\omega_c/\omega)\bar{\rho} \sin \tilde{\phi} - s\epsilon_2 \cos(\xi - sl\tilde{\phi} + s\eta_x \bar{\rho} \sin \tilde{\phi}), \quad (70)$$

$$p_z/mc = \eta_z P_\xi - \eta_x P_\mu + s\epsilon_3 \sin(\xi - sl\tilde{\phi} + s\eta_x \bar{\rho} \sin \tilde{\phi}), \quad (71)$$

with  $\bar{\rho}(P_\xi, \tilde{I})$  given by Eq. (60). In Paper I, the relation between the canonical coordinates  $(\xi, \tilde{\phi}, \mu, P_\xi, \tilde{I}, P_\mu)$  and conventional action-angle guiding center canonical variables is discussed. The Hamiltonian  $H$  and corresponding canonical variables differ from Hamiltonian formulations used in previous studies of wave-particle interactions<sup>5,10</sup> in that there is no singular behavior in the canonical coordinates as  $\eta_z \rightarrow 0$ .

The cyclotron resonance approximation used in Paper I and in the construction of the PMAP (Sec. II) is founded on the assumption that there are two widely varying dynamical time scales, with the faster time scale being on the order of the nonrelativistic cyclotron period. In the Hamiltonian formulation, this separation of time scales is determined by the relative magnitude of the two frequencies  $\omega_1 = d\xi/d\hat{t}$  and  $\omega_2 = d\tilde{\phi}/d\hat{t}$ . These nondimensional frequencies can be computed from  $H$  and are found to be

$$\omega_1 = (1/Y) [ (sl\omega_c/\omega) + \eta_z(\eta_z P_\xi - \eta_x P_\mu) - 1 + O(\epsilon) ], \quad (72)$$

$$\omega_2 = \omega_c/Y\omega + O(\epsilon). \quad (73)$$

Defining the winding number  $r$  to be the ratio of the slow to fast frequency, we see

$$r = sl + (\omega/\omega_c)\eta_z(\eta_z P_\xi - \eta_x P_\mu) - (\omega/\omega_c)Y + O(\epsilon). \quad (74)$$

The cyclotron resonance approximation assumes  $r \sim O(\epsilon)$  with  $l$  chosen to satisfy this as well as possible. When expressed in terms of the physical variables, the assumption of small winding number is equivalent to the resonance condition [Eq. (1)] normalized to the relativistic cyclotron frequency  $\Omega$ . In the above analysis, it has been implicitly assumed that  $\partial H_1 / \partial P_{\xi} \sim O(\epsilon)$ , which seems reasonable given  $H_1 \sim O(\epsilon)$ . We shall discover later (Sec. III C 2) that this is not always the case.

Reduction of the Hamiltonian  $H$  in the cyclotron resonance approximation can be carried out either discretely or continuously. Though the discrete mapping approach presented in Sec. III A is often the method of choice (since the time averaging process is explicit), there are difficulties with accuracy in certain regions of phase space. We are thus led to construct equations of motion with a continuous time variable in Sec. III B from an orbit-averaged reduced Hamiltonian. Details of the particle trajectories in the small momentum limit are studied in Sec. III C.

### A. Orbit-averaged mapping equations

Our goal in this section is to construct a set of area-preserving mapping equations that will approximate the particle trajectory in the canonical variable phase space. The mapping equations will determine the slowly varying variables  $P_{\xi}$  and  $\xi$  on the phase space surface of constant  $\tilde{\phi} \pmod{2\pi}$  with successive iterations of the map (denoted by the subscript  $n$ ) indicating an increase of  $\tilde{\phi}$  by  $2\pi$ , i.e.,  $\tilde{\phi}_{n+1} = \tilde{\phi}_n + 2\pi$ . The map construction outlined below employs standard methods of Hamiltonian analysis that are discussed in detail elsewhere.<sup>11</sup>

We seek a mapping of the form

$$P_{\xi_{n+1}} = P_{\xi_n} + \Delta P_{\xi_n}(P_{\xi_{n+1}}, \xi_n), \quad (75)$$

$$\xi_{n+1} = \xi_n + 2\pi r(P_{\xi_{n+1}}) + g(P_{\xi_{n+1}}, \xi_n), \quad (76)$$

where  $r$  is the winding number given by Eq. (74) without the " $O(\epsilon)$ " term. When  $\epsilon = 0$ , then  $\Delta P_{\xi_n} = g = 0$  and  $P_{\xi_n}$  is a constant of the motion. In this limit,  $\xi_n$  will advance by an amount equal to the slow frequency  $\omega_1$  times the fast period  $T = 2\pi/\omega_2$ , with  $\omega_2$  given by Eq. (73) without the " $O(\epsilon)$ " term.

The first-order correction  $\Delta P_{\xi_n}$  to the trivial zeroth-order behavior of  $P_{\xi_n}$  is computed by integrating the equation of motion for  $dP_{\xi}/dt$  from time  $\hat{t}_n$  to  $\hat{t}_n + T$ ,

$$\begin{aligned} \Delta P_{\xi_n} &= \int_{\hat{t}_n}^{\hat{t}_n + T} d\hat{t} \frac{dP_{\xi}}{d\hat{t}} \\ &= - \int_0^T d\hat{t} \frac{\partial H_1}{\partial \xi}(\xi_n + \omega_1 \hat{t}, \tilde{\phi}_0 + \omega_2 \hat{t}, P_{\xi_{n+1}}, \tilde{I}), \end{aligned} \quad (77)$$

where the zeroth-order trajectories are substituted in for the canonical variables in the integrand. For purposes of area preservation, the value  $P_{\xi_{n+1}}$  is used instead of  $P_{\xi_n}$ . Also,  $\tilde{I}$  is a constant to  $O(\epsilon^2)$  independent of  $n$ . This can be deduced by integrating the expression  $d\tilde{I}/d\hat{t} = -\partial H_1/\partial \tilde{\phi}$  to lowest order between  $\hat{t}_n$  and  $\hat{t}_n + T$ .

Evaluating the  $\Delta P_{\xi_n}$  integral [Eq. (77)] using the first-

order Hamiltonian [Eq. (56)] and keeping in mind the resonance approximation, we find

$$\Delta P_{\xi_n} = -(\pi\omega/\omega_c) a_l \cos \xi_n, \quad (78)$$

where  $a_l(P_{\xi_n})$  is given by Eq. (58) with  $P_{\xi_{n+1}}$  substituted in for  $P_{\xi}$ .

The first-order correction  $g$  to the zeroth-order rotation of  $\xi_n$  is determined by demanding that the map be area-preserving in  $(P_{\xi}, \xi)$  phase space. A consideration of the Jacobian of the map transformation defined by Eqs. (75) and (76) yields the following condition for area preservation:

$$\frac{\partial(\Delta P_{\xi_n})}{\partial P_{\xi_{n+1}}} + \frac{\partial g}{\partial \xi_n} = 0. \quad (79)$$

This differential equation can be easily integrated upon substitution of the  $\Delta P_{\xi_n}$  expression [Eq. (78)] to yield

$$g = (\pi\omega/\omega_c) a'_l \sin \xi_n, \quad (80)$$

where

$$\begin{aligned} a'_l &= -(sl^2/\bar{\rho}) [(\epsilon_1 - \epsilon_2) J_{l-1}(\eta_x \bar{\rho}) \\ &\quad - (\epsilon_1 + \epsilon_2) J_{l+1}(\eta_x \bar{\rho})] - 2sl \eta_x \epsilon_2 J_l(\eta_x \bar{\rho}) \\ &\quad + 2s\epsilon_3 \{ \eta_z J_l(\eta_x \bar{\rho}) + (sl\omega/\bar{\rho}^2 \omega_c) (\eta_z P_{\xi_{n+1}} - \eta_x P_{\mu}) \\ &\quad \times [\eta_x \bar{\rho} J_{l-1}(\eta_x \bar{\rho}) - l J_l(\eta_x \bar{\rho})] \}. \end{aligned} \quad (81)$$

The map is now complete. Starting with values for  $(\xi_n, P_{\xi_n})$ , the value of  $P_{\xi_{n+1}}$  is obtained by solving the  $P_{\xi}$  map equation [Eq. (75)] for  $P_{\xi_{n+1}}$  given the function  $\Delta P_{\xi_n}(P_{\xi_{n+1}}, \xi_n)$  [Eq. (78)]. Direct substitution of  $P_{\xi_{n+1}}$  and  $\xi_n$  into the  $\xi$  map equation (76) with  $r(P_{\xi_{n+1}})$  given by Eq. (75) and  $g(P_{\xi_{n+1}}, \xi_n)$  given by Eq. (80) yields  $\xi_{n+1}$ . Initial conditions fix the value of  $\tilde{\phi} \pmod{2\pi}$  and the constants of the motion  $\tilde{I}$  and  $P_{\mu}$ . We denote the map constructed above as the "QMAP" since it is more quantitatively accurate than the PMAP constructed in Sec. II.

The QMAP can be simplified by assuming small momenta. In physical variables, the small momentum limit demands  $|p/mc| \ll 1$ , which, when translated to canonical variables, is equivalent to the conditions  $\tilde{I} + slP_{\xi_n} \ll 1$  and  $\eta_x P_{\xi_n} - \eta_x P_{\mu} \ll 1$ . Expanding the  $\Delta P_{\xi_n}$ ,  $\omega$ , and  $g$  functions of the QMAP in the small arguments [making use of Eq. (27)] we arrive at the following set of mapping equations for negatively charged particles:

$$P_{\xi_{n+1}} = P_{\xi_n} - (\pi\omega/\omega_c) b_{|l|} \bar{\rho}^{|l|} \cos \xi_n, \quad (82)$$

$$\begin{aligned} \xi_{n+1} &= \xi_n + 2\pi \left( |l| - \frac{\omega}{\omega_c} - (\tilde{I} + |l| P_{\xi_{n+1}}) \right. \\ &\quad \left. + \frac{\eta_z \omega}{\omega_c} (\eta_z P_{\xi_{n+1}} - \eta_x P_{\mu}) \right) \\ &\quad + \frac{\pi\omega}{\omega_c} c_{|l|} \bar{\rho}^{|l|-2} \sin \xi_n, \end{aligned} \quad (83)$$

where

$$b_{|l|} = -(-\eta_x)^{|l|-1} \omega_c (\epsilon_1 + \epsilon_2) / 2^{|l|-1} \Gamma(|l|) \omega, \quad (84)$$

$$c_{|l|} = (|l|^2 \omega/\omega_c) b_{|l|}, \quad (85)$$



and  $\bar{\rho}(P_{\xi_{n+1}})$  is given by Eq. (59) with  $P_{\xi} \rightarrow P_{\xi_{n+1}}$ . In the small momentum approximation  $\bar{\rho} \ll 1$ .

To see if the QMAP provided a reasonably accurate estimate of the true phase space trajectories, we compared QMAP solutions with numerical solutions of the full equations of motion [Eqs. (2) and (3)] over a range of the free parameters ( $|l|$ ,  $\omega/\omega_c$ ,  $\eta$ ,  $\alpha$ ,  $\epsilon$ ,  $\mathbf{k} \cdot \mathbf{x}_0$ ) for cold initial conditions ( $\mathbf{p}_0 = 0$ ). We found good agreement when  $|l| \geq 2$ , albeit we did not do as complete a survey as will be discussed in Sec. III B. There is a problem, however, when  $|l| = 1$  and the true behavior of  $\xi$  in certain regions of phase space is not well modeled by the QMAP.

This difficulty can be understood as follows. When  $|l| = 1$ , the  $\xi$  QMAP equation [Eq. (83)] contains a term proportional to  $(\sin \xi_n)/\bar{\rho}(P_{\xi_{n+1}})$ . For cold initial particles, there are portions of the phase space orbits (where the momenta are very small) that pass very close to those values of  $P_{\xi}$  that make  $\bar{\rho} = 0$ . Fortunately, the true phase trajectory is also in a region near  $\xi = 0$  or  $\pi$  so that the value of  $\sin \xi_n$  also approaches 0. The behavior of the ratio  $(\sin \xi_n)/\bar{\rho}(P_{\xi_{n+1}})$  is extremely sensitive to the exact values of  $(\xi, P_{\xi})$  to the extent that a slight deviation from the true trajectory as  $\xi \rightarrow 0$  or  $\pi$  results in a value much greater than unity. Unfortunately, as a consequence of the fixed time-step size of the QMAP and the implicit nature in which the quantities are advanced, the discrete jump in  $P_{\xi}$  is computed *before* the corresponding jump in  $\xi$ , and the quantity  $(\xi_n, P_{\xi_{n+1}})$  deviates enough from the true trajectory that QMAP ratio  $\sin \xi_n/\bar{\rho}(P_{\xi_{n+1}})$  becomes extremely large. The deviation is enough, in fact, to cause large inaccuracies in the values of  $\xi_{n+1} - \xi_n$ . More will be said about these regions of singular behavior in Sec. III C.

In trying to circumvent this problem, we are immediately led to consider the possibility of decreasing the time step of the jump so that the quantity  $(\xi_n, P_{\xi_{n+1}})$  more closely approximates the desired quantity  $[\xi(t), P_{\xi}(t)]$ . This can be done most effectively by abandoning the discrete jumps of a map altogether and constructing orbit-averaged equations of motion with a continuous time variable.

## B. Orbit-averaged continuum equations

With the aid of adiabatic canonical perturbation theory,<sup>12</sup> it is possible to transform the Hamiltonian  $H$  to a new Hamiltonian  $\bar{H}$  that will depend only on slowly varying variables to  $O(\epsilon)$ , provided the resonance approximation is satisfied. This transformation was used in the course of deriving the HPP theory in Appendix B of Paper I. We outline the transformation below in the context of the dimensionless canonical variables that have been introduced in this paper.

The generating function  $S$  for the transformation can be written as a function of the old coordinates and new momenta as

$$S(\xi, \bar{\phi}, \mu, \bar{P}_{\xi}, \bar{I}, \bar{P}_{\mu}) = \xi \bar{P}_{\xi} + \bar{\phi} \bar{I} + \mu \bar{P}_{\mu} + S_1(\xi, \bar{\phi}, \bar{P}_{\xi}, \bar{I}, \bar{P}_{\mu}), \quad (86)$$

where

$$S_1(\xi, \bar{\phi}, \bar{P}_{\xi}, \bar{I}, \bar{P}_{\mu})$$

$$= \frac{\omega}{2\omega_c} \sum_{n=-\infty}^{\infty} \frac{a_n}{s(n-l)} \cos[\xi + s(n-l)\bar{\phi}] \quad (87)$$

and  $a_n(\bar{P}_{\xi}, \bar{I}, \bar{P}_{\mu})$  is given by Eq. (58) with  $(P_{\xi}, \bar{I}, P_{\mu}) \rightarrow (\bar{P}_{\xi}, \bar{I}, \bar{P}_{\mu})$ . To  $O(\epsilon)$ , the new canonical variables  $(\xi, \bar{\phi}, \bar{P}_{\xi}, \bar{I})$  are defined in terms of the old variables according to the relations

$$\bar{\xi} = \xi + \frac{\partial S_1}{\partial P_{\xi}}, \quad (88)$$

$$\bar{\phi} = \bar{\phi} + \frac{\partial S_1}{\partial \bar{I}}, \quad (89)$$

$$\bar{\mu} = \mu + \frac{\partial S_1}{\partial P_{\mu}}, \quad (90)$$

$$\bar{P}_{\xi} = P_{\xi} - \frac{\partial S_1}{\partial \xi}, \quad (91)$$

$$\bar{I} = \bar{I} - \frac{\partial S_1}{\partial \bar{\phi}}, \quad (92)$$

$$\bar{P}_{\mu} = P_{\mu}, \quad (93)$$

where  $(P_{\xi}, \bar{I}, P_{\mu})$  have been substituted in for  $(\bar{P}_{\xi}, \bar{I}, \bar{P}_{\mu})$  in the  $S_1$  definition [Eq. (87)]. The Hamiltonian  $H$  [Eq. (54)] transforms to  $\bar{H}$ , where

$$\bar{H} = \Upsilon - \bar{P}_{\xi} + (a_l/2\Upsilon) \sin \bar{\xi} \quad (94)$$

and  $\Upsilon(\bar{P}_{\xi}, \bar{I}, \bar{P}_{\mu})$  is given by Eq. (57) with  $(P_{\xi}, \bar{I}, P_{\mu}) \rightarrow (\bar{P}_{\xi}, \bar{I}, \bar{P}_{\mu})$ . By choosing  $S_1$  properly, the fast varying terms have been displaced to  $O(\epsilon^2)$  in transforming from  $H$  to  $\bar{H}$ . What remains in  $\bar{H}$  is essentially  $H$  averaged over one period in  $\bar{\phi}$  while the other variables are held constant. Thus, like the QMAP, dynamic details occurring on time scales less than  $2\pi/\omega_2$  (roughly the cyclotron period) are absent.

From the orbit-averaged Hamiltonian  $\bar{H}$ , we can compute the orbit-averaged equations of motion for the canonical variables  $\bar{\xi}$  and  $\bar{P}_{\xi}$ :

$$\frac{d\bar{\xi}}{dt} = \Upsilon' - 1 + \frac{1}{2\Upsilon} (a_l' - a_l \frac{\Upsilon'}{\Upsilon}) \sin \bar{\xi}, \quad (95)$$

$$\frac{d\bar{P}_{\xi}}{dt} = -\frac{a_l}{2\Upsilon} \cos \bar{\xi}, \quad (96)$$

where

$$\Upsilon' = sl\omega_c/\omega\Upsilon + (\eta_z/\Upsilon)(\eta_z \bar{P}_{\xi} - \eta_x \bar{P}_{\mu}) \quad (97)$$

and  $a_l'$  is given by Eq. (81) with  $P_{\xi} \rightarrow \bar{P}_{\xi}$  and  $\bar{I} \rightarrow \bar{I}$ . The canonical momenta  $\bar{I}$  and  $\bar{P}_{\mu}$  are constants of the motion and the linear time variation of the corresponding angles can be written as

$$\bar{\phi} = \bar{\phi}_0 + \frac{\partial \bar{H}}{\partial \bar{I}} \hat{t}, \quad (98)$$

$$\bar{\mu} = \bar{\mu}_0 + \frac{\partial \bar{H}}{\partial \bar{P}_{\mu}} \hat{t}. \quad (99)$$

In the small momentum limit, the orbit-averaged equa-

tions of motion can be reduced to the simpler form [cf. the QMAP reduction, Eqs. (82) and (83)]

$$\frac{d\bar{P}_\xi}{dt} = -\frac{b_{|l|}}{2} \left[ \left( \frac{2\omega}{\omega_c} \right) (\bar{I} + |l| \bar{P}_\xi) \right]^{|l|/2} \cos \bar{\xi}, \quad (100)$$

$$\begin{aligned} \frac{d\bar{\xi}}{dt} = & \frac{|l| \omega_c}{\omega} - \left( \frac{\omega_c}{\omega} \right) (\bar{I} + |l| \bar{P}_\xi) \\ & + \eta_z (\eta_z \bar{P}_\xi - \eta_x \bar{P}_\mu) - 1 \\ & + \frac{c_{|l|}}{2} \left[ \left( \frac{2\omega}{\omega_c} \right) (\bar{I} + |l| \bar{P}_\xi) \right]^{|l|/2-1} \sin \bar{\xi}, \end{aligned} \quad (101)$$

where  $b_{|l|}$  and  $c_{|l|}$  are given by Eqs. (84) and (85), respectively, and we have assumed negatively charged particles. We also make use of the fact that, in the small momenta limit, the resonance condition is satisfied when  $\omega = |l| \omega_c + O(\epsilon)$ .

To complete the orbit-averaged continuum description, we need a prescription that gives the canonical variables  $(\bar{\xi}, \bar{\phi}, \bar{P}_\xi, \bar{I}, \bar{\mu}, \bar{P}_\mu)$  in terms of the physical variables and vice versa. In theory, this is straightforward, given the definitions of these variables in terms of  $(\xi, \phi, P_\xi, I, \mu, P_\mu)$  [Eqs. (88)–(93)] and the explicit relations between  $(\xi, \phi, P_\xi, I, \mu, P_\mu)$  and the physical variables [Eqs. (60)–(71)]. In practice, we have chosen to simply set  $(\bar{\xi}, \bar{\phi}, \bar{P}_\xi, \bar{I}, \bar{\mu}, \bar{P}_\mu) = (\xi, \phi, P_\xi, I, \mu, P_\mu)$  and ignore the  $S_1$  corrections. Equating the angles  $(\bar{\xi}, \bar{\phi}, \bar{\mu}) = (\xi, \phi, \mu)$  is undoubtedly a reasonable approximation since the angular variations are  $O(2\pi)$  and the corrections are  $O(\epsilon)$ . Equating the actions  $(\bar{P}_\xi, \bar{I}) = (P_\xi, I)$  is reasonable if we interpret  $(P_\xi, I)$  as representing quantities time-averaged over the fast period  $2\pi/\omega_2$ . We must then assume that the physical initial conditions represent the initial time-averaged values of  $(P_\xi, I)$  through Eqs. (60)–(65). Conversely, the physical variables derived from Eqs. (66)–(71), assuming  $(P_\xi, I) = (\bar{P}_\xi, \bar{I})$ , will be characteristic of the time average.

With  $(\bar{\xi}, \bar{\phi}, \bar{P}_\xi, \bar{I}, \bar{\mu}, \bar{P}_\mu) = (\xi, \phi, P_\xi, I, \mu, P_\mu)$ , the orbit-averaged continuum equations are identical to the continuous limit of the QMAP [Eqs. (75) and (76)] in the sense that

$$\frac{d\bar{P}_\xi}{dt} = \frac{\Delta P_{\xi_{n+1}}}{T}, \quad (102)$$

$$\frac{d\bar{\xi}}{dt} = \frac{2\pi r + g}{T}, \quad (103)$$

when  $P_{\xi_{n+1}} \rightarrow \bar{P}_\xi$  and  $\xi_n \rightarrow \bar{\xi}$ .

Being ordinary differential equations in a continuous time variable, the orbit-averaged equations of motion can be solved numerically with arbitrary time steps (i.e., as small as needed for stability) and hence avoid the difficulties that were imposed on the QMAP by a fixed time step interval. The freedom to impose an arbitrary time step should be viewed solely as a mathematical convenience since short time-scale physical effects have been averaged out.

To numerically solve the equations of motion, we use a standard fourth-order accurate Runge–Kutta<sup>13</sup> algorithm. As a demonstration of the validity of the orbit-averaged continuum approach, we compare numerical solutions of the orbit-averaged equations to numerical solutions of the full

equations of motion [Eqs. (2) and (3)], which were also solved with a Runge–Kutta algorithm. In particular, we compare predictions of the maximum kinetic energy  $U_{\max}$  and the oscillation period  $\tau_p$  characteristic of solutions in the cyclotron resonance regime, over a broad range of the parameters  $|l|, \omega/\omega_c, \eta, \mathbf{k} \cdot \mathbf{x}_0, \alpha$ , and  $\epsilon$  for circularly polarized waves and cold initial conditions. The size of the parameter space surveyed is somewhat greater than that surveyed in the extensive comparison of predictions of the HPP theory to solutions of the full equations of motion that was presented in Sec. IV of Paper I.

Referring to the “deviation” as the difference between the orbit-averaged prediction and the full equation prediction normalized to the full equation prediction, we find that, on the average, when  $|l| = 1$ , the deviation in  $U_{\max}$  is typically 1% with a maximum around 11%. The deviation in  $\tau_p$  is typically 3% with a maximum of around 17%. When  $|l| = 2$ , typical deviations in  $U_{\max}$  and  $\tau_p$  are 5% and 17%, respectively, with maximums around 39% ( $U_{\max}$ ) and 50% ( $\tau_p$ ). For  $|l| = 3$ , we compared only solutions with  $\eta_z \approx 1$  and found typical deviations of  $U_{\max}$  to be 4% with a maximum of 13%. Typical deviations of  $\tau_p$  were 40% with a maximum of 56%. In short, the  $U_{\max}$  and  $\tau_p$  estimates from the orbit-averaged equations are accurate to the same order as those from the HPP theory.

Examination of the particle trajectories generated from the full equations of motion reveals that when the larger than typical deviations occurred, it was often for the following reasons. First, solutions that have large values of  $\tau_p$  (e.g., when  $|l| = 3$ ) require extremely large numbers of time steps and the numerical solutions of the full equations can become inaccurate. Second, some parameter values (for example,  $\beta_0 = \pi$  when  $|l| = 2$ ) place the particle trajectories uncomfortably close to separatrices, i.e., boundaries in phase space defined by the orbit-averaged Hamiltonian theory that separate regimes of qualitatively different behavior. Higher-order effects not included in the orbit-averaged theory will cause the actual particle trajectory to jump between regions of phase space both inside and outside the separatrix, whereas the trajectory generated from the orbit-averaged theory will remain smoothly on one side or the other. We have more to say about the detailed phase space structure in the next subsection.

### C. Phase space structure in the small momentum limit

The orbit-averaged continuum equations can be readily employed to predict details of the particle trajectories beyond the scope of both the Hamiltonian pseudopotential theory (Paper I) and the PMAP (Sec. II). In what follows we explore the character of the trajectories for negatively charged particles in the  $\bar{P}_\xi$ – $\bar{\xi}$  canonical phase space as determined by the orbit-averaged equations of motion in the small momentum limit [Eqs. (100) and (101)]. To keep within this realm of parameter space, we will only consider parameter sets where  $\eta_z \neq 1$ . We limit our analysis to  $|l| = 1$  and  $|l| = 2$ , since they are the only values of  $|l|$  that lead to energies above the quiver energy when  $\eta_z \neq 1$ .

Of primary importance in determining the properties of

the particle trajectories in phase space is the location and nature of the fixed points, i.e., those points where  $d\bar{\xi}/dt = d\bar{P}_\xi/dt = 0$ . Setting  $d\bar{P}_\xi/dt = 0$  [Eq. (101)], we find that any fixed points must satisfy one of two possible conditions:

$$A: \cos \bar{\xi}_A = 0, \quad (104)$$

$$B: a_{|l|}(\bar{P}_{\xi_B}) = 0, \quad (105)$$

where we denote the candidate fixed points that satisfy condition *A* or condition *B* as  $(\bar{\xi}_A, \bar{P}_{\xi_A})$  and  $(\bar{\xi}_B, \bar{P}_{\xi_B})$ , respectively.

Before pursuing the fixed point solutions, we pause to introduce some new notation. Consideration of the canonical cyclotron radius  $\bar{\rho}$  [Eq. (59)] indicates that, for physically realizable problems (where  $\bar{\rho}$  is a real number), the values permissible for  $\bar{P}_\xi$  are bounded from below by  $\bar{P}_{\xi_{\min}}$ , where  $\bar{P}_{\xi_{\min}} = -\bar{l}/|l|$ . It is convenient to introduce the dimensionless variable  $\bar{P}'_\xi$  defined as

$$\bar{P}'_\xi = \bar{P}_\xi - \bar{P}_{\xi_{\min}}. \quad (106)$$

When expressed in terms of the physical variables [Eqs. (60)–(65)],  $\bar{P}'_\xi$  reduces to an expression involving only the perpendicular momentum and the phase:

$$\bar{P}'_\xi = \frac{\omega}{2|l|\omega_c} \left[ \left( \frac{p_x}{mc} + s\epsilon_1 \sin \beta \right)^2 + \left( \frac{p_y}{mc} + s\epsilon_2 \cos \beta \right)^2 \right]. \quad (107)$$

Another useful quantity is a constant of the motion  $P'_{z\min}$ , where

$$P'_{z\min} = \eta_z \bar{P}_{\xi_{\min}} - \eta_x \bar{P}_\mu. \quad (108)$$

Written in terms of the initial values of the physical variables,  $P'_{z\min}$  becomes

$$P'_{z\min} = p_{z0}/mc - s\epsilon_3 \sin \beta_0 - \eta_z \bar{P}'_{\xi_0}. \quad (109)$$

The assumption of small momenta is equivalent to the assumption that  $\bar{P}'_\xi \ll 1$  and  $P'_{z\min} \ll 1$ .

The existence of fixed points is established by solving the equation  $d\bar{\xi}/dt = 0$  [Eq. (100)] for either  $\bar{P}'_{\xi_A}$  (case *A*) or  $\bar{\xi}_B$  (case *B*). The nature of the particle motion near the fixed point is then investigated via linear stability analysis. Using the case *A* fixed point as an example, we assume solutions of the form

$$\bar{P}'_\xi(\hat{t}) = \bar{P}'_{\xi_A} + \delta\bar{P}'_{\xi_0} \exp(\lambda\hat{t}), \quad (110)$$

$$\bar{\xi}(\hat{t}) = \bar{\xi}_A + \delta\bar{\xi}_0 \exp(\lambda\hat{t}), \quad (111)$$

where  $\delta\bar{P}'_\xi$  and  $\delta\bar{\xi}$  are perturbations sufficiently small so that the equations of motion can be linearized about  $(\bar{\xi}_A, \bar{P}'_{\xi_A})$ . Solving the resultant set of linear equations for the eigenvalues  $\lambda$ , the fixed point can be classed as the stable type if both eigenvalues are imaginary, or of the unstable type if both eigenvalues are real. When the eigenvalues are real, there will be both a positive and negative branch, in which case the fixed point is of the hyperbolic type.

The remaining discussion is broken up into separate sections, the first describing phase space properties for  $|l| = 2$  and the second for  $|l| = 1$ . In addition to the fixed point

structure, we will examine the behavior of the phase angle  $\bar{\xi}$  and determine under what physical initial conditions  $\bar{\xi}$  becomes an oscillatory (as opposed to monotonic) function of time. An oscillatory  $\bar{\xi}$  implies that the particles are “phase trapped,” which is an important process, for example, in interactions of whistler waves with charged particles in the Earth’s magnetosphere.<sup>14,15</sup>

### 1. The $|l|=2$ resonance

We consider first the  $|l| = 2$  resonance since the candidate fixed points are of a more standard variety than what we will find for  $|l| = 1$ . In Fig. 3(a), we show curves of constant  $\bar{H}$  (denoting possible particle orbits) in  $(\bar{\xi}, \bar{P}_\xi)$  phase space. Fixed points corresponding to cases *A* and *B* are labeled with an “*A*” and “*B*,” respectively.

The fixed points for case *A* must clearly have  $\bar{\xi}_A = \pi/2$  or  $3\pi/2$ . Solving the  $d\bar{\xi}/dt = 0$  equation for  $\bar{P}'_{\xi_A}$ , we find

$$\bar{P}'_{\xi_A} = [1/(1 - \eta_z^2)] \times [2\omega_c/\omega - 1 + \eta_z P'_{z\min} + \eta_x (\epsilon_1 + \epsilon_2) \sin \bar{\xi}_A]. \quad (112)$$

Performing the stability analysis we find that the eigenvalues satisfy the equation

$$\lambda^2 = - (1 - \eta_z^2) \eta_x (\epsilon_1 + \epsilon_2) \bar{P}'_{\xi_A} \sin \bar{\xi}_A, \quad (113)$$

indicating that  $(\bar{\xi}_A, \bar{P}'_{\xi_A})$  is a stable fixed point for  $\bar{\xi}_A = \pi/2$  ( $3\pi/2$ ) when  $\eta_z < 1$  ( $> 1$ ). A flipping of the stable point from  $\bar{\xi}_A = \pi/2$  to  $\bar{\xi}_A = 3\pi/2$  as  $\eta_z$  increases through the value of 1 does occur and has been observed in numerical solutions of the full equations of motion.

The oscillation period about the stable fixed point provides a crude estimate of the oscillation period  $\tau_p$  characteristic of the cyclotron resonance acceleration process. Assuming  $\omega = 2\omega_c$  and cold initial particles, the eigenvalue relation [Eq. (113)] and definition of  $\bar{P}'_{\xi_A}$  yield the estimate

$$\tau_p = [\eta_x^2 (\epsilon_1 + \epsilon_2)^2 + \eta_z P'_{z\min} \sin \bar{\xi}_A]^{-1/2}, \quad (114)$$

where  $\tau_p$  is in units of the wave period ( $2\pi/\omega$ ). Comparing this estimate to those obtained in Paper I, we find that Eq. (114) predicts a significantly lower value than that found from either the HPP theory [Eq. (44) of Paper I] or the numerical solutions of the equations of motion [Sec. IV of Paper I]. The reason for this is that all trajectories for cold initial particles lie close to the separatrix (a point discussed later in this section) and will therefore have a longer oscillation period than those near the stable fixed point.

Turning to the case *B* fixed points, a solution to the equation  $a_{|l|}(\bar{P}_{\xi_B}) = 0$  is  $\bar{P}_{\xi_B} = P_{\xi_{\min}}$ , or  $\bar{P}'_{\xi_B} = 0$ . Other solutions might exist, but they will have  $\bar{P}'_{\xi_B} \sim O(1)$  and are therefore beyond the scope of this study. The solutions  $\bar{\xi}_B$  to  $d\bar{\xi}/dt = 0$  must satisfy the relation

$$\sin \bar{\xi}_B = - [1/\eta_x (\epsilon_1 + \epsilon_2)] (2\omega/\omega_c - 1 + \eta_z P'_{z\min}). \quad (115)$$

There will be two solutions for  $\bar{\xi}_B$  if the right-hand side of Eq. (115) is less than one, and no solutions otherwise. Assuming that solutions exist, the stability analysis yields the eigenvalues

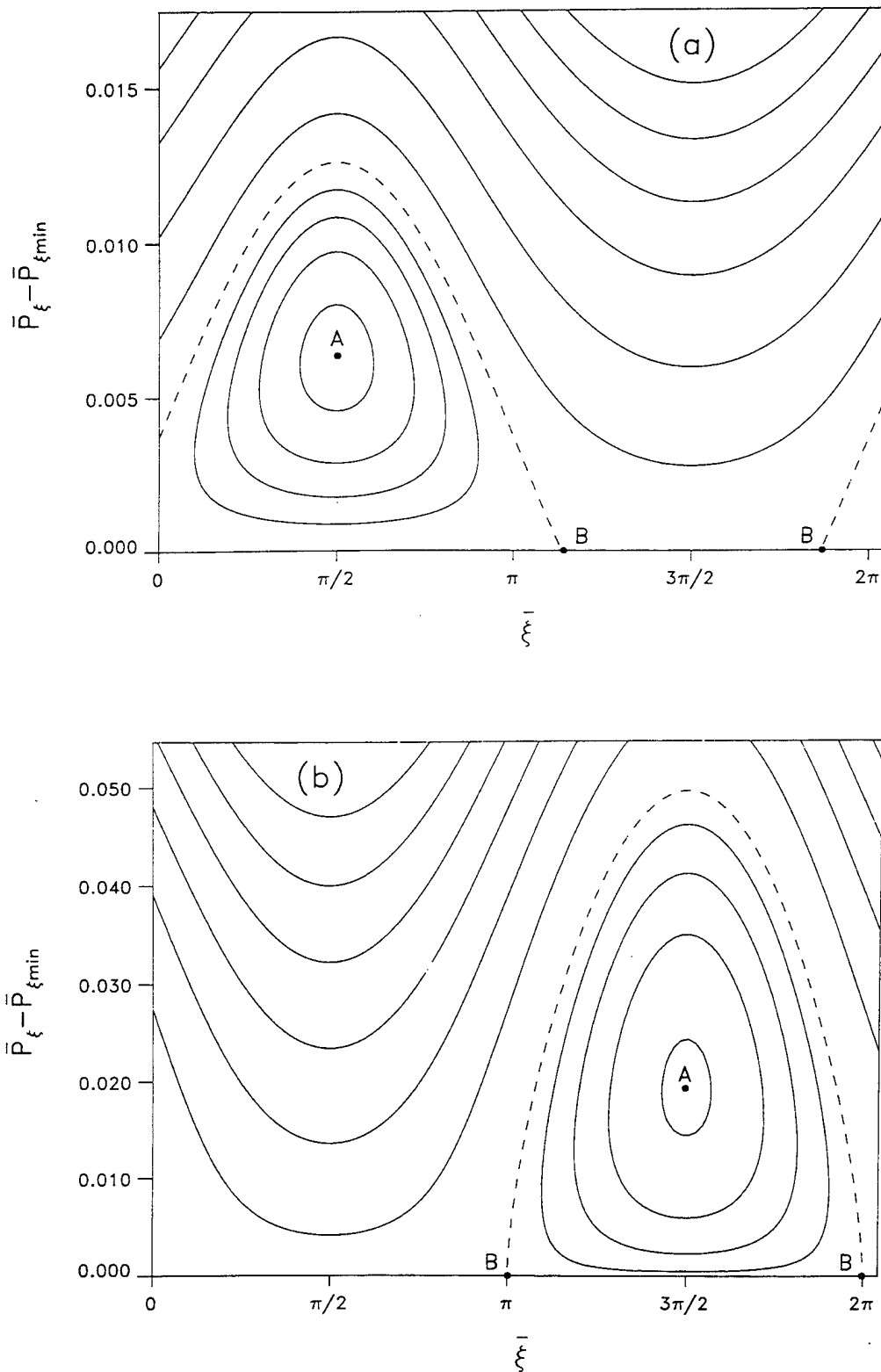


FIG. 3. Contours of constant  $\bar{H}$  in the  $(\bar{\xi}, \bar{P}_{\xi})$  phase plane representing the possible trajectories when  $|l| = 2$  (a) and  $|l| = 1$  (b). Throughout the small momentum regime, the distribution of trajectories resembles that shown here. Separatrices are indicated with a dashed line and the stable fixed points are labeled "A". The label "B" corresponds to unstable fixed points in (a) and unstable singular points in (b). The particular parameters used to generate this figure were  $\eta = 0.8$ ,  $\alpha = 45^\circ$ ,  $\epsilon = 3.16 \times 10^{-3}$ ,  $\omega/\omega_c = |l|$ , and  $\beta_0 = \pi/2$  ( $\beta_0 = 0.0$ ) for  $|l| = 2$  ( $|l| = 1$ ) with right-hand circularly polarized waves.

$$\lambda = \pm \eta_x (\epsilon_1 + \epsilon_2) \cos \bar{\xi}_B. \quad (116)$$

The points  $(\bar{\xi}_B, \bar{P}'_{\xi_B})$  are thus fixed points of the unstable hyperbolic variety.

The structure of the orbits in  $(\bar{\xi}, \bar{P}_{\xi})$  phase space [Fig. 3(a)] is not unlike that for a classic nonlinear oscillator, i.e., a stable fixed point flanked by two unstable fixed points.

There exists a separatrix connecting the two unstable fixed points that separates the orbits that are oscillatory in  $\bar{\xi}$  from those that are monotonic [dashed line in Fig. 3(a)]. Qualitatively, the phase space structure throughout the small momentum regime resembles Fig. 3(a) when fixed-point solutions for  $\bar{\xi}$  exist, though the locations of the fixed points vary depending on parameter values and initial conditions.

Whether  $\bar{\xi}$  is monotonic or oscillatory in time depends on which side of the separatrix the initial conditions place the trajectory. This can be determined in the following manner. When  $\eta_z < 1$  we consider the functional dependence of  $\bar{H}$  on  $\bar{\xi}$  as we move along line of constant  $\bar{P}'_{\xi}$  when  $\bar{P}'_{\xi} = \bar{P}'_{\xi_A}$ . Starting at the stable fixed point  $\bar{\xi}_A = \pi/2$  and moving in the direction of increasing  $\bar{\xi}$ , we see that  $\bar{H}$  is monotonically decreasing in the interval  $\bar{\xi} = [\pi/2, 3\pi/2]$ . Thus, if the value of  $\bar{H}$  corresponding to a given set of initial conditions is greater than the value of  $\bar{H}$  evaluated on the separatrix,  $\bar{H}_B = \bar{H}(\bar{\xi}_B, \bar{P}'_{\xi_B})$ , the orbit will be oscillatory in  $\bar{\xi}$ . Evaluating  $\bar{H}$  and  $\bar{H}_B$  [Eq. (54)] in terms of the initial conditions using the estimates for  $(\bar{\xi}_B, \bar{P}'_{\xi_B})$  and assuming  $\omega = 2\omega_c$ , the oscillatory condition  $\bar{H} - \bar{H}_B > 0$  can be written

$$\sin \bar{\xi}_0 + \eta_z P'_{z \min} / \eta_x (\epsilon_1 + \epsilon_2) > 0. \quad (117)$$

When  $\eta_z > 1$ , the stable fixed point shifts to  $\bar{\xi}_A = 3\pi/2$  and  $\bar{H}(\bar{\xi}, \bar{P}'_{\xi_A})$  is monotonically increasing as  $\bar{\xi}$  decreases from  $3\pi/2$  to  $\pi/2$ . In this case, the condition for oscillatory  $\bar{\xi}$  behavior  $\bar{H} - \bar{H}_B < 0$  and the direction of the inequality in Eq. (117) must be reversed.

As an example, we investigate the condition for oscillatory  $\bar{\xi}$  when  $\eta_z < 1$  and the particles are initially cold. We first note that whether the orbits are oscillatory or not, they will all be close to the separatrix in the sense that the initial conditions place  $\bar{H}$  much closer to the value of  $\bar{H}_B$  than to the value of  $\bar{H}$  at the stable fixed point. This claim follows from the fact that  $\bar{P}'_{\xi_0} / \bar{P}'_{\xi_A} \sim \theta(\epsilon) 1$  for the initially cold particles. Recalling the definitions of the canonical variables in terms of the physical variables [Eqs. (60)–(65)], the oscillatory condition can be written to lowest order as

$$G_2(\beta_0) > 0, \quad (118)$$

where

$$G_2 = \sin \beta_0 \left( \frac{\epsilon_1^2 \sin^2 \beta_0 - \epsilon_2^2 \cos^2 \beta_0 + 2\epsilon_1 \epsilon_2 \cos^2 \beta_0}{\epsilon_1^2 \sin^2 \beta_0 + \epsilon_2^2 \cos^2 \beta_0} + \frac{\eta_z \epsilon_3}{\eta_x (\epsilon_1 + \epsilon_2)} \right). \quad (119)$$

Figure 4(a) contains plots of  $G_2$  for circularly polarized waves as a function of the initial phase  $\beta_0$ . Several different curves are shown, each with a unique value of the propagation angle  $\alpha$ . The condition for oscillatory  $\bar{\xi}$  behavior is satisfied for a variety of initial conditions and exhibits a nontrivial dependence on angle. These predictions of the onset of oscillatory behavior agree with numerical solutions of the orbit-averaged equations of motion. Comparing to the solutions of the full equations of motion, we find good agreement for  $\alpha = 5^\circ$  and  $45^\circ$ . When  $\alpha = 85^\circ$ , the full equation solutions have a tendency to jump between the oscillatory and monotonic branches if  $\beta_0$  is not close to  $\pi/2$  or  $3\pi/2$ .

## 2. The $|l|=1$ resonance

In Fig. 3(b), curves of constant  $\bar{H}$  are plotted in  $(\bar{\xi}, \bar{P}'_{\xi})$  phase space for the  $|l|=1$  resonance. The curves look qualitatively similar to the  $|l|=2$  curves and in many ways they are. Both resonances have stable fixed points (labeled by "A") and have a clear separation between the orbits that oscillate in  $\bar{\xi}$  and those that do not. The primary difference between the two resonances is that for  $|l|=1$ , there are no fixed points that satisfy condition B [Eq. (106)]. Rather, "singular points" satisfying condition B exist and they behave like fixed points in certain respects.

Before considering the details of case B, we examine case A. For angles  $\bar{\xi}_A = \pi/2, 3\pi/2$  the  $d\bar{\xi}/dt = 0$  equation dictates that  $\bar{P}'_{\xi_A}$  satisfies the relation

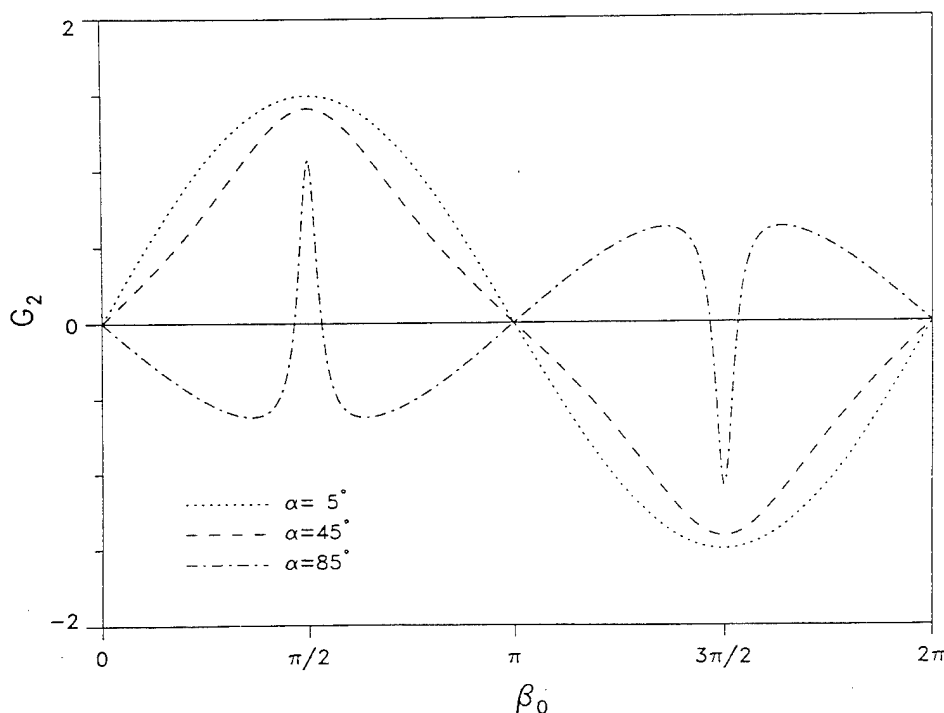


FIG. 4. The function  $G_2$  versus initial phase  $\beta_0$  when  $|l|=2$  for various angles of propagation  $\alpha$  when  $\eta = 0.8$ ,  $\epsilon = 3.16 \times 10^{-3}$ , and  $\omega = 2\omega_c$  for cold initial particles and right-hand circularly polarized waves. When  $G_2 > 0$ , the behavior of  $\bar{\xi}$  is oscillatory.

$$\begin{aligned} \bar{P}'_{\xi_A} \left[ \bar{P}'_{\xi_A} \left( \frac{\omega_c}{\omega} - \eta_z^2 \right) + 1 - \frac{\omega_c}{\omega} - \eta_z P'_{z \min} \right]^2 \\ = \frac{\omega_c}{8\omega} (\epsilon_1 + \epsilon_2)^2. \end{aligned} \quad (120)$$

The stability analysis yields the eigenvalue equation

$$\begin{aligned} \lambda^2 = \frac{(\epsilon_1 + \epsilon_2)^2 \left( \frac{\omega_c}{\omega} \right)^{1/2}}{\bar{P}'_{\xi_A}} \\ \times \left[ (1 - \eta_z^2) \frac{\bar{P}'_{\xi_A}{}^{3/2}}{\sin \bar{\xi}_A} - \frac{(\epsilon_1 + \epsilon_2)}{4} \left( \frac{\omega_c}{\omega} \right)^{1/2} \right]. \end{aligned} \quad (121)$$

Thus  $\bar{\xi}_A = 3\pi/2 (\pi/2)$  corresponds to a stable fixed point when  $\eta_z < 1 (> 1)$ . The shifting of the fixed point as  $\eta_z$  passes through 1 has been verified with numerical solutions of the full equations of motion. In Fig. 3(b), we show the stable fixed point (A) for  $\eta_z < 1$ .

Considering cold initial particles and setting  $\omega = \omega_c$ , we obtain from Eq. (120) the following expression for  $\bar{P}'_{\xi_A}$ :

$$\bar{P}'_{\xi_A} = \frac{1}{2} |(\epsilon_1 + \epsilon_2)/(1 - \eta_z^2)|^{2/3}, \quad (122)$$

when we assume  $P'_{z \min} \ll \bar{P}'_{\xi_A}$  (justified *a posteriori*). As was done for  $|I| = 2$ , we can estimate the resonance oscillation period  $\tau_p$  using the stable fixed point eigenvalues [Eq. (121)] and the  $\bar{P}'_{\xi_A}$  relation [Eq. (12)]. Normalizing  $\tau_p$  to the wave period, we find

$$\tau_p = \frac{2/\sqrt{3}}{|1 - \eta_z^2|^{1/3} |\epsilon_1 + \epsilon_2|^{2/3}}. \quad (123)$$

Contrary to what was found for  $|I| = 2$ , the  $\tau_p$  estimate resulting from the stable fixed point eigenvalue analysis is remarkably close to the  $\tau_p$  estimate from the HPP theory [Eq. (41) of Paper I] and the predictions of numerical solutions to the full equations of motion [Sec. IV of Paper I]. Like the  $|I| = 2$  case, the orbits of cold initial particles lie near the separatrix. However, unlike the  $|I| = 2$  case, the oscillation periods for orbits near the separatrix are approximately equivalent to the oscillation periods of orbits near the stable fixed point. Anticipating our upcoming analysis, we conjecture that the fast periods near the separatrix are a manifestation of the particle behavior in the vicinity of the case B singular points, where changes in  $\bar{\xi}$  become quite rapid.

Moving on to the analysis of case B, the solution of interest to the equation  $a_{|I|}(\bar{P}_{\xi_B}) = 0$  is  $\bar{P}_{\xi_B} = \bar{P}_{\xi_{\min}}$ , the same as we found for  $|I| = 2$ . Consequently, any candidate fixed points must have angles  $\bar{\xi}_B$  that solve the equation

$$\begin{aligned} 0 = \frac{\omega_c}{\omega} - 1 + \eta_z P'_{z \min} - (\epsilon_1 + \epsilon_2) \left( \frac{\omega_c}{8\omega} \right)^{1/2} \\ \times \lim_{(\bar{\xi}_B, \bar{P}_{\xi_B}) \rightarrow (\bar{\xi}_B, \bar{P}_{\xi_B})} \left( \frac{\sin \bar{\xi}}{(\bar{P}_{\xi} - \bar{P}_{\xi_B})^{1/2}} \right). \end{aligned} \quad (124)$$

The only hope for a solution is  $\bar{\xi}_B = 0$  or  $\pi$  so that the limit as  $\bar{\xi} \rightarrow \bar{\xi}_B$  and  $\bar{P}_{\xi} \rightarrow \bar{P}_{\xi_B}$  has a chance of remaining finite. Even so, the limit in Eq. (124) is not uniquely determined so we will have to content ourselves with examining the trajectories in the vicinity of the candidate fixed points.

Letting  $\bar{\xi}$  and  $\bar{P}_{\xi}$  take the form  $\bar{\xi} = \bar{\xi}_B + \delta\bar{\xi}(\hat{t})$  and

$\bar{P}_{\xi} = \bar{P}_{\xi_B} + \delta\bar{P}_{\xi_B}(\hat{t})$ , where  $\delta\bar{\xi}$  and  $\delta\bar{P}_{\xi}$  are infinitesimal perturbations, the orbit-averaged equations of motion [Eqs. (100) and (101)] to lowest order become

$$\frac{d\delta\bar{P}_{\xi}}{d\hat{t}} = (\epsilon_1 + \epsilon_2) \cos \bar{\xi}_B \left( \frac{\omega_c}{2\omega} \right)^{1/2} \delta\bar{P}_{\xi}^{1/2}, \quad (125)$$

$$\begin{aligned} \frac{d\delta\bar{\xi}}{d\hat{t}} = \frac{\omega_c}{\omega} - 1 + \eta_z P'_{z \min} \\ - (\epsilon_1 + \epsilon_2) \cos \bar{\xi}_B \left( \frac{\omega_c}{8\omega} \right)^{1/2} \frac{\delta\bar{\xi}}{\delta\bar{P}_{\xi}^{1/2}}. \end{aligned} \quad (126)$$

Analytic solutions to these time-differential equations are found to be

$$\delta\bar{P}_{\xi} = \delta\bar{P}_{\xi_0} (1 + \hat{t}/C_1)^2, \quad (127)$$

$$\begin{aligned} \delta\bar{\xi} = (\omega_c/\omega - 1 + \eta_z P'_{z \min}) \\ \times [(\hat{t} + C_1)^2 - C_1^2 + 2C_2]/2(\hat{t} + C_1), \end{aligned} \quad (128)$$

where

$$C_1 = [\delta\bar{P}_{\xi_0}^{1/2}/(\epsilon_1 + \epsilon_2) \cos \bar{\xi}_B] (8\omega/\omega_c)^{1/2}, \quad (129)$$

$$C_2 = \frac{C_1 \delta\bar{\xi}_0}{\omega_c/\omega - 1 + \eta_z P'_{z \min}}, \quad (130)$$

and  $(\delta\bar{\xi}_0, \delta\bar{P}_{\xi_0})$  are the initial values at time  $\hat{t} = 0$ . If we make the assumption that  $\delta\bar{P}_{\xi_0}$  is small enough so that

$$\delta\bar{\xi}_0 \gg C_1 (\omega_c/\omega - 1 + \eta_z P'_{z \min}), \quad (131)$$

then the  $\delta\bar{\xi}$  solution takes the relatively simple form

$$\delta\bar{\xi} = \delta\bar{\xi}_0 (1 - \hat{t}/C_1) \quad (132)$$

when  $\hat{t}/C_1 \ll 1$ . In the discussion to follow, we will use the full  $\delta\bar{P}_{\xi}$  solution and the approximate  $\delta\bar{\xi}$  solution [Eq. (132)], though we realize the approximation might not encompass all physically possible trajectories.

Caveats notwithstanding, the local  $\delta\bar{P}_{\xi}$  and  $\delta\bar{\xi}$  solutions indicate the following general behavior. If  $\bar{\xi}_B = 0$ , then trajectories approaching  $(\bar{\xi}_B, \bar{P}_{\xi_B})$  will have  $|\delta\bar{\xi}|$  decreasing with  $\delta\bar{P}_{\xi}$  increasing. Conversely, trajectories approaching  $\bar{\xi}_B = \pi$  will have  $|\delta\bar{\xi}|$  increasing with  $\delta\bar{P}_{\xi}$  decreasing. This behavior in the vicinity of the singular points is consistent with the many numerical solutions of the equations of motion we have examined, and is similar to that found near the unstable hyperbolic fixed points at  $(\bar{\xi}_B, \bar{P}_{\xi_B})$  when  $|I| = 2$ . We cannot, however, deduce that  $(\bar{\xi}_B, \bar{P}_{\xi_B})$  is a fixed point for  $|I| = 1$  using the local analytic solutions because the same problems exist in taking the limit  $\delta\bar{\xi}_0 \rightarrow 0$ ,  $\delta\bar{P}_{\xi_0} \rightarrow 0$  as did in evaluating Eq. (124). In fact, numerical solutions of the full equations of motion indicate that, as trajectories approach the point  $(0, \bar{P}_{\xi_B})$ , values of  $d\bar{\xi}/d\hat{t}$  can become very large. The rate of change of the fast angle  $\bar{\phi}$  becomes large also and the ratio of the fast angle to slow angle variation becomes of  $O(1)$ , stretching the validity of the resonance approximation. It is this rapid evolution of  $\bar{\xi}$  near the singular points that causes the convergence problems for the QMAP (Sec. III A).

We will sidestep the issue of the precise characterization of the  $(\bar{\xi}_B, \bar{P}_{\xi_B})$  points when  $|I| = 1$  and assert that these

“unstable singular points” [labeled with a “B” in Fig. 3(b)] behave in a manner similar to hyperbolic fixed points. The contour connecting the two singular points separates trajectories monotonic in  $\xi$  from those oscillatory in  $\xi$  and is therefore a separatrix [dashed line in Fig. 3(b)]. Full numerical solutions of the equation of motion have verified that the phase space structure throughout the small momentum regime resembles Fig. 3(b) and the locations of the points  $(\xi_A, \bar{P}'_{\xi_A})$  and  $(\xi_B, \bar{P}'_{\xi_B})$  are in good agreement with the locations predicted by the preceding analysis.

The range of parameters and initial conditions that produce oscillatory  $\xi$  behavior can be deduced by the method that was used in the  $|I| = 2$  analysis. When  $|I| = 1$ , the Hamiltonian  $\bar{H}$  is monotonically decreasing (increasing) away from the stable fixed point when  $\eta_z < 1$  ( $\eta_z > 1$ ) so that the condition for oscillatory  $\xi$  is  $\bar{H} - \bar{H}_B > 0$  ( $\bar{H} - \bar{H}_B < 0$ ). Assuming  $\omega = \omega_c$ , this condition simplifies to

$$\sin \bar{\xi}_0 < 0 \quad (133)$$

when  $\eta_z < 1$  with a reversal of the inequality for  $\eta_z > 1$ . Expanding  $\bar{\xi}_0$  in terms of the physical variables, the condition for oscillatory  $\xi$  can be written to lowest order as

$$G_1(\beta_0, p_0) < 0, \quad (134)$$

where

$$G_1 = -\left(\frac{p_{x0}}{mc} - \epsilon_1 \sin \beta_0\right) \sin\left(\beta_0 + \eta_x \frac{p_{y0}}{mc}\right) - \left(\frac{p_{y0}}{mc} - \epsilon_2 \cos \beta_0\right) \cos\left(\beta_0 + \eta_x \frac{p_{y0}}{mc}\right). \quad (135)$$

Addressing the specific case of cold initial conditions, it can be shown that, like the  $|I| = 2$  situation, all physically realizable orbits are very close to the separatrix, i.e.,  $\bar{P}'_{\xi_0}/\bar{P}'_{\xi_A} \sim O(\epsilon^{4/3})$ . Unlike the situation when  $|I| = 2$ , all cold particle orbits will be monotonic for  $|I| = 1$  when the

angle of propagation  $\alpha < 90^\circ$  [Eq. (134)]. Oscillatory behavior can be found for some combination of parameters if  $\alpha > 90^\circ$  or if the initial perpendicular momentum is nonzero. Figure 5 illustrates this point with plots of  $G_1$  versus initial phase  $\beta_0$  for several different values of  $p_{x0}$  when  $p_{y0} = p_{x0} = 0$  and the wave is circularly polarized. Numerical solutions of both the orbit-averaged equations of motion and the full equations of motion have verified that the sign of  $G_1$  is an accurate predictor of the  $\xi$  behavior.

#### IV. SUMMARY

The objectives of this paper have been twofold: first, to understand the physical mechanisms responsible for generating large kinetic energy gains in the cyclotron resonance acceleration process; and second, to obtain a set of reduced equations of motion that still allow the accurate determination of details of the particle orbits in the cyclotron resonance regime.

The phenomenology of the acceleration mechanism is addressed with the PMAP, a set of mapping equations jumping the momentum and phase of the test particle from one cyclotron orbit to the next. For each orbit, the change in kinetic energy is proportional to the corotating component of the wave electric field and is of the order of the quiver energy or less. This small change in kinetic energy is the result of either the corotation effect ( $|I| = 1$ ) or the Doppler effect ( $|I| > 1$ ) with the sign and magnitude of the change depending on the relative phase of the wave at certain points during the orbit. For the Doppler effect to be operative, there must be a nonzero  $k_x$ . Large changes in the kinetic energy arise from the accumulation of the small changes over many orbits.

Crucial to the energy accumulation process and the long time scale periodic behavior is a small shifting in the wave

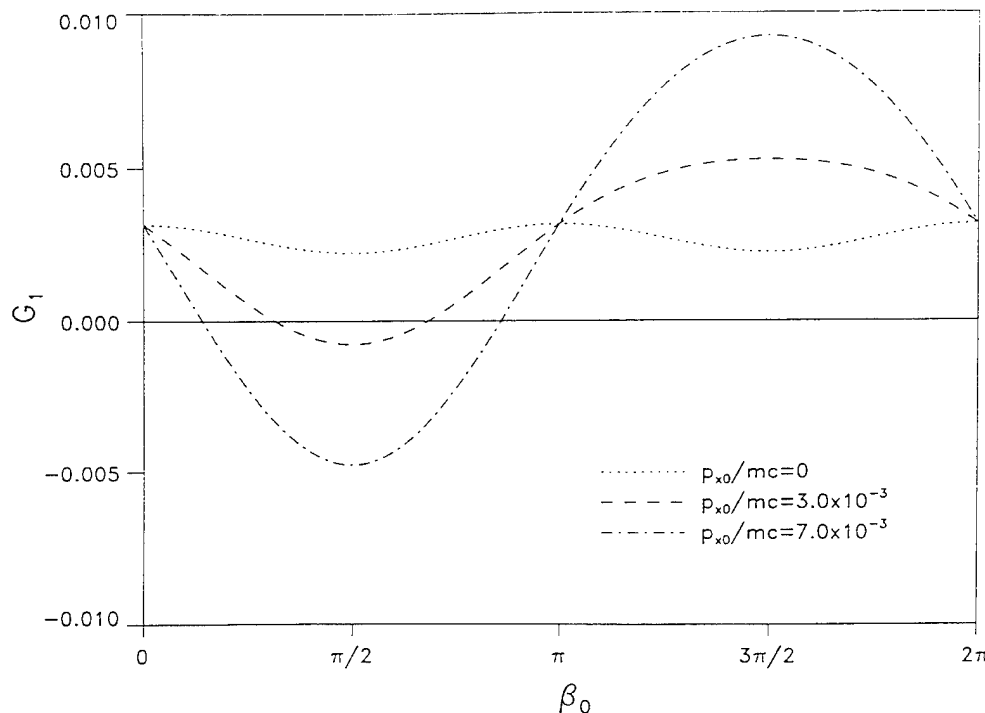


FIG. 5. The function  $G_1$  versus initial phase  $\beta_0$  when  $|I| = 1$  for various values of initial momenta  $p_{x0}/mc$  when  $\eta = 0.8$ ,  $\epsilon = 3.16 \times 10^{-3}$ ,  $\alpha = 45^\circ$ , and  $\omega = \omega_c$  for right-hand circularly polarized waves. When  $G_1 < 0$  the behavior of  $\xi$  is oscillatory.

phase  $\psi \pmod{2\pi}$  of each cyclotron orbit. The shift in phase has two energy-dependent contributions arising from the wave interaction; one is a result of streaming along the background magnetic field caused by the acceleration of the particle parallel to  $\mathbf{B}_0$ , and the other is a result of an increase in the cyclotron period arising from relativistic effects. There is also a constant parallel streaming contribution due to the initial conditions. We find that, when  $\eta_z \neq 1$ , the behavior of the  $\psi \pmod{2\pi}$  can be either monotonic or oscillatory, depending on the value of the initial streaming term. It is a limitation of the PMAP that we can only predict the existence of both monotonic and oscillatory phase behavior for initial momenta  $p_0/mc \leq O(\epsilon)$  and not the exact functional dependence. When  $\eta_z = 1$ , the energy-dependent terms cancel each other out and, at least for some ranges of initial phase and momentum, the phase remains constant in the small momentum limit. This allows for kinetic energy gains of order of the rest mass energy.

It can be concluded from the PMAP analysis that the magnetic field of the wave plays a significant, if not dominant role in altering the relative phase of the wave of each cyclotron orbit. Furthermore, the energy-dependent cyclotron frequency plays a large role in altering the phase even when the particle energies are far below the rest mass energy. Clearly, it is not reasonable to ignore the wave magnetic field or relativistic cyclotron frequency effects in studies of resonance acceleration no matter what the particle energy.

Reduced equations of motion more accurate than the PMAP are obtained by turning to a Hamiltonian formulation of the problem. A set of mapping equations (QMAP) is derived that jump the slowly varying canonical action  $P_\xi$  and angle  $\xi$  over a  $2\pi$  period of variation in the fast angle  $\phi$ . The QMAP performs well when  $|I| > 1$  but runs into accuracy problems for cold initial conditions when  $|I| = 1$ . Difficulties arise because the particle orbits in phase space pass close to singular points where the rate of change of the slow angle apparently diverges.

The QMAP difficulties are avoided by working with a set of orbit-averaged equations of motion obtained from a Hamiltonian that was derived using adiabatic perturbation theory. In terms of the physical processes being modeled, the orbit-averaged continuum equations and the QMAP are of identical scope. However, with a continuous time variable the orbit-averaged equations of motion can be numerically solved with an arbitrary time step and therefore avoid convergence difficulties near the  $|I| = 1$  singular points. An extensive comparison of numerical solutions of the full equations of motion to solutions of the orbit-averaged equations demonstrates the viability of the orbit-averaged approach.

Details of the orbit distribution in the phase space defined by the orbit-averaged continuum variables  $(\bar{\xi}, \bar{P}_\xi)$  [which have been equated to the QMAP variables  $(\xi, P_\xi)$ ] are examined for  $|I| = 1$  and  $|I| = 2$  in the limit of small momentum. When  $|I| = 2$ , the structure is similar to that of a one-dimensional nonlinear oscillator, i.e., a stable fixed point between two unstable fixed points that define a separatrix. A general criterion for oscillatory  $\bar{\xi}$  behavior is derived, which is a function of the wave parameters and particle initial conditions. For initially cold particles and  $\omega = 2\omega_c$ , we

find that all particle orbits will be close to the separatrix and that the existence of oscillatory behavior depends strongly on the values of the initial phase, wave polarization, and index of refraction [Eq. (119)].

The phase space structure when  $|I| = 1$  differs from the  $|I| = 2$  structure in that there are no unstable fixed points. Instead, there are unstable singular points where fixed points might be expected. Though the time rate of change of  $\bar{\xi}$  is not uniquely determined at these singular points, analysis of the behavior of nearby orbits suggests divergence. Numerical solutions of the full equations of motion also show divergent behavior in the vicinity of the singular points and indicate that  $\bar{\xi}$  ceases to be a slowly varying variable. Despite the singular nature of these points, they play much the same role as unstable hyperbolic fixed points; they can attract and repel orbits along different axes, and they define a separatrix between orbits oscillatory and monotonic in  $\bar{\xi}$ . Like the  $|I| = 2$  case, a general criterion for oscillatory behavior can be derived. When  $\omega = \omega_c$  and the particles are initially cold all the orbits are near the separatrix and all are monotonic in  $\bar{\xi}$  for angles of propagation  $0^\circ \leq \alpha \leq 90^\circ$ . Only when the initial perpendicular momentum is nonzero or  $\alpha > 90^\circ$  can oscillatory motion occur, and then only for certain values of the initial phase that depend on the wave polarization and index of refraction [Eq. (134)].

## ACKNOWLEDGMENTS

One of us (G.P.G.) wishes to thank Gareth Guest and Michael Heinemann for useful discussions.

This work was partially sponsored by AF Contract No. F 19628-86-C-0224 while one of us (J.M.A.) was an Air Force Geophysics Laboratory Geophysics Scholar. The United States Government is authorized to reproduce and distribute reprints for governmental purposes notwithstanding any copyright notation hereon.

## APPENDIX: SCALING LAWS FROM THE PMAP WHEN $\eta_z \neq 1$

In this appendix, we use the PMAP to derive scaling relations for the kinetic energy  $U_{\max}$  and oscillation period  $\tau_p$  associated with the resonance acceleration process. The small momentum approximation to the PMAP is employed and we assume cold initial particles with  $\omega = |I|\omega_c$ . Having the benefit of the Paper I results, we know this to be a reasonable approximation when  $\eta_z \neq 1$ .

We will work with the small momentum version of the PMAP [Eqs. (30)–(32)] in the following form:

$$\frac{\Delta p_{1n}}{mc} = \bar{d}_{|I|}(\epsilon_1 + \epsilon_2) \left( \frac{p_{1n}}{mc} \right)^{|I|-1} \cos \left( \psi'_n + \frac{|I|\pi}{2} \right), \quad (\text{A1})$$

$$\frac{\Delta p_{zn}}{mc} = \bar{d}_{|I|}\eta_z(\epsilon_1 + \epsilon_2) \left( \frac{p_{1n}}{mc} \right)^{|I|} \cos \left( \psi'_n + \frac{|I|\pi}{2} \right), \quad (\text{A2})$$

$$\Delta \psi'_n = -\pi |I| (1 - \eta_z^2) (p_{1n}/mc)^2, \quad (\text{A3})$$

where

$$\bar{d}_l = (-\eta_x/2)^{|l|-1} [\pi |l|^{1/2} / \Gamma(|l|)] \quad (\text{A4})$$



and the truncated phase has been defined to be  $\psi'_n = \psi_n \pmod{2\pi}$ . The quantities  $\epsilon_i$ ,  $i = 1, 2$  are defined in Eq. (10).

Consider the ratio of  $\Delta p_{1n}$  to  $\Delta\psi'_n$  arising from the mapping equations (A1) and (A3),

$$\frac{\Delta(p_{1n}/mc)}{\Delta\psi'_n} = -\frac{\bar{d}_{|l|} \eta_x^{|l|-1} (\epsilon_1 + \epsilon_2)}{\pi |l| (1 - \eta_z^2)} \left( \frac{p_{1n}}{mc} \right)^{|l|-3} \times \cos\left(\psi'_n + \frac{|l|\pi}{2}\right). \quad (\text{A5})$$

Approximating the finite differences as continuous differentials, we obtain the following differential equation:

$$\frac{d}{d\psi'_n} \left( \frac{p_{1n}}{mc} \right)^{4-|l|} = - (4 - |l|) \frac{\bar{d}_{|l|} \eta_x^{|l|-1} (\epsilon_1 + \epsilon_2)}{\pi |l| (1 - \eta_z^2)} \times \cos\left(\psi'_n + \frac{|l|\pi}{2}\right). \quad (\text{A6})$$

Integrating this differential equation assuming  $p_{10} = 0$ , we find with the appropriate choice of initial phase,

$$\frac{p_{1\max}}{mc} = \left| 2 \frac{(4 - |l|) \bar{d}_{|l|} \eta_x^{|l|-1} (\epsilon_1 + \epsilon_2)}{\pi |l| (1 - \eta_z^2)} \right|^{2/(4-|l|)}. \quad (\text{A7})$$

For  $|l| = 1$ , the maximum kinetic energy computed from  $p_{1\max}$  is

$$U_{\max} = 1.65 |(\epsilon_1 + \epsilon_2)/(1 - \eta_z^2)|^{2/3} \quad (\text{A8})$$

and for  $|l| = 2$ , we find

$$U_{\max} = 2\eta_x |(\epsilon_1 + \epsilon_2)/(1 - \eta_z^2)|. \quad (\text{A9})$$

For  $|l| = 3$ ,  $U_{\max} \sim O(\epsilon^2)$ , the same order as the quiver energy. The scaling of  $U_{\max}$  in  $\epsilon$ ,  $\eta$ , and  $\alpha$  given by Eqs. (A8) and (A9) is identical to that obtained from the HPP theory (Paper I). Even the constants of proportionality are fairly close to those obtained from the HPP theory (1.26 for  $|l| = 1$  and 2 for  $|l| = 2$ ).

To probe the scaling of the long time oscillation period  $\tau_p$ , we consider the change in phase  $\Delta\psi'_n$ , which can be either positive definite ( $\eta_z > 1$ ) or negative definite ( $\eta_z < 1$ ) if we ignore the unstable fixed point at  $p_{1n} = 0$ . The phase  $\psi'_n$  will then be either monotonically increasing or decreasing leading to alternating periods of acceleration and deceleration, as we discussed in Sec. II C. Letting  $N$  be the number of orbits that  $\Delta p_{1n} > 0$  (which is equivalent to the number of orbits that  $\Delta p_{1n} < 0$  by the symmetry of the map), we deduce from the  $\Delta p_{1n}$  mapping equation (41)

$$\pi = \sum_{n=1}^N |\Delta\psi'_n|. \quad (\text{A10})$$

Substituting in the  $\Delta\psi'_n$  mapping equation (A3) we find the sum relation

$$1 = |l| |1 - \eta_z^2| \sum_{n=1}^N \left( \frac{p_{1n}}{mc} \right)^2. \quad (\text{A11})$$

Defining  $\langle p_{1n}^2 \rangle$  to be the average value of  $p_{1n}^2$  over the acceleration range of  $\psi'_n$ , we can further reduce the sum relation to

$$1 = |l| |1 - \eta_z^2| N (\langle p_{1n}^2 \rangle / m^2 c^2). \quad (\text{A12})$$

Since the acceleration process is cyclic, we can express the average of  $p_{1n}^2$  as a function of the maximum of  $p_{1n}^2$ :

$$p_{1\max}^2 = C \langle p_{1n}^2 \rangle, \quad (\text{A13})$$

where  $C$  is of order unity and, we hypothesize, weakly dependent on  $\epsilon$ ,  $\eta$ , and  $\alpha$ . Noting that  $\tau_p$  is the long time scale oscillation period normalized to the wave period, i.e.,  $\tau_p = 2|l|N$ , we manipulate the reduced sum relation (A12) to find

$$U_{\max} \tau_p = C / |1 - \eta_z^2|. \quad (\text{A14})$$

Using the previously derived expressions for  $U_{\max}$  [Eqs. (A8) and (A9)], the expression for  $\tau_p$  when  $|l| = 1$  is found to be

$$\tau_p \propto 1 / |1 - \eta_z^2|^{1/3} |\epsilon_1 + \epsilon_2|^{2/3} \quad (\text{A15})$$

and, when  $|l| = 2$ , the scaling relation becomes

$$\tau_p \propto 1 / \eta_x |\epsilon_1 + \epsilon_2|. \quad (\text{A16})$$

By depicting only a proportionality, we have neglected constants of order unity and the  $C$  factor in the above  $\tau_p$  estimate. The scaling of  $\tau_p$  with  $\epsilon$ ,  $\eta$ , and  $\alpha$  are the same as that derived from the HPP theory except for a logarithmic factor that appears in the HPP expressions when  $|l| = 2$ .

The agreement of the PMAP and HPP scaling laws, at least to order unity when  $\eta_z \neq 1$ , demonstrates that the PMAP does reasonably represent the main features of the physical processes that underlie the resonance acceleration mechanism when the momenta are small compared to  $mc$ . We reiterate, however, that the PMAP is limited and does not explain very well the initial phase and momentum dependence (Sec. II A).

<sup>1</sup> Y. Ya. Davydovski, Zh. Eksp. Teor. Fiz. **43**, 886 (1962) [Sov. Phys. JETP **16**, 629 (1963)].

<sup>2</sup> C. S. Roberts and S. J. Buchsbaum, Phys. Rev. **135**, A 381 (1964).

<sup>3</sup> P. J. Palmedesso, Phys. Fluids **15**, 2006 (1972).

<sup>4</sup> H. Karimabadi, C. R. Menyuk, P. Sprangle, and L. Vlahos, Astrophys. J. **316**, 462 (1987).

<sup>5</sup> H. Karimabadi, K. Akimoto, N. Omidi, and C. R. Menyuk, Phys. Fluids B **2**, 606 (1990).

<sup>6</sup> G. Ginat and M. Heinemann, Phys. Fluids B **2**, 700 (1990).

<sup>7</sup> G. E. Guest, M. E. Fetzner, and R. A. Dandl, Phys. Fluids B **2**, 1210 (1990).

<sup>8</sup> M. Abramowitz and I. A. Stegun, *Handbook of Mathematical Functions* (U.S. Government Printing Office, Washington, DC, 1972), p. 361.

<sup>9</sup> See Ref. 8, p. 360.

<sup>10</sup> C. R. Menyuk, A. T. Drobot, D. Papadopoulos, and H. Karimabadi, Phys. Fluids **31**, 2071 (1988); K. Akimoto and H. Karimabadi, Phys. Fluids **31**, 1505 (1988).

<sup>11</sup> A. J. Lichtenberg and M. A. Lieberman, *Regular and Stochastic Motion* (Springer-Verlag, New York, 1983), p. 157.

<sup>12</sup> See Ref. 11, p. 88.

<sup>13</sup> W. H. Press, B. P. Flannery, S. A. Teukolsky, and W. T. Vetterling, *Numerical Recipes* (Cambridge U. P., Cambridge, 1986), p. 550.

<sup>14</sup> T. F. Bell, Phys. Fluids **8**, 1829 (1965).

<sup>15</sup> K. B. Dysthe, J. Geophys. Res. **76**, 6915 (1971).

# Cyclotron resonance in an inhomogeneous magnetic field

Jay M. Albert

Center for Electromagnetics Research, Northeastern University, Boston, Massachusetts 02115

(Received 23 December 1993; accepted 28 April 1993)

Relativistic test particles interacting with a small monochromatic electromagnetic wave are studied in the presence of an inhomogeneous background magnetic field. A resonance-averaged Hamiltonian is derived which retains the effects of passage through resonance. Two distinct regimes are found. In the strongly inhomogeneous case, the resonant phase angle at successive resonances is random, and multiple resonant interactions lead to a random walk in phase space. In the other, adiabatic limit, the phase angle is determined by the phase portrait of the Hamiltonian and leads to a systematic change in the appropriate canonical action (and therefore in the energy and pitch angle), so that the cumulative effect increases directly with the number of resonances.

## I. INTRODUCTION

Charged particle motion is considered under the combined influence of an inhomogeneous background magnetic field and an electromagnetic wave. When there is a resonance between harmonics of the cyclotron frequency and the Doppler-shifted wave frequency, even a weak wave can significantly perturb the particle motion. This process has been studied by many authors, particularly for radiation belt particles in the Earth's dipole field, where phase bunching leads to further, coherent whistler wave emission, and pitch angle scattering into the loss cone leads to particle precipitation.<sup>1-5</sup> These effects have also been studied in laboratory experiments, especially in the context of electron cyclotron heating applications.<sup>6-8</sup> For sufficiently large amplitude waves, large changes in the particle energy and pitch angle are possible due to both stochastic<sup>9-11</sup> and coherent, surfatronlike<sup>12</sup> mechanisms.

Ginet and Heinemann<sup>13</sup> and Ginet and Albert<sup>14</sup> studied in detail a relativistic particle interacting with a small-amplitude electromagnetic wave propagating at arbitrary angle to the background magnetic field  $\mathbf{B}_0$ . A two-dimensional, resonance-averaged Hamiltonian was developed which allowed simple and accurate determination of the motion. The major restriction was to a constant  $\mathbf{B}_0$ , so that the effect of passage through resonance was not included. In the present paper, the spatial dependence of the resonance condition is considered as a crucial feature of the dynamics. This type of behavior has also been studied for nonrelativistic particles and electrostatic waves by Shklyar,<sup>15</sup> in connection with observed proton precipitation from the radiation belts. He considers the case of strong inhomogeneity, and derives a random walk for the appropriate particle canonical momentum, assuming the relevant phase angle at resonance to be randomly distributed over  $(0, 2\pi)$ . Here, connection is made with that analysis, using a time-dependent pendulum model. It is also shown that in the opposite, weakly inhomogeneous limit, adiabatic considerations apply, giving a different expression for the change in canonical momentum. The use of adiabatic invariants is similar to the methodology used by several researchers to consider the power absorbed from a

$z$ -dependent electromagnetic wave perturbation of finite extent, propagating perpendicular to a constant background magnetic field.<sup>16,17</sup> The results obtained here find the phase angle restricted to a narrow range about a deterministic value, leading to a systematic change of the momentum, so that after a series of resonant interactions the cumulative change can be much larger than for the nonadiabatic random walk. Numerical simulations check the resonance-averaged Hamiltonian against the full equations of motion, and demonstrate the different resonant phase-angle ranges and cumulative effects of many resonances in the two regimes.

## II. THE EQUATIONS OF MOTION

For simplicity a slab model is used, with background magnetic field determined by the vector potential  $A_0 = -yB_0g(z)\hat{x}$ , where the inhomogeneity function  $g$  satisfies  $g(0) = 1$ ,  $g'(0) = 0$ . The resultant  $\mathbf{B}_0 = (0, -yB_0g', B_0g)$  satisfies  $\nabla \cdot \mathbf{B} = 0$  exactly for any  $g$ . The electromagnetic wave is specified by

$$A_w = A_1 \sin \psi \hat{e}_1 + A_2 \cos \psi \hat{e}_\otimes - A_3 \sin \psi \hat{e}_\parallel, \quad (1)$$

$$\psi = \int \mathbf{k} \cdot d\mathbf{x} - \omega t. \quad (2)$$

A constant  $k_\perp$  is used, and  $k_\parallel$  is considered only as a function of  $z$  because the perpendicular scale length over which it changes is large compared to the Larmor radius  $\rho$ , although  $k_\perp \rho$  is taken  $\sim O(1)$ . With  $\mathbf{k} = k_\parallel \hat{e}_\parallel + k_\perp \hat{e}_1$ , the angle between  $\mathbf{k}$  and  $\hat{z}$  is  $\alpha$  and between  $\hat{e}_1$  and  $\hat{x}$  is  $\beta$ ; thus  $\hat{e}_\parallel = \hat{z}$ ,  $\hat{e}_1 = \cos \beta \hat{x} + \sin \beta \hat{y}$ , and  $\hat{e}_\otimes \equiv \hat{e}_\parallel \times \hat{e}_1 = -\sin \beta \hat{x} + \cos \beta \hat{y}$ . In the homogeneous situation, the  $(x, y)$  axes could be rotated to set  $\beta = 0$  without loss of generality, but here the inhomogeneity introduces a physical distinction between  $x$  and  $y$ . Note that the decomposition of  $\mathbf{k}$  into  $k_\parallel$  and  $k_\perp$  is done relative to  $\mathbf{B}_0$  at  $z=0$ ;  $g'(z)$  is tacitly assumed small enough that  $\alpha$  and  $\beta$  do not change much over the distances involved. Rigorously introducing curvilinear coordinates and their associated Jacobian factors, as done by Shklyar,<sup>15</sup> leads to the same results as those obtained below.

The relativistic Hamiltonian of the particle motion in the combined fields is given by

$$H(\mathbf{P}, \mathbf{x}; t) = mc^2 \sqrt{1 + \left( \frac{\mathbf{P} - q\mathbf{A}/c}{mc} \right)^2}, \quad (3)$$

where  $\mathbf{P}$  is the canonical momentum and  $\mathbf{A} = \mathbf{A}_0 + \mathbf{A}_w$ . Defining  $\Omega = |q| B_0/mc$  and  $s = q/|q|$ , a canonical transformation is made from  $(x, P_x, y, P_y, z, P_z)$  to  $(X, P_X, \phi, I, \bar{z}, \bar{P}_z)$  via the generating function  $F(x, y, \phi, P_X, z, P_z)$ :

$$F = m\Omega g \left[ -\frac{1}{2} \left( y + \frac{sP_X}{m\Omega g} \right)^2 \tan \phi + \frac{xP_X}{m\Omega g} \right] + z\bar{P}_z, \quad (4)$$

which is effectively the same as the one used in Refs. 10 and 11 with  $\Omega$  replaced by  $\Omega g$ . In the new variables, the Hamiltonian is given by

$$\bar{H} = \sqrt{1 + 2 \frac{\Omega g}{\omega} \bar{I} + Q^2} + 2 \sqrt{2 \frac{\Omega g}{\omega} \bar{I}} (-\epsilon_1 \sin \psi \cos \bar{\phi}_1 + s\epsilon_2 \cos \psi \sin \bar{\phi}_1) + 2s\epsilon_3 \bar{P}_z \sin \psi, \quad (5)$$

where  $Q = \bar{P}_z - (g'/g) \sin \bar{\phi} (\bar{I} \cos \bar{\phi} - s\rho \bar{P}_X)$  and  $\rho$  is defined in Eq. (9) below. (Actually,  $Q$  is just  $P_z/mc$ .) The wave amplitudes are expressed by  $\epsilon_i = |q| A_i/mc^2$ ,  $i = (1, 2, 3)$ . The overbarred variables  $(\bar{X}, \bar{P}_X, \bar{\phi}, \bar{I}, \bar{z}, \bar{P}_z, t)$  are the normalized quantities

$$(\omega X/c, P_X/mc, \phi, \omega I/mc^2, \omega \bar{z}/c, \bar{P}_z/mc, \omega t)$$

and  $\bar{H}$  is  $H/mc^2$ . From now on, the overbars will be suppressed. The higher-order terms  $(\epsilon_1^2 + \epsilon_3^2) \sin^2 \psi + \epsilon_2^2 \cos^2 \psi$  in Eq. (5) have been dropped, and  $\bar{P}_z$  has been used instead of the full expression for  $Q$  in the  $\epsilon_3$  term. To zeroth order in  $\epsilon$ ,  $I$  is equal to the usual adiabatic invariant  $\mu$  times constant factors.

After using the familiar Bessel function identity

$$\exp(ia \sin \theta) = \sum_{n=-\infty}^{\infty} J_n(a) \exp(in\theta)$$

and expanding to first order in  $\epsilon_i$ , the Hamiltonian takes the form

$$H(X, P_X, \phi, I, z, P_z; t)$$

$$= \Upsilon - \frac{g'}{g} \sin \phi \frac{I \cos \phi - s\rho P_X}{2\Upsilon} + \sum_{n=-\infty}^{\infty} \frac{a_n}{2\Upsilon} \sin \xi_n, \quad (6)$$

where

$$\Upsilon = \left( 1 + 2 \frac{\Omega g}{\omega} I + P_z^2 \right)^{1/2}, \quad (7)$$

$$a_n = -\sqrt{2 \frac{\Omega g}{\omega}} I [(\epsilon_1 - \epsilon_2) J_{n-1} + (\epsilon_1 + \epsilon_2) J_{n+1}] + 2sP_z \epsilon_3 J_n, \quad (8)$$

$$J_n = J_n(\eta_1 \rho), \quad \rho = \sqrt{2 \frac{\omega}{\Omega g}}, \quad (9)$$

$$\xi_n = \delta + sn\phi_1, \quad \phi_1 = \phi + s\beta, \quad (10)$$

$$\delta = \eta_x X + \int \eta_z dz - t - s\eta_y \frac{\omega}{\Omega g} P_X, \quad (11)$$

and  $\eta_{(x,y,z)} = k_{(x,y,z)} c/\omega$  is the index of refraction. The quantity  $\Upsilon$  is the canonical analog of the usual relativistic factor  $\gamma$ .

In the neighborhood of the  $l$ th resonance, all terms in the sum except  $n=l$  can be dropped by averaging over the rapidly oscillating cyclotron phase  $\phi$ , which also eliminates the term proportional to  $g'/g$ . Then constants of the motion,  $c_1 = P_X - \eta_x H$  and  $c_2 = I - slH$ , can be used to eliminate  $P_X$  and  $P_z$ :

$$P_X = c_1 + \frac{\eta_x}{sl} (I - c_2), \quad (12)$$

$$P_z = \sigma_z P_0, \quad P_0(I, z) \equiv \sqrt{\left( \frac{I - c_2}{sl} \right)^2 - 1 - 2 \frac{\Omega g}{\omega} I}, \quad (13)$$

where  $\sigma_z$  is the sign of  $P_z$ . Here,  $P_z$  is given neglecting terms of order  $\epsilon$ , which will be adequate. To this approximation,  $\Upsilon$  and  $a_l$  are functions only of  $I$  and  $z$ . A closed set of equations of motion can now be written as

$$\frac{dI}{dt} = -sl \frac{a_l}{2\Upsilon} \cos \xi, \quad (14)$$

$$\frac{d\xi}{dt} = \frac{\sigma_z \eta_z P_0}{\Upsilon} + sl \frac{\Omega g}{\omega \Upsilon} - 1 + s\eta_y \frac{\omega}{\Omega g} P_X \frac{g'}{g} \frac{dz}{dt} + O(\epsilon), \quad (15)$$

$$\frac{dz}{dt} = \frac{\sigma_z P_0}{\Upsilon} + O(\epsilon), \quad (16)$$

or, following Shklyar,

$$\frac{dI}{dz} = -sl \sigma_z \frac{a_l}{2P_0} \cos \xi, \quad (17)$$

$$\frac{d\xi}{dz} = \frac{\sigma_z \eta_z P_0 + sl \Omega g / \omega - \Upsilon}{\sigma_z P_0} + s\eta_y \frac{\omega}{\Omega g} P_X \frac{g'}{g} + O(\epsilon). \quad (18)$$

The resonance condition is  $d\xi/dz = 0$ , which is equivalent to lowest order to the familiar condition  $\omega - k_z v_z = sl\Omega/\gamma$ . For an electron in  $l = -1$  resonance with a right-hand circularly polarized wave propagating along  $\mathbf{B}_0$ , the standard scenario for whistler emissions in the magnetosphere,<sup>1-5</sup>  $\xi + \pi/2$  is the angle between  $\mathbf{v}_1$  and the wave magnetic field  $\mathbf{B}_w$ .

To a good approximation, this nonautonomous system of two ordinary differential equations can be derived from a Hamiltonian with  $1\frac{1}{2}$  degrees of freedom, with  $z$  playing the role of time:

$$K(I, \xi; z) = K_0(I, z) + \epsilon K_1(I, z) \sin \xi, \quad (19)$$

$$K_0(I, \xi; z) \equiv \left( \eta_z + s\eta_y \frac{\omega}{\Omega g} \frac{g'}{g} c_1 \right) (I - c_2) + s \frac{\eta_x \eta_y}{2} \frac{\omega}{sl \Omega g} \frac{g'}{g} (I - c_2)^2 - sl \sigma_z P_0(I, z), \quad (20)$$

$$K_1 \equiv s l \sigma_z \frac{a_l}{2P_0}, \quad (21)$$

where an explicit factor of  $\epsilon$  has been introduced in Eq. (19) as a reminder that  $a_l$  consists of terms proportional to  $\epsilon_{(1,2,3)}$ . The location(s) of resonance can be found approximately from  $(\partial K_0/\partial I)(I_i, z_{\text{res}}) = 0$ , where  $I_i$  is the initial value of  $I$ . The equation for  $d\xi/dz$  deriving from  $K$  does not agree with Eq. (18) in the  $O(\epsilon)$  terms, but this is acceptable by virtue of the following argument. It is only important to evaluate  $d\xi/dz$  accurately near resonance, since otherwise the deviations in  $I$  are small and average to zero. Near resonance, where  $d\xi/dz \approx (d^2\xi/dz^2)_{\text{res}}(z - z_{\text{res}})$ , one has

$$\frac{d^2\xi}{dz^2} = \left( \frac{\partial}{\partial z} + \frac{dI}{dz} \frac{\partial}{\partial I} + \frac{d\xi}{dz} \frac{\partial}{\partial \xi} \right) \frac{d\xi}{dz}. \quad (22)$$

Using  $d\xi/dz = (\partial K_0/\partial I) + \epsilon(\partial K_2/\partial I) \sin \xi$  to define  $K_2(I, z)$ , the last two terms in Eq. (22) have the estimates

$$\frac{dI}{dz} \frac{\partial}{\partial I} \frac{d\xi}{dz} \approx \epsilon K_1 \frac{\partial^2 K_0}{\partial I^2} \cos \xi + O(\epsilon^2), \quad (23)$$

$$\frac{d\xi}{dz} \frac{\partial}{\partial \xi} \frac{d\xi}{dz} \approx \epsilon \frac{\partial K_0}{\partial I} \frac{\partial K_2}{\partial I} \cos \xi + O(\epsilon^2). \quad (24)$$

Now, since near resonance  $(\partial K_0/\partial I)$  is  $O(\epsilon)$  while  $K_1$ ,  $(\partial^2 K_0/\partial I^2)$ , and  $(\partial K_2/\partial I)$  are  $O(1)$ ,  $K_2$  only affects  $d\xi/dz$  through a term small by a factor of  $\epsilon$ . Therefore, the form of  $K_2$  does not appreciably affect the dynamics and may be replaced by  $K_1$ , so that Eqs. (19)–(21) may be used.

Writing the normalized relativistic kinetic energy of the particle in terms of the mechanical (noncanonical) momentum,  $U = \sqrt{1 + (p/mc)^2} - 1$ , expressing this in terms of the transformed variables, and evaluating  $P_z$  via Eq. (13) yields  $U = (I - c_2)/sl + O(\epsilon)$ . This shows the direct relationship between a change in  $I$  of  $\delta I$  and the corresponding  $\delta U = \delta I/sl$ . Similarly, changes in the pitch angle  $\xi$  induced by changes in  $I$  can be found through  $\sin^2 \xi = v_\perp^2/v^2 = 2\Omega g I/\omega[(U+1)^2 - 1]$ .

### III. ANALYSIS

Shklyar considers the strongly inhomogeneous case where, by definition, the first term on the right-hand side of Eq. (22) dominates the other two. Conditions for this to hold will be arrived at below. In this case,

$$\xi \approx \xi_{\text{res}} + \frac{a}{2} (z - z_{\text{res}})^2, \quad a \equiv \left( \frac{\partial^2 K_0}{\partial z \partial I} \right)_{\text{res}} \quad (25)$$

and the change in  $I$  across the resonance is

$$\begin{aligned} (\delta I)_1 &= \int_{-\infty}^{\infty} -\epsilon K_1 \cos \xi \, dz \\ &= -\epsilon K_1 \sqrt{\frac{2\pi}{|a|}} \cos \left( \xi_{\text{res}} \pm \frac{\pi}{4} \right), \end{aligned} \quad (26)$$

where  $\pm$  is  $+$  if  $a > 0$  and *vice versa*. Taking the resonant phase  $\xi_{\text{res}}$  uniformly random over  $(0, 2\pi)$  yields a random walk for the action  $I$ . Since both the energy and pitch angle

can be expressed as functions of  $I$  plus terms of order  $\epsilon$  oscillating with frequency  $\Omega$ , they, too, undergo a random walk.

In the other limit, when the inhomogeneity term in Eq. (22) is small compared to the last two terms on the right-hand side of (22), which taken alone represent one-degree-of-freedom motion, it is worthwhile to consider contours of  $K(I, \xi; z)$  in the  $(I, \xi)$ -plane for fixed  $z$ . The picture is like the standard one for a plane pendulum, with an island of closed orbits inside a separatrix, outside of which lie open orbits. At any  $z$ , the location of the fixed points is given approximately by  $(\partial K_0/\partial I)(I_{\text{res}}, z) = 0$ , with  $\xi = \pi/2$  and  $-\pi/2$ . In the homogeneous case, motion would be along a curve of constant  $K$ , and these contours would be stationary. The  $z$  dependence has two related effects: The particle trajectory is not strictly along lines of constant  $K$ , and the entire picture of  $K$  contours moves with the passage of "time"  $z$ , as described by the above estimate for  $I_{\text{res}}(z)$ .

Intuitively, when the island is at large  $I$  from the particle, the particle approximately moves at constant  $I \approx I_i$  and  $d\xi/dz \approx \partial K_0/\partial I$ . As the island slowly approaches  $I_i$ , the particle is affected, still moving roughly along the curved  $K$  contours while slowly crossing them. The island edge, or separatrix, guides the particle towards the  $x$  point, which is a resonance since  $d\xi/dz = 0$  there; therefore, the particle should cross the resonance near  $\xi = \xi_x$ . Following the separatrix leads to a change in  $I$  of order the island width, which is  $O(\sqrt{\epsilon})$ . In more detail, the oscillation  $d\xi/dz$  is usually much faster than the speed of the  $x$  point so that the particle almost follows a  $K$  contour, but near the  $x$  point  $d\xi/dz$  goes to zero, so that the particle is stationary while the island structure passes through it. As soon as it does, the particle resumes its fast motion at nearly constant  $I$ . This is illustrated numerically in Sec. IV below.

To be more quantitative,  $K$  is Taylor expanded in  $I$  about  $I_{\text{res}}(z)$  to get the model Hamiltonian

$$M(I, \xi; z) = \frac{G_r}{2} [I - I_{\text{res}}(z)]^2 + F_r \sin \xi \quad (27)$$

with  $G_r = (\partial^2 K_0/\partial I^2)(I_{\text{res}}, z_{\text{res}})$ ,  $F_r = K_1(I_{\text{res}}, z_{\text{res}})$ , and  $I_{\text{res}}(z)$  given approximately by  $(\partial K_0/\partial I)(I_{\text{res}}, z) = 0$  as above. This form for  $M$  neglects the small, slow deformation of the separatrix shape. Defining  $\sigma_F$  to be the sign of  $F_r$  and  $\sigma_G$  to be the sign of  $G_r$ , a canonical transformation from  $(I, \xi)$  to  $(P, Q)$  via the generating function  $\mathcal{F}(\xi, P) = P(\xi + \sigma_F \sigma_G \pi/2)$  yields

$$M(P, Q; z) = \sigma_G \left( \frac{G}{2} [P - P_{\text{res}}(z)]^2 - F \cos Q \right) \quad (28)$$

with  $F = \sigma_F F_r > 0$ ,  $G = \sigma_G G_r > 0$ , and  $P_{\text{res}}(z) = I_{\text{res}}(z)$ . Then,  $M(P, Q; z)$  is clearly the Hamiltonian for a pendulum with linearized frequency  $\omega_0 = \sqrt{FG}$  and island width  $W = 4\sqrt{F/G}$ , moving in  $P$  with time  $z$ , with  $o$  point at  $Q = 0$  and  $x$  point at  $Q = \pm \pi$ . The sign  $\sigma_G$  only affects the sense of the  $(P, Q)$  motion.

As above, the strongly inhomogeneous analysis yields  $\delta P = -\sigma_G F \sqrt{2\pi/|GP'_{\text{res}}|} \sin(Q_{\text{res}} \pm \pi/4)$ , where  $\pm$  is  $-$  if  $\sigma_G P'_{\text{res}} > 0$ . In the other limit, it is valid to use the adia-

batic invariant  $\mathcal{I} = \oint PdQ/2\pi$  to calculate  $\delta P$ . When the particle is outside the separatrix  $\mathcal{I}$  has the form

$$\mathcal{I} = P_{\text{res}}(z) \pm \mathcal{I}_0(\kappa), \quad (29)$$

$$\mathcal{I}_0(\kappa) = \frac{4}{\pi} \sqrt{\frac{F}{G}} \kappa \mathcal{E}(1/\kappa), \quad 2\kappa^2 \equiv 1 + \frac{M}{\sigma_G F}, \quad (30)$$

where  $\mathcal{E}$  is the complete elliptic integral of the second kind. The argument  $\kappa$  is greater than 1 outside the separatrix, less than 1 inside, and equal to 1 on the separatrix. The choice of sign in the expression for  $\mathcal{I}$  is critical, and is different before and after crossing the resonance. It may be determined by noting that for  $z \rightarrow \pm \infty$ , the island is far from the particle so  $P$  is approximately constant and  $\mathcal{I} \rightarrow P$ , while  $\mathcal{I}_0 \rightarrow |P - P_{\text{res}}(z)|$ . For Eq. (29) to be satisfied, if  $P_{\text{res}}(z)$  increases with increasing  $z$ ,  $\pm$  must be  $-$  for  $z \rightarrow \infty$  and  $+$  for  $z \rightarrow -\infty$ . Thus  $\mathcal{I}$  tends to the value of  $P$  for large positive and negative  $z$ , while suffering a jump as the particle crosses the resonance, where the adiabatic condition is violated. The jump in  $P$  is therefore equal to the jump in  $\mathcal{I}$  across the resonance. This may be estimated by evaluating  $\mathcal{I}$  just before and after the particle crosses the separatrix, where  $\kappa = 1$ . Thus, for  $P_{\text{res}}(z)$  increasing with  $z$ ,

$$\begin{aligned} \delta P &= P(z = \infty) - P(z = -\infty) \\ &= \delta \mathcal{I} \approx [P_{\text{res}}(z_{\text{res}}) - \mathcal{I}_0(\kappa = 1^+)] \\ &\quad - [P_{\text{res}}(z_{\text{res}}) + \mathcal{I}_0(\kappa = 1^+)] \\ &= -\frac{8}{\pi} \sqrt{\frac{F}{G}}. \end{aligned} \quad (31)$$

As throughout,  $P_{\text{res}}(z)$  refers to the resonant value of  $P$  for a given  $z$ ;  $P_{\text{res}}(z_{\text{res}})$  is that value actually attained by the particle when it hits the resonance at  $z_{\text{res}}$ . Evaluating  $P_{\text{res}}(z)$  as  $P_{\text{res}}(z_{\text{res}})$  assumes that  $P_{\text{res}}(z)$  does not change much in the time it takes the particle to go across the island.

For  $P_{\text{res}}(z)$  decreasing with  $z$ , the jump in  $P$  has the opposite sign. The corresponding change in  $I$  is just

$$(\delta I)_2 = -\sigma_r \frac{8}{\pi} \sqrt{\frac{F_r}{G_r}}, \quad (32)$$

where  $\sigma_r$  is the sign of  $dI_{\text{res}}/dz$ , which itself is given by

$$\frac{dI_{\text{res}}}{dz} = -\frac{\partial^2 K_0 / \partial z \partial I}{\partial^2 K_0 / \partial I^2}. \quad (33)$$

The magnitude of  $(\delta I)_2$  is just  $2/\pi$  times the width of the island, confirming the intuitive analysis presented above.

It is interesting to note that, from Eq. (22), the condition for adiabatic behavior to hold, leading to  $(\delta I)_2$ , is

$$\mathcal{R} \equiv \left| \frac{\partial^2 K_0 / \partial z \partial I}{K_1(\partial^2 K_0 / \partial I^2)} \right| \ll 1 \quad (\text{for adiabaticity}), \quad (34)$$

while  $(\delta I)_1$  applies in the opposite limit. Ignoring constants of order unity,  $\mathcal{R}$  is also seen to be essentially the ratio of the island oscillation period,  $2\pi/\omega_0$ , to the time it takes the island to move across its own width,

$W/(dI_{\text{res}}/dz)$ . This is exactly the quantity one would expect to control the adiabaticity of the motion.

The magnitudes of the two expressions for  $\delta I$  have the ratio  $(\delta I)_2/(\delta I)_1 \approx \sqrt{\mathcal{R}}$ . Therefore, the applicable  $\delta I$  is always the smaller of the two. A harmonic mean,  $[1/(\delta I)_1 + 1/(\delta I)_2]^{-1}$ , might be a convenient composite estimate for the jump due to a single resonance. Crossing many resonances, however, brings in an important difference: The strongly inhomogeneous mechanism involves a random phase, which leads jumps at isolated resonances to combine diffusively, as in a random walk, while for the adiabatic case the sign of the jump in action is systematically determined by the motion of the resonance island. If this has the same direction for many consecutive resonances, the jumps in  $\delta I$  add directly, leading to much larger cumulative changes in  $I$  and in quantities that depend on  $I$ , such as the particle energy and pitch angle.

It can also be seen that  $\mathcal{R}$  is related to the ratio of wave-particle interaction times for the two mechanisms. For the strongly inhomogeneous case, the interaction time is estimated<sup>15</sup> from Eq. (25) to be  $\tau_1 = v_z^{-1} \cdot a^{-1/2}$ , while for the adiabatic process  $\tau_2 = v_z^{-1} \cdot W/(dI_{\text{res}}/dz)$ , so that  $\mathcal{R} = (\tau_1/\tau_2)^2$ . Therefore, Eq. (34) implies that of the two mechanisms, the applicable one is the one with the longer interaction time. Note that this concept of interaction time is not the same as the "effective time,"<sup>18</sup> which might be defined here as  $v_z^{-1} \cdot (\delta I/\epsilon)$ .

Next, we make some simple estimates of these expressions in terms of physical variables. Using the 0th order constancy of energy and  $I$  leads to

$$\left( \frac{\partial^2 K_0}{\partial I^2} \right)_r \approx \frac{\eta_z^2 - 1}{slp_z}, \quad (35)$$

$$\left( \frac{\partial^2 K_0}{\partial z \partial I} \right)_r \approx \frac{1}{p_z} \left[ 1 - \eta_z p_z \left( 1 + \frac{1}{2} \tan^2 \xi \right) \right] \frac{g'}{g}, \quad (36)$$

where  $p$  is the mechanical momentum, normalized by  $mc$ , and  $g'/g$  can be interpreted as the normalized inverse scale length  $(\omega L_z/c)^{-1}$ . Estimating  $K_1$  is more difficult because the Bessel functions involved, especially for large index, are sensitive to their argument, which is approximately  $k_\perp \rho$ . It can be written as

$$\begin{aligned} K_1 &\approx sl\sigma_z \left\{ -\frac{1}{2} \tan^2 \xi [(\epsilon_1 - \epsilon_2)J_{l-1} + (\epsilon_1 + \epsilon_2)J_{l+1}] \right. \\ &\quad \left. + s\epsilon_3 J_l \right\}, \quad \equiv sl\sigma_z \tilde{J}_l. \end{aligned} \quad (37)$$

Using these estimates to approximate  $\mathcal{R}$  in Eq. (34) gives

$$\mathcal{R} \approx \frac{1 - \eta_z p_z \left( 1 + \frac{1}{2} \tan^2 \xi \right) \frac{g'}{g}}{\epsilon \tilde{J}_l (\eta_z^2 - 1)} \frac{g'}{g}. \quad (38)$$

As is well known, for large  $|l|$ ,  $J_l(x)$  is small for  $|x| < |l|$ , quickly reaches its maximum near  $|x| = |l|$ , and oscillates with slowly decreasing amplitude for  $|x| > |l|$ .

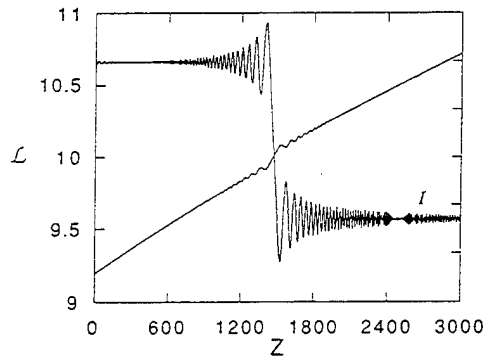


FIG. 1. The resonance function  $\mathcal{L}$  and action  $I$  of a test particle according to the  $1\frac{1}{2}D$  Hamiltonian  $K$ . As the particle crosses the  $l$ th resonance, indicated by  $\mathcal{L}=l$ ,  $I$  takes a large jump.

For weak waves  $\epsilon \ll g'/g$ , but the bracketed expression can be small and often  $\eta_z \gg 1$ , so that the adiabatic condition  $\mathcal{R} \ll 1$  can be met.

With the above approximations, the change in action can be expressed as

$$(\delta I)_1 \approx \frac{-s\sigma_z \epsilon \tilde{J}_l}{\sqrt{g'/g}} \sqrt{\frac{2\pi p_z}{1 - \eta_z p_z (1 + \frac{1}{2} \tan^2 \xi)}}, \quad (39)$$

$$(\delta I)_2 \approx -\sigma_r \frac{8}{\pi} \sqrt{\frac{\epsilon J p_z}{\eta_z^2 - 1}}. \quad (40)$$

In terms of  $\delta I$ , the change in energy  $U$  (normalized by  $mc^2$ ) and pitch angle  $\xi$  are given by  $\delta U = \delta I/sl$  and  $\delta(\cos \xi) = [(\eta_z p_z - \cos \xi)/p^2](\delta I/sl)$ .

#### IV. SIMULATIONS

Numerical simulations were performed of both the reduced Hamiltonian  $K(I, \xi; z)$  of Eq. (19) and the full  $H(X, P_X, I, \phi, z, P_z; t)$  of Eq. (5). A right-hand circularly polarized wave was used, with  $\epsilon_1 = \epsilon_0 \sin \alpha$ ,  $\epsilon_2 = \epsilon_0$ ,  $\epsilon_3 = \epsilon_0 \cos \alpha$ , amplitude  $\epsilon_0 = 10^{-7}$ ,  $\alpha = 30^\circ$ ,  $\beta = 0$ , and constant index of refraction  $\eta = 50$ . A positively charged particle was used, with normalized initial energy  $U = 3 \times 10^{-4}$  and pitch angle  $\xi = 35^\circ$ , and  $\omega/\Omega = 70$ . The background field inhomogeneity function was taken to be  $g = 1 + g_1 z$ , with various values of  $g_1$  and initial particle gyrophase  $\phi_0$ .

Figure 1 shows the behavior of a typical particle across the  $l=10$  resonance, according to the  $1\frac{1}{2}D$  resonant Hamiltonian  $K(I, \xi; z)$  with  $g_1 = 10^{-4}$ . This corresponds to  $\mathcal{R} = 0.4$ , which moderately satisfies the condition for adiabatic behavior. The action  $I$  is seen to oscillate rapidly about a constant value except for a large, negative jump when the particle's parallel motion carries it through a resonance. The occurrence of a resonance is identified by  $\partial K_0 / \partial I = 0$  or, in terms of physical variables,  $\mathcal{L}(z) \equiv s(\omega/\Omega g) \gamma (1 - \eta_z v_z/c)$  attaining an integer value  $l$ . Figure 2(a) illustrates the adiabatic process in the  $(I, \xi)$  plane. The instantaneous location of the particle is shown for several values of  $z$  very near resonance, along with the separatrix of  $K(I, \xi; z)$  corresponding to the first and last  $z$  (solid and dashed curves, respectively). The separatrix

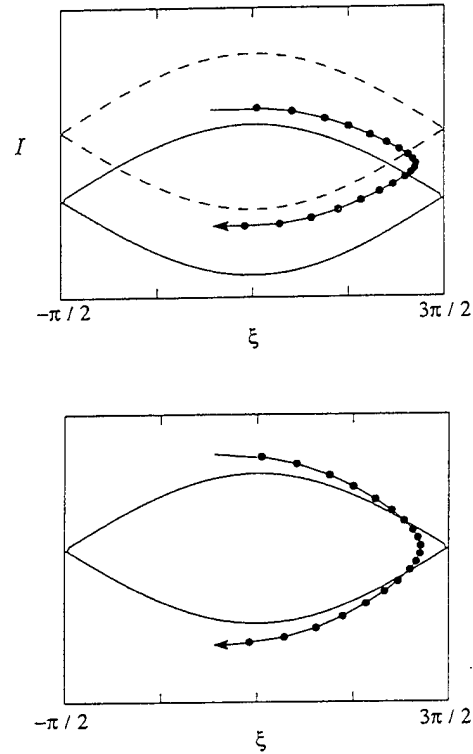


FIG. 2. A series of snapshots of the particle position in the  $(I, \xi)$  plane, for the adiabatic regime discussed in the text. (a) Separatrices are drawn corresponding to the first (solid curve) and last (dashed curve) shown particle positions. (b) The same particle positions are shown in the frame of the moving island.

moves up as  $z$  advances, and the particle initially moves to the right. For earlier  $z$ , when the island is far below, the particle is undisturbed and moves left to right at nearly constant  $I$ . As the island nears, the  $K$  contours become more and more distorted, leading to bigger oscillations in the  $I$  of the particle. The island eventually moves past the particle when the particle is near the  $x$  point, changing the particle's adiabatic invariant and mean  $I$  value. The island continues upward, leaving the particle to resume nearly undisturbed periodic motion at its new  $I$  value. Figure 2(b) shows the same particle positions in the frame of the moving island, clearly showing how the particle crosses the island near the  $x$  point.

The issue of phase trapping has not been addressed. Occasionally, a particle will cross into the island far from the  $x$  point, and by conservation of an adiabatic invariant inside the island, will remain trapped for a long time before managing to cross out again. During this time both the island and particle move upwards in  $I$  together, so that the net change in the particle  $I$  can be positive and very large. This typically happens for 0, 1, or 2 out of 24 particles in an ensemble of different initial gyrophases, for both the  $1\frac{1}{2}D$  and  $3\frac{1}{2}D$  Hamiltonians. This exceptional behavior may be related to the time-dependent deformation of the island shape, since it is not observed for the pendulum Hamiltonian of Eq. (27). The occurrence of this trapping should diminish as the adiabatic condition becomes more strongly satisfied. It bears more investigation, since it shows how

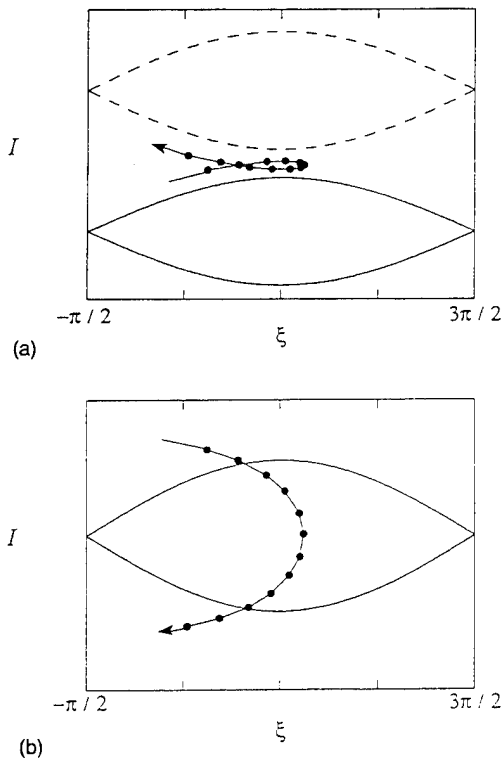


FIG. 3. The same as Fig. 2, but for the strongly inhomogeneous regime. (a) Unlike in the adiabatic regime, the particle crosses resonance far from the island's  $x$  point. (b) The same motion shown in the frame of the island, which is moving upwards fast enough that the actual change in  $I$ , shown in (a), is positive.

particles can become phase entrapped even by a weak, constant-amplitude wave. (The more common picture is that the particle becomes trapped by moving into a region of space where the wave strength increases.) Here, however, this study is deferred.

Figure 3(a) illustrates the passage through the  $l=10$  resonance with stronger inhomogeneity, with  $g_1=5 \times 10^{-4}$ , corresponding to  $\mathcal{R}=2.0$ . Because the rising of the island is faster than the particle motion, the island crosses the particle's  $I$  without concern for the particle's  $\xi$ . The influence of the  $H$  contours once the island is past can even lead to an increased value of the particle  $I$ , as shown. Figure 3(b) shows the particle motion in the island frame.

An ensemble of particles with 24 different  $\phi_0$  values  $15^\circ$  apart were simulated, according to both the full  $H$  and the resonance averaged  $K$ . Because  $K$  is a good approximation to  $H$  only near resonance, the initial phase  $\xi$  from the  $K$  simulation will not correspond to the value from the  $H$  simulation; only ensembles of initial  $\xi$  values, or equivalently  $\phi_0$  values, can be compared. The resulting changes in  $I$  and resonant  $\xi$  values are shown in Fig. 4(a) for the adiabatic regime. An "X" marks the theoretical estimate of  $(\delta I/W=2/\pi, \xi=3\pi/2)$ , where  $W$  is the island width. Two points from the ensemble of  $K$  runs that exhibit phase entrapping have been omitted. With this proviso, it is seen that the particles go through resonance with  $\xi$  near the  $x$ -point value, and also that the sign of  $\delta I$  is negative in almost each case. The same results for the strongly inho-

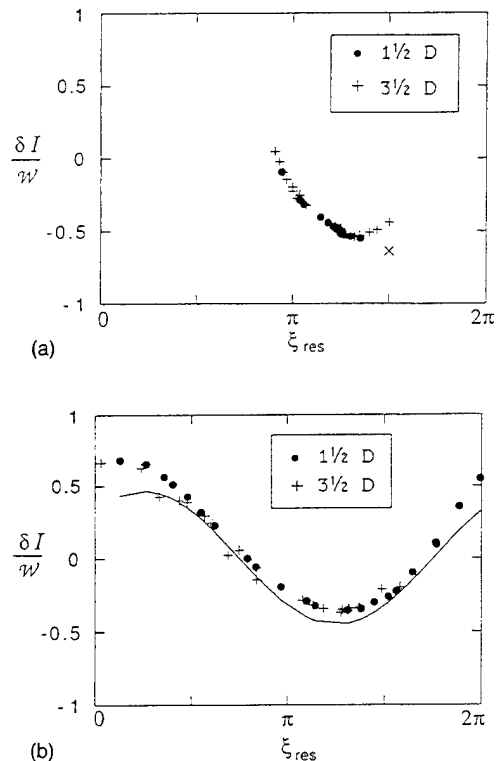


FIG. 4. The change in action across a resonance versus the phase angle at resonance, for an ensemble of initial conditions, according to both the  $3\frac{1}{2}D$  and  $1\frac{1}{2}D$  Hamiltonians. (a) In the adiabatic regime, the results cluster around the analytical estimate, indicated by the "X", with most values of  $\delta I$  of the same sign, and phase angle near the island  $x$  point. Two particles that became phase entrapped are not shown. (b) In the strongly inhomogeneous regime, all values of  $\xi$  are present, and positive and negative  $\delta I$  are about equally likely. The solid curve shows the analytical estimate.

homogeneous regime are shown in Fig. 4(b); the sinusoidal dependence of  $\delta I$  on  $\xi$  expected from Eq. (26) is shown by a solid line, with the numerical results in close agreement. In particular, positive and negative changes in  $I$  are almost equally likely.

Figure 5 shows the change in the particle's action,  $I-I_0$ , as a function of time for a 6D run, carried out long enough to show several consecutive passages through resonance (identified by integer values of  $\mathcal{L}$ ). In the strongly inhomogeneous regime, shown in Fig. 5(a), the change in  $I$  can have either sign, so that  $I$  (and therefore energy and pitch angle) executes a random walk. Figure 5(b), showing the adiabatic regime, illustrates changes in  $I$  with the same sign across several resonances, leading to a large cumulative effect.

## V. SUMMARY

Resonant wave-particle interactions have been considered in the presence of spatial inhomogeneity of the background magnetic field, from a Hamiltonian point of view. The reduced, or resonance-averaged, Hamiltonian derived depends only on one action-angle pair of canonical variables, plus the distance along the field line  $z$ , which plays the role of time. Since the waves are perturbatively weak, the parallel motion of the particle neglecting the wave gives

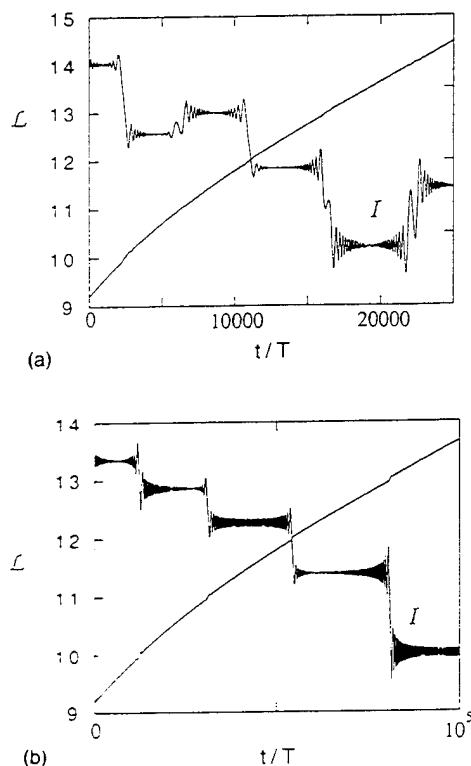


FIG. 5. An illustration of several consecutive resonance crossings, according to the  $3\frac{1}{2}D$  Hamiltonian. (a) In the strongly inhomogeneous case,  $\delta I$  undergoes a random walk. (b) In the adiabatic regime, the changes in  $I$  have the same sign.

the correspondence between  $z$  and time. Using constants of the motion, all other quantities can be expressed in terms of the canonical action and angle, including the particle kinetic energy and pitch angle. Two limiting regimes of behavior were found, depending on the strength of the field variation, and the reduced equations gave results that agreed with the full Hamiltonian in each case.

The reduced Hamiltonian was shown to be accurately modeled by the standard pendulum Hamiltonian, modified so that the location of the separatrix depends on time, at a rate determined by the strength of the field variation. A single parameter was found that differentiated the two regimes, namely the rising rate of the separatrix compared to the oscillation frequency about the island center [Eq. (34); see also Eq. (38)]. When this parameter is small, the particle motion is adiabatic except while crossing the reso-

nance, and computing the adiabatic invariant long before and after the resonance crossing gives an expression for the change in the action. The sign of this change depends only on the background parameters, since the phase canonical angle is constrained to be in the vicinity of the  $x$  point, as illustrated in Figs. 2 and 4(a). In the other limit, the time dependence of the reduced Hamiltonian is strong enough to destroy the adiabatic invariant even far from resonance, giving a different expression for the change in action, as calculated by Shklyar.<sup>15</sup> An important aspect of this expression is that it depends sinusoidally on the phase angle, which is unconstrained over the range  $(0, 2\pi)$ . Therefore, considering the effect of  $n$  independent resonant interactions, the action undergoes a random walk, with a mean displacement proportional to  $\sqrt{n}$ . In the adiabatic case, on the other hand, the change in action is proportional to  $n$ , leading to larger changes as the result of many consecutive resonant interactions.

### ACKNOWLEDGMENTS

The author wishes to thank Dr. G. Ginat for many useful discussions, and for a careful reading of the manuscript.

This work was supported by Air Force Contract No. F19628-K-92-0007.

- <sup>1</sup>R. A. Helliwell, *J. Geophys. Res.* **72**, 4773 (1967).
- <sup>2</sup>T. F. Bell, *Phys. Fluids* **8**, 1829 (1965); *J. Geophys. Res.* **89**, 905 (1984).
- <sup>3</sup>K. B. Dysthe, *J. Geophys. Res.* **76**, 6915 (1971).
- <sup>4</sup>P. J. Palmadesso, *Phys. Fluids* **15**, 2006 (1972).
- <sup>5</sup>R. N. Sudan and E. Ott, *J. Geophys. Res.* **76**, 4463 (1971).
- <sup>6</sup>T. Consoli and R. B. Hall, *Nucl. Fusion* **3**, 237 (1963).
- <sup>7</sup>E. Canobbio, *Nucl. Fusion* **9**, 27 (1969).
- <sup>8</sup>B. H. Quon and R. A. Dandl, *Phys. Fluids B* **1**, 2010 (1989); G. E. Guest, M. E. Fetzner, and R. A. Dandl, *Phys. Fluids B* **2**, 1210 (1990).
- <sup>9</sup>C. F. F. Karney, *Phys. Fluids* **21**, 1584 (1978).
- <sup>10</sup>G. R. Smith and A. N. Kaufman, *Phys. Fluids* **21**, 2230 (1978).
- <sup>11</sup>C. R. Menyuk, A. T. Drobot, K. Papadopoulos, and H. Karimabadi, *Phys. Rev. Lett.* **58**, 2071 (1987); H. Karimabadi, K. Akimoto, N. Omidi, and C. R. Menyuk, *Phys. Fluids B* **2**, 606 (1990).
- <sup>12</sup>S. M. Carlioli, A. A. Chernikov, and A. I. Neishtadt, *Phys. Scr.* **40**, 707 (1989); A. A. Chernikov, G. Smith, and A. I. Neishtadt, *Phys. Rev. Lett.* **68**, 1507 (1992).
- <sup>13</sup>G. P. Ginat and M. A. Heinemann, *Phys. Fluids B* **2**, 700 (1990).
- <sup>14</sup>G. P. Ginat and J. M. Albert, *Phys. Fluids B* **3**, 2994 (1991).
- <sup>15</sup>D. R. Shklyar, *Planet. Space Sci.* **34**, 1091 (1986).
- <sup>16</sup>W. M. Nevins, T. D. Rognlien, and B. I. Cohen, *Phys. Rev. Lett.* **59**, 60 (1987).
- <sup>17</sup>D. Farina and R. Pozzoli, *Phys. Lett. A* **156**, 84 (1991); *Phys. Fluids B* **3**, 1570 (1991).
- <sup>18</sup>J. E. Howard, *Plasma Phys.* **23**, 597 (1981).



# Quasi-linear pitch angle diffusion coefficients: Retaining high harmonics

J. M. Albert

Center for Electromagnetics Research, Northeastern University, Boston, Massachusetts

**Abstract.** Diffusion coefficients for electrons pitch angle scattered by plasmaspheric hiss are reconsidered, as given by quasi-linear theory, overcoming practical problems in keeping high cyclotron harmonics  $n$ . Upper bounds are used to identify ranges of latitude,  $n$ , and wave-normal angle which give only negligible contributions, so that the detailed computation of these values may be avoided, resulting in large savings of computational effort. A simple way of obtaining precipitation lifetimes from the diffusion coefficients is also given, using a shooting method. The lifetimes and steady state fluxes are computed, leading to shorter lifetimes and lower fluxes than previously reported, for energies above 500 keV and McIlwain parameter  $L$  greater than 3.

## Introduction

Pitch angle scattering of radiation belt electrons by plasmaspheric hiss is of continuing interest. Although two decades old, the formulation of Lyons *et al.* [1972], in terms of a bounce-averaged quasi-linear pitch angle diffusion coefficient [Lyons *et al.*, 1971], remains standard. A key innovation of the earlier work was the retention, in principle, of all harmonics to account for resonant interactions at all latitudes. However, the numerical results included only a limited number (namely,  $-5 \leq n \leq 5$ ), since even with a drastically simplified dispersion relation for the whistlers, the evaluation of these diffusion coefficients can be computationally expensive (L. R. Lyons, personal communication, 1993). Here some analytical techniques are used that reduce the computations to manageable levels, making it feasible to include as many cyclotron harmonics terms as required to obtain any specified accuracy. Keeping more harmonics naturally leads to larger diffusion coefficients. It is also shown how to use them to obtain precipitation lifetimes, using a shooting method. Lifetimes and the resulting steady state fluxes are recomputed with the full range of cyclotron harmonics, for a specific set of wave parameters, leading to shorter precipitation lifetimes and lower flux levels.

The expressions for the diffusion coefficients are double integrals over latitude  $\lambda$  and wave-normal angle  $\theta$ , summed over all cyclotron resonance numbers  $n$ , plus the Landau term  $n = 0$ . At each  $\lambda$ , only a few harmonics contribute, and only for restricted ranges of  $\theta$ ; thus there can be much wasted computation of terms

in regions where their contributions are negligible. Because the interactions take place for wide and overlapping ranges of  $\lambda$ ,  $n$ , and  $\theta$ , it is unsatisfactory to try to simply estimate which terms seem to be unimportant, in an ad hoc fashion. Instead, by exploiting the tractable form of the functions used to model the waves, analytical upper bounds can be used to identify regions of integration whose results are guaranteed in advance to be less than a given value, and rigorously reject them. Computer time is then spent only on significant contributions. The effect of the additional harmonics is found to be significant for the outer electron belt, at energies above 500 keV.

## Upper Bounds

With a few additions, the underlying physical formulation and notation are the same as that of Lyons *et al.* [1972]. Wave energy is distributed in frequency  $\omega$  as a Gaussian centered at  $\omega_m$  with width  $\delta\omega$  and lower cutoff  $\omega_{LC}$ , and distributed over  $\theta$  with weight  $\exp(-\tan^2 \theta / \tan^2 \theta_w)$ . The Earth's magnetic field is represented as a dipole, with strength  $B_0 = B_{eq} h(\lambda) = (0.31 G/L^3) h(\lambda)$ , where  $L$  is the usual McIlwain parameter and  $h(\lambda)$  is the dipole function  $(1 + 3 \sin^2 \lambda)^{1/2} / \cos^6 \lambda$ . The local pitch angle  $\alpha$  is given in terms of  $\lambda$  and the equatorial pitch angle  $\alpha_0$  by  $\sin^2 \alpha / \sin^2 \alpha_0 = h(\lambda)$ . The quantity  $\Omega_e$  is the magnitude of the cyclotron frequency of a nonrelativistic electron and has the value  $\Omega_{eq}$  at the equator, so that  $\Omega_e = \Omega_{eq} h(\lambda)$ . A useful quantity is  $P_{\parallel,m}$ , given by  $P_{\parallel,m}^2 = m_e (\Omega_e / \omega_m) (B_0^2 / 4\pi N)$ , where  $m_e$  is the electron rest mass and the cold electron density  $N$  depends on  $L$  only. This is approximately the parallel momentum  $P_{\parallel}$  required for primary cyclotron resonance with a wave of frequency  $\omega_m$  and  $\theta = 0$ .  $P_m$  is further defined as  $P_{\parallel,m}$  at  $\lambda = 0$ , so that  $P_{\parallel,m} = P_m h^{3/2}(\lambda)$ . In the whistler dispersion relation, all terms of order  $\omega / \Omega_e$  and  $\Omega_i / \omega$  have been dropped.

The diffusion coefficient  $D(\alpha_0)$  is computed via relativistic quasi-linear theory, for fixed energy  $E$ ,  $L$ , and  $\alpha_0$ . It is written as

$$D(\alpha_0) = \int_0^{\lambda_m} d\lambda \sum_{n \neq 0} \hat{D}_2(\lambda) W_2(\lambda, n) + \int_0^{\lambda_m} d\lambda \hat{D}_3(\lambda) W_3(\lambda), \quad (1)$$

where the mirror latitude  $\lambda_m$  is given by  $h(\lambda_m) = 1/\sin^2 \alpha_0$ .  $W_2$  and  $W_3$  are integrals over  $\theta$ , and  $\hat{D}_2$  and  $\hat{D}_3$  are independent of  $\theta$ , given by

$$\left\{ \begin{array}{l} \hat{D}_2 \\ \hat{D}_3 \end{array} \right\} = \left[ \frac{\sqrt{\pi}}{2} \frac{B_w^2}{B_{eq}^2} \frac{\Omega_{eq}}{\gamma} \frac{P_m}{P} W_1 \right] \times \frac{\cos^7 \lambda}{T(\alpha_0) \cos^2 \alpha_0} \left\{ \begin{array}{l} \sqrt{g} \\ \cos \alpha \sin^2 \alpha \end{array} \right\}. \quad (2)$$

$W_2$  and  $W_3$  are defined below.  $T(\alpha_0) = 1.30 - 0.56 \sin \alpha_0$  is an approximation to the mirror latitude dependence of the bounce period, and  $W_1$  is a normalization integral that depends only on the wave parameters  $\omega_m$ ,  $\omega_{LC}$ ,  $\delta\omega$ , and  $\theta_w$ :

$$\frac{1}{W_1} = \frac{\delta\omega}{\omega_m} \left[ 1 + \operatorname{erf} \left( \frac{\omega - \omega_m}{\delta\omega} \right) \right] \times \int_1^\infty dx \exp \left[ - \left( \frac{x^4 - 1}{\tan^2 \theta_w} \right) \right] \quad (3)$$

Upper bounds on  $W$  are used in the following way, where  $W$  refers to either  $W_2$  or  $W_3$ . Regardless of its details, any conventional numerical algorithm for performing the integrals requires evaluating  $W$  many times at different values of  $\lambda$  and  $n$ , and summing the results weighted by some  $\delta\lambda$ . Because  $W$  is itself an integral over  $\theta$ , these evaluations are very time-consuming. If  $W$  is known in advance to be less than some appropriate minimum value  $W_{\min} = D_{\min}/\hat{D}\delta\lambda$ , one can simply set it to zero and proceed to the next value of  $\lambda$ . Initially, one sets  $D_{\min}$  to be less than some physically reasonable minimum value of interest. It is then updated after each nonzero increment to  $D(\alpha_0)$  to be no more than a small fraction, say  $10^{-4}$ , of the value of  $D(\alpha_0)$  obtained so far. Actually, instead of  $D_{\min}/\hat{D}\delta\lambda$ , it is convenient to use the more conservative value  $W_{\min} = D_{\min}/\hat{D}\lambda_m$ .

The upper bounds will be presented in some detail. The reader may then use them to reperform the calculations for different particle energies, etc., and using different wave parameters, which may vary greatly with circumstances.

### Cyclotron Terms

For cyclotron terms, because of the simplified dispersion relation used, the resonant frequency has the form  $\omega = \omega_2 \sec \theta$ , where  $\omega_2(\lambda) = \omega_m(nP_{\parallel,m}/P_{\parallel})^2$ .  $W_2$  can be expressed as an integral over  $x = \sec \theta$ :

$$W_2 = \sqrt{\frac{\omega_2}{\omega_m}} e^{\Delta} \int_{x_{\min}}^\infty dx x^{\frac{1}{2}} \exp[-\beta(x - x_0)^2] \Phi_n(x), \quad (4)$$

where  $\beta = (\omega_2/\delta\omega)^2 + 1/\tan^2 \theta_w$ ,  $x_0 = \omega_m\omega_2/\beta(\delta\omega)^2$ , and  $\Delta = \beta(1 + x_0^2) - [(\omega_m/\delta\omega)^2 + (\omega_2/\delta\omega)^2]$ . The lower limit  $x_{\min}$  is the larger of  $\omega_{LC}/\omega_2$  and 1, which ensures that  $\omega \geq \omega_{LC}$ .

The term  $\Phi_n$  is defined as a combination of Bessel functions of the first kind, namely  $\Phi_n = [\cos^2 \frac{\theta}{2} J_{n+1} + \sin^2 \frac{\theta}{2} J_{n-1}]^2$ , with argument  $n \tan \alpha \tan \theta$ . Of course, to do the integration,  $\Phi_n$  must be expressed in terms of  $x$ . Note, however, that since the absolute value of each Bessel function is less than or equal to unity, so is  $\Phi_n$ . Setting  $\Phi_n$  to 1 thus gives an upper bound on  $W_2$ . Furthermore, as  $x$  is integrated out to infinity, the Bessel functions will go through their peaks, which decline from unity slowly with large  $x$ , so that the upper bound may not be a large overestimate. Physically, the simplified dispersion relation allows a resonant wave frequency for every possible value of wave-normal angle, but there is significant wave energy only for  $\omega$  greater than  $\omega_{LC}$  and within  $\delta\omega$  of  $\omega_m$ , and for  $\theta$  less than  $\theta_w$ . The upper bound accounts for these energy weightings but not the efficiency of the particle coupling with each mode, which is described by  $\Phi_n$ .

This upper bound is itself bounded above by an integral that is expressible in closed form in terms of standard special functions. The resulting expression for  $W_2^{UB}/V_2$  is

$$\Gamma\left(\frac{3}{4}, y_{\min}^2\right), \quad y_0 \leq y_{\min} \\ \Gamma\left(\frac{3}{4}, y_0^2\right) + \sqrt{\pi} y_0 [\operatorname{erf}(y_0) - \operatorname{erf}(y_{\min})], \quad y_0 > y_{\min} \quad (5)$$

where  $y_0 = \beta^{\frac{1}{2}} x_0$ ,  $y_{\min} = \beta^{\frac{1}{2}} (x_{\min} - x_0)$ , and  $V_2 = \sqrt{\omega_2/2\omega_m} e^{\Delta}/\beta^{\frac{3}{4}}$ . While  $y_0$  must be positive,  $y_{\min}$  need not be. For  $n$  large enough that  $\omega_2$  is larger than  $\omega_{LC}$ ,  $2\omega_m$ , and  $\omega_m + \delta\omega$ , the upper bound is less than  $(\delta\omega/2\omega_m)^{3/2} \exp[(\{\omega_2 - \omega_m\}/\delta\omega)^2]$ . This gives a  $\lambda$ -dependent upper limit on the number of harmonics that must be considered:  $W_2$  is guaranteed negligible for  $|n|$  greater than

$$n_{\max} = \frac{P_{\parallel}}{P_{\parallel,m}} \sqrt{1 + \frac{\delta\omega}{\omega_m} \sqrt{\log \left[ \left( \frac{\delta\omega}{2\omega_m} \right)^{3/2} \frac{1}{W_2^{\min}} \right]}}. \quad (6)$$

Furthermore, it is straightforward to derive a generalization of (4) for finite subintervals of  $x$ .

### Landau Term

For  $n = 0$ , the resonant frequency takes the form  $\omega = \omega_3 \cos \theta$ , where  $\omega_3(\lambda) = \omega_m(P_{\parallel}/\gamma P_{\parallel,m})^2 (\Omega_e/\omega_m)^2$  and can be written as  $\omega_3^{(0)} \cos^2 \alpha/g(\lambda)$ , with  $\omega_3^{(0)}$  independent of  $\lambda$ .  $W_3$  can be expressed as an integral over  $z = \cos \theta$ :

$$W_3 = \exp \left[ \left( \frac{1}{\tan^2 \theta_w} - \frac{\omega_m}{\delta\omega} \right)^2 \right] \times \int_{z_{LC}}^1 dz z^{\frac{1}{2}} \exp \left[ - \left( a_1 z^2 - 2a_2 z + \frac{a_3}{z^2} \right) \right] \Psi_0(z), \quad (7)$$

where  $a_1 = (\omega_3/\delta\omega)^2$ ,  $a_2 = \omega_3\omega_m/(\delta\omega)^2$ , and  $a_3 = 1/\tan^2 \theta_w$ . The lower limit  $z_{LC}$  is  $\omega_{LC}/\omega_3$ , and the

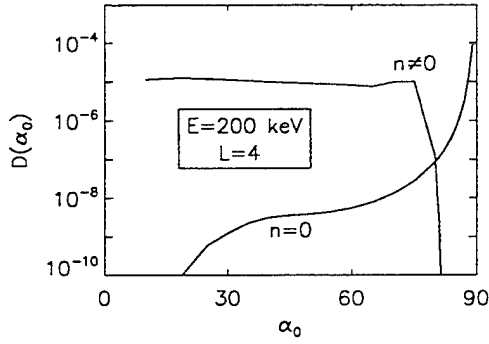


Figure 1. Cyclotron and Landau contributions to the diffusion coefficient  $D(\alpha_0)$  for  $E = 200$  keV,  $L = 4$ . For  $\alpha_0$  below  $80^\circ$ , the Landau term is negligible.

integral is zero for  $z_{LC} \geq 1$ . This vanishing of the Landau damping term occurs for values of  $\lambda$  greater than  $\lambda_L$ , where  $h(\lambda_L) = 1/[\sin^2 \alpha_0 + (\omega_{LC}/\omega_3^{(0)})]$ . Because  $h(\lambda)$  is a strictly increasing function,  $\lambda_L$  is less than  $\lambda_m$ .

The term  $\Psi_0$  differs from Lyons'  $\Phi_0$  by a factor of  $\cos^2 \theta$  and is given by  $[J_1(\eta) - (\cot^2 \alpha/\gamma)\eta J_0(\eta)]^2$ , where  $\eta = \eta_0 \sin \theta$  and  $\eta_0 = \gamma(\omega_3^{(0)}/\Omega_e) \tan \alpha$ . The factor  $\Psi_0$  is bounded above by  $[j_1 + (\cot^2 \alpha/\gamma)\eta_0 j_0]^2$ , where  $j_0$  is an upper bound for  $J_0(\eta)$  and  $j_1$  is an upper bound for  $J_1(\eta)$ . A permissible value for  $j_0$  and  $j_1$  is unity, but in some cases one can do much better. If  $\eta_0$  is less than the location of the first peak of  $J_1(\eta)$ , namely  $\eta = 1.841$ , then  $J_1(\eta_0)$  can be used for  $j_1$ . Similarly, if  $\eta_0$  is less than 1.256, where  $\eta J_0(\eta)$  reaches its first peak, then  $J_0(\eta_0)$  can be used for  $j_0$ .

An upper bound is still required for the integral of

$$I(z) = z^{\frac{1}{2}} \exp(-a_1 z^2) \exp(2a_2 z) \exp\left(-\frac{a_3}{z^2}\right), \quad (8)$$

which describes the distribution of wave energy in  $\theta$  and  $\omega$ . Unfortunately, no single approximation is satisfactory for all possible values of  $a_1$ ,  $a_2$ , and  $a_3$ . Several different upper bounds may be derived, by a variety of methods. The integral left after replacing  $\exp(-a_3/z^2)$  by  $\exp(-a_3)$  is of the same form as the finite interval version of the upper bound in (5) for the cyclotron terms. Another useful bound is

$$\max \left[ \exp(-a_1 z^2 + 2a_2 z) \right] \int_{z_{LC}}^1 dz z^{\frac{1}{2}} \exp\left(-\frac{a_3}{z^2}\right), \quad (9)$$

which may be evaluated in closed form. For the parameters tested, the most powerful bound turns out to be simply  $\max[I(z)] (1 - z_{LC})$ . Finding the maximum of  $I(z)$  requires an iterative solution for the zero of its derivative; one can easily show that there is exactly one such zero, and that it is bracketed by the smallest and largest of  $3a_2/a_1$ ,  $(3a_3/4)^{1/4}$ , and  $(3/4a_1)^{2/3}$ . The Cauchy-Schwarz inequality and its generalizations may also be used to obtain upper bounds. Of course, one tests each bound against the minimum value of interest before computing any others. The cost of computing these bounds is far outweighed by the savings of skipping unnecessary integrations of the full expression for  $W_3$ .

## Use of the Upper Bounds

As a concrete illustration, Figure 1 shows the separate contributions to  $D(\alpha_0)$  from  $n = 0$  and from  $n \neq 0$ , for the particular case  $E = 200$  keV,  $L = 4$ . The same parameters were used by Lyons *et al.* [1972], namely,  $\omega_m/2\pi = 600$  Hz,  $\delta\omega/2\pi = 300$  Hz,  $\omega_{LC}/2\pi = 300$  Hz,  $\tan \theta_w = 5$ ,  $B_w = 35 m\gamma$ , and electron density  $N = 1000 (4/L)^4 \text{ cm}^{-3}$ . The diffusion coefficients are significant for a wide range of  $n$  and  $\alpha_0$ . Figure 2 shows the situation at  $\alpha_0 = 80^\circ$ , where the cyclotron and Landau contributions are comparable. The full cyclotron part of  $D(\alpha)$  was computed as an integral over  $\lambda$  according to (1). It was then used to determine, at each  $\lambda$ , the level  $W_3^{\min}$  which  $W_3$  must exceed for its contribution to the Landau term to be nonnegligible. The endpoint  $\lambda_L$  is  $4.7^\circ$ , and the analytical upper bound for  $W_3$  indicates that  $W_3$  is of no interest below about  $\lambda = 4.4^\circ$ . Also shown is the actual value of  $W_3$ , revealing that  $W_3$  is in fact significant only for  $\lambda$  greater than about  $4.6^\circ$ . For lower  $\lambda$ , its evaluation is a wasted effort. For lower values of  $\alpha_0$ , the upper bounds successfully predict that  $W_3$  is negligible for all  $\lambda$ , in agreement with Figure 1 which shows that then the total Landau term is much smaller than the cyclotron term and need not be computed.

## Precipitation Lifetimes and Fluxes

The pitch angle diffusion coefficients are of direct interest in themselves, but perhaps more important is their effect on the radial profiles of the flux distribution. An equation can be written for the phase space distribution as a function of  $L$ ,  $\mu$ , and  $\alpha_0$ , but it is simpler and often sufficient to consider the flux of equatorially mirroring particles only. This is accomplished by using a precipitation lifetime for particles to pitch angle scatter into the loss cone, which reduces the di-

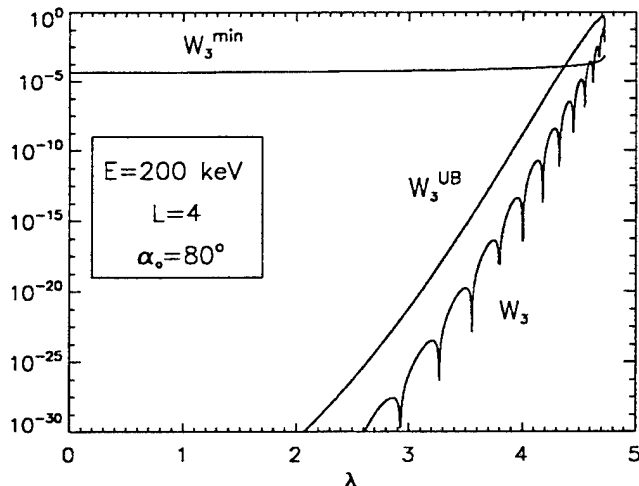


Figure 2. The exact  $W_3(\lambda)$ , and its upper bound. Also shown is the minimum value below which the contribution of  $W_3$  to the Landau part of  $D(\alpha_0)$  is negligible compared to the total cyclotron part.

dimensionality of the problem while retaining much of the essential physics.

### Lifetimes

In the formulation of Lyons *et al.* [1972], the bounce-averaged electron distribution function  $f$  is assumed to be factorizable into  $F(t) g(\alpha_0)$ , which allows the separation of variables in the pitch angle diffusion equation and the identification of the precipitation lifetime  $\tau$  with  $F/(dF/dt)$ . A complicated nonlinear integral equation is found for  $g$ , involving the previously determined diffusion coefficients  $D(\alpha_0)$ . Once  $g$  is found,  $\tau$  can be determined. Here a simpler, alternate procedure is presented which only requires solving ordinary differential equations (ODEs), not integral equations. Invoking the separation of variables,  $g$  satisfies

$$\frac{d}{d\alpha_0} \left[ DT \sin 2\alpha_0 \frac{dg}{d\alpha_0} \right] + \frac{T \sin 2\alpha_0}{\tau} g = 0, \quad (10)$$

where  $T(\alpha_0)$  is the  $\alpha_0$ -dependent part of the bounce period as given earlier, and  $\tau$  is still to be found. The boundary conditions (BCs) used by Lyons are

$$g(\alpha_L) = 0, \quad (11a)$$

$$\frac{dg}{d\alpha_0} \left( \frac{\pi}{2} \right) = 0, \quad (11b)$$

$$2 \int_{\alpha_L}^{\pi/2} g \sin \alpha_0 d\alpha_0 = 1, \quad (11c)$$

where  $\alpha_L$  is the loss cone pitch angle, given by  $\sin \alpha_L = [4L^5(L - \frac{3}{4})]^{-1/4}$ . For any choice of  $\tau$ , a solution of the second-order ODE is determined by two BCs; only for the desired value of  $\tau$  is the third satisfied as well.

The problem can be recast as a two-point boundary value problem (BVP) for the variables

$$z_1 = 2 \int_{\alpha_L}^{\alpha_0} g(\alpha) \sin \alpha d\alpha, \quad (12a)$$

$$z_2 = D\tau T \sin 2\alpha_0 \frac{dg}{d\alpha_0}, \quad (12b)$$

$$z_3 = g(\alpha_0), \quad (12c)$$

$$z_4 = 1/D\tau, \quad (12d)$$

which obey

$$z_1' = 2z_3 \sin \alpha_0, \quad (13a)$$

$$z_2' = -z_3 T \sin 2\alpha_0, \quad (13b)$$

$$z_3' = \frac{z_2 z_4}{T \sin 2\alpha_0}, \quad (13c)$$

$$z_4' = -(D'/D) z_4, \quad (13d)$$

where the primes mean  $d/d\alpha_0$ . In these variables, the BCs of (11) become

$$z_1 \left( \frac{\pi}{2} \right) = 1, \quad z_2 \left( \frac{\pi}{2} \right) = 0, \quad (14a)$$

$$z_1(\alpha_L) = 0, \quad z_3(\alpha_L) = 0. \quad (14b)$$

The effect of pitch angle scattering on the phase space distribution function has been considered in more detail by Retterer *et al.* [1983], who derive an equation for  $g$

inside the loss cone, which will not be empty if scattering into it is strong enough. Treating the loss cone as a boundary layer, they derive a simple expression for the asymptotic behavior of  $g$  as a function of  $u(\alpha_0) = \sin^2 \alpha_0 / 2DT$  in the limit  $u \gg u_L$ , where  $u_L = u(\alpha_L)$ . This has the form  $g/g_0 = \log(u/u_L) + A(u_L)$ , where  $g_0$  is an undetermined constant and the function  $A(u)$  is obtained numerically. The quantity  $u_L$  indicates the size of the loss cone relative to the strength of the scattering. The logarithmic derivative of this expression for  $g$  is matched to that of the solution of (10) at  $\alpha_L$ , which gives, in place of the fourth BC in (14), the condition  $z_3(\alpha_L) = \hat{A} z_2(\alpha_L) z_4(\alpha_L)$ , where  $\hat{A} = A(u_L) / \{4 \cos^2 \alpha_L - \sin 2\alpha_L [T'/T(\alpha_L) + D'/D(\alpha_L)]\}$ . In principle, the first BC in (14) should be modified as well, but we can neglect this as long as the fraction of particles in the loss cone is small.

With either set of BCs, the BVP can be solved by a shooting method, in which, in essence, one integrates the ODEs from  $\pi/2$  to  $\alpha_L$  using an initial guess for  $z_3$  and  $z_4$  at  $\pi/2$ , and then adjusts the guesses based on how nearly the BCs at  $\alpha_L$  are satisfied, repeating until convergence. Standard algorithms exist which make this adjustment efficiently [Press *et al.*, 1992]. The shooting, or integration, is done from  $\pi/2$  to  $\alpha_L$  because in this direction the true  $g$ , and errors in the trial  $g$ , exponentially decrease rather than increase. The procedure works quickly and reliably, typically converging in five or six iterations. Of course, once  $z_4$  is found,  $\tau$  is given by  $1/Dz_4$  evaluated at any  $\alpha_0$ . The distribution function profile  $g(\alpha_0)$  is also obtained, being given by  $z_3$ .

Figure 3 shows the lifetimes obtained using the same parameter values as Figure 1, considering cyclotron harmonics up to  $n = \pm 100$ , which is found to be sufficient to include all non-negligible terms. The results originally published by Lyons *et al.* kept  $n$  only up to  $\pm 5$ , due to computational limitations. For energies above 500 keV and  $L$  larger than about 3, the additional harmonics lead to significantly shorter precipitation lifetimes. The BCs of (14) were used, but using the boundary conditions of Retterer *et al.* instead made no appreciable

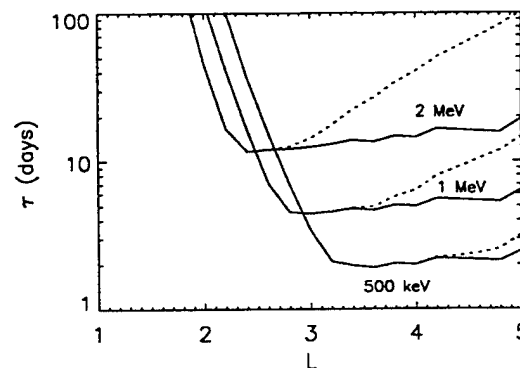


**Figure 3.** Precipitation lifetimes from diffusion coefficients computed using a maximum of  $n = \pm 100$  (solid curves) or  $n = \pm 5$  (dotted curves).

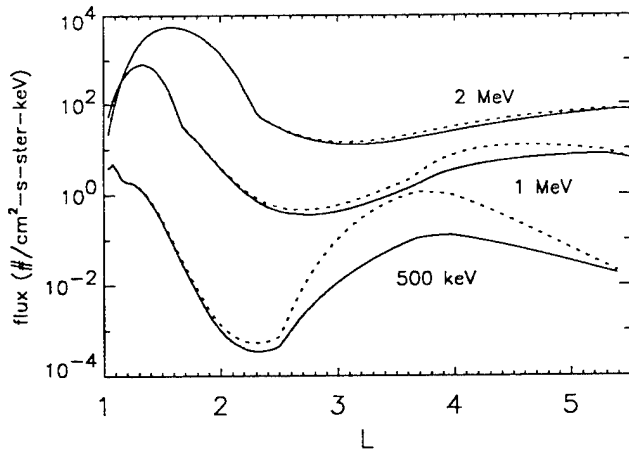


**Figure 4.** Steady state fluxes using precipitation lifetimes from diffusion coefficients computed using a maximum of  $n = \pm 100$  (solid curves) or  $n = \pm 5$  (dotted curves).

difference, due to the weakness of the diffusion relative to the loss cone size, as reflected by large values of  $u_L$ .

### Steady State Fluxes

Lyons and Thorne [1973] model the steady state flux for equatorially mirroring particles as a function of  $L$  and energy by imposing a flux level at an outer boundary and finding a balance between radial diffusion and losses due to precipitation and Coulomb scattering. The distribution function  $f$ , which determines the flux, is given by

$$\frac{\partial f}{\partial t} = 0 = L^2 \frac{\partial}{\partial L} \left( \frac{D_{LL}}{L^2} \frac{\partial f}{\partial L} \right) - \left( \frac{1}{\tau} + \frac{1}{\tau_c} \right) f. \quad (15)$$

Here  $\tau$  is the precipitation lifetime discussed directly above, and the Coulomb scattering lifetime is modeled by  $\tau_c = 3 \times 10^8 [E(\text{MeV})]^{3/2} / N(L)$ . The radial diffusion coefficient  $D_{LL}$  is due to electric field fluctuations  $\delta E$  at the azimuthal drift frequency  $\omega_D$ , whose autocorrelation is assumed to have a rapid rise and exponential decay time  $T$  [Cornwall, 1968] and is given by

$$D_{LL} = \left( c \frac{\delta E}{B} \right)^2 \frac{T/4}{1 + (\omega_D T/2)^2}.$$

Equation (15) is simply a one-dimensional diffusion equation for  $f(L, \mu)$  at each value of  $\mu$ , and can be solved by standard finite differencing, with  $f(L, \mu)$  then converted to flux  $j(L, E)$ . For a given value of  $\mu$ , Coulomb scattering is only effective at low  $L$ , while pitch angle scattering is responsible for increasing depletion of  $f$  at larger  $L$ . This, combined with energization of particles as they diffuse inward in  $L$  at constant  $\mu$ , generates the slot region of  $j(L, E)$  as shown in Figure 4 (with the whistler amplitude  $B_w$  set to  $10 \text{ m}\gamma$ ,

$\delta E = 0.1 \text{ mV/m}$ , and  $T = 45 \text{ min}$ ). Compared to the corresponding results of Lyons and Thorne [1973], the shorter lifetimes naturally lead to lower flux levels, although the results are qualitatively similar.

### Summary

We have retained the original formulation of the bounce-averaged quasi-linear electron pitch angle diffusion coefficient, which has proven quite successful, even with its greatly simplified whistler dispersion relation. A key point of that work was that all cyclotron harmonics must be considered, not just the primary one. We have presented a method of making this principle practical, by avoiding much of the evaluation of negligibly small contributions while concentrating on the important ones. We have also presented a simple procedure for obtaining precipitation lifetimes from the diffusion coefficients, which can be used to find the distribution of equatorially mirroring particles,  $f(L, \mu)$ . Earlier calculations of these quantities have been improved, leading to modified lifetimes and fluxes of high-energy electrons in the outer radiation belt.

**Acknowledgments.** The author thanks L. Lyons for a helpful discussion and for making available his notes on the derivations of his previous work, and J. Retterer for pointing out the applicability of his boundary layer analysis of the loss cone.

The Editor thanks P. B. Dusenbery and another referee for their assistance in evaluating this paper.

### References

- Cornwall, J. M., Diffusion processes influenced by conjugate-point wave phenomena, *Radio Sci.*, **3**, 740, 1968.
- Lyons, L. R., R. M. Thorne, and C. F. Kennel, Electron pitch angle diffusion driven by oblique whistler-mode turbulence, *J. Plasma Phys.*, **6**, 589, 1971.
- Lyons, L. R., R. M. Thorne, and C. F. Kennel, Pitch angle diffusion of radiation belt electrons within the plasmasphere, *J. Geophys. Res.*, **77**, 3455, 1972.
- Lyons, L. R. and R. M. Thorne, Equilibrium structure of radiation belt electrons, *J. Geophys. Res.*, **78**, 2142, 1973.
- Press, W. H., S. A. Teukolsky, W. T. Vetterling, and B. P. Flannery, *Numerical Recipes*, Cambridge University Press, New York, 1992.
- Retterer, J. M., J. R. Jasperse, and T. S. Chang, A new approach to pitch angle scattering in the magnetosphere, *J. Geophys. Res.*, **88**, 201, 1983.

J. M. Albert, Center for Electromagnetics Research, Northeastern University, Boston, MA 02115.

(Received March 29, 1994; revised July 25, 1994; accepted September 2, 1994.)

# Proton-Whistler Interactions in the Radiation Belts

*E. Villalón<sup>1</sup> and W.J. Burke<sup>2</sup>*

<sup>1</sup>Center for Electromagnetics Research, Northeastern University,  
Boston, MA 02115, USA

<sup>2</sup>Geophysics Directorate, PL/OL-AA, Hanscom AFB, MA 01731

The interactions of whistlers with radiation belt protons is investigated. In the inhomogeneous geomagnetic field, near the equator, the spacing between cyclotron resonances is very small. After crossing multiple harmonic resonances, a significant change of particle energy takes place, and the protons pitch-angle scatter toward the atmospheric loss cone. A test-particle hamiltonian formalism is investigated for first and second order resonant protons. Quasilinear theory is applied for first-order resonant particles to obtain bounce-averaged, diffusion coefficients. The Fokker Planck equation, containing pitch-angle, energy and the cross energy/ pitch-angle diffusion terms, is investigated to calculate diffusion life times.

## I. INTRODUCTION

We consider the interaction of plasmaspheric electrons and protons with whistler waves. The particles are trapped within the earth's radiation belts moving back and forth along field lines between magnetic mirror points. We call  $\tau_B$  the bounce period, the time required for a particle to go from one mirror point to the other and return. In the region of interest, the geomagnetic field,  $B_0$ , is described as a dipole. The interaction region is limited to the plasmasphere,  $L < 4$ , where  $L$  is the equatorial distance of the field line measures in Earth radii ( $R_E$ ). The plasmasphere is made up of cold particles of ionospheric origin whose distribution is isotropic and Maxwellian. During magnetic storms the radiation belts fill with energetic, trapped particles whose density is much smaller than that of the cold plasma. Whistlers are right-hand polarized electromagnetic waves whose magnetic field,  $|B_1| \ll B_0$ . Often they propagate in field-aligned ducts due to density depletions in local flux tubes. They can either be launched from ground sources or be generated in the plasmasphere. The dielectric properties for wave propagation are determined by the magnetized cold plasma distribution. These waves interact with the energetic particles, if the Doppler-shifted frequency of the waves is some harmonic of the gyrofrequency. For electron-whistler interactions the waves and particles travel in opposite directions. For protons they travel in the same direction and the wave phase velocity is very close to the proton parallel velocity. The situation is depicted in the Figure 1.

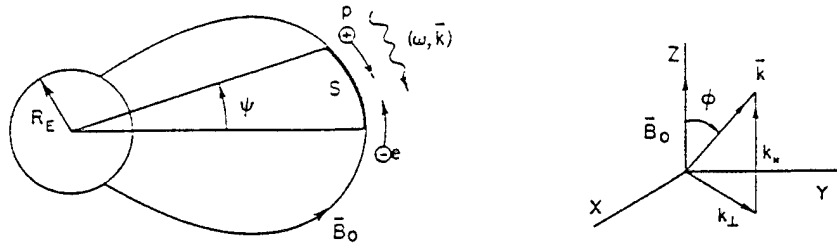


Figure 1. Schematic representation of whistler  $(\omega, \vec{k})$ , interacting with electrons and protons near the equator. The coordinate system used in this paper is depicted here.

Whistler-electron interactions have been extensively studied over the years<sup>1,2,3</sup>. The electrons typically have energies between 10 to 50 keV. The interaction occurs mainly at the first gyroharmonic of the electron gyrofrequency, although higher gyroharmonics may also be important<sup>4</sup>. The electron energies change very little during these interactions. The electron pitch angle is  $\theta$ , where  $\tan \theta = v_\perp/v_\parallel$ , the ratio between the parallel and perpendicular components of the particle velocity. The pitch angle can be significantly changed and, as a result, the particle is scattered into the loss cone and precipitates into the ionosphere. Because large numbers of electrons interact with the waves, they grow in amplitude to values whose limits depend on the degree of anisotropy of the electron distribution function<sup>2</sup>. Detailed analyses are given in the papers by Villalón and coworkers<sup>4,5</sup>. These investigations were based on relativistic, quasilinear theory that simultaneously considers wave growth and particle depletion from the radiation belts.

Proton-whistler interactions have not received as much attention. Recent experiments have shown<sup>6,7</sup> that protons whose energies are in the hundreds of keV range, can be scattered from the radiation belts by analogous interactions. The frequency of the wave must be close to the equatorial electron gyrofrequency. The particle energy changes significantly during the interactions<sup>8</sup>. Thus, the changes in pitch angle are due to both direct pitch angle and energy diffusion. Because of the small population of high-energy protons we neglect their effects on the amplitudes of the waves. We present a study of proton whistler interactions by using a test particle formalism and a statistical approach based on the Fokker-Planck equation. In Sec. II, we present the main dielectric properties of whistler waves; because the whistler proton interactions require large refractive indices, we limit ourselves to the pararesonance mode<sup>9</sup>. Sec. III presents the resonance condition for multiple harmonics of the gyrofrequency. The geomagnetic latitudes of high harmonic resonances are obtained based on a parabolic approximation for the near equatorial geomagnetic field. We show that the distance between subsequent resonances is very small. The crossing of multiple resonances near the equator makes the interactions very effective<sup>10</sup>. Sec. IV contains the equations for the test particle in a varying geomagnetic field using

hamiltonian formalism. Sec V studies the evolution of the action ( $I$ ) angle ( $\xi_L$ ) variables as function of the distance ( $s$ ) along the flux tube using Taylor expansions around isolated resonances. Let us expand  $\xi_L$  around the equator:  $\xi_L(s) = \xi_L(0) + \xi_L^{(1)}s + \xi_L^{(2)}s^2$ . First-order resonant particles are such that  $\xi_L^{(1)} = 0$  (i. e., at the equator  $d\xi_L/ds = 0$ ). This is the resonance condition as given in Eq. (5). The second-order term  $\xi_L^{(2)} \sim dB_0/ds + O(B_k)$ . For large wave amplitudes  $O(B_k)$  is larger than the contribution of the inhomogeneous geomagnetic field  $dB_0/ds$ . In this case, we say that protons which are in gyroresonance (i. e.  $\xi_L^{(1)} = 0$ ), satisfy the second-order resonance condition. This is because to zero order in the electric field amplitudes  $d\xi_L/ds = d^2\xi_L/ds^2 \simeq 0$ . For first-order resonant particles, the change in action is proportional to the electric field amplitude. For second-order resonant protons the change in action is proportional to the square root of the electric field amplitude. The second-order resonance condition is met when the field amplitude is large<sup>11,12</sup>, the threshold is calculated in this paper. Sec. VI contains a quasilinear formulation for the distribution function of first order resonant protons. We assume that the protons are unmagnetized in time scales of the order of  $2\pi/\omega$ , where  $\omega$  is the frequency of the whistler wave. They are magnetized in times comparable to the bounce period. Because diffusion occurs over many bounce periods, we average the diffusion equation along the flux tube. The bounce averaged, Fokker-Planck equation contains the diffusion coefficients for the pitch angle, energy, and the cross energy/ pitch angle terms. These coefficients are shown to have the same orders of magnitude. We reduce the equation to a one-dimensional diffusion equation to be solved for the energy part of the distribution function. This eigenvalue equation gives the diffusion life-times of protons in the radiation belts.

## II. QUASI-ELECTROSTATIC WHISTLER WAVES

We consider a whistler wave of frequency  $\omega$  and wave vector  $\mathbf{k}$ , propagating in a field aligned duct. The geomagnetic field  $B_0$  is along the  $z$  direction and  $\phi$  is the angle between  $\mathbf{k}$  and  $B_0$ . The dispersion relation for the refractive index  $\eta = ck/\omega$  is

$$\eta^2 = 1 + \frac{(\omega_p/\omega)^2}{(\Omega_e/\omega) |\cos \phi| - 1} \quad (1)$$

where  $\omega_p$  and  $\Omega_e$  are the electron plasma and gyro frequencies, respectively.

The electric fields components are denoted by  $\mathcal{E}_z = \mathcal{E}_1$ ,  $\mathcal{E}_y = i\mathcal{E}_2$ , and  $\mathcal{E}_x = -\mathcal{E}_3$ , where

$$\frac{\mathcal{E}_2}{\mathcal{E}_1} = \frac{1}{\eta^2 - 1} \frac{(\omega_p/\omega)^2}{(\Omega_e/\omega) - |\cos \phi|} \quad (2)$$

$$\frac{\mathcal{E}_1}{\mathcal{E}_3} = \frac{1 - (\omega_p/\omega)^2 - (\eta \sin \phi)^2}{\eta^2 \sin \phi \cos \phi} \quad (3)$$

For the case where  $\omega \sim \Omega_e(L)|\cos \phi|$ , the equatorial refractive index  $\eta^2(L) \gg 1$ , then  $\mathcal{E}_2/\mathcal{E}_1 \ll 1$ , and  $\mathcal{E}_1/\mathcal{E}_3 \sim -\sin \phi / \cos \phi$ . The wave becomes quasi-electrostatic, i.e.  $\mathbf{E}$  is



in the direction of  $\mathbf{k}$ , and the group velocities  $v_g \sim 1/\eta$  are very small. These waves can interact with protons which energies are in the hundreds of keV.

Near the equator, the Earth's magnetic field approximates a parabolic profile

$$\frac{\Omega}{\Omega(L)} = 1 + \left(\frac{s}{r_L}\right)^2 \quad (4)$$

where  $s \simeq R_E L \psi$ ,  $R_E$  is the Earth's radius,  $L$  is the magnetic shell and  $\psi$  is the geomagnetic latitude (see the figure), and  $r_L = (\sqrt{2}/3)R_E L$ . The equatorial gyrofrequency is  $\Omega(L)$ ;  $\Omega$  stands for the gyrofrequencies either for electrons or protons, along the field line.

### III. RESONANT PROTON-WHISTLER INTERACTIONS

For whistler waves to interact strongly with protons near equatorial regions, they must satisfy the resonance condition

$$\omega - k_{\parallel} v_{\parallel} - \ell \Omega_p = 0 \quad (5)$$

where,  $\ell = 0, 1, 2, \dots$ ;  $\Omega_p$  is the proton gyrofrequency, and  $k_{\parallel}$  and  $v_{\parallel}$  are the parallel components of the wave vector and particle's velocity, respectively. We call  $\mu = \sin^2 \theta_L$ , where  $\theta_L$  is the equatorial pitch angle. Here  $\theta_L > \theta_c(L)$ , where  $\theta_c(L)$  is the pitch angle at the boundary of the loss cone, and  $\mu_c$  the corresponding value of  $\mu$ . As function of the  $L$  shell, the mirror ratio is  $\sigma = 1/\mu_c = L^3(4 - 3/L)^{1/2}$ . To zero order in electric field amplitudes, the first adiabatic invariant is conserved. Then we may write for the parallel and perpendicular components of the particle velocity  $v$ :  $v_{\parallel} = v[1 - \mu\Omega/\Omega(L)]^{1/2}$ ,  $v_{\perp} = v[\mu\Omega/\Omega(L)]^{1/2}$ .

If we assume that at the equator the protons interact with the harmonic  $\ell = 1$ , the energy of resonant particles is found solving for the equation:  $\omega - k_{\parallel} v_{\parallel} - \Omega_p(L) = 0$ . We show

$$\frac{v}{c} = \frac{1}{\eta(L) \cos \phi} \frac{1}{(1 - \mu)^{1/2}} \left(1 - \frac{m_e}{m_p} f_e\right) \quad (6)$$

where  $L$  denotes equatorial values,  $m_e, m_p$  are the electron, proton masses, and  $f_e = \Omega_e(L)/\omega$ .

By solving for Eq. (5), using the parabolic profile in Eq. (4), we find the geomagnetic latitude  $\psi_{\ell}$  of higher order resonances (i.e.,  $\ell \geq 1$ ),

$$\psi_{\ell}^2 = \frac{4}{9} \frac{m_e}{m_p} (\ell - 1) (f_e |\cos \phi| - 1) \frac{1}{g(\mu)} \quad (7)$$

where

$$g(\mu) = \frac{\mu}{1 - \mu} \left(|\cos \phi| - \frac{1}{f_e}\right) + |\cos \phi|. \quad (8)$$

The distance along the flux tube where resonant interactions take place is given by,  $s_{\ell} = R_E L \psi_{\ell}$ . The distance between sequential resonances is  $\Delta s_{\ell} = R_E L (\psi_{\ell+1} - \psi_{\ell})$ .

For example, we take  $L = 3.5$ ,  $\omega_p/\Omega_e(L) = 7.9$ ,  $\omega/\Omega_e(L) = 0.75$ , and  $\theta_L = 10^\circ$ . For  $\phi = 37^\circ$ , we show that  $\eta(L) = 41.4$  and the energy of the resonant protons is 437 keV.

The location along the geomagnetic field of the gyroresonances are:  $\psi_2 = 0.25^\circ, \psi_3 = 0.35^\circ, \dots, \psi_{17} = 1.^\circ$ . As another example we take  $\phi = 40^\circ$ , then  $\eta(L) = 72$  and the proton energy is 158.6 keV. The location of the gyroresonances are:  $\psi_2 = 0.15^\circ, \psi_3 = 0.21^\circ, \dots, \psi_{47} = 1.^\circ$ . Thus there are multiple resonances crossings (17 for the first and 47 for the second examples) within one degree of the magnetic equator, which makes the proton whistler interactions very efficient.

#### IV. THE HAMILTONIAN EQUATIONS

We normalize time  $t$  to  $\Omega_p(L)$ , velocity  $v$  to  $c^{-1}$ , and length  $s$  to  $r_L^{-1}$ , and from now on we always refer to these normalized variables. Let us define

$$\xi_\ell = \ell\lambda + \int_0^s ds' r_L k_\parallel(s') - \frac{\omega}{\Omega_p(L)} t \quad (9)$$

where  $\tan \lambda = v_y/v_x$ , and  $v_{x,y}$  are the components of the particle velocity in the  $x$  and  $y$  directions, respectively. The dimensionless electric field amplitudes are

$$\epsilon_i = \frac{q\mathcal{E}_i}{m_p c \omega} \quad (10)$$

for  $i = 1, 2, 3$ , and where  $q$  is the proton charge. The action-angle variables are  $(I, \lambda)$ , where

$$I = \frac{v_\perp^2}{2} \frac{\Omega_p(L)}{\Omega_p} \quad (11)$$

To first order in the electric field amplitudes  $\epsilon_i$ , the normalized, time-dependent hamiltonian, as function of the canonical pairs,  $(v_\parallel, s)$ , and action-angle variables, is

$$\mathcal{H} = \frac{v_\parallel^2}{2} + I \frac{\Omega}{\Omega(L)} + \sum_{\ell=-\infty}^{\infty} \sin \xi_\ell \left\{ \epsilon_3 v_\parallel J_\ell(k_\perp \rho) - \left[ \frac{I\Omega}{2\Omega(L)} \right]^{1/2} \Gamma_\ell \right\} \quad (12)$$

Here

$$\Gamma_\ell = (\epsilon_1 - \epsilon_2) J_{\ell+1}(k_\perp \rho) + (\epsilon_1 + \epsilon_2) J_{\ell-1}(k_\perp \rho) \quad (13)$$

where  $J_\ell$  are Bessel functions whose arguments are  $k_\perp \rho = (ck_\perp/\Omega_p) [2I\Omega/\Omega(L)]^{1/2}$ . If, in addition to the electromagnetic wave, there is an electrostatic potential  $\phi_s$ , then we replace in Eq. (12),  $\epsilon_3$  by  $\epsilon_3 + \epsilon_s/v_\parallel$ , where  $\epsilon_s = q\phi_s/m_p c^2$ .

For particles crossing a single isolated cyclotron resonance, we consider only one term  $\ell$  in the summation in Eq. (12). In this case, we find the following constant of motion

$$C_\ell = \ell\mathcal{H} - \frac{\omega}{\Omega_p(L)} I \quad (14)$$

By calling  $\chi = (\omega/\Omega_p) \sin^2 \theta(s)$ , where  $\theta(s)$  is the local pitch angle, we find

$$\chi = \frac{\ell\omega}{\Omega_p(L)} \frac{I}{C_\ell + [\omega/\Omega_p(L)] I} \quad (15)$$

This defines the evolution of the pitch angle as a function of the action  $I$ .

By defining  $v_o$  so that  $K = v_o^2/2 + I\Omega/\Omega(L)$ , we obtain

$$v_o = \left\{ \frac{2}{\ell} \left[ C_\ell + I \left( \frac{\omega}{\Omega_p(L)} - \ell \frac{\Omega}{\Omega(L)} \right) \right] \right\}^{1/2} \quad (16)$$

We can now reduce the problem to one-dimension; in which case we find

$$\begin{aligned} v_{\parallel} &= v_o + \sin \xi_\ell \left\{ -\varepsilon_3 J_\ell(k_{\perp} \rho) + \frac{1}{v_o} \left[ \frac{I\Omega}{2\Omega(L)} \right]^{1/2} \Gamma_\ell \right\} \\ \frac{ds}{dt} &= v_o + \frac{1}{v_o} \left[ \frac{I\Omega}{2\Omega(L)} \right]^{1/2} \Gamma_\ell \sin \xi_\ell \end{aligned} \quad (17)$$

To zero order in  $\varepsilon_i$ , the dimensionless length  $s = t v_o$ . The equation of motion for  $I$  as a function of  $s$  is

$$\frac{dI}{ds} = \ell \cos \xi_\ell \Upsilon_\ell(I, v_o) \quad (18)$$

$$\Upsilon_\ell(I, v_o) = -\varepsilon_3 J_\ell(k_{\perp} \rho) + \frac{1}{v_o} \left[ \frac{I\Omega}{2\Omega(L)} \right]^{1/2} \Gamma_\ell \quad (19)$$

As  $\varepsilon_i \rightarrow 0$ , then

$$\frac{d\xi_\ell}{ds} \rightarrow k_{\parallel} r_L + \frac{\ell \Omega_p - \omega}{\Omega_p(L) v_o} \quad (20)$$

The gyroresonance condition is obtained by setting Eq. (20) equal to zero. When this is satisfied  $s = s_\ell$  (the resonance length) which is defined as  $s_\ell = 3/\sqrt{2} \psi_\ell$  and  $\psi_\ell$  is given in Eq. (7).

By assuming that the protons are in gyroresonance, we show that  $\xi_\ell$  satisfies the second order differential equation

$$\frac{d^2 \xi_\ell}{ds^2} = \alpha_\ell + \frac{(k_{\parallel} r_L)^2}{v_o} \frac{1}{\ell} \frac{dI}{ds} \quad (21)$$

Here

$$\alpha_\ell = \frac{\beta_\ell}{\Omega(L)} \frac{d\Omega}{ds} \quad (22)$$

$$\beta_\ell = \Omega_p(L) r_L \frac{m_p}{m_e} \frac{dk_{\parallel}}{d\Omega_e} + \frac{1}{v_o} \left[ \frac{\ell}{2} + \frac{C_\ell}{v_o^2} \right] \quad (23)$$

where  $d\Omega/ds = 2s \Omega(L)$ .

## V. SECOND-ORDER RESONANCE

We next solve the pair of coupled Eqs. (18) and (21) under the assumption that  $s$  is very close to the resonance length  $s_\ell$ . The parallel velocity  $v_o$  is given by setting Eq. (20) equal to zero, i.e.

$$v_o(R) = \frac{\omega}{ck_{\parallel}} \frac{c}{\Omega_p(L) r_L} \quad (24)$$

In this case we may use a Taylor expansion around  $s_\ell$ , then

$$I \approx I_\ell(R) + \left(\frac{dI}{ds}\right)_{(R)} (s - s_\ell) \quad (25)$$

$$\xi_\ell \approx \xi_\ell(R) + \xi_\ell^{(1)} (s - s_\ell) + \frac{\xi_\ell^{(2)}}{2} (s - s_\ell)^2 \quad (26)$$

where  $I_\ell(R)$ ,  $\xi_\ell(R)$  are constants, and  $R$  denotes values at the resonance ( $s = s_\ell$ ). Here  $(dI/ds)_{(R)}$  is given by Eqs. (18) and (19), with  $\xi_\ell = \xi_\ell(R)$ ,  $I = I(R)$ , and  $v_o = v_o(R)$ , evaluated for resonant values. For protons satisfying the resonance condition,  $\xi_\ell^{(1)} = 0$ . For convenience we choose  $\cos[\xi_\ell(R)] = 1$ .

Using Eq. (14) and setting  $v_o = v_o(R)$ , we find

$$I(R) = \frac{f_p}{[1 - \ell f_p \Omega(R)/\Omega(L)]} \left\{ -C_\ell + \frac{\ell}{2} v_o^2(R) \right\} \quad (27)$$

where  $f_p = \Omega_p(L)/\omega \ll 1$ , and  $\Omega(R)/\Omega(L) = 1 + s_\ell^2$ . By substituting Eq. (26) into Eq. (21) we show

$$\xi_\ell^{(2)} = \alpha_\ell(R) + \frac{(k_q r_L)^2}{v_o(R)} \frac{1}{\ell} \left(\frac{dI}{ds}\right)_{(R)} \quad (28)$$

where  $\alpha_\ell(R)$  is evaluated at the resonance.

The change of the action  $I$  after crossing the  $\ell$ 'th resonance,  $\Delta I$ , obtained by integrating Eq. (18), is approximately

$$\Delta I = \left(\frac{dI}{ds}\right)_{(R)} \delta s_\ell \quad (29)$$

The change in  $\chi$  after crossing a resonance is

$$\Delta \chi = \chi(R) \left[ \frac{1}{I(R)} - \frac{1/f_p}{C_\ell + I(R)/f_p} \right] \left(\frac{dI}{ds}\right)_{(R)} \delta s_\ell \quad (30)$$

where  $\chi(R)$  is given by Eq. (15) setting  $I = I(R)$ .

The resonance length  $\delta s_\ell$  is defined as

$$\delta s_\ell = \int_{-\infty}^{+\infty} ds \cos \xi_\ell \quad (31)$$

By combining Eqs. (26), (28), and integrating along  $s$  we show

$$\delta s_\ell = \Gamma(1/2) \cos(\pi/4) \left[ \frac{2}{|\xi_\ell^{(2)}|} \right]^{1/2} \quad (32)$$

The condition of isolated resonances is  $\delta s_\ell < \Delta s_\ell$ , where  $\Delta s_\ell = 3/\sqrt{2} (\psi_{\ell+1} - \psi_\ell)$  and  $\psi_\ell$  is given in Eq. (7).

In the case where the inhomogeneity of the magnetic field is larger than the contribution of the resonance, we may neglect the term proportional to  $(dI/ds)_{(R)}$  in Eq. (28), we get

$$\Delta I = \left(\frac{dI}{ds}\right)_{(R)} \Gamma(1/2) \cos(\pi/4) \left[ \frac{1}{\beta_\ell(R) s_\ell} \right]^{1/2} \quad (33)$$

where  $\beta_\ell(R)$  is given by Eq. (23) and must be evaluated at resonance. From the definition of  $\Gamma_\ell$  in Eq. (13), the change in the action is proportional to the electric field amplitudes.

For interactions such that the contribution of  $\alpha_\ell(R)$  in Eq. (28) is smaller than the contribution of  $(dI/ds)_R$ , we get

$$\Delta I = \pm \left[ \left| \ell \left( \frac{dI}{ds} \right)_{(R)} \right| \right]^{1/2} \Gamma(1/2) \frac{|2|v_o(R)||^{1/2}}{k_{\parallel} r_L} \cos(\pi/4) \quad (34)$$

where the  $\pm$  sign depends on the sign of  $(dI/ds)_R$ . We see that the change in particle momentum  $I$  is now proportional to the square root of the electric field amplitudes, i.e.  $\sqrt{\mathcal{E}_r}$ . We call this the second order resonance condition because to zero order in the electric field amplitudes  $d^2 \xi_\ell / ds^2 \simeq 0$ . For the case of equatorial interactions ( $s_\ell = 0$ ), the condition for the validity of this approximation is

$$\left[ \frac{k_{\parallel} r_L}{\sqrt{2} v_o} \left( \frac{1}{\ell} \left| \left( \frac{dI}{ds} \right)_{(R)} \right| \right)^{1/2} \right]^2 \gg \beta_\ell(R) \Gamma(1/2) \cos \pi/4 \quad (35)$$

Note that for a fix value of  $\omega$  the second order resonance condition is most likely satisfied for equatorial interactions, because then the inhomogeneity of the magnetic field is small. Thus the first harmonic will dominate the second-order interactions. If we allow  $\omega$  to be a function of  $s$ , then

$$\alpha_\ell = \beta_\ell \frac{1}{\Omega(L)} \frac{d\Omega}{ds} + r_L \frac{dk_{\parallel}}{d\omega} \frac{d\omega}{ds} \quad (36)$$

By changing  $\omega$  so that  $\alpha_\ell(R) = 0$  for  $s_\ell > 0$ , the second-order resonance condition is satisfied for other harmonics, and the change in the particle velocity is proportional to  $\sqrt{\mathcal{E}_r}$ . This should be contrasted with the result in Eq. (33) where the change in action is linear with the electric fields and thus smaller than when the condition for second order resonance is satisfied.

## VI. QUASILINEAR THEORY

The distribution function of protons which satisfy the first order resonance condition is given by solving for the quasilinear equation Lyons and Williams (1984):

$$\left( \frac{1}{\tau_{atm}} + \frac{\partial}{\partial t} \right) f = \pi q^2 \sum_{\ell=-\infty}^{+\infty} \int \frac{d^3 k}{(2\pi)^3} \left[ \hat{G} + \frac{\omega - k_{\parallel} v_{\parallel}}{\omega p_{\perp}} \right] \delta(k_{\parallel} v_{\parallel} - \ell \Omega_p - \omega) \Theta_\ell(k) \hat{G} f \quad (37)$$

where  $p$  is momentum and  $\tau_{atm}$ , the atmospheric loss time is defined in<sup>1</sup>. By assuming that  $\omega/\Omega p \ll \sin^2 \theta_c$  (where  $\theta_c$  is the local pitch angle at the loss cone boundary) we may approximate

$$\hat{G} = -\frac{2}{p} \frac{\Omega_c(L)}{\Omega_c} \left( \frac{p_{\perp}}{p} \right)^2 \frac{\partial}{\partial \mu} + \frac{p_{\perp}}{p} \frac{\partial}{\partial p} \quad (38)$$

$$\hat{G} + \frac{\omega - k_{\parallel} v_{\parallel}}{\omega p_{\perp}} = \frac{1}{p^2} \frac{\partial}{\partial p} p^2 \sin \theta - \frac{2}{p} \frac{\Omega_c(L)}{\Omega_c} \frac{p_{\parallel}}{p} \frac{\partial}{\partial \mu} \left( \frac{p_{\perp}}{p} \right)^2 \frac{p}{p_{\parallel}} \quad (39)$$

$$\sum_{k=-\infty}^{+\infty} \delta(k_{\parallel} v_{\parallel} + \ell \Omega_p - \omega) \Theta_{\ell}(k) \approx (2\pi)^3 \delta(k_{\parallel} v_{\parallel} - \omega) \frac{\omega \Omega_e}{\omega_p^2} \frac{W_k(\phi, t)}{|\cos \phi|} b(\phi) \quad (40)$$

where

$$b(\phi) = 1 + \cos^2 \phi + \frac{1}{2} \left[ \frac{p_{\parallel}}{p_{\perp}} \frac{\omega}{\Omega_e} \sin \phi \right]^2 \quad (41)$$

If  $B_k$  is the wave magnetic field ( $B_k \ll B_0$ , the geomagnetic field), then the energy density of waves is

$$W_k(\phi, t) = \frac{1}{8\pi} \left( \frac{B_k}{2\pi} \right)^2 \quad (42)$$

We assume that diffusion occurs on time scales such  $t \gg \tau_B$ , where  $\tau_B$  is the proton bounce time between ionospheric conjugates. We integrate the diffusion equation along the flux tube by applying the operator  $1/\tau_B \int dz/v_{\parallel}$  to both sides of Eq. (37). The bounce-averaged diffusion equation, in terms of equatorial pitch-angles  $\theta_L$  and particle momentum, is

$$\left( \frac{1}{\tau_{atm}} + \frac{\partial}{\partial t} \right) f = \frac{1}{p \sin \theta_L \cos \theta_L} \frac{\partial}{\partial \theta_L} \sin \theta_L \cos \theta_L \left[ D_{\theta, \theta} \frac{1}{p} \frac{\partial f}{\partial \theta_L} + D_{\theta, p} \frac{\partial f}{\partial p} \right] + \frac{1}{p^2} \frac{\partial}{\partial p} \left\{ p \left[ p D_{p, p} \frac{\partial f}{\partial p} + D_{p, \theta} \frac{\partial f}{\partial \theta_L} \right] \right\} \quad (43)$$

The bounce-averaged diffusion coefficients are

$$D_{\theta, \theta} = \tan^2 \theta_L D_{p, p} \quad (44)$$

$$D_{\theta, p} = D_{p, \theta} = -\tan \theta_L D_{p, p} \quad (45)$$

The energy-diffusion coefficient is

$$D_{p, p} = \frac{\pi q^2}{v \tau_B} \int_0^{\infty} k^2 dk \int_{-\pi/2}^{+\pi/2} \sin \phi \Delta(k, \phi) d\phi \quad (46)$$

where

$$\Delta(k, \phi) = \frac{4\pi \Omega_e(L)^3}{\omega_p^2} \frac{W_k(\phi, t)}{|\cos \phi|} \left( \frac{ds}{d\Omega} \right)_{(R)} \left[ \frac{\Omega(R)}{\Omega(L)} \right]^2 \frac{p_{\parallel}}{p} b(\phi) \quad (47)$$

Here  $R$  denotes values at the resonance where  $v_{\parallel} \sim v$ , and  $\omega - k_{\parallel} v \approx 0$ . Note that for small values of  $\phi$ , we can neglect the contribution of the parallel component of the wave field in  $b(\phi)$  (see Eq. (41)), then  $D_{p, p}$  is approximately independent of  $\mu$ , the equatorial pitch angle, and we write

$$f = F(t) \mu^{\sigma} K(p) \quad (48)$$

where  $\sigma > 0$  is a free parameter. We define the precipitation lifetime as

$$\tau_p = - \left[ \frac{1}{F} \frac{dF}{dt} \right]^{-1} \quad (49)$$

By combining Eqs. (43) through (45) and Eq. (48), we show

$$\left\{ \frac{2\kappa_c}{\tau_E} - \frac{1}{\tau_p} \right\} K(p) = \frac{4\sigma(\sigma+1)}{p^2} D_{p,p} K + \frac{d}{dp} \left[ D_{p,p} \frac{dK}{dp} \right] - \frac{4\sigma}{p} D_{p,p} \frac{dK}{dp} - \frac{2\sigma}{p^2} K \frac{d}{dp} [p D_{p,p}] \quad (50)$$

where  $\kappa_c = \mu_c^{(\sigma+1)}$ . This is an eigenvalue equation for  $\tau_p$  as a function of the free parameter  $\sigma$ . The eigenfunction  $K(p)$  is such that must be regular as  $p \rightarrow 0$ , and well behaved for large  $p$ , i. e. as  $p \rightarrow \infty$  then  $K \ll p^{-2}$ .

## VII. SUMMARY AND CONCLUSIONS

We have presented a theoretical analysis of proton-whistler interactions near the equator in the plasmasphere. Whistler waves which are near the parametric mode<sup>2</sup>, can interact with protons whose energies are in the hundreds of keV. In an inhomogeneous geomagnetic field, we show that the spacing between subsequent cyclotron resonances is very small. Because of that, protons are scattered into the atmospheric loss cone after crossing multiple resonances. A test-particle hamiltonian formalism is given in terms of the action ( $I$ ), angle ( $\xi_L$ ), variables as function of the distance ( $s$ ) along the flux tube. We show that for second-order resonant protons,  $d\xi_L/ds = d^2\xi_L/ds^2 = 0$ , and the change in the particle's momentum is proportional to the square root of the electric field amplitudes. The thresholds in electric fields for second-order resonance conditions are calculated. A quasi-linear formulation for the distribution function of first-order resonant protons is presented. The bounce-averaged diffusion equation contains diffusion coefficients for the pitch angle, energy, and cross energy/ pitch angle terms. They are shown to be of the same orders of magnitude. We reduce the diffusion equation to a one-dimensional energy dependent equation to be solved for the precipitation life times of protons in the Radiation Belts.

*Acknowledgements.* This work has been supported in part by the U. S. Air Force contract F19628-89-K-0014 with Northeastern University.

## REFERENCES

1. L. R. Lyons and D. J. Williams, *Quantitative Aspects of Magnetospheric Physics*, D. Reidel Publishing Company, The Netherlands, 1984.
2. C. F. Kennel and H. E. Petschek, *J. Geophys. Res.*, 1966, **71**, 1.
3. P. A. Bespalov and V. Yu. Trakhtengerts, *Rev. Plasma Phys.*, 1980, **10**, 88.
4. E. Villalón and W. J. Burke, *J. Geophys. Res.*, 1991, **96**, 9655.
5. E. Villalón, W. J. Burke, P. L. Rothwell, M. B. Silevitch, *J. Geophys. Res.*, 1989, **94**, 15243.

6. H. C. Koons, Geophys. Res. Lett., 1975, 2, 281.
7. R. A. Kovrazhkin, M. M. Mogilevskii, O. A. Molchanov, Yu. I. Gal'perin, N. V. Dzhordzhio, Zh. M. Bosbe, and A. Rem, JETP Lett., 1984, 39, 228.
8. R. Gendrin, J. Atmospheric Terrest. Phys., 1968, 30, 1313.
9. M. G. Morgan, J. Geophys. Res., 1980, 85, 130.
10. D. R. Shklyar, Planet. Space Phys., 1986, 34, 1091.
11. R. A. Helliwell, J. Geophys. Res., 1967, 72, 4773.
12. K. B. Dysthe, J. Geophys. Res., 1971, 76, 6915.



## WHISTLER INTERACTIONS WITH ENERGETIC PROTONS

Elena Villalón

Center for Electromagnetics Research,  
Northeastern University, Boston MA 02115

William J. Burke

Geophysics Directorate, PL/OL-AA, Hanscom AFB, MA 01731

### ABSTRACT

Whistler waves, near the electrostatic limit, can interact with trapped, energetic protons close to the equator in the Earth's Radiation Belts. In an inhomogeneous geomagnetic field, the spacing between cyclotron resonances is very small due to large ion Larmor radii. After crossing multiple resonances, the pitch angles change significantly and the protons are scattered toward the atmospheric loss cone. A test-particle, Hamiltonian formalism is investigated. For second-order resonant protons, the change in particle momentum is proportional to the square root of the wave electric field amplitudes. The thresholds in electric fields for second-order resonance conditions are calculated. Quasilinear theory is studied to describe the distribution functions and calculate the diffusion life times of first-order resonant protons. The diffusion coefficients for the energy, pitch angle, and the cross energy/ pitch angle terms are shown to be of the same orders of magnitude.

### I. INTRODUCTION

Interactions between whistler waves and energetic electrons in the magnetosphere have been the subject of intensive research during the past two decades [1 – 3]. The wave-electron, resonant interactions are believed to account for many phenomena such as growth of signals [2], emissions of varying frequencies [4] and electron precipitation into the ionosphere [5]. Most of the theoretical work is based on resonant interactions at the first harmonic of the electron gyrofrequency, although higher harmonics interactions may also be important [1]. Detailed theoretical analyses taking into account wave growth and particle depletion, is given in the papers by Villalón and coworkers (see Refs. [6, 7] and references therein).

The interactions of plasmaspheric protons and whistler waves have not received as much attention. This is because the energies required are very large and the population of protons with energies larger than 500 keV, is small. Since the proton gyrofrequency  $\Omega_p$ , is much lower than the wave frequency  $\omega$ , the resonant velocity  $v_{||}$  is of the order of the wave phase velocity  $\omega/k_{||}$

(where  $k_{\parallel}$  is the parallel component of the wave vector). However recent experiments [8, 9] have demonstrated that protons precipitate by interactions with VLF waves launched into the magnetosphere from ground sources. The wave frequencies are close to the equatorial electron gyrofrequency. Thus, near the equator,  $k_{\parallel}$  is very large and the resonant energies of protons relatively low. We limit our studies to regions near the magnetic equator of the plasmasphere  $L < 4$  (where  $L$  is the equatorial crossing distance of the field line measured in Earth radii  $R_E$ ).

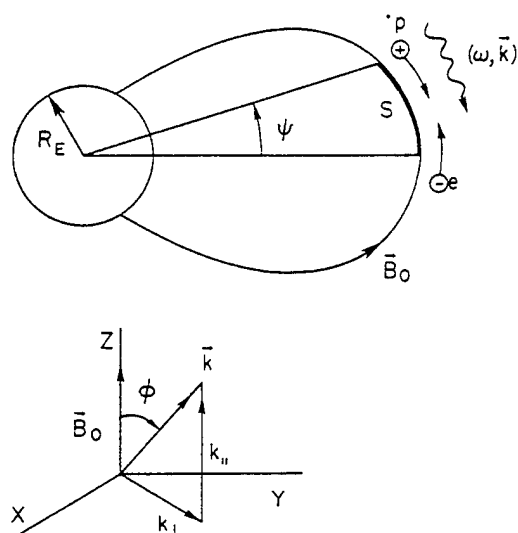


Figure 1. Schematic representation of whistler  $(\omega, \mathbf{k})$ , interacting with electrons and protons near the equator. The coordinate system used in this paper is depicted here.

The plasmasphere contains a relatively dense population of cold particles of ionospheric origin whose distribution function is isotropic in pitch angle. The energetic particles originate from stationary sources (convective transfer across  $L$  shells) and pulsed sources (sudden impulses during magnetic storms and substorms). They are trapped within the radiation belts traveling back and forth along field lines between magnetic mirror points, and interacting with the quasi-electrostatic whistler waves near the magnetic equator. The predominant feature of the resonant interactions is the

crossing of multiple harmonics of the proton gyrofrequency. The proton pitch angle is  $\theta$ , where  $\tan \theta = v_{\perp}/v_{\parallel}$  (the ratio between the perpendicular and parallel components of the velocity). The pitch angles can change due to direct pitch-angle scattering or to energy diffusion [10]. This should be contrasted with the analogous whistler-electron interactions, where the predominant harmonic is the first. Also, electron energies do not change during the interactions. For proton-whistler interactions, the waves and particles travel in the same direction, with the waves slightly overtaking the protons. For electron-whistler interactions the waves and particles travel in opposite directions. The situation is depicted in the Figure 1.

The paper is organized as follows: Sec. II describes the propagation of whistler waves in a cold plasma, near the electrostatic limit [11]. Sec. III studies the resonance conditions for multiple harmonics of the proton gyrofrequency. The inhomogeneous, near-equatorial geomagnetic field is described by a parabolic profile. Due to the large ion Larmor radii, we show that the distance between resonances is very small. Because of the inclusion of multiple harmonics, these interactions are very effective [12]. The test-particle Hamiltonian formalism for each isolated cyclotron resonance, is given in Sec. IV. Sec V studies the evolution of the action ( $I$ ) and angle ( $\xi_l$ ) variables as function of the distance ( $s$ ) along the flux tube using Taylor expansions around isolated resonance points. Let us expand  $\xi_l$  around the equator:  $\xi_l(s) = \xi_l(0) + \xi_l^{(1)} s + 1/2 \xi_l^{(2)} s^2$ . First-order resonant particles are such that  $\xi_l^{(1)} = 0$ . That is, at the equator  $d\xi_l/ds = 0$ , which is the resonance condition as given in Eq. (5). The second-order term  $\xi_l^{(2)} \sim dB_o/ds + O(B_k)$ . For large wave amplitudes  $O(B_k)$  is larger than the contribution of the inhomogeneous geomagnetic field  $dB_o/ds$ . In this case, we say that protons which are in gyroresonance (i. e.  $\xi_l^{(1)} = 0$ ), satisfy the second-order resonance condition. This is because to zero order in the electric field amplitude  $d\xi_l/ds = d^2\xi_l/ds^2 \simeq 0$ . For first-order resonant particles, the change in action is proportional to the electric field amplitude. For second-order resonant protons, the change in action is proportional to the square root of the electric field amplitude. The second-order resonance condition is met when the field amplitude is large [13, 14]. The thresholds in electric fields, are then calculated. Sec. VI contains a quasilinear formulation for the distribution function of first order resonant protons. We assume that the protons are unmagnetized in time scales of the order of  $2\pi/\omega$ , where  $\omega$  is the frequency of the whistler wave. They are however magnetized in times comparable to the bounce period. Because diffusion occurs over many bounce periods, we average the diffusion equation along the flux tube. The bounce averaged, Fokker-Planck equation contains the diffusion coefficients for the pitch angle, energy, and the cross energy/ pitch angle terms. These coefficients are shown to have the same orders of magnitude. We reduce the equation to a

one-dimensional diffusion equation to be solved for the energy part of the distribution function. This eigenvalue equation estimates the VLF diffusion life times of protons in the radiation belts.

## II. QUASI-ELECTROSTATIC WHISTLER WAVES

We consider a whistler wave of frequency  $\omega$  and wave vector  $\mathbf{k}$ , propagating in a field-aligned duct. The geomagnetic field  $\mathbf{B}_0$  is along the  $z$  direction and  $\phi$  is the angle between  $\mathbf{k}$  and  $\mathbf{B}_0$ . The dispersion relation for the refractive index  $\eta = ck/\omega$  is

$$\eta^2 = 1 + \frac{(\omega_p/\omega)^2}{(\Omega_e/\omega) |\cos \phi| - 1} \quad (1)$$

where  $\omega_p$  and  $\Omega_e$  are the electron plasma and gyro frequencies, respectively.

The electric field is [15]

$$\mathbf{E} = \hat{x} \mathcal{E}_1 \cos \Psi - \hat{y} \mathcal{E}_2 \sin \Psi - \hat{z} \mathcal{E}_3 \cos \Psi \quad (2)$$

where  $\hat{x}, \hat{y}$  and  $\hat{z}$  are unit vectors;  $\Psi = k_\perp x + k_\parallel z - \omega t$ , and  $k_\parallel, k_\perp$  are the components along and perpendicular to  $\mathbf{B}_0$  of the wave vector. The ratios of electric field components are

$$\frac{\mathcal{E}_2}{\mathcal{E}_1} = \frac{1}{\eta^2 - 1} \frac{(\omega_p/\omega)^2}{(\Omega_e/\omega) - |\cos \phi|} \quad (3)$$

$$\frac{\mathcal{E}_3}{\mathcal{E}_1} = \frac{1 - (\omega_p/\omega)^2 - (\eta \sin \phi)^2}{\eta^2 \sin \phi \cos \phi} \quad (4)$$

For the case where  $\omega \sim \Omega_e(L) |\cos \phi|$ , the equatorial refractive index  $\eta^2(L) \gg 1$ , then  $\mathcal{E}_2/\mathcal{E}_1 \ll 1$ , and  $\mathcal{E}_1/\mathcal{E}_3 \sim -\sin \phi / \cos \phi$ . The wave becomes quasi-electrostatic, i.e.  $\mathbf{E}$  has a significant component in the direction of  $\mathbf{k}$ , and the group velocity  $v_g \sim 1/\eta$ . This wave can interact with protons which energies are in the hundreds of keV.

Near the equator, the Earth's magnetic field may be approximated as having a parabolic profile

$$\frac{\Omega}{\Omega(L)} = 1 + \left(\frac{s}{r_L}\right)^2 \quad (5)$$

where  $s \simeq R_E L \psi$  and  $\psi$  is the geomagnetic latitude (see the figure), and  $r_L = (\sqrt{2}/3) R_E L$ . The equatorial gyrofrequency is denoted by  $\Omega(L)$ , and  $\Omega$  stands for the gyrofrequencies either for electrons or protons at a location  $s$  away from the equator along the field line.

### III. RESONANCE PROTON WHISTLER INTERACTIONS

For whistler waves to interact strongly with protons near equatorial regions, they must satisfy the resonance condition

$$\omega - k_{\parallel} v_{\parallel} - \ell \Omega_p = 0 \quad (6)$$

where,  $\ell = 0, 1, 2, \dots$ ;  $\Omega_p$  is the proton gyrofrequency, and  $v_{\parallel}$  is the parallel component of the particle's velocity. We call  $\mu = \sin^2 \theta_L$ , where  $\theta_L$  is the equatorial pitch angle. Here  $\theta_L > \theta_c(L)$ , where  $\theta_c(L)$  is the pitch angle at the boundary of the loss cone, and  $\mu_c$  the corresponding value of  $\mu$ . As function of the  $L$  shell, the mirror ratio is  $\sigma = 1/\mu_c = L^3 (4 - 3/L)^{1/2}$ . To zero order in electric field amplitudes, the first adiabatic invariant is conserved. Then we may write for the parallel and perpendicular components of the particle velocity  $v$ :  $v_{\parallel} = v[1 - \mu\Omega/\Omega(L)]^{1/2}$ ,  $v_{\perp} = v[\mu\Omega/\Omega(L)]^{1/2}$ .

At the equator the protons interact with the harmonic  $\ell = 0$ , and then the energy of resonant particles is found solving for the equation:  $\omega - k_{\parallel} v_{\parallel} = 0$ . We show

$$\frac{v}{c} = \frac{1}{\eta(L) \cos \phi} \frac{1}{(1 - \mu)^{1/2}} \quad (7)$$

where  $\eta(L)$  denotes equatorial values of the refractive index, and  $f_e = \Omega_e(L)/\omega$ .

By solving for Eq. (6), using the parabolic profile in Eq. (5), we find the geomagnetic latitude  $\psi_{\ell}$  of higher order resonances (i.e.,  $\ell \geq 0$ ),

$$\psi_{\ell}^2 = \frac{4}{9} \frac{m_e}{m_p} \ell (f_e |\cos \phi| - 1) \frac{1}{g(\mu)} \quad (8)$$

where

$$g(\mu) = \frac{\mu}{1 - \mu} (|\cos \phi| - \frac{1}{f_e}) + |\cos \phi|. \quad (9)$$

where  $m_{e,p}$  are the electron, proton masses. The distance along the flux tube where resonant interactions take place is given by,  $s_{\ell} = R_E L \psi_{\ell}$ . The distance between two subsequent resonances is obtained from  $\Delta s_{\ell} = R_E L (\psi_{\ell+1} - \psi_{\ell})$ .

For example, we take  $L = 3.5$ ,  $\omega_p/\Omega_e(L) = 7.9$ ,  $\omega/\Omega_e(L) = 0.75$ , and  $\theta_L = 10^\circ$ . For  $\phi = 37^\circ$ , we find that  $\eta(L) = 41.4$  and the energy of the resonant protons is 437 keV. The location along the geomagnetic field of the gyroresonances are:  $\psi_2 = 0.25^\circ, \psi_3 = 0.35^\circ, \dots, \psi_{17} = 1.^\circ$ . As another example we take  $\phi = 40^\circ$ , then  $\eta(L) = 72$  and the proton energy is 158.6 keV. The location of the gyroresonances are:  $\psi_2 = 0.15^\circ, \psi_3 = 0.21^\circ, \dots, \psi_{47} = 1.^\circ$ . We also show that  $\psi_{\ell}$  is very weakly dependent upon pitch angle  $\mu$ . Thus there are multiple resonances crossings (17 for the first and 47 for the second examples) within one degree of the magnetic equator, which makes the proton whistler interactions very efficient.

#### IV. THE HAMILTONIAN EQUATIONS

We normalize time  $t$  to  $\Omega_p(L)$ , velocity  $v$  to  $c^{-1}$ , and length  $s$  to  $r_L^{-1}$ , and from now on we always refer to these normalized variables. Let us define

$$\xi_\ell = \ell\lambda + \int_0^s ds' r_L k_{||}(s') - \frac{\omega}{\Omega_p(L)} t \quad (10)$$

where  $\tan \lambda = v_y/v_x$ , and  $v_{x,y}$  are the components of the particle velocity in the  $x$  and  $y$  directions, respectively. The dimensionless electric field amplitudes are

$$\varepsilon_i = \frac{q\mathcal{E}_i}{m_p c \omega} \quad (11)$$

for  $i = 1, 2, 3$ , and where  $q$  is the proton charge. The action-angle variables are  $(I, \lambda)$ , where

$$I = \frac{v_\perp^2}{2} \frac{\Omega_p(L)}{\Omega_p} \quad (12)$$

To first order in the electric field amplitudes  $\varepsilon_i$ , the normalized, time-dependent hamiltonian, as function of the canonical pairs,  $(v_{||}, s)$ , and action-angle variables, is

$$\mathcal{H} = \frac{v_{||}^2}{2} + I \frac{\Omega}{\Omega(L)} + \sum_{\ell=-\infty}^{\infty} \sin \xi_\ell \left\{ \varepsilon_3 v_{||} \mathcal{J}_\ell(k_\perp \rho) - \left[ \frac{I\Omega}{2\Omega(L)} \right]^{1/2} \Gamma_\ell \right\} \quad (13)$$

Here  $\Gamma_\ell$  is a linear combination of Bessel functions  $\mathcal{J}_\ell$ ,

$$\Gamma_\ell = (\varepsilon_1 - \varepsilon_2) \mathcal{J}_{\ell+1}(k_\perp \rho) + (\varepsilon_1 + \varepsilon_2) \mathcal{J}_{\ell-1}(k_\perp \rho) \quad (14)$$

whose arguments are  $k_\perp \rho = (ck_\perp/\Omega_p) [2I\Omega/\Omega(L)]^{1/2}$ . If, in addition to the electromagnetic wave, there is an electrostatic potential  $\phi_o$ , then we replace in Eq. (13),  $\varepsilon_3$  by  $\varepsilon_3 + \varepsilon_o/v_{||}$ , where  $\varepsilon_o = q\phi_o/m_p c^2$ .

For particles crossing a single isolated cyclotron resonance, we consider only one term  $\ell$  in the summation in Eq. (13). In this case, we find the following constant of motion

$$C_\ell = \ell\mathcal{H} - \frac{\omega}{\Omega_p(L)} I \quad (15)$$

The criterion for overlapping of resonances is given later on in Eq. (37).

By defining  $v_o$  so that  $\mathcal{H} = v_o^2/2 + I\Omega/\Omega(L)$ , we obtain

$$v_o = \left\{ \frac{2}{\ell} \left[ C_\ell + I \left( \frac{\omega}{\Omega_p(L)} - \ell \frac{\Omega}{\Omega(L)} \right) \right] \right\}^{1/2} \quad (16)$$

We can now reduce the problem to one-dimension, in which case we find

$$v_{\parallel} = v_o + \sin \xi_{\ell} \Upsilon_{\ell}(I, v_o)$$

$$\frac{ds}{dt} = v_o + \frac{1}{v_o} \left[ \frac{I\Omega}{2\Omega(L)} \right]^{1/2} \Gamma_{\ell} \sin \xi_{\ell} \quad (17)$$

where  $\Upsilon_{\ell}(I, v_o)$  is defined in Eq. (19).

To zero order in  $\epsilon_i$ , the dimensionless length  $s = t v_o$ . The equation of motion for  $I$  as a function of  $s$  is

$$\frac{dI}{ds} = \ell \cos \xi_{\ell} \Upsilon_{\ell}(I, v_o) \quad (18)$$

$$\Upsilon_{\ell}(I, v_o) = -\epsilon_3 \mathcal{J}_{\ell}(k_{\perp} \rho) + \frac{1}{v_o} \left[ \frac{I\Omega}{2\Omega(L)} \right]^{1/2} \Gamma_{\ell} \quad (19)$$

As  $\epsilon_i \rightarrow 0$ , then

$$\frac{d\xi_{\ell}}{ds} \rightarrow k_{\parallel} r_L + \frac{\ell \Omega_p - \omega}{\Omega_p(L) v_o} \quad (20)$$

The gyroresonance condition is obtained by setting Eq. (20) equal to zero. When this is satisfied  $s = s_{\ell}$  (the resonance length) which is defined as  $s_{\ell} = 3/\sqrt{2} \psi_{\ell}$  and  $\psi_{\ell}$  is given in Eq. (8).

By assuming that the protons are in gyroresonance, we show that  $\xi_{\ell}$  satisfies the second order differential equation

$$\frac{d^2 \xi_{\ell}}{ds^2} = \alpha_{\ell} + \frac{(k_{\parallel} r_L)^2}{v_o} \frac{1}{\ell} \frac{dI}{ds} \quad (21)$$

Here

$$\alpha_{\ell} = \frac{\beta_{\ell}}{\Omega(L)} \frac{d\Omega}{ds} \quad (22)$$

$$\beta_{\ell} = \Omega_p(L) r_L \frac{m_p}{m_e} \frac{dk_{\parallel}}{d\Omega_e} + \frac{1}{v_o} \left[ \frac{\ell}{2} + \frac{C_{\ell}}{v_o^2} \right] \quad (23)$$

where  $d\Omega/ds = 2s \Omega(L)$ .

## V. SECOND ORDER RESONANCE

We next solve the pair of coupled Eqs. (18) and (21) under the assumption that  $s$  is very close to the resonance length  $s_{\ell}$ . The parallel velocity  $v_o$  is given by setting Eq. (20) equal to zero, *i.e.*

$$v_o(R) = \frac{\omega}{ck_{\parallel}} \frac{c}{\Omega_p(L) r_L} \left( 1 - \ell \frac{\Omega_p}{\omega} \right) \quad (24)$$

In this case we may use a Taylor expansion around  $s_\ell$ , then

$$I \simeq I_\ell(R) + \left(\frac{dI}{ds}\right)_{(R)} (s - s_\ell) \quad (25)$$

$$\xi_\ell \simeq \xi_\ell(R) + \xi_\ell^{(1)} (s - s_\ell) + \frac{\xi_\ell^{(2)}}{2} (s - s_\ell)^2 \quad (26)$$

where  $I_\ell(R)$ ,  $\xi_\ell(R)$  are constants, and  $R$  denotes values at the resonance ( $s = s_\ell$ ). Here  $(dI/ds)_{(R)}$  is given by Eqs. (18) and (19), with  $\xi_\ell = \xi_\ell(R)$ ,  $I = I(R)$ , and  $v_o = v_o(R)$ , evaluated for resonant values. For protons satisfying the resonance condition,  $\xi_\ell^{(1)} = 0$ . For convenience we choose  $\cos[\xi_\ell(R)] = 1$ .

The constant of motion  $C_\ell$  is obtained evaluating Eq. (15) at the equator, we show

$$C_\ell = \left( \frac{1}{\sqrt{2} \eta(L) \cos \phi} \frac{c}{\Omega_p(L) r_L} \right)^2 \frac{1}{1 - \mu} \left[ \frac{-\mu}{f_p} + \ell \right] \quad (27)$$

where  $f_p = \Omega_p(L)/\omega \ll 1$ . Using Eq. (16) and setting  $v_o = v_o(R)$ , we find

$$I_\ell(R) = \frac{f_p}{[1 - \ell f_p \Omega(R)/\Omega(L)]} \left\{ -C_\ell + \frac{\ell}{2} v_o^2(R) \right\} \quad (28)$$

where  $\Omega(R)/\Omega(L) = 1 + s_\ell^2$ . By substituting Eq. (26) into Eq. (21) we show

$$\xi_\ell^{(2)} = \alpha_\ell(R) + \frac{(k_{\parallel} r_L)^2}{v_o(R)} \frac{1}{\ell} \left( \frac{dI}{ds} \right)_{(R)} \quad (29)$$

where  $\alpha_\ell(R)$  is evaluated at the resonance.

The change of the action  $I$  after crossing the  $\ell$ 'th resonance,  $\Delta I$ , obtained by integrating Eq. (18), is approximately

$$\Delta I = \left( \frac{dI}{ds} \right)_{(R)} \delta s_\ell \quad (30)$$

The resonance length  $\delta s_\ell$  is defined as

$$\delta s_\ell = \int_{-\infty}^{+\infty} ds \cos \xi_\ell \quad (31)$$

By combining Eqs. (26), (29), and integrating along  $s$  we show

$$\delta s_\ell = \Gamma(1/2) \cos(\pi/4) \left[ \frac{2}{|\xi_\ell^{(2)}|} \right]^{1/2} \quad (32)$$

Resonances are isolated in space if  $\delta s_\ell < \Delta s_\ell$ , where  $\Delta s_\ell = 3/\sqrt{2}(\psi_{\ell+1} - \psi_\ell)$  and  $\psi_\ell$  is given in Eq. (8).

In the case where the inhomogeneity of the magnetic field is larger than



the contribution of the resonance, we may neglect the term proportional to  $(dI/ds)_{(R)}$  in Eq. (29), we get

$$\Delta I = \left(\frac{dI}{ds}\right)_{(R)} \Gamma(1/2) \cos(\pi/4) \left[ \frac{1}{\beta_L(R) s_L} \right]^{1/2} \quad (33)$$

where  $\beta_L(R)$  is given by Eq. (23) and must be evaluated at resonance. From the definition of  $\Gamma_L$  in Eq. (14), the change in the action is proportional to the electric field amplitudes.

For interactions such that the contribution of  $\alpha_L(R)$  in Eq. (29) is smaller than the contribution of  $(dI/ds)_R$ , we get

$$\Delta I = \pm \left[ \ell \left( \frac{dI}{ds} \right)_{(R)} \right]^{1/2} \Gamma(1/2) \frac{[2|v_o(R)|]^{1/2}}{k_{||} r_L} \cos(\pi/4) \quad (34)$$

where the  $\pm$  sign depends on the sign of  $(dI/ds)_R$ . We see that the change in particle momentum  $I$  is now proportional to the square root of the electric field amplitudes, i.e.  $\sqrt{\epsilon_i}$ . We call this the second order resonance condition because to zero order in the electric field amplitudes  $d^2 \xi_L / ds^2 \simeq 0$ . For the case of equatorial interactions ( $s_L = 0$ ), the condition for the validity of this approximation is

$$\left[ \frac{k_{||} r_L}{\sqrt{2} v_o} \left( \frac{1}{\ell} \left| \left( \frac{dI}{ds} \right)_{(R)} \right| \right)^{1/2} \right]^3 \gg \beta_L(R) \Gamma(1/2) \cos \pi/4 \quad (35)$$

Note that for a fix value of  $\omega$  the second order resonance condition is most likely satisfied for equatorial interactions, because then the inhomogeneity of the magnetic field is small. Thus the first harmonic will dominate the second-order interactions. If we allow  $\omega$  to be a function of  $s$ , then

$$\alpha_L = \beta_L \frac{1}{\Omega(L)} \frac{d\Omega}{ds} + r_L \frac{dk_{||}}{d\omega} \frac{d\omega}{ds} \quad (36)$$

By changing  $\omega$  so that  $\alpha_L(R) = 0$  for  $s_L > 0$ , the second-order resonance condition is satisfied for other harmonics, and the change in the particle velocity is proportional to  $\sqrt{\epsilon_i}$ . This should be contrasted with the result in Eq. (33) where the change in action is linear with the electric fields and thus smaller than when the condition for second order resonance is satisfied.

We have carried out some preliminary calculations applying the theory presented in this section; for waves such that  $0.5 \leq \omega/\Omega_L \leq 1$ , and  $\cos \phi \geq \omega/\Omega_L$ , and for electric field amplitudes which are in the range  $10^{-6}$  to  $10^{-4}$  Volt/cm. They show the contribution of large harmonic resonances, i.e.  $\ell \geq 50$  in the change of the action  $\Delta I$  as defined in Eq. (30). As a matter of fact

of fact the largest contributions to  $\Delta I$  come from values of  $\ell$  which are close to the argument of the Bessel functions  $k_{\perp} \rho$ . For equatorial pitch angles between 7.5 and 20 degrees, at the  $L$  shell 3.5, the values of  $\ell$  which give maximum change in the action are larger than 50 and smaller than 150. Overlapping of resonances occur when

$$\frac{\Delta I}{I_{\ell-1}(R) - I_{\ell}(R)} \geq 1 \quad (37)$$

For electric fields greater than  $10^{-4}$  Volt/cm all resonances ( $150 \geq \ell \geq 1$ ) overlap, but for smaller electric fields only some of them do for particles which equatorial pitch angles are near the loss cone. Note that even if resonances overlap in space (see comments after Eq. (32)), we must still treat them as independent of each other if the criterion in Eq. (37) is not met.

## VI. QUASILINEAR THEORY

The distribution function of protons which satisfy the first order resonance condition is given by solving for the quasilinear equation Lyons and Williams (1984):

$$\left(\frac{1}{\tau_{atm}} + \frac{\partial}{\partial t}\right) f = \pi q^2 \sum_{\ell=-\infty}^{+\infty} \int \frac{d^3 \mathbf{k}}{(2\pi)^3} \left[ \hat{G} + \frac{\omega - k_{\parallel} v_{\parallel}}{\omega p_{\perp}} \right] \delta(k_{\parallel} v_{\parallel} - \ell \Omega_p - \omega) \Theta_{\ell}(\mathbf{k}) \hat{G} f \quad (38)$$

where  $p$  is momentum and  $\tau_{atm}$ , the atmospheric loss time is defined in [1]. By assuming that  $\omega/\Omega_p \ll \sin^2 \theta_c$  (where  $\theta_c$  is the local pitch angle at the loss cone boundary) we may approximate

$$\hat{G} + \frac{\omega - k_{\parallel} v_{\parallel}}{\omega p_{\perp}} = \frac{1}{p^2} \frac{\partial}{\partial p} p^2 \sin \theta - \frac{2}{p} \frac{\Omega_e(L)}{\Omega_e} \frac{p_{\parallel}}{p} \frac{\partial}{\partial \mu} \left(\frac{p_{\perp}}{p}\right)^3 \frac{p}{p_{\parallel}} \quad (39)$$

$$\hat{G} = -\frac{2}{p} \frac{\Omega_e(L)}{\Omega_e} \left(\frac{p_{\perp}}{p}\right)^3 \frac{\partial}{\partial \mu} + \frac{p_{\perp}}{p} \frac{\partial}{\partial p} \quad (40)$$

$$\sum_{\ell=-\infty}^{+\infty} \delta(k_{\parallel} v_{\parallel} + \ell \Omega_p - \omega) \Theta_{\ell}(\mathbf{k}) \simeq (2\pi)^3 \delta(k_{\parallel} v_{\parallel} - \omega) \frac{\omega \Omega_e}{\omega_p^2} \frac{W_k(\phi, t)}{|\cos \phi|} b(\phi) \quad (41)$$

where

$$b(\phi) = 1 + \cos^2 \phi + \frac{1}{2} \left[ \frac{p_{\parallel}}{p_{\perp}} \frac{\omega}{\Omega_e} \sin \phi \right]^2 \quad (42)$$

If  $B_k$  is the wave magnetic field ( $B_k \ll B_0$ , the geomagnetic field), then the energy density of waves is

$$W_k(\phi, t) = \frac{1}{8\pi} \left(\frac{B_k}{2\pi}\right)^2 \quad (43)$$

We assume that diffusion occurs on time scales such  $t \gg \tau_B$ , where  $\tau_B$  is the proton bounce time between ionospheric conjugates. We integrate the diffusion equation along the flux tube by applying the operator  $1/\tau_B \int dz/v_{||}$  to both sides of Eq. (38). The bounce-averaged diffusion equation, in terms of equatorial pitch-angles  $\theta_L$  and particle momentum, is

$$\left(\frac{1}{\tau_{atm}} + \frac{\partial}{\partial t}\right) f = \frac{1}{p \sin \theta_L \cos \theta_L} \frac{\partial}{\partial \theta_L} \sin \theta_L \cos \theta_L \left[ \mathcal{D}_{\theta, \theta} \frac{1}{p} \frac{\partial f}{\partial \theta_L} + \mathcal{D}_{\theta, p} \frac{\partial f}{\partial p} \right] + \frac{1}{p^2} \frac{\partial}{\partial p} \left\{ p \left[ p \mathcal{D}_{p, p} \frac{\partial f}{\partial p} + \mathcal{D}_{p, \theta} \frac{\partial f}{\partial \theta_L} \right] \right\} \quad (44)$$

The bounce-averaged diffusion coefficients are

$$\mathcal{D}_{\theta, \theta} = \tan^2 \theta_L \mathcal{D}_{p, p} \quad (45)$$

$$\mathcal{D}_{\theta, p} = \mathcal{D}_{p, \theta} = -\tan \theta_L \mathcal{D}_{p, p} \quad (46)$$

The energy-diffusion coefficient is

$$\mathcal{D}_{p, p} = \frac{\pi q^2}{v \tau_B} \int_0^\infty k^2 dk \int_{-\pi/2}^{+\pi/2} \sin \phi \Lambda(k, \phi) d\phi \quad (47)$$

where

$$\Lambda(k, \phi) = \frac{4\pi \Omega_e(L)^3}{\omega_p^2} \frac{W_k(\phi, t)}{|\cos \phi|} \left( \frac{ds}{d\Omega} \right)_{(R)} \left[ \frac{\Omega(R)}{\Omega(L)} \right]^2 \frac{p_{||}}{p} b(\phi) \quad (48)$$

Here  $R$  denotes values at the resonance where  $v_{||} \sim v$ , and  $\omega - k_{||} v \simeq 0$ . Note that for small values of  $\phi$ , we can neglect the contribution of the parallel component of the wave field in  $b(\phi)$  (see Eq. (42)), then  $\mathcal{D}_{p, p}$  is approximately independent of  $\mu$ , the equatorial pitch angle, and we write

$$f = F(t) \mu^\sigma K(p) \quad (49)$$

where  $\sigma > 0$  is a free parameter. We define the precipitation lifetime as

$$\tau_p = -\left[ \frac{1}{F} \frac{dF}{dt} \right]^{-1} \quad (50)$$

By combining Eqs. (44) through (46) and Eq. (49), we show

$$\left[ \frac{2\kappa_c}{\tau_B} - \frac{1}{\tau_p} \right] K(p) = \frac{4\sigma(\sigma+1)}{p^2} \mathcal{D}_{p, p} K + \frac{d}{dp} \left[ \mathcal{D}_{p, p} \frac{dK}{dp} \right] - \frac{4\sigma}{p} \mathcal{D}_{p, p} \frac{dK}{dp} - \frac{2\sigma}{p^2} K \frac{d}{dp} [p \mathcal{D}_{p, p}] \quad (51)$$

where  $\kappa_c = \mu_c^{(\sigma+1)}$ . This is an eigenvalue equation for  $\tau_p$  as a function of the free parameter  $\sigma$ . The eigenfunction  $K(p)$  is such that must be regular as  $p \rightarrow 0$ , and well behaved for large  $p$ , i. e. as  $p \rightarrow \infty$  then  $K \ll p^{-2}$ .

## ACKNOWLEDGEMENTS

We are grateful to J. M. Albert and J. U. Kozyra for helpful conversations. This work has been supported in part by the U. S. Air Force contract F19628-89-K-0014 with Northeastern University.

## REFERENCES

- [ 1 ] L. R. Lyons and D. J. Williams, *Quantitative Aspects of Magnetospheric Physics* (D. Reidel Publishing Company, The Netherlands, (1984).
- [ 2 ] C. F. Kennel and H. E. Petschek, *J. Geophys. Res.* **71**, 1 (1966).
- [ 3 ] P. A. Bespalov and V. Yu. Trakhtengerts, *Rev. Plasma Phys.* **10**, 88 (1980).
- [ 4 ] R. A. Helliwell, *J. Geophys. Res.* **72**, 4773 (1967).
- [ 5 ] W. L. Imhof, H. D. Voss, J. B. Reagan, D. W. Datlowe, E. E. Gaines, J. Mobilia and D. S. Evans, *J. Geophys. Res.* **91**, 3077 (1986).
- [ 6 ] E. Villalón, W. J. Burke, P. L. Rothwell, M. B. Silevitch, *J. Geophys. Res.* **94**, 152 (1989).
- [ 7 ] E. Villalón and W. J. Burke, *J. Geophys. Res.* **96**, 9655 (1991).
- [ 8 ] H. C. Koons, *Geophys. Res. Lett.* **2**, 281 (1975).
- [ 9 ] R. A. Kovrazhkin, M. M. Mogilevskii, O. A. Molchanov, Yu. I. Gal'perin, N. V. Dzhordzhio, Zh. M. Bosbe, and A. Rem, *JETP Lett.* **39**, 228 (1984).
- [ 10 ] R. Gendrin, *J. Atmospheric Terrest. Phys.* **30**, 1313 (1968).
- [ 11 ] M. G. Morgan, *J. Geophys. Res.*, **85**, 130 (1980).
- [ 12 ] D. R. Shklyar, *Planet. Space Phys.* **34**, 1091 (1986).
- [ 13 ] K. B. Dysthe, *J. Geophys. Res.* **76**, 6915 (1971).
- [ 14 ] D. Nunn, *Planet. Space Sci.* **19**, 1141 (1971).
- [ 15 ] E. Villalón and W. J. Burke, *Phys. Fluids*, **30**, 3695 (1987).

## PROTON DIFFUSION BY PLASMASPHERIC WHISTLER WAVES

Elena Villalón

Center for Electromagnetics Research,  
Northeastern University, Boston MA 02115

William J. Burke

Phillips Laboratory, Hanscom AFB, MA 01731

## ABSTRACT

Whistler waves propagating near the quasi-electrostatic limit can interact with energetic protons (80 - 500 keV), that are transported into the inner radiation belts. The waves may be launched either from the ground or generated in the magnetosphere due to the resonant interactions with trapped electrons. The wave frequencies are significant fractions of the equatorial electron gyrofrequency, and propagate obliquely to the geomagnetic field. Because of the finite wave spectrum, the inhomogeneity of the geomagnetic field is compensated by the frequency variation, thus the protons stay in gyroresonance with the waves over long distances along the field line. The Fokker-Planck equation is integrated along the flux tube considering the contribution of multiple resonances crossing. The quasilinear diffusion coefficients in energy, cross energy/ pitch angle and pitch angle are obtained for second-order resonant interactions. They are shown to be proportional to the electric fields amplitudes. Numerical calculations for the second order interactions, shows that diffusion dominates near the loss cone and is almost negligible at large pitch angles. The dominant diffusion coefficient is in energy, although the cross energy/ pitch angle diffusion term is also important for small pitch angles. This may explain the induced proton precipitation observed in active space experiments [1, 2].

## 1. INTRODUCTION

Experimental observations of proton precipitation by controlled VLF transmission experiments occur in a wide range of plasmaspheric  $L$  shells. Whistler waves transmitted from the ground are ducted along the field lines to the magnetic equator where they become quasi-electrostatic [1, 2], and interact with the protons in the energy range (80 - 500 keV). It is also known that lightning discharges [3] generate VLF waves that, after entering the magnetosphere, can become trapped bouncing back and forth between hemispheres. These waves can also interact with energetic protons.

The waves considered here are such that the ratios of the wave frequencies to the equatorial electron gyrofrequencies are  $0.5 < \omega/\Omega_e(L) < 1$ . The

*MIT Center for Theoretical Geo/Cosmo Plasma Physics, Cambridge, MA*

frequency range we propose to investigate has been observed in a number of experimental papers [1, 2, 4]. In addition these waves have also been observed by the electric field detector on the CRRES satellite [5]. The electric field amplitudes as measured by the satellite range between  $10^{-5}$  and  $10^{-4}$  V/m.

The wavevectors  $\mathbf{k}$ , form an angle  $\phi$  with the background geomagnetic field  $\mathbf{B}_0$ , which is assumed to be along the  $z$  direction. Figure 1 represents the geometry of the problem. Near the equator the waves propagate obliquely to the geomagnetic field with  $60^\circ < \phi < 90^\circ$ .

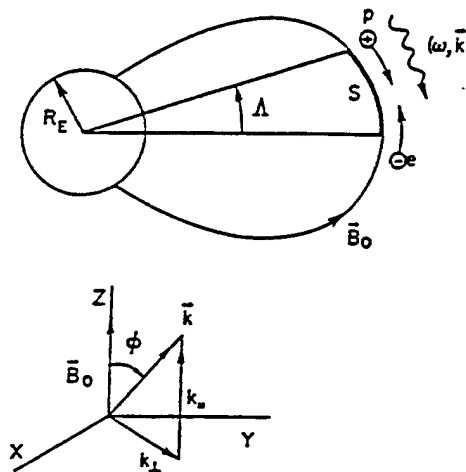


Figure 1. Schematic representation of whistler  $(\omega, \mathbf{k})$ , interacting with electrons and protons near the equator. The coordinate system used in this paper is depicted.

For proton-whistler interactions the particles' parallel velocities  $v_{\parallel}$  and the wave phase velocities are in the same direction. The predominant feature of the proton-whistler interactions is the crossing of multiple harmonics of the proton gyrofrequency [6]. In addition, interactions in the magnetosphere between the transmitted signals and energetic electrons can lead to the amplification and frequency spreading of the original waves [7, 8]. Triggered emissions sometimes have amplitudes which are larger than the initially transmitted wave [9]. They also have narrow spectral bandwidths in frequency and propagation-angle which are closely limited to those of the transmitted waves. Having a finite bandwidth of waves is a key element to enhance the efficiency of proton-whistler interactions. Since resonant interactions with energetic electrons are important sources of wave energy, the

proton-whistler interaction is a complicated process, involving more than one plasma species.

Finite wave bandwidths allow protons and whistlers to satisfy the conditions for second-order resonances [9, 10], where inhomogeneities of the magnetic field are compensated by frequency variations. Thus, the wave packets and particles may remain in resonance for long distance along magnetic field lines. The resonant wave frequency varies as a function of the distance along the field line, compensating for the variation of the geomagnetic field.

This article extends previous work using a Hamiltonian formulation [11] for test-particle interactions with the whistlers which, near the magnetospheric equatorial plane, appear Doppler shifted to some harmonic of the proton gyrofrequency. The affected protons both gain energy from the waves and decrease their pitch-angles while crossing many resonances. Here, we evaluate the diffusion coefficients, for second-order, resonant interactions between protons and whistlers based on this Hamiltonian formulation. The diffusion coefficients are shown to be linearly proportional to the wave's electric field amplitudes.

The paper is organized as follows. Section II contains the resonance condition for the proton whistler interactions at multiple harmonics of the proton gyrofrequency. For a given bandwidth we present the equations that describe the length of the interaction region along the flux tube, and the number of interacting harmonics cover by this length. In Section III the quasilinear diffusion equation is integrated along the flux tube considering the contribution of all harmonics. Section IV contains the diffusion coefficients for the case of a weakly inhomogeneous plasma, where the inhomogeneity of the magnetic field is compensated by the frequency spread of the wave packet. Numerical applications are given in Section V. The main results of our analysis are summarized in Section VI.

## II. RESONANT PROTON WHISTLER INTERACTIONS

We consider a whistler wave of frequency  $\omega$  and wave vector  $\mathbf{k}$ , propagating in a field aligned duct. The geomagnetic field  $\mathbf{B}_0$  is along the  $z$  direction and  $\phi$  is the angle between  $\mathbf{k}$  and  $\mathbf{B}_0$ . The dispersion relation for the refractive index  $\eta = ck/\omega$  is

$$\eta^2 = 1 + \frac{(\omega_p/\omega)^2}{(\Omega_e/\omega) |\cos \phi| - 1} \quad (1)$$

where  $\omega_p$  and  $\Omega_e$  are the electron plasma and gyro frequencies, respectively.

The electric field is  $\mathbf{E} = \hat{x} \mathcal{E}_1 \cos \Psi - \hat{y} \mathcal{E}_2 \sin \Psi - \hat{z} \mathcal{E}_3 \cos \Psi$ , where  $\hat{x}, \hat{y}$  and  $\hat{z}$  are unit vectors;  $\Psi = k_\perp z + k_\parallel z - \omega t$ , and  $k_\parallel, k_\perp$  are the components

along and perpendicular to  $B_0$  of the wave vector. For the case of waves propagating near the resonance cone,  $\omega \sim \Omega_e(L)|\cos \phi|$ , the equatorial refractive index  $\eta^2(L) \gg 1$ . The wave electric field which is linearly polarized, has components  $\mathcal{E}_2/\mathcal{E}_1 \ll 1$ , and  $\mathcal{E}_1/\mathcal{E}_3 \sim -\sin \phi/\cos \phi$ . In this case the wave becomes quasi-electrostatic since  $E$  is almost in the direction of  $k$ , and the group velocities  $v_g \sim 1/\eta$  are very small.

Near the equator, we approximate the Earth's magnetic field by a parabolic profile

$$\frac{\Omega}{\Omega(L)} = 1 + \left(\frac{s}{r_L}\right)^2 \quad (2)$$

where  $s \simeq R_E \Lambda$ ,  $R_E$  is the Earth's radius,  $L$  is the magnetic shell parameter,  $\Lambda$  is the geomagnetic latitude, and  $r_L = (\sqrt{2}/3)R_E L$ . The equatorial gyrofrequency is denoted by  $\Omega(L)$ , and  $\Omega$  stands for the gyrofrequencies either for electrons or protons at a location  $s$  away from the equator along the field line.

Whistler-proton interactions satisfy the resonance condition

$$\omega - k_{\parallel} v_{\parallel} - \ell \Omega_p = 0 \quad (3)$$

where,  $\ell = 0, \pm 1, \pm 2, \dots$  is the harmonic number;  $\Omega_p$  is the proton gyrofrequency; and  $v_{\parallel}$  is the parallel components of the particle's velocity. We call  $\mu = \sin^2 \theta_L$ , where  $\theta_L$  is the equatorial pitch angle. Here  $\theta_L > \theta_c$ , where  $\theta_c$  is the pitch angle at the boundary of the loss cone, and  $\mu_c$  the corresponding value of  $\mu$ . As a function of the  $L$  shell, the mirror ratio is  $\sigma = \mu_c^{-1} = L^3 (4 - 3/L)^{1/2}$ . Protons of energies less than a few hundreds keV, satisfy the resonance condition with waves whose refractive indices  $\eta$  are very large. In fact, the numerical calculations show that  $\eta > 50$ , for energies  $> 50$  keV. As proton energies decrease and pitch angles increase,  $\eta$  increases. If  $\eta$  becomes too large the dispersion relation in Eq. (1) is no longer valid. In this case, we must consider thermal corrections for the plasmaspheric electron population that supports the waves as described by Sazhin, [12]. These thermal corrections limit the magnitudes of  $\eta_{\parallel} = \eta \omega / \Omega_e(L)$ , to finite values. These finite values of  $\eta$ , yield the lower limits for the proton energies, and the upper limits for the pitch angles that may satisfy the resonance condition in Eq. (3).

Here we assume a given wave frequency spectrum of width  $\Delta\omega/\omega$ . The interaction region along the flux tube extend to geomagnetic latitudes such  $0 < \Lambda < \Delta\Lambda$ , where

$$(\Delta\Lambda)^2 = \frac{2}{9} \frac{\Delta\omega}{\omega} \left[ 1 + \tan^2 \theta_L \left( 1 - \frac{\omega}{\cos \phi \Omega_e(L)} \right) \right]^{-1} \quad (4)$$

This interaction region is such that  $0 < \Omega_e - \Omega_e(L) < \Delta\Omega_e$ , where  $\Delta\Omega_e/\Omega_e(L) = 4.5 (\Delta\Lambda)^2$ . The number of possible interacting harmonics,  $n$ , cover by this



spectrum is,

$$n = \frac{m_p}{m_e} \frac{\cos \phi}{(\Omega_e(L)/\omega) |\cos \phi| - 1} (\Delta\Lambda)^2 \quad (5)$$

If  $\rho = v_\perp/\Omega_p$ , is the Larmor radius and  $v_\perp$  is the perpendicular component of the particle velocity, we show  $n < k_\perp \rho$ . Combining Eqs. (4) and (5), yields the number of contributing resonant harmonics  $n$  as function of the width of the spectrum  $\Delta\omega/\omega$ .

The interaction region along the field line has a maximum extent in geomagnetic latitude  $\Delta\Lambda_L$ , i.e.  $\Delta\Lambda \leq \Delta\Lambda_L$ . We show [11]

$$(\Delta\Lambda_L)^2 = \frac{8m_e}{9m_p} k_\perp \rho \left( \frac{\Omega_e(L)}{\omega} - \frac{1}{|\cos \phi|} \right) \quad (6)$$

Note that  $\Delta\Lambda_L$  increases with the particle energy and with the pitch angle. By substituting in Eq. (4),  $\Delta\Lambda$  by  $\Delta\Lambda_L$ , and solving for the bandwidth leads to  $(\Delta\omega/\omega)_L$ . If the widths of the spectrum are equal or larger than  $(\Delta\omega/\omega)_L$  the entire range of resonant harmonics is included in the interactions.

### III. THE DIFFUSION EQUATION

We normalize velocity  $v$  by  $c^{-1}$ , length  $s$  by  $\tau_L^{-1}$ , call  $\tau = t\Omega_p(L)$ , and define  $\kappa = \Omega_p(L) \tau_L/c \sim 1$ . The dimensionless electric field amplitudes are

$$\varepsilon_i = \frac{q\mathcal{E}_i}{m_p c \omega} \quad (7)$$

for  $i = 1, 2, 3$ , and where  $q$  is the proton charge.

The relative wave-proton phase angle is

$$\xi_L = \ell\lambda + \int_0^\tau ds' \tau_L k_\parallel(s') - \frac{\omega}{\Omega_p(L)} \tau \quad (8)$$

where  $\lambda = \arctan[v_y/v_x]$ .

In terms of the three components of the normalized electric field amplitudes, the diffusion equation as given by Lyons [13] is:

$$\begin{aligned} \frac{\partial f}{\partial \tau} + \frac{v_\parallel}{\kappa} \frac{\partial f}{\partial s} &= \frac{\omega}{\Omega_p(L)} \sum_{l=-\infty}^{+\infty} \int \left(\frac{c}{\omega}\right)^3 \frac{d^3 k}{(2\pi)^3} \left[ \hat{G} + \frac{1}{v_\perp} (1 - \eta \cos \phi v_\parallel) \right] \\ &\delta(\eta \cos \phi v_\parallel + l \frac{\Omega_p}{\omega} - 1) \left( \sqrt{\pi} \frac{v_\parallel}{v_\perp} \Upsilon_l \right)^2 \hat{G} f \end{aligned} \quad (9)$$

where the operator  $\hat{G}$  is a function of  $\partial/\partial\mu$  and  $\partial/\partial v$ , and is defined in [13]. Here  $\Upsilon_l$  is

$$\Upsilon_l = \frac{1}{2} [(\varepsilon_1 - \varepsilon_2) \mathcal{J}_{l+1}(k_\perp \rho) + (\varepsilon_1 + \varepsilon_2) \mathcal{J}_{l-1}(k_\perp \rho)] \frac{v_\perp}{v_\parallel} - \varepsilon_3 \mathcal{J}_l(k_\perp \rho) \quad (10)$$

where  $J_\ell$  are Bessel functions of argument  $k_\perp \rho$ .

To include the effects of the atmospheric loss cone, we introduce the term  $f/\tau_{atm}$ . Here  $\tau_{atm} = \tau_B/2$ , if  $\theta_L$  is within the loss cone and  $\tau_{atm} = \infty$ , if  $\theta_L$  is outside the loss cone. The proton bounce period,  $\tau_B$ , is the time for a particle to travel from one mirror point to the other and back again. Next integrate along the flux tube by applying the operator:  $\int_{-\infty}^{+\infty} ds/(\tau_B v_\parallel)$  to both sides of Eq. (9), which becomes:

$$\frac{\partial f}{\partial \tau} + \frac{f}{\tau_{atm}} = \sum_{\ell=-\infty}^{+\infty} \int_0^\infty \eta^2 d\eta \int_{-\pi/2}^{\pi/2} \sin \phi d\phi \frac{1}{v^2} \mathcal{T}_\ell \quad (11)$$

where

$$\begin{aligned} \mathcal{T}_\ell = & \frac{\partial}{\partial \mu} \left[ v \mathcal{D}_{\mu,v} \frac{\partial}{\partial v} + \mathcal{D}_{\mu,\mu} \frac{\partial}{\partial \mu} \right] f + \\ & \frac{\partial}{\partial v} \left[ v^2 \mathcal{D}_{v,v} \frac{\partial}{\partial v} + v \mathcal{D}_{v,\mu} \frac{\partial}{\partial \mu} \right] f \end{aligned} \quad (12)$$

The diffusion coefficients are obtained after integrating along the field lines as follows:

$$\mathcal{D}_{v,v} = \left[ \frac{\omega}{\Omega_p(L)} \kappa \right]^2 \frac{1}{4\pi \tau_B v} \frac{\Upsilon_\ell^2}{v |d^2 \xi_\ell / ds^2|} \quad (13)$$

$$\mathcal{D}_{v,\mu} = \mathcal{D}_{\mu,v} = 2\mu \left[ \ell \frac{\Omega_p(L)}{\omega \mu} - 1 \right] \mathcal{D}_{v,v} \quad (14)$$

$$\mathcal{D}_{\mu,\mu} = 4\mu^2 \left[ \ell \frac{\Omega_p(L)}{\omega \mu} - 1 \right]^2 \mathcal{D}_{v,v} \quad (15)$$

where  $\Upsilon_\ell$  must be evaluated at the resonance,  $\tau_B v \sim 6\sqrt{2}\kappa \times 1.3802$  is independent of  $v$ , and  $d^2 \xi_\ell / ds^2$  will be defined in Eq. (22).

We define the diffusion functions

$$\mathcal{W}(\mu, v) = \beta \sum_{\ell=-n}^{+n} \mathcal{D}_{v,v} \quad (16)$$

$$\mathcal{N}(\mu, v) = \beta \sum_{\ell=-n}^{+n} \mathcal{D}_{v,\mu} \quad (17)$$

$$\mathcal{P}(\mu, v) = \beta \sum_{\ell=-n}^{+n} \mathcal{D}_{\mu,\mu} \quad (18)$$

where

$$\beta \sim \eta(L)^2 [\Omega_e(L) \left( \frac{d\eta}{d\omega} \right)_L] \left[ \frac{\Delta\omega}{\Omega_e(L)} \right]^2 \quad (19)$$

depends on the width of the frequency spectrum. The summation extends to all the resonant harmonics, where  $n$  is defined in Eq. (5). If the interaction region,  $\Delta\Lambda$ , spans the entire range of resonant harmonics,  $\Delta\Lambda = \Delta\Lambda_L$ , then we may take  $n \rightarrow \infty$ .

Next take  $f = F(\tau_0) G(v, \mu)$ , where  $\tau_0 = \tau v$  is independent of  $v$  and  $\mu$ . We define the precipitation life times,

$$\hat{\tau}_p = -[F \frac{dF}{d\tau_0}]^{-1} \quad (20)$$

and  $\hat{\tau}_{atm} = \tau_{atm} v$ , which are independent of  $v$ . After substituting in Eqs. (11) and (12), we find that

$$\begin{aligned} \left[ -\frac{1}{\hat{\tau}_p} + \frac{1}{\hat{\tau}_{atm}} \right] v \quad G(v, \mu) = \frac{1}{v^2} \frac{\partial}{\partial \mu} \left[ v \mathcal{N}(\mu, v) \frac{\partial}{\partial v} + \mathcal{P}(\mu, v) \frac{\partial}{\partial \mu} \right] G + \\ \frac{1}{v^2} \frac{\partial}{\partial v} \left[ v^2 \mathcal{W}(\mu, v) \frac{\partial}{\partial v} + v \mathcal{N}(\mu, v) \frac{\partial}{\partial \mu} \right] G \end{aligned} \quad (21)$$

#### IV. THE WEAKLY INHOMOGENEOUS CASE

By differentiating along the field line, we show [11]

$$\frac{d^2 \xi_L}{ds^2} = \alpha + \cos \xi_L \frac{(k_{\parallel} r_L)^2}{v_{\parallel}} \Upsilon_L \quad (22)$$

The inhomogeneity factor  $\alpha$  depends on the variation of the geomagnetic field, and the frequency spectrum,

$$\begin{aligned} \alpha = \kappa \frac{\omega}{\Omega_p(L)} \left[ \Omega_e(L) \frac{d\eta}{d\Omega_e} \cos \phi - \eta(L) \cos \phi \frac{\mu}{2(1-\mu)} \right] \frac{1}{\Omega(L)} \frac{d\Omega}{ds} + \\ \kappa \frac{\omega}{\Omega_p(L)} \frac{d(\eta \cos \phi)}{d\omega_\phi} \frac{d\omega_\phi}{ds} \end{aligned} \quad (23)$$

where  $\omega_\phi = \omega / \cos \phi$ , and we assume that  $d\xi_L/ds = 0$ .

For sufficiently large waves amplitudes, and for a wave spectrum such that we can neglect the contribution of  $\alpha$  in the right-hand-side of Eq. (22), the inhomogeneity of the magnetic field is compensated by the wave spectrum and the solutions of the equations of motion resemble that of a homogeneous plasma. From Eq. (13) and (22) we obtain that the energy diffusion coefficient is:

$$\mathcal{D}_{v,v} = \frac{1}{8 (\eta \cos \phi)^2} \frac{1}{\tau_B v} \frac{v_{\parallel}}{v} \Upsilon_L \quad (24)$$

The other coefficients are given in terms of  $\mathcal{D}_{v,v}$  by means of Eqs. (14) and (15). A comparison with Eq. (10) shows that  $\mathcal{D}_{v,v}$  depends linearly on the electric fields amplitudes.

The diffusion functions  $\mathcal{W}, \mathcal{N}$  and  $\mathcal{P}$ , are given by Eqs. (16) – (19). If the interaction region  $\Delta\Omega_e$  extends to the entire spectrum of resonant harmonics, we may take  $n \rightarrow \infty$ . In this case, we can add over all the harmonics, by considering that  $(\Omega_p(L)/\omega \mu) \ll 1$  we obtain

$$\mathcal{W}(\theta_L) = \beta \frac{1}{8(\eta \cos \phi_r)^2} \frac{1}{\tau_B v} [\varepsilon_1 \sin \theta_L - \varepsilon_3 \cos \theta_L] \quad (25)$$

$$\mathcal{N}(\theta_L) = 2 \mathcal{W}(\theta_L) [\tan \theta_L \tan \phi_r - \sin^2 \theta_L] \quad (26)$$

$$\mathcal{P}(\theta_L) = 4 \mathcal{W}(\theta_L) [\tan \theta_L \tan \phi_r - \sin^2 \theta_L]^2 \quad (27)$$

For small pitch angles  $\sin \theta_L \rightarrow 0$ , energy diffusion dominates over pitch angle diffusion.

In the strongly inhomogeneous case, the changes in the magnetic field and the wave spectrum are such that  $\alpha \neq 0$ . In this case Eq. (22) is approximated as,  $d^2 \xi_L / ds^2 \sim \alpha$  and protons are only able to achieve first-order resonances. For waves near the quasi-electrostatic limit, the energy diffusion coefficient, becomes

$$\mathcal{D}_{v,v} = \left[ \frac{\omega}{2 \Omega_p(L)} \right]^{3/2} \frac{\kappa}{2 \pi \tau_B v} \frac{\omega_p}{\Omega_e(L)} v [\Upsilon_L^2 (1 - \mu)] \quad (28)$$

The other coefficients are readily obtained combining Eqs. (28), (14) and (15). By comparing Eqs. (28) and (24), we see that for second-order resonant interaction the diffusion coefficient is  $\sim \varepsilon$ , the amplitudes of the electric fields. For first-order interactions  $\sim \varepsilon^2$ , and thus the diffusion coefficient for first-order resonances is much smaller than for second-order interactions.

## V. NUMERICAL APPLICATIONS

We have carried out some numerical calculations based on the model we presented in the previous sections for the shell  $L = 3.5$ , where the equatorial geomagnetic field is  $B_0 = 7.25 \times 10^2$  nT. The ratio between the electron plasma frequency and the equatorial cyclotron frequency is  $\omega_p / \Omega_e(L) = 7.9$ . The width of the equatorial loss cone is  $\theta_c = 6.5^\circ$ . Calculations were conducted for the three frequencies  $\omega / \Omega_e(L) = 0.5, 0.75$  and  $0.9$ .

In Figure 2 we show  $\Delta\Lambda_L$  (in degrees) as given in Eq. (4) versus the proton energy (in keV), for the three frequencies. For the left and right pannels  $\theta_L = 6.5^\circ$  and  $25^\circ$ , respectively. The resonant interaction along the flux tube is such that  $\Delta\Omega_e / \Omega_e(L) = 4.5(\Delta\Lambda_L)^2$ . As the pitch angle increases so does  $\Delta\Lambda_L$ . The width of the frequency spectrum corresponding to the maximum

extent of the interaction region, is  $(\Delta\omega/\omega)_L$  is defined at the end of Section II.

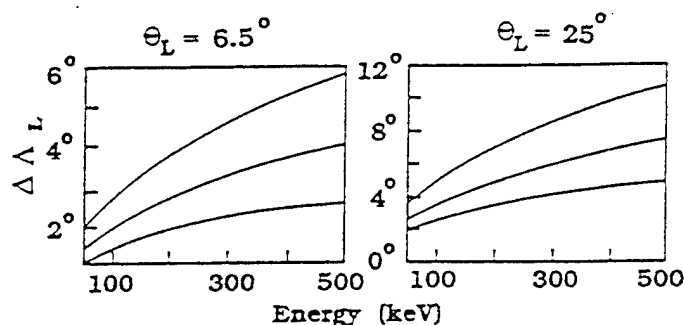


Figure 2. Maximum extent in the geomagnetic latitude for resonant interactions versus the proton energy in keV.

In Figure 3 we represent  $(\Delta\omega/\omega)_L$  as function of the energy and for the same parameters as in Fig. 2; for the left and right pannels  $\theta_L = 6.5^\circ$  and  $25^\circ$ .

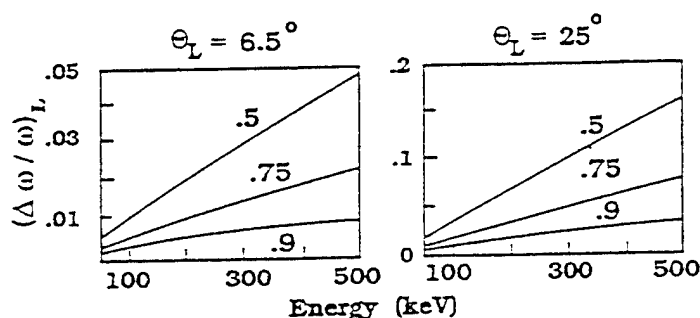


Figure 3. Bandwidth of the frequency spectrum corresponding to the geomagnetic latitudes of Fig. 2 versus proton energy in keV.

We see that near the loss cone the bandwidth of the spectrum needed to cover the entire interaction region for second-order resonant protons, is much smaller than for larger pitch-angles. The bandwidth increases with increasing energy, and as  $\omega/\Omega_e(L)$  decreases. Thus particles are more easily scattered in pitch angles for smaller energies ( $\sim 100$  keV) and for pitch-angles that are near the loss cone. Because the bandwidth of the spectrum becomes unrealistically large for larger pitch angles and energies, the protons may not stay in gyroresonance with the waves over the entire range of resonant

harmonics and the interaction is not very efficient. Thus we expect most of the diffusion take place near the loss cone and at small energies (i.e.  $\sim 100$  keV).

We have performed some calculations of the diffusion coefficients for second-order resonant interactions. The diffusion functions are given in Eqs. (16) – (18), where the number of interacting harmonics  $n$ , is a function of the width of the spectrum  $\Delta\omega/\omega$ , by combining Eqs. (4) and (5). They depend on the normalized electric field amplitudes  $\varepsilon = 2.5 \times 10^{-6} \times f_e \mathcal{E}$ , where  $f_e = \Omega_e(L)/\omega$ , and  $\mathcal{E}$ , the electric field amplitude, should be given in V/m. The energy diffusion coefficient is given in Eq. (24). The cross pitch angle/energy and pitch angle coefficients are obtained combining Eq. (24) with Eqs. (14) and (15).

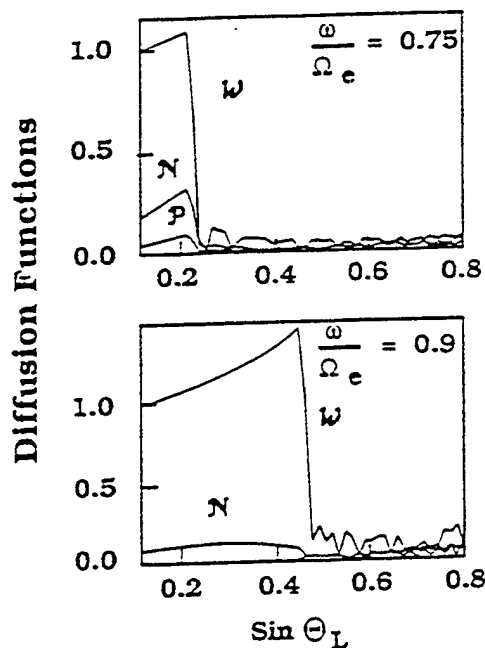


Figure 4. Diffusion functions normalized to the values of the energy term at the edge of the loss cone versus  $\sin \theta_L$ , for  $\theta_L > 6.5^\circ$ .

Figure 4 gives the normalized diffusion coefficients versus  $\sin \theta_L$ , for  $\theta_L > \theta_c =$

6.5°, for 100 keV protons, and for a spectral bandwidth of  $\Delta\omega/\omega = 0.01$ . The upper and lower pannels correspond to  $\omega/\Omega(L) = 0.75$  and 0.9, respectively. The diffusion functions are normalized to the value that the energy diffusion function,  $\mathcal{W}$ , takes at the edge of the loss cone which is represented by  $w_e = \mathcal{W}_e/\varepsilon_1$ . Here  $\varepsilon_1 \sim \varepsilon \sin \phi_r$ , and  $\mathcal{W}_e$  is given by Eq. (25) taking  $\theta_L = \theta_e$ .

Significant diffusion takes place mostly near the loss cone. It extends to larger pitch angles as  $\omega \rightarrow \Omega_e(L)$ . The reasons for this have already been explained since near the loss cone protons and whistlers stay in gyroresonance over the entire range of possible resonant harmonics that contribute to the interaction. We also observed that the dominant diffusion coefficient is the energy term. However the contribution of the cross energy/pitch angle coefficient is also significant. For  $\omega/\Omega(L) = 0.75$ , the normalized energy diffusion function at the edge of the loss cone is  $w_e = 2.5 \times 10^{-3}$ . For  $\omega/\Omega(L) = 0.9$ ,  $w_e = 3. \times 10^{-3}$ . We have calculated  $w_e$  for 500 keV protons, and  $\omega/\Omega(L) = 0.75$ , and found that *i.e.*  $w_e = 2. \times 10^{-7}$ . In addition, protons and waves do not stay in gyroresonance over the whole length of resonant interaction for larger energies even at the edge of the loss cone. Thus as explained above, second-order resonant diffusion will be more efficient for protons with energies of  $\sim 100$ , keV and with pitch angles near the loss cone.

## VI. CONCLUSIONS

We have investigated the diffusion of protons by quasi-electrostatic whistler waves, by using the Fokker-Planck diffusion equation. We assume a spectrum such that the ratios of the waves- to the equatorial electron gyro-frequencies are  $0.5 < \omega/\Omega_e(L) < 1$ . The main results of our theoretical analysis and the numerical applications are:

- (1) For second-order resonant interactions the inhomogeneity of the geomagnetic field is compensated by the frequency variation along the field line, and protons and waves can stay in gyroresonance over long distance along the field lines.
- (2) The extent of the regions of resonant interactions along the flux tube decrease with the protons energies and pitch angles. The interactions are most efficient for protons of relatively small energies ( $\sim 100$  keV), and small pitch angles.
- (3) For second-order resonant interactions, the diffusion coefficients are linearly proportional to the amplitudes of the electric fields .
- (4) The dominant diffusion coefficient is in energy but the cross energy/pitch angle coefficients is also significant for pitch angles near the loss cone.

## ACKNOWLEDGEMENTS

This work has been supported in part by the U. S. Air Force contract F19628-89-K-0014 with Northeastern University.

## REFERENCES

- [1] H. C. Koons, *Geophys. Res. Lett.* 2, 281 (1975).
- [2] R. A. Kovrazhkin, M. M. Mogilevskii, O. A. Molchanov, Yu. I. Gal'perin, N. V. Dzhordzhio, Zh. M. Boske, and A. Rem, *JETP Lett.* 39, 228 (1984).
- [3] W. C. Burgess, and U. S. Inan, *Geophys. Res. Lett.*, 17, 259 (1990).
- [4] R. L. Dowden, A. D. McKay, L. E. S. Amon, H. C. Koons and M. H. Dazey, *J. Geophys. Res.* 83, 169 (1978).
- [5] M. S. Gussenhoven, E. G. Mullen and R. C. Sagalyn, CRRES/SPACERAD Experiment Descriptions, Environmental Research Papers, No. 906, AFGL-TR-85-0017. Air Force Geophysics Laboratory, Hanscom AFB 01731.
- [6] D. R. Shklyar, *Planet. Space Phys.* 34, 1091 (1986).
- [7] C. F. Kennel and H. E. Petschek, *J. Geophys. Res.* 71, 1 (1966).
- [8] P. A. Bespalov and V. Yu. Trakhtengerts, *Rev. Plasma Phys.* 10, 88 (1980).
- [9] R. A. Helliwell, *J. Geophys. Res.* 72, 4773 (1967).
- [10] K. B. Dysthe, *J. Geophys. Res.* 76, 6915 (1971).
- [11] E. Villalón and W. J. Burke, *J. Geophys. Res.* 98, 13,509 (1993).
- [12] S. Sazhin, *Whistler-Mode Waves in a Hot Plasma* (Cambridge Atmospheric and Space Science Series, Cambridge University Press, Great Britain, 1993).
- [13] L. R. Lyons and D. J. Williams, *Quantitative Aspects of Magnetospheric Physics* (D. Reidel Publishing Company, The Netherlands, 1984).



# Proton Whistler Interactions Near the Equator in the Radiation Belts

ELENA VILLALÓN

*Center for Electromagnetics Research, Northeastern University, Boston, Massachusetts*

WILLIAM J. BURKE

*Geophysics Directorate, Hanscom Air Force Base, Massachusetts*

The interactions of energetic protons with whistlers propagating near the quasi-electrostatic limit, are investigated using a test particle, Hamiltonian formalism. We assume that wave packets exist with finite bandwidths of frequencies, which are close to the equatorial electron gyrofrequency and propagate obliquely with respect to the geomagnetic field. Near the equator the protons interact with the waves which appear Doppler shifted to some harmonic of their cyclotron frequency. In an inhomogeneous geomagnetic field the spacing between cyclotron harmonic resonances is very small. The Hamiltonian equations of motion are solved including multiple, independent harmonics for each resonance. The wave frequency varies as a function of the distance along the field line, with only one frequency being resonant at a given point. Thus the inhomogeneity of the magnetic field is compensated by the frequency variation. The proton whistler interactions satisfy the conditions for second-order resonances for all the harmonics. The resonances may also overlap in phase space, leading to significant changes in the protons energies and pitch angles. The combined contributions of positive and negative harmonics allow protons to diffuse toward smaller pitch angles. Numerical calculations applying this formalism to parameters relevant to the plasmasphere and controlled VLF transmission experiments are presented.

## 1. INTRODUCTION

The interactions between whistler waves and electrons in the plasmasphere [see, *Lyons and Williams*, 1984, and references therein], account for phenomena such as energetic electron precipitation [*Imhof et al.*, 1986; *Inan*, 1987; *Schulz and Davidson*, 1988] enhancements of naturally occurring waves [*Kennel and Petschek*, 1966; *Bespalov and Trakhtengerts*, 1980], and the artificially triggered emissions [*Helliwell*, 1967, 1988; *Dysthe*, 1971; *Sudan and Ott*, 1971]. These phenomena are most likely due to the resonant interactions at some harmonic of the electron gyrofrequency. The first harmonic and the Landau resonance play the most important role in the electron whistler interactions, although higher harmonics may also contribute [*Villalón et al.*, 1989; *Villalón and Burke*, 1991]. They are most significant at the magnetospheric equator where the geomagnetic field changes slowly allowing particles to stay in resonance over relatively long distances. The component of the wave phase velocities along the Earth's magnetic field  $\omega/k_{\parallel}$  of whistlers and the parallel velocities  $v_{\parallel}$  of resonant electrons are oppositely directed.

Interactions of whistlers with protons have not received as much attention as those with electrons [*Gendrin*, 1972]. However, a number of experimental observations [*Kovrazhkin et al.*, 1983, 1984; *Koons*, 1975, 1977] have shown that VLF transmission pulses can precipitate 80- to 500-keV protons into the ionosphere. They occur in a range of plasmaspheric  $L$  shells, and are due to the resonant interactions near the magnetic equator. In the quasi-electrostatic limit [*Sazhin*, 1986; *Morgan*, 1980] the whistlers satisfy the relationship,  $\omega \simeq$

$\Omega_e(L) \cos \phi$ , where  $\phi$  is the angle between the wave vector,  $\mathbf{k}$ , and the geomagnetic field,  $\mathbf{B}_0$  and  $\Omega_e(L)$  is the equatorial electron gyrofrequency. Here the parallel component of the wave vector  $k_{\parallel}$  is large and the resonant energies of protons relatively low. In this paper we assume that the propagation properties of waves in the plasmasphere are described by a dense population of cold particles of ionospheric origin whose distribution function is isotropic in pitch angle. The predominant feature of the whistler proton interactions is the crossing of multiple harmonics of the proton gyrofrequency [*Shklyar*, 1985]. As summarized in Figure 1, resonant protons and whistlers travel in the same direction, with the wave phase velocity which may be slightly larger or smaller than the proton parallel velocity, depending on the interacting harmonics. By way of contrast, resonant whistler electron interactions travel in opposite directions and the dominant harmonic is the first.

*Shklyar* [1986] devised an electrostatic, single-frequency wave theory to explain the proton whistler interactions as causes of experimentally observed proton precipitations. It is based on a Hamiltonian analysis that includes multiple-cyclotron resonances in a strongly inhomogeneous field. He finds that for large wave amplitudes ( $\sim 10^{-2}$  V/m), resonances can overlap and lead to pitch angle diffusion toward the loss cone. Here we also present a Hamiltonian formulation of proton whistler interactions for multiple-resonances crossing. However, we use an electromagnetic formulation of the Hamiltonian, and take the quasi-electrostatic limit near the magnetic equator where most of the significant interactions occur. Our work also differs from *Shklyar's* in that we invoke interactions with the multiple-frequencies of a propagating wave packet. We assume the wave frequency with which a test particle interacts, is a function of the distance along the field line  $s$ , with only one frequency being resonant at a given location. Thus

Copyright 1993 by the American Geophysical Union.

Paper Number 93JA00727.  
0148-0227/93/93JA-00727\$05.00

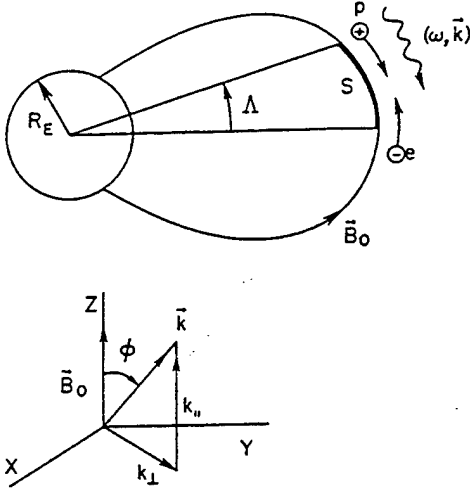


Fig. 1. Schematic representation of whistler  $(\omega, \vec{k})$ , interacting with electrons and protons near the equator. The Earth's dipole magnetic field is  $\vec{B}_0$ , the geomagnetic latitude is  $\Lambda$ , and  $s$  is the coordinate along the flux tube. The coordinate system used in this paper is depicted here.

the inhomogeneity of the magnetic field is compensated by the frequency variation. Because of this, protons and whistlers satisfy the conditions for second-order, resonances making the interactions more efficient. If we restrict ourselves to a wave of constant frequency [Matsumoto, 1979], large electric field amplitudes are required to produce considerable changes in pitch angle.

As a matter of fact in VLF transmissions experiments natural whistlers whose frequencies are close to the transmitter frequency, are also amplified due to the linear and nonlinear interactions with the radiation belt electrons. The amplitudes of the stimulated waves sometimes become larger than the originally transmitted wave [Dowden *et al.*, 1978]. In this paper we assume there exists a spectrum of wave frequencies of comparable electric-field amplitudes. Based on these assumptions, we show that the field amplitudes required to overlap the resonances and achieve efficient interactions with the protons, are relatively small ( $\sim 10^{-4}$  V/m).

Our main contribution is a detailed analysis of conditions leading to second-order resonances [Nunn, 1973; Carlson, *et al.*, 1985], which are responsible for the efficiency of the interactions. We call

$$\zeta_{\ell} = 1 - \eta \cos \phi \frac{v_{\parallel}}{c} - \ell \frac{\Omega_p}{\omega} \quad (1)$$

where  $\ell = 0, \pm 1, \pm 2, \dots$ ,  $\eta$  is the refractive index, and  $\Omega_p$  is the proton gyrofrequency. In the articles by Shklyar the proton whistler interactions only satisfy first-order resonant conditions, i.e.,  $\zeta_{\ell} = 0$ ; and the changes in particle's energy and momentum are linearly proportional to the wave electric fields. Second-order resonant particles must also satisfy the condition  $d\zeta_{\ell}/ds = 0$ , which requires a frequency variation,  $\omega(s)$ , along the field line. Here  $d/ds$  represents differentiation with respect to distance along a given field line. Second-order resonant protons interacting with frequency-varying,  $\omega(s)$ , wave packets encounter multiple harmonics of their gyrofre-

quency along the field lines. The accumulative effect of the multiple-resonance crossings is a change in the particle's momentum and energy proportional to the square root of the electric fields. Note that this result resembles that of a homogeneous plasma [Chirikov, 1979] but, because of the geomagnetic field, multiple resonances are present in small distances along the field lines.

The paper is organized as follows. Section 2 contains a description of the whistlers propagating near the quasi-electrostatic limit in an inhomogeneous magnetic field which, near the equator, we approximate as having a parabolic profile. In section 3 we analyze resonance conditions at multiple harmonics of the proton gyrofrequency and find the locations of these resonances along the flux tube. We show that the separation distance between nearby resonances is proportional to  $[m_e/m_p]^{1/2}$  where  $m_{e,p}$  are the electron and proton masses, respectively. In section 4 the Hamiltonian equations are presented. After reducing the problem to one dimension and isolating a single cyclotron resonance, the differential equations for the action  $I$ , angle  $\xi_{\ell}$ , variables as function of the distance  $s$  along the flux tube are derived. In section 5 we solve these equations near resonance by using a Taylor expansion. The changes in action,  $\Delta I$ , energy, and pitch angle are calculated for each resonance. Resonances overlap if  $\Delta I_{\ell}$  is larger than the separation,  $|I_{\ell+1} - I_{\ell}|$ , between nearby resonances. Section 6 contains the formulation of the second order-resonances.

The numerical applications are presented in sections 7 and 8. We assume a bandwidth of frequencies and wave propagation vectors such that the second-order resonance condition and overlapping criterion are met for all the harmonics. We study interactions along the  $L = 3.5$  geomagnetic shell; the wave frequencies are such that  $0.5 \leq f_e^{-1} \leq 1$ , where  $f_e^{-1} = \omega/\Omega_e(L)$ . As an example we study the equatorial pitch angle to be  $\theta(L) = 7.5^\circ$ , where  $\tan \theta(L) = v_{\perp}/v_{\parallel}$ , and present two examples for the particle energies of  $\sim 150$ - and  $500$ -keV. Resonances are confined to within about a few degrees latitude of the equator; positive  $\ell > 0$ , and negative  $\ell < 0$ , harmonics are considered. We show that although smaller frequencies, i.e.,  $\omega \sim 0.5\Omega_e(L)$ , yields larger changes in pitch angle than higher frequencies,  $\omega \rightarrow \Omega_e(L)$ , the band-width of the frequencies and wave angles needed for  $f_e^{-1} = 0.5$ , are larger than for frequencies  $\omega \rightarrow \Omega_e(L)$ . We add the contributions of all resonances, taking the same electric field amplitudes for the whole spectrum of waves. For amplitudes of about  $10^{-4}$  V/m, the pitch angles can decrease one degree or more in a single bounce time. Section 9 summarizes our results.

## 2. QUASI-ELECTROSTATIC WHISTLER WAVES

Consider a whistler wave of frequency  $\omega$  and wave vector  $\vec{k}$ , propagating in a field aligned duct. The geomagnetic field  $\vec{B}_0$  is along the  $z$  direction and  $\phi$  is the angle between  $\vec{k}$  and  $\vec{B}_0$ . The refractive index  $\eta = ck/\omega$  satisfies the dispersion relation

$$\eta^2 = \frac{(\omega_p/\omega)^2}{(\Omega_e/\omega)|\cos \phi| - 1} \quad (2)$$

where  $\omega_p$  and  $\Omega_e$  are the electron plasma and gyro frequencies, respectively.

The electric field is

$$\mathbf{E} = \hat{x} \mathcal{E}_1 \cos \Psi - \hat{y} \mathcal{E}_2 \sin \Psi - \hat{z} \mathcal{E}_3 \cos \Psi \quad (3)$$

where  $\hat{x}$ ,  $\hat{y}$ , and  $\hat{z}$  are unit vectors;  $\Psi = k_\perp x + k_\parallel z - \omega t$ , and  $k_\parallel$ ,  $k_\perp$  are the components along and perpendicular to  $\mathbf{B}_0$  of the wave vector. The ratios of the electric field components are

$$\frac{\mathcal{E}_2}{\mathcal{E}_1} = \frac{1}{\eta^2} \frac{(\omega_p/\omega)^2}{(\Omega_e/\omega) - |\cos \phi|} \quad (4)$$

$$\frac{\mathcal{E}_3}{\mathcal{E}_1} = \frac{1 - (\omega_p/\omega)^2 - (\eta \sin \phi)^2}{\eta^2 \sin \phi \cos \phi}$$

For the case of waves propagating near the resonance cone,  $\omega \sim \Omega_e(L)|\cos \phi|$ , the equatorial refractive index  $\eta^2(L) \gg 1$ . The wave electric field which is linearly polarized, has components  $\mathcal{E}_2/\mathcal{E}_1 \ll 1$ , and  $\mathcal{E}_1/\mathcal{E}_3 \sim -\sin \phi/\cos \phi$ . In this case the wave becomes quasi-electrostatic since  $\mathbf{E}$  is almost in the direction of  $\mathbf{k}$ , and the group velocities  $v_g \sim 1/\eta$  are very small.

Near the equator, we approximate the Earth's magnetic field by a parabolic profile

$$\frac{\Omega}{\Omega(L)} = 1 + \left(\frac{s}{r_L}\right)^2 \quad (5)$$

where  $s \simeq R_E L \Lambda$ ,  $R_E$  is the Earth's radius,  $L$  is the magnetic shell parameter,  $\Lambda$  is the geomagnetic latitude, and  $r_L = (\sqrt{2}/3)R_E L$ . The equatorial gyrofrequency is denoted by  $\Omega(L)$ , and  $\Omega$  stands for the gyrofrequencies either for electrons or protons at a location  $s$  away from the equator along the field line. For interactions that occur near the equator the cold plasma density and  $\cos \phi$  remains nearly constant over the region of interaction along the flux tube [Bell, 1984, 1986]. The refractive index  $\eta$  changes according to (2) and the magnetic field profile in (5). For quasi-electrostatic whistlers  $\cos \phi \sim \omega/\Omega_e$ ; if we consider interactions that occur within  $5^\circ$  off the equator the variation in  $\phi$  will be less than one degree.

### 3. RESONANT PROTON WHISTLER INTERACTIONS

Interactions between whistlers and protons satisfy the resonance condition

$$\omega - k_\parallel v_\parallel - \ell \Omega_p = 0 \quad (6)$$

where,  $\ell = 0, \pm 1, \pm 2, \dots$  is the harmonic number;  $\Omega_p$  is the proton gyrofrequency; and  $v_\parallel$  is the parallel component of the particle's velocity. We call  $\mu = \sin^2 \theta(L)$ , where  $\theta(L)$  is the equatorial pitch angle. Here  $\theta(L) > \theta_c(L)$ , where  $\theta_c(L)$  is the pitch angle at the boundary of the loss cone, and  $\mu_c$  the corresponding value of  $\mu$ . As a function of the  $L$  shell, the mirror ratio is  $\sigma = 1/\mu_c = L^3 (4 - 3/L)^{1/2}$ . To zero order in the electric field amplitudes, the first adiabatic invariant is conserved. Then we may write for the parallel

and perpendicular components of the particle velocity  $v$ :  $v_\parallel = v[1 - \mu\Omega/\Omega(L)]^{1/2}$ ,  $v_\perp = v[\mu\Omega/\Omega(L)]^{1/2}$ . Note that as the particles and waves move away from the equator, the parallel velocities  $v_\parallel$  of particles decrease, while the waves' phase velocities  $\omega/k_\parallel$  increase.

For purpose of bookkeeping it is useful to introduce an integer variable  $\nu > 0$  such that if a proton interacts at the equator with the harmonic  $\ell = -\nu$ , then its velocity is given solving for the equation:  $\omega - k_\parallel v_\parallel = -\nu\Omega_p(L)$ ,

$$\frac{v}{c} = \frac{1}{\eta(L) \cos \phi} \frac{1}{(1 - \mu)^{1/2}} (1 + \nu f_p) \quad (7)$$

where  $f_p = \Omega_p(L)/\omega \ll 1$  and  $\eta(L)$  is the equatorial value of  $\eta$ . The cyclotron harmonic number  $\nu$ , will be given in terms of  $k_\perp v_\perp/\Omega_p$ , after we analyze the Hamiltonian equations in section 4.

We solve (6), using the parabolic magnetic field profile in (5). See Appendix A for details. If the particle's velocity is as given in (7), the geomagnetic latitude  $\Lambda_\ell$  of higher harmonics turn out to be

$$\Lambda_\ell^2 = \frac{4}{9} \frac{m_e}{m_p} (\ell + \nu) (f_e |\cos \phi| - 1) \frac{1}{g(\mu)} \quad (8)$$

where  $f_e = \Omega_e(L)/\omega \sim 1$ ,  $m_e, m_p$  are the electron, proton masses, and

$$g(\mu) = \frac{\mu}{1 - \mu} (|\cos \phi| - \frac{1}{f_e}) + |\cos \phi|. \quad (9)$$

Near the resonance cone  $g(\mu) \sim |\cos \phi|$ . The distance along the flux tube at which the resonant interaction occurs is given by,  $s_\ell = R_E L \Lambda_\ell$ . The distance between the location of two subsequent resonances is obtained from  $\Delta s_\ell = R_E L (\Lambda_{\ell+1} - \Lambda_\ell)$ . Since  $m_e/m_p$  and  $(f_e |\cos \phi| - 1)$  are small, resonances, as given by (8), occur at close separation distances.

The harmonics that contribute to the resonant interactions are such that  $\ell \geq -\nu$ . The Landau resonance occurs at a location,  $\Lambda_0$ , off the equator given by solving (8) with  $\ell = 0$ . The negative harmonics  $-\nu \leq \ell < 0$  are located along the flux tube at magnetic latitudes  $0 \leq \Lambda < \Lambda_0$ . For waves and particles to interact at the negative harmonics, the wave phase velocity  $\omega/k_\parallel$  is slightly smaller than the protons parallel velocities  $v_\parallel$ . Positive harmonics,  $0 \leq \ell < \nu$ , are located at equatorial magnetic latitudes  $\Lambda \geq \Lambda_0$ . Here  $\omega/k_\parallel$  is slightly larger than  $v_\parallel$ . For the Landau resonance  $\omega/k_\parallel = v_\parallel$ .

### 4. THE HAMILTONIAN EQUATIONS

We normalize velocity  $v$  by  $c^{-1}$ , length  $s$  by  $r_L^{-1}$ , call  $\tau = t\Omega_p(L)$ , and define  $\kappa = \Omega_p(L) r_L/c \sim 1$ . Henceforth we only refer to these normalized variables. The dimensionless electric field amplitudes are

$$\epsilon_i = \frac{q\mathcal{E}_i}{m_p c \omega \kappa} \quad (10)$$

for  $i = 1, 2, 3$ , and where  $q$  is the proton charge. We define the canonical velocities,

$$V_{\parallel} = \frac{v_{\parallel}}{\kappa} - \varepsilon_3 \sin \Psi$$

$$V_{\perp}^2 = \left( \frac{v_x}{\kappa} + \varepsilon_1 \sin \Psi \right)^2 + \left( \frac{v_y}{\kappa} + \varepsilon_2 \cos \Psi \right)^2 \quad (11)$$

where  $v_{\parallel}, v_x, v_y$  are the components of the physical velocity in the  $z, x$  and  $y$  directions, respectively. The relative wave-proton phase angle is

$$\xi_L = \ell \lambda + \int_0^s ds' r_L k_{\parallel}(s') - \frac{\omega}{\Omega_p(L)} \tau \quad (12)$$

where

$$\lambda = \arctan \left[ \frac{v_y + \kappa \varepsilon_2 \cos \Psi}{v_x + \kappa \varepsilon_1 \sin \Psi} \right] \quad (13)$$

The canonical action-angle variables are  $I$  and  $\lambda$ , where

$$I = \frac{V_{\perp}^2}{2} \frac{\Omega_p(L)}{\Omega_p} \quad (14)$$

To first order in the electric field amplitudes  $\varepsilon_i$ , the normalized, time-dependent Hamiltonian is a function of the canonical pairs of variables,  $(V_{\parallel}, s)$ , and  $(I, \lambda)$  [Shklyar, 1986; Menyuk et al., 1987; Ginat and Heinemann, 1990]

$$\mathcal{H} = \frac{V_{\parallel}^2}{2} + I \frac{\Omega}{\Omega(L)} + \sum_{\ell=-\infty}^{\infty} \sin \xi_L \left\{ \varepsilon_3 V_{\parallel} \mathcal{J}_{\ell}(k_{\perp} \rho) - \left[ \frac{I \Omega}{2 \Omega(L)} \right]^{1/2} \Gamma_{\ell} \right\} \quad (15)$$

Here

$$\Gamma_{\ell} = (\varepsilon_1 - \varepsilon_2) \mathcal{J}_{\ell+1}(k_{\perp} \rho) + (\varepsilon_1 + \varepsilon_2) \mathcal{J}_{\ell-1}(k_{\perp} \rho) \quad (16)$$

where  $\mathcal{J}_{\ell}$  represents a Bessel function whose argument is  $k_{\perp} \rho$ , where  $\rho = (c\kappa/\Omega_p) [2I\Omega/\Omega(L)]^{1/2}$  is the Larmor radius. The number of harmonics that effectively contribute to the summation in (15),  $|\ell| \leq \nu$ , reflect the behaviors of Bessel functions with large arguments and is discussed in Appendix B.

For particles crossing an isolated cyclotron resonance, we need only consider a single term  $\ell$  in the summation in (15). In this case, we find the following constant of motion [Walker and Ford, 1969]:

$$C_{\ell} = \ell \mathcal{H} - \frac{\omega}{\Omega_p(L)} I \quad (17)$$

Defining  $v_{\ell}$  such that  $\mathcal{H} = v_{\ell}^2/2 + I\Omega/\Omega(L)$ , leads to

$$v_{\ell} = \left\{ \frac{2}{\ell} \left[ C_{\ell} + I \left( \frac{\omega}{\Omega_p(L)} - \ell \frac{\Omega}{\Omega(L)} \right) \right] \right\}^{1/2} \quad (18)$$

The problem can be reduced to one dimension, by considering that

$$\frac{ds}{d\tau} = V_{\parallel} + \varepsilon_3 \mathcal{J}_{\ell}(k_{\perp} \rho) \sin \xi_L$$

$$= v_{\ell} + \frac{1}{v_{\ell}} \left[ \frac{I \Omega}{2 \Omega(L)} \right]^{1/2} \Gamma_{\ell} \sin \xi_L. \quad (19)$$

If  $\varepsilon_i \ll 1$ , keeping terms to first order in  $\varepsilon_i$  yields the equation of motion for  $I$  as a function of  $s$

$$\frac{dI}{ds} = \ell \cos \xi_L \Upsilon_{\ell}(I, v_{\ell}) \quad (20)$$

where

$$\Upsilon_{\ell}(I, v_{\ell}) = -\varepsilon_3 \mathcal{J}_{\ell}(k_{\perp} \rho) + \frac{1}{v_{\ell}} \left[ \frac{I \Omega}{2 \Omega(L)} \right]^{1/2} \Gamma_{\ell} \quad (21)$$

If there is no interaction then  $dI/ds = 0$ , and  $I$  is a constant of motion.

Combining (12) and (19) leads to

$$\frac{d\xi_L}{ds} = \ell \frac{d\lambda}{ds} + r_L k_{\parallel} - \frac{\omega}{\Omega_p(L) v_{\ell}} \times$$

$$\left\{ 1 + \frac{1}{v_{\ell}^2} \left[ \frac{I \Omega}{2 \Omega(L)} \right]^{1/2} \Gamma_{\ell} \sin \xi_L \right\}^{-1} \quad (22)$$

The evolution of the gyro phase angle  $\lambda$  as function of  $s$  is obtained from the Hamiltonian equation  $d\lambda/d\tau = \partial \mathcal{H} / \partial I$  and (19). As  $\varepsilon_i \rightarrow 0$ , then

$$\frac{d\xi_L}{ds} \rightarrow k_{\parallel} r_L + \frac{\ell \Omega_p - \omega}{\Omega_p(L) v_{\ell}} \quad (23)$$

The gyroresonance condition is obtained by setting (23) equal to zero. This is satisfied at  $s = s_{\ell}$  (the resonance location) defined as  $s_{\ell} = 3/\sqrt{2} \Lambda_{\ell}$ , where  $\Lambda_{\ell}$  is given in (8). By comparing (6) and (23), we see that  $v_{\ell} = v_{\parallel}/\kappa$ . By means of (23) we show that, for gyroresonant protons, the phase-angle  $\xi_L$ , satisfies the second-order differential equation

$$\frac{d^2 \xi_L}{ds^2} = \alpha_{\ell} + \frac{(k_{\parallel} r_L)^2}{v_{\ell}} \frac{1}{\ell} \frac{dI}{ds} \quad (24)$$

Here

$$\alpha_{\ell} = \frac{\gamma_{\ell}}{\Omega(L)} \frac{d\Omega}{ds} \quad (25)$$

where

$$\gamma_{\ell} = \Omega_e(L) r_L \frac{dk_{\parallel}}{d\Omega_e} + \frac{1}{v_{\ell}} \left[ \frac{\ell}{2} + \frac{C_{\ell}}{v_{\ell}^2} \right] \quad (26)$$

and  $d\Omega/ds = 2s \Omega(L)$ . The pair of coupled equations (20) and (24) describe the evolution along the field line of the physical action,  $I = (v_{\perp}/\sqrt{2}\kappa)^2 \Omega(L)/\Omega$ , as function of the phase-angle for gyroresonant protons. Here  $v_{\perp} = (v_x^2 + v_y^2)^{1/2}$ , is the perpendicular component of the particle velocity normalized to  $c^{-1}$ .

By using the constant of motion in (17), we find that the evolution of the particle kinetic energy,  $W$ , as function of the distance  $s$  is given solving for

$$\frac{dW}{ds} = \frac{\omega}{\ell \Omega_p(L)} \frac{dI}{ds} \quad (27)$$

We define  $\chi = \sin^2 \theta \Omega(L)/\Omega$ , where  $\theta$ , the local pitch angle, is a function of  $s$ . Note that if there are no waves (i.e.,  $\epsilon_i = 0$ )  $\chi = \mu$ , a constant. Rewriting  $I = W\chi$ , the evolution of  $\chi$  as function of  $s$  is

$$\frac{1}{\chi} \frac{d\chi}{ds} = \frac{1}{I} \frac{dI}{ds} - \frac{1}{W} \frac{dW}{ds} \quad (28)$$

where  $dI/ds$  and  $dW/ds$  are given in (20) and (27), respectively.

##### 5. SOLUTIONS TO THE EQUATIONS OF MOTION NEAR RESONANCE

At the resonance ( $s = s_\ell$ ), the parallel velocity and action are

$$v_\ell(R) = \frac{1}{\kappa \eta \cos \phi} (1 - \ell f_p) \frac{\Omega(R)}{\Omega(L)} \quad (29)$$

$$I_\ell(R) = \frac{v_\ell(R)^2}{2} \frac{\mu}{1 - \mu \Omega(R)/\Omega(L)} \quad (30)$$

where  $f_p = \Omega_p(L)/\omega$ ,  $\Omega(R)/\Omega(L) = 1 + s_\ell^2$ , and  $(R)$  denotes resonant values. Combining (18), (29), and (30) yields

$$C_\ell = \frac{\ell}{2} v_\ell(R)^2 - I_\ell \left( \frac{1}{f_p} - \ell \frac{\Omega(R)}{\Omega(L)} \right). \quad (31)$$

Using a Taylor expansion to solve the coupled (20) and (24) under the assumption that  $s$  is very close to the resonance length  $s_\ell$  [Shklyar, 1986], yields for the physical action

$$I \simeq I_\ell(R) + \left( \frac{dI}{ds} \right)_{(R)} (s - s_\ell) \quad (32)$$

and for the relative wave-proton phase angle

$$\xi_\ell \simeq \xi_\ell(R) + \xi_\ell^{(1)} (s - s_\ell) + \frac{\xi_\ell^{(2)}}{2} (s - s_\ell)^2 \quad (33)$$

where  $I_\ell(R)$ ,  $\xi_\ell(R)$  are constants. Here  $(dI/ds)_{(R)}$  is given by (20) and (21), with  $\xi_\ell = \xi_\ell(R)$ ,  $I = I_\ell(R)$ , and  $v_\ell = v_\ell(R)$ , evaluated for resonant particles. For protons satisfying the resonance condition,  $\xi_\ell^{(1)} = 0$ . For protons staying in gyroresonance with successive harmonics,  $\cos[\xi_\ell(R)] = \pm 1$ . Substituting (33) into (24) leads to

$$\xi_\ell^{(2)} = \alpha_\ell(R) + \frac{(k_\parallel r_L)^2}{v_\ell(R)} \frac{1}{\ell} \left( \frac{dI}{ds} \right)_{(R)} \quad (34)$$

where  $\alpha_\ell(R)$  is evaluated at the resonance.

The change of the action  $I$  after crossing the  $\ell$ 'th resonance,  $\Delta I$ , is obtained by integrating (20). Approximately we find

$$\Delta I = \left( \frac{dI}{ds} \right)_{(R)} \delta s_\ell = \ell \Upsilon_\ell(R) \delta s_\ell \quad (35)$$

where  $\Upsilon_\ell(R)$  is given by (21), substituting  $I = I_\ell(R)$  and  $v_\ell = v_\ell(R)$ . The resonance width  $\delta s_\ell$  is defined as

$$\delta s_\ell = \int_{-\infty}^{+\infty} ds \cos \xi_\ell \quad (36)$$

Combining (33), (34), and (36), shows that

$$\delta s_\ell = \Gamma(1/2) \cos(\pi/4) \left[ \frac{2}{|\xi_\ell^{(2)}|} \right]^{1/2} \quad (37)$$

The change in the particle's kinetic energy,  $\Delta W = (dW/ds)_{(R)} \delta s_\ell$ , can be obtained from (27) as approximately

$$\Delta W = \frac{\omega}{\ell \Omega_p(L)} \Delta I = \frac{\omega}{\Omega_p(L)} \Upsilon_\ell(R) \delta s_\ell \quad (38)$$

By means of (28) we find that  $\Delta \chi$  is

$$\Delta \chi = \frac{1}{W(R)} \left[ 1 - \mu \frac{\omega}{\ell \Omega_p(L)} \right] \Delta I \quad (39)$$

We define  $\ell_o$  as the closest integer to  $\mu\omega/\Omega_p(L)$ , and consider three cases: (1)  $-\infty \leq \ell \leq 0$ , (2)  $0 < \ell < \ell_o$ , and (3)  $\ell_o \leq \ell \leq \infty$ . In case 1 for the negative harmonics  $-\nu \leq \ell \leq 0$ , (39) shows that  $\Delta \chi / \Delta I > 0$ . Thus, from (38) if  $\Delta I < 0$  and  $\Delta W > 0$ , a particle's pitch angle decreases toward the loss cone, i.e.,  $\Delta \chi < 0$ . For the Landau resonance  $\Delta I = 0$  and  $\Delta \chi = -\mu \Delta W / W(R)$ , if  $\Delta \chi < 0$  then  $\Delta W > 0$ . The positive harmonics are located off the equator at geomagnetic latitudes  $\Lambda > \Lambda_o$  as given in (8) and (9). In case 2,  $0 < \ell < \ell_o$  and  $\Delta \chi / \Delta I > 0$ . Thus if  $\Delta I$  and  $\Delta W < 0$ , the pitch angles will decrease. In case 3,  $\ell \geq \ell_o$ , we find that  $\Delta \chi / \Delta I < 0$ . By taking  $\Delta I$  and  $\Delta W > 0$ , then  $\Delta \chi < 0$ .

In Figure 2 we represent the net particle diffusion along single wave characteristics defined as

$$(v_\parallel - \omega/k_\parallel)^2 + v_\perp^2 = \text{constant} \quad (40)$$

A proton whose location in phase space is indicated by a dot, at the intersection of the characteristic with the constant energy surfaces, diffuses toward smaller pitch angles as indicated by the arrows. For the negative and positive harmonics,  $\omega/k_\parallel < v_\parallel$  and  $\omega/k_\parallel > v_\parallel$ , respectively. If  $0 < \ell < \ell_o$ , a proton diffuses toward decreasing energy and pitch angle as indicated by the arrow. For  $\ell > \ell_o$  and  $\ell < 0$ , the particle's energy increases as the pitch angle decreases.

The interaction of waves and particles is more effective if resonances overlap. The criterion for overlapping of resonances is

$$\left| \frac{\Delta I}{I_{\ell-1}(R) - I_\ell(R)} \right| \geq 1 \quad (41)$$

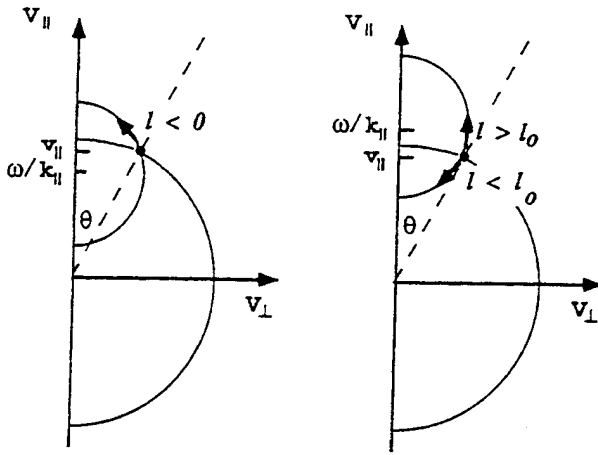


Fig. 2. Schematic phase space representations of particle diffusion paths toward smaller pitch angles following wave characteristics as defined in (40). The small circles represent single-wave characteristics; the large circles, centered at the origin, surfaces of constant energies. The initial position of the proton is indicated by a dot. It diffuses depending on the value of the harmonic number  $\ell$  and according to the directions indicated by the arrows. Here  $\ell_0 > 0$  is defined after (39). The particle's energy decreases for  $0 \leq \ell \leq \ell_0$ , and increases for all other harmonics.

where  $\Delta I$  is given in (35), and  $I_{\ell-1}$ ,  $I_\ell$  are defined by (30). In this case, particles continue in resonance with the waves over longer distances along the flux tube and more effectively interchange energy with them. Because of the behavior of Bessel functions, in our numerical calculations we find that sometimes two nearby resonances such as  $n-1$  and  $n$  do not overlap. However even if  $n-1$  and  $n$  do not satisfy the overlap criterion, it may be that  $n-1$  and  $n+1$  satisfy (41) with  $\Delta I$  as obtained for any of the values  $n \pm 1$ . In this case the contribution of the  $n$ 'th resonance is small but there is still a resonance overlap.

## 6. SECOND-ORDER RESONANCE

In the strongly inhomogeneous case the contribution of the magnetic field is larger than that of the resonance, we may neglect the term proportional to  $(dI/ds)_{(R)}$  in (34), which leads to

$$\Delta I = \left( \frac{dI}{ds} \right)_{(R)} \Gamma(1/2) \cos(\pi/4) \left[ \frac{1}{|\gamma_\ell(R) s_\ell|} \right]^{1/2} \quad (42)$$

where  $\gamma_\ell(R)$  is given by (26) and must be evaluated at resonance. Note from (35) and (21) that the change in the action is proportional to the electric field amplitudes. These interactions are called first-order because  $d\xi_\ell/ds = 0$  and  $d^2\xi_\ell/ds^2 \sim \alpha_\ell(R) \neq 0$ .

In the weakly inhomogeneous case, the contribution of  $\alpha_\ell(R)$  in (34) is smaller than that of  $(dI/ds)_{(R)}$ , then

$$\Delta I = \left[ \ell \left( \frac{dI}{ds} \right)_{(R)} \right]^{1/2} \Gamma(1/2) \frac{[2|v_\ell(R)|]^{1/2}}{k_{\parallel} \tau_L} \cos(\pi/4) \quad (43)$$

The change in particle momentum  $I$  is now proportional to the square root of the electric field amplitudes,  $\epsilon_i^{1/2}$ . We call this the second-order resonance condition

because to zero order in the electric field amplitudes  $d^2\xi_\ell/ds^2 \simeq 0$ .

Note that for a fixed constant value of  $\omega$ , the second-order resonance condition can only be satisfied in equatorial interactions. For constant-frequency waves, the electric field amplitudes required to satisfy second-order resonance conditions for a given harmonic (i.e.,  $\alpha_\ell(R)$  is neglected in (34)), are such that

$$\left[ \frac{k_{\parallel} \tau_L}{\sqrt{2} v_\ell} \left( \frac{1}{\ell} \left| \left( \frac{dI}{ds} \right)_{(R)} \right| \right)^{1/2} \right]^3 \gg \gamma_\ell(R) \Gamma(1/2) \cos \pi/4 \quad (44)$$

Here  $k_{\parallel} \tau_L = \eta \kappa \cos \phi \omega / \Omega_p(L)$ , where  $v_\ell = v_{\parallel}/\kappa$  is given by (29), and  $\kappa$  is defined before (10).

By allowing for wave packets with finite bands of frequencies, resonant protons experience  $\omega$  as a function of  $s$ . Note that  $\eta_{\parallel} = \eta \cos \phi$ , depends on  $\omega$  and  $\phi$  through the variable  $\omega_\phi = \omega / \cos \phi$ . The inhomogeneity factor,  $\alpha_\ell$ , in (24) as function of a varying  $\omega_\phi(s)$ , becomes

$$\alpha_\ell = \gamma_\ell \frac{1}{\Omega(L)} \frac{d\Omega}{ds} + \tau_L \frac{dk_{\parallel}}{d\omega_\phi} \frac{d\omega_\phi}{ds} \quad (45)$$

By changing  $\omega_\phi$  so that  $\alpha_\ell(R) = 0$  for interactions off the equator, the second-order resonance condition is satisfied regardless of the electric fields amplitudes. In this case, the change in particle energies are proportional to  $\epsilon_i^{1/2}$ . We consider the contribution of only one frequency at any given point along the field line and neglect all others contributions because they are small  $\sim \epsilon$ . Thus, in a wave of varying frequency,  $\omega(s)$ , protons stay in resonance longer than in a constant-frequency wave. This is because the inhomogeneity of the magnetic field is compensated by the frequency variation along the field line. Note that the result  $\Delta W \sim \epsilon_i^{1/2}$  resembles that obtained in a homogeneous plasma [Menyuk and Dobrot, 1987]. The electric fields amplitudes needed to satisfy the overlapping criterion in (41), are smaller for second-order resonant particles.

In the case of the Landau resonance, the frequency variation obtained from (45), is

$$\frac{d\omega_\phi}{ds} = - \frac{1}{(d\eta_{\parallel}/d\omega_\phi)} \left[ \frac{d\eta_{\parallel}}{d\Omega_e} + \eta_{\parallel} \frac{1}{v_{\parallel}} \frac{dv_{\parallel}}{d\Omega_e} \right] \frac{d\Omega_e}{ds} \quad (46)$$

where  $d\eta_{\parallel}/d\Omega_e$ ,  $d\eta_{\parallel}/d\omega_\phi$  are obtained from (2), and  $dv_{\parallel}/d\Omega_e = -v_{\perp}^2/[2\Omega_e(L) v_{\parallel}]$ . By setting (45) equal to zero, we obtain the frequency increment for each resonance located at a distance  $s_\ell$  from the equator,

$$\frac{\Delta\omega_\phi}{\omega} = -\gamma_\ell s_\ell^2 \frac{c}{\tau_L \omega} \frac{1}{\omega (d\eta_{\parallel}/d\omega_\phi)} \quad (47)$$

Note that  $\Delta\omega_\phi$  is proportional to the harmonic number  $\ell$ , see (8). Integrating (46) reduces to (47) for the case  $\ell = 0$ .

Next we assume that  $\cos \phi$  is also a function of the distance  $s$ , due to a spectrum of waves that exists near equatorial regions. We call  $\phi(L)$  and  $I(L)$  the equatorial values of the wave angle  $\phi$  and the action  $I$ , respectively.

By taking  $I_\ell(R) = I(L)$  for all harmonics  $\ell$ , where  $I(L)$  satisfies the resonance condition at the equator and  $I_\ell$  is given in (30), the overlapping criterion (41) is satisfied regardless of the amplitudes of the electric fields. Then the variation of  $\cos \phi(s)$  as function of the frequency  $\omega$  and angle  $\phi(L)$  as defined at the equator, is

$$\frac{\cos \phi}{\cos \phi(L)} = \left[ \frac{1 - \mu}{1 - \mu \Omega(R)/\Omega(L)} \right]^{1/2} \frac{\eta(L)}{\eta(R)} \times \frac{1 - \ell f_p \Omega(R)/\Omega(L)}{1 + \nu f_p} \quad (48)$$

where  $\eta \simeq \eta(L) + (d\eta/d\Omega_e)_{(L)} [\Omega_e(R) - \Omega_e(L)]$ . The frequency shift  $\Delta\omega$ , is given after substituting  $\phi(s_\ell)$  in (47). If the wave spectrum is such that the harmonics overlap their effect can be added together, then the changes in a particle's energy and momentum are proportional to  $\epsilon^{1/2}$ . The interaction between waves and particles become more efficient than for a single frequency wave with constant wave angle  $\phi(L)$ .

#### 7. NUMERICAL APPLICATIONS: THE RESONANT HARMONICS

The density of cold plasmaspheric electrons,  $n_e$ , is approximated as a function of the magnetic shell  $L$ , by  $n_e = 3 \times 10^3 (2/L)^4 \text{ cm}^{-3}$  [Chappell et al., 1970]. The equatorial magnetic field is also a function of  $L$ ,  $B(L) = B_0/L^3$ , where  $B_0 = 3.11 \times 10^4 \text{ nT}$ , is the magnetic field at the Earth's surface. As an example we study proton whistler interactions that take place at the  $L = 3.5$  shell. Then according to the density and magnetic field models given above, the ratio between the electron plasma and equatorial cyclotron frequencies is  $\omega_p/\Omega_e(L) = 7.9$ , where  $\Omega_e(L) = 1.275 \times 10^5 \text{ rad/s}$ . The proton gyrofrequency is  $\Omega_p(L) = 69.44 \text{ rad/s}$ , and  $\kappa = \Omega_p(L)r_L/c = 2.43$ . The width of the equatorial loss cone is  $\theta_c(L) \simeq 6.5^\circ$  and we consider particles whose pitch angles are  $\theta(L) = 7.5^\circ$ . The dimensionless electric field  $\epsilon = q\mathcal{E}/m_p c \omega = 2.5 \times 10^{-6} f_e \mathcal{E}$ , where  $\mathcal{E}$  should be given in volts per meter and  $f_e = \Omega_e(L)/\omega$ . Calculations were conducted for wave frequencies such  $0.5 \leq f_e^{-1} \leq 1$ , and for  $|\cos \phi| \sim f_e^{-1}$ . Table 1 gives the approximate values of relevant parameters for three different frequencies, i.e.,  $f_e^{-1} = 0.5, 0.75$  and  $0.85$ , and for particles whose energies are 150-keV. Note that the refractive index  $\eta(L)$  increases with decreasing frequency,  $\omega$ . The maximum number of resonances,  $n$ , that can contribute to the interaction is given considering the properties of Bessel functions as explained in Appendix B. For the cases  $-n \leq \ell \leq n$ , the Landau resonance is located off the equator, and other harmonics occur at magnetic latitudes  $\Delta\Lambda$  as defined in (8). We represent by

$$\Lambda_L = \frac{2}{3} \left[ \frac{m_e}{m_p} \left( f_e - \frac{1}{|\cos \phi|} \right) \right]^{1/2} \quad (49)$$

which is obtained taking  $g(\mu) \sim |\cos \phi|$  in (8). Note that as  $\Lambda_L^{-1}$  increases the separation between resonances  $\Lambda_{\ell+1} - \Lambda_\ell \sim \Lambda_L$ , decreases. The geomagnetic latitudes  $\Delta\Lambda$  (in degrees) extend to the range of the interacting,

$-n \leq \ell \leq n$ , harmonics. As  $\omega$  approaches to  $\Omega_e(L)$ , the interaction length decreases and resonances occur closer to each other. The values in Table 2 were obtained by assuming that the particle energies are  $\sim 500$ -keV, and for the cases  $-n \leq \ell \leq n$ . Here the distance between resonances is larger than in the case of 150-keV particles. Thus, for a fixed value of  $\omega$ , the interaction-lengths increase with the particle's energy,

Figure 3 shows the change in the normalized action  $|\Delta I|$ , divided by the normalized equatorial energy  $W_0$ , versus the harmonic number  $\ell$ , for the entire range harmonics. The wave frequencies at the equator are such that  $f_e^{-1} = 0.75$  and  $0.5$  as indicated in the panels, and the electric field amplitudes are  $\mathcal{E} = 10^{-4} \text{ V/m}$ . The upper and lower panels correspond to particles whose energies are  $\sim 150$ -, and  $500$ -keV, respectively. The calculations are based on (43), for which we assume that the wave frequency changes according to the spectrum in (47). By increasing the electric fields,  $\epsilon$ , the change in action scales as  $\epsilon^{1/2}$ . For  $f_e^{-1} = 0.75$ , the frequency range is  $\Delta\omega/\omega < 0.55 \times 10^{-2}$ , and  $0.22 \times 10^{-1}$ , for the 150- and 500-keV particles, respectively. For  $f_e^{-1} = 0.5$ , then  $\Delta\omega/\omega < 0.15 \times 10^{-1}$  and  $0.6 \times 10^{-1}$  for 150- and 500-keV cases, respectively. Note that a larger number of harmonics contribute for  $f_e^{-1} = 0.5$  than for  $f_e^{-1} = 0.75$ . However, the bandwidth of frequencies needed to satisfy the second-order resonance condition is larger, because the separation between resonances is also larger.

Figure 4 shows the change in energy divided by its equatorial value, i.e.,  $|\Delta W|/W_0$ , versus harmonic number  $\ell$ . The physical parameters are as described for Figure 3, and as indicated in the panels. The calculations were performed by combining (38) and (43). Thus the change in energy is proportional to the  $\epsilon^{1/2}$ . Comparing Figures 3 and 4, we see that  $|\Delta W|/W_0 \gg |\Delta I|/W_0$ , thus the change in the particle energies is due to a change in the parallel component of their velocities. Also note that the magnitude of  $|\Delta W|/W_0$ , is approximately the same for  $f_e^{-1} = 0.75$  and  $0.5$ . However, since the number of contributing overlapping harmonics increases as  $f_e^{-1}$  decreases, the total gain in energy is larger for  $f_e^{-1} = 0.5$  than for  $0.75$ .

Figure 5 represents  $\Delta\chi/\mu \leq 0$  versus  $\ell$  for the same cases as in Figures 3 and 4. The results are obtained from (39) and (43). Here  $\ell_0$  which is the closest integer to  $\mu\omega/\Omega_p(L)$ , is equal to 23 and 15 for  $f_e^{-1} = 0.75$  and

TABLE 1. Physical Parameters for 150 keV Particles

$f_e^{-1}$	$\cos \phi$	$\eta(L)$	$\Lambda_L^{-1}$	$n$	$\Delta\Lambda$
0.50	0.510	112	325	100	$2.50^\circ$
0.75	0.765	75	398	75	$1.75^\circ$
0.85	0.867	66	423	60	$1.50^\circ$

TABLE 2. Physical Parameters for 500-keV Particles

$f_e^{-1}$	$\cos \phi$	$\eta(L)$	$\Lambda_L^{-1}$	$n$	$\Delta\Lambda$
0.50	0.540	56	167	100	$4.85^\circ$
0.75	0.810	37	205	75	$3.50^\circ$
0.85	0.915	34	222	60	$2.80^\circ$

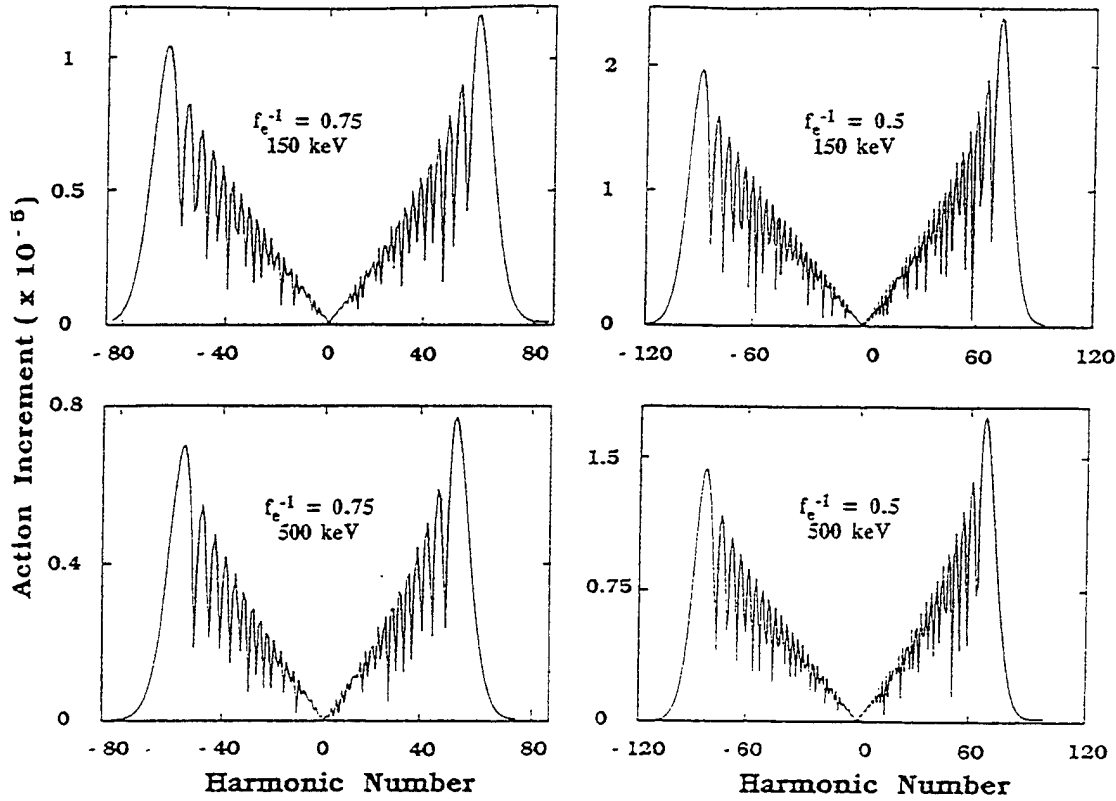


Fig. 3. Absolute value of the change in action divided by the equatorial energy,  $|\Delta I|/W_0$ , versus the harmonic number  $L$ . The wave frequencies are as indicated in the panels,  $\omega = 0.75$  and  $0.5 \times \Omega_e(L)$ . The electric field is  $\mathcal{E} = 10^{-4}$  V/m. The particles energies are for the upper and lower panels  $\sim 150$ - and  $500$ -keV, respectively; their pitch angles  $7.5^\circ$ . Others physical parameters can be found in Tables 1 and 2.

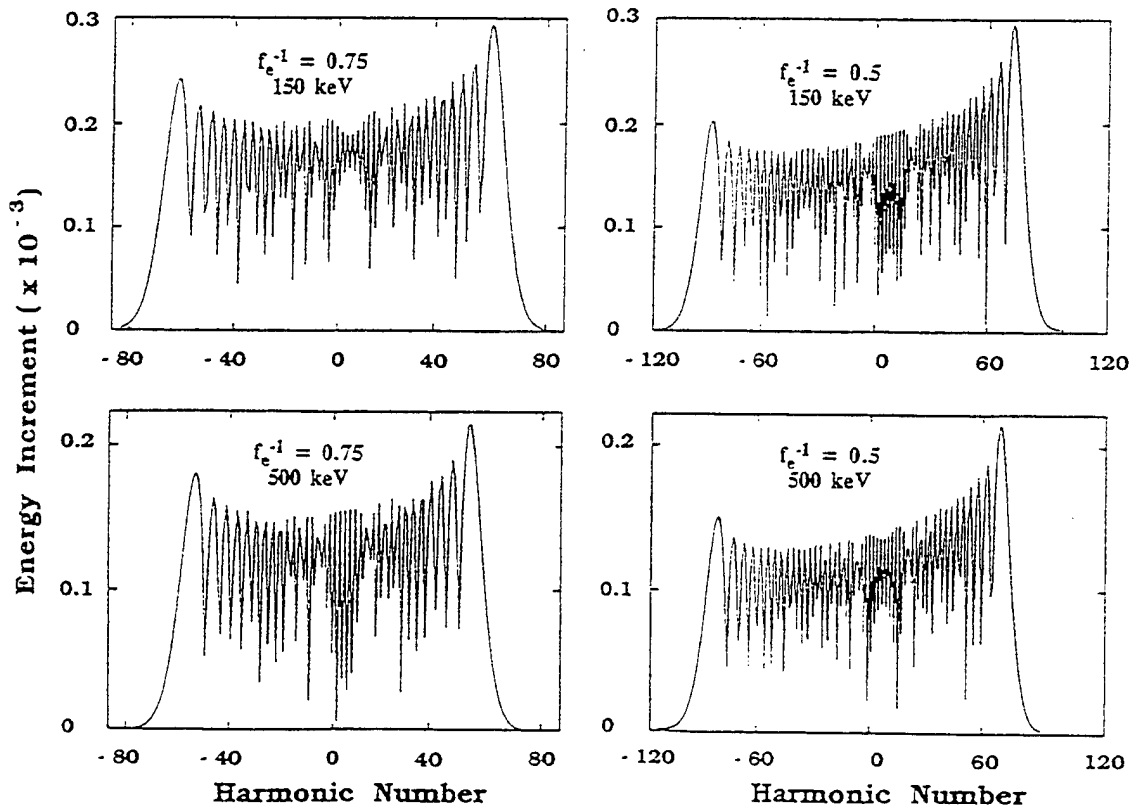


Fig. 4. Absolute value of the change in energy divided by its equatorial value,  $|\Delta W|/W_0$ , versus harmonic number  $L$ . The physical parameters are as given in Figure 3.



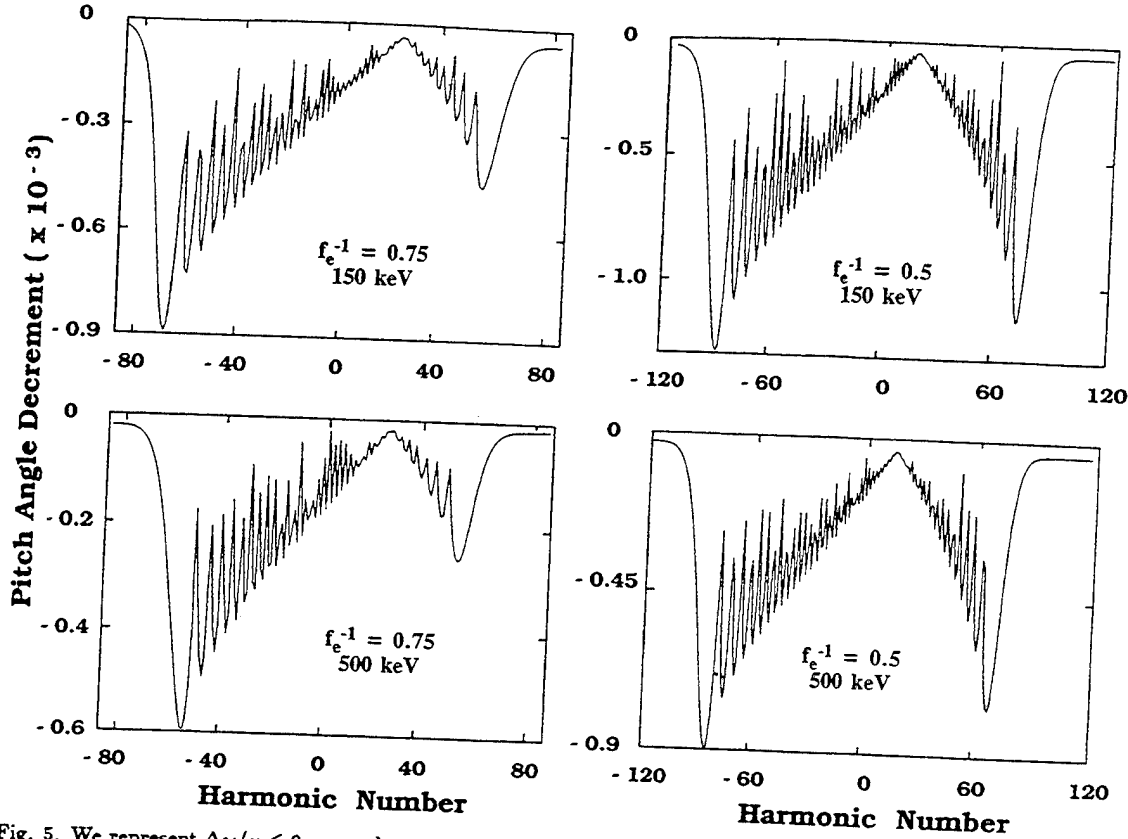


Fig. 5. We represent  $\Delta\chi/\mu \leq 0$  versus harmonic number  $\ell$ . Here  $\chi = \sin^2 \theta (\Omega(L)/\Omega)$ ,  $\theta$  is the local pitch angle,  $\mu = \sin^2 \theta(L)$ , and  $\theta(L)$  is the equatorial pitch angle. The physical parameters are as in Figures 3 and 4.

0.5, respectively. For the negative harmonics  $\Delta I < 0$  thus  $\Delta W > 0$ . If  $0 \leq \ell \leq \ell_o$ ,  $\Delta I < 0$  and then  $\Delta W < 0$ . For  $\ell > \ell_o$ ,  $\Delta I > 0$  and  $\Delta W > 0$ .

#### 8. NUMERICAL APPLICATIONS: THE OVERLAPPING CRITERION

Figure 6, represents the number of overlapping resonances, as a function of  $\lg(\mathcal{E})$ , with  $\mathcal{E} = (\mathcal{E}_1^2 + \mathcal{E}_2^2 + \mathcal{E}_3^2)^{1/2}$  in volts per meter. The wave propagation angles  $\cos \phi$  are the constants given in Tables 1 and 2. We assume a bandwidth in frequencies so that  $\Delta I$  is calculated for each harmonic as in (43). We consider positive  $\ell > 0$ , and negative  $\ell < 0$ , harmonics as indicated in the panels. The upper and lower panels refer to  $\sim 150$ - and 500-keV protons; the equatorial wave frequencies are  $f_e^{-1} = 0.5, 0.75$  and  $0.85$ . Overlapping resonances are calculated as explained in section 5, following the criterion given in (41). The harmonics with the largest possible  $|\ell|$  overlap first as function of  $\lg(\mathcal{E})$ . For example, if  $0 \leq |\ell| \leq 70$ , the number of overlapping harmonics is equal to  $70 - |\ell|$ . Resonances overlap if the electric field amplitudes exceed certain thresholds. Above these thresholds, the numbers of harmonics contributing to the interaction reach some limits increasing very little with  $\mathcal{E}$ . These limits are established for amplitudes which are larger than  $\sim 10^{-4}$  V/m. The electric fields required for overlapping become smaller as  $\omega \rightarrow \Omega_e(L)$  and as the particle's energy decreases.

The calculations in Figure 6, assume a wave field of varying-frequency  $\omega(s)$ , and constant values for  $\cos \phi$ . They illustrate the importance of having a spectrum

of waves to achieve a more efficient interaction with the trapped protons. As a matter of comparison, in a constant frequency wave, the overlapping criterion in (41) is proportional to  $\epsilon$ . Thus, the electric fields require to overlap the resonances in a constant frequency wave, are larger than  $10^{-2}$  V/m. On the other hand, if  $\cos \phi$  and  $\omega$  are both functions of  $s$  as given in (47) and (48), the overlapping criterion (41) is satisfied for all the contributing resonances regardless of the electric field amplitudes. In what follows we assume that there exists such spectrum with a bandwidth in frequencies and propagation angles, thus the resonances overlap and satisfy second-order resonance conditions.

If the particle motion is essentially a diffusive process in velocity space, the net fluxes are toward decreasing values of the distribution function. When the net flux is towards increasing the particles energies then the waves damp. Because of the atmospheric loss cone, distribution functions are anisotropic in pitch angle  $\theta(L)$ , with a minimum at  $\theta(L) \rightarrow 0$ . Near the loss cone  $\partial F / \partial \theta > 0$ , and particles tend to diffuse toward smaller values of  $\theta$ . As illustrated in Figure 2, to decrease the pitch angles  $\Delta\chi < 0$ , we need: a) for  $0 \leq \ell \leq \ell_o$ ,  $\Delta W < 0$  and b) for  $\ell > \ell_o$  or  $\ell < 0$ ,  $\Delta W > 0$ . Since the number of contributing harmonics is larger if  $\Delta W > 0$  than if  $\Delta W < 0$ , there is a net gain of energy for the interacting protons. Given that  $\ell_o \sim \mu\omega/\Omega_p(L)$ , then  $\ell_o = 15, 23$ , and 26 for  $\theta(L) = 7.5^\circ$  and for  $f_e^{-1} = 0.5, 0.75$ , and  $0.85$ , respectively.

Let us assume there exists a spectrum of waves which has widths in wave propagation angles  $\Delta\phi$  and frequencies  $\Delta\omega$ , so that all harmonics meet the conditions for

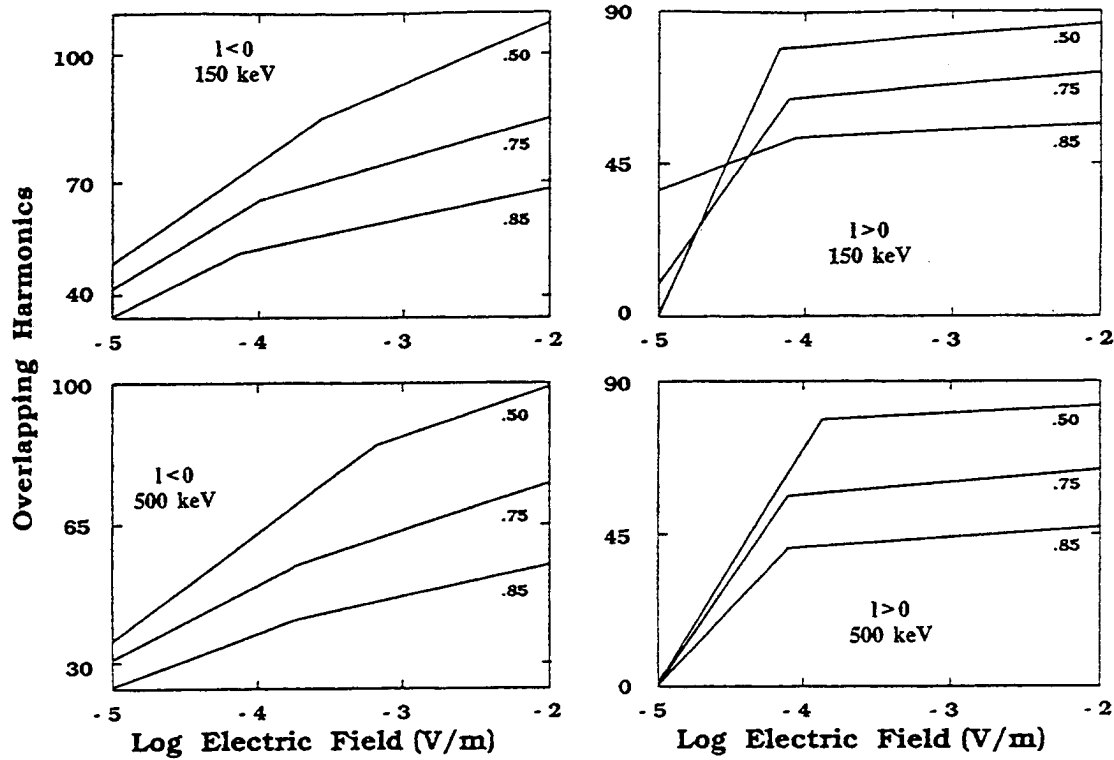


Fig. 6. Number of overlapping resonances versus  $\lg(\mathcal{E})$ , where  $\mathcal{E}$  is given in volts per meter. We consider positive  $l > 0$  and negative  $l < 0$ , harmonics as indicated in the panels. The wave frequencies are  $\omega = 0.5, 0.75, 0.85 \Omega_e(L)$  and the wave angles  $\cos \phi$  are constants as defined in Tables 1 and 2. The particles energies  $\sim 150$ - and  $500$ -keV, and their pitch angles  $7.5^\circ$ .

second-order resonances and overlap, for all values of  $\mathcal{E}$ . Because of this we can combine the contributions of all the harmonics. Figure 7 shows the logarithm of the net energy gain in a quarter of a bounce period during the interaction,  $\lg(W_G)$ , as a function of  $\lg(\mathcal{E})$ , where  $\mathcal{E}$  is given in V/m. The total energy gain which is divided by the equatorial energy  $W_0$ , is given by considering that the contributions of the resonances is such the particles pitch angles are always decreasing, i.e.,  $\Delta\chi < 0$  for all values of  $l$ . Then

$$W_G = \left\{ \sum_{l=-\infty}^0 + \sum_{l=L_0}^{+\infty} - \sum_{l=0}^{L_0} \right\} \frac{|\Delta W|}{W_0} \quad (50)$$

Here  $\Delta W$  is defined as in (38), and  $\Delta I$  is given by (43). The upper and lower panels correspond to  $\sim 150$ - and  $500$ -keV particles, respectively. We consider the frequencies  $f_e^{-1} = 0.5$  and  $0.75$ , and the initial equatorial pitch angle of  $7.5^\circ$ . For smaller frequencies the gain in energy is larger because the number of harmonics is larger. To obtain these results we have approximated

$$\lg(W_G) = C_W \lg(\sqrt{\mathcal{E}(V/m)}) \quad (51)$$

where  $\mathcal{E}$  is given in volts per meter. For  $150$ -keV protons,  $C_W \sim 0.85$  and  $0.75$  for  $f_e^{-1} = 0.75$  and  $0.5$ , respectively. For  $500$ -keV protons,  $C_W \sim 0.925$  and  $0.825$  for  $f_e^{-1} = 0.75$  and  $0.5$ , respectively. The estimates of  $C_W$  are obtained from the results for  $\mathcal{E} = 10^{-4}$  V/m, in Figure 4. For example, consider  $150$ -keV protons and

$f_e^{-1} = 0.5$ , if in average we can take  $\Delta W/W_0 \sim 0.2 \times 10^{-3}$  and since  $|\ell| \leq 90$ , then  $W_G \sim 0.2 \times 10^{-3} \times 150$ , which leads to  $C_W \sim 0.75$ .

Figure 8 represents the logarithm of the net loss in pitch angle,  $\lg(\chi_D)$ , in a quarter of a bounce period versus  $\lg(\mathcal{E})$ . We represent the same parameters as in Figure 7. The change in pitch angle is obtained by adding over all resonances,

$$\chi_D = \sum_{l=-\infty}^{+\infty} \frac{|\Delta\chi|}{\mu} \quad (52)$$

where  $\Delta\chi$  is obtained by means of (39) and (43), and  $\mu = \sin^2 \theta(L)$ . Here  $\Delta\chi$  is  $< 0$  for all values of  $l$ , thus the particles are driven toward the loss cone. Although smaller frequencies yield a larger change in pitch angles, the frequency and wave propagation angle spectrum is also larger when  $\omega \sim 0.5\Omega_e(L)$ , than when  $\sim \Omega_e(L)$ . As the proton's energy increases, the changes in pitch angle become smaller for constant wave amplitudes. In a single bounce period,  $150$ -keV protons in the presence of waves amplitudes  $\sim 10^{-4}$  V/m, pitch angles can change by more than one degree. These results are obtained assuming that

$$\lg(\chi_D) = C_\chi \lg(\sqrt{\mathcal{E}(V/m)}) \quad (53)$$

Here for  $150$ -keV protons,  $C_\chi \sim 0.65$  and  $0.45$  for  $f_e^{-1} = 0.75$  and  $0.5$ , respectively. For  $500$ -keV protons,  $C_\chi \sim 0.75$  and  $0.55$  for  $f_e^{-1} = 0.75$  and  $0.5$ , respectively.

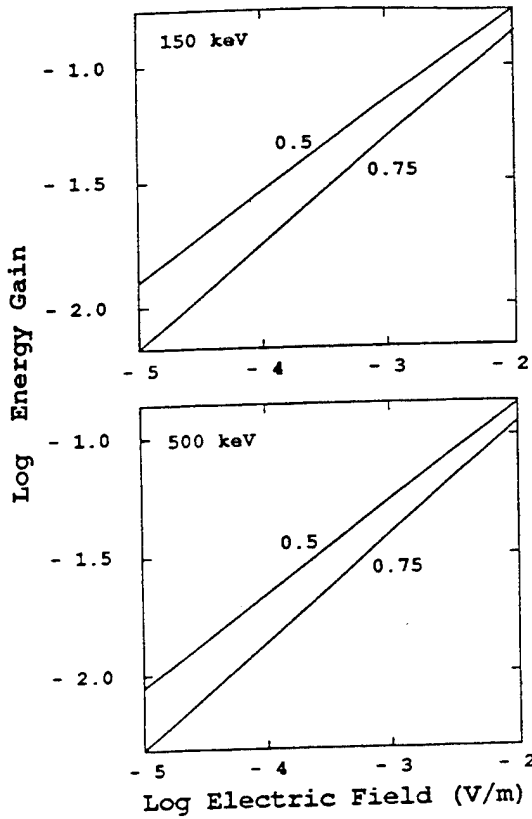


Fig. 7. Logarithm of the energy gain in a quarter of a bounce period as defined in (50) and (51), versus  $\lg(\mathcal{E})$ , where  $\mathcal{E}$  is given in volts per meter. The wave frequencies are  $\omega = 0.5, 0.85 \Omega_e(L)$ . The particle energies are  $\sim 150$ - and  $500$ -keV, and their pitch angles  $7.5^\circ$ .

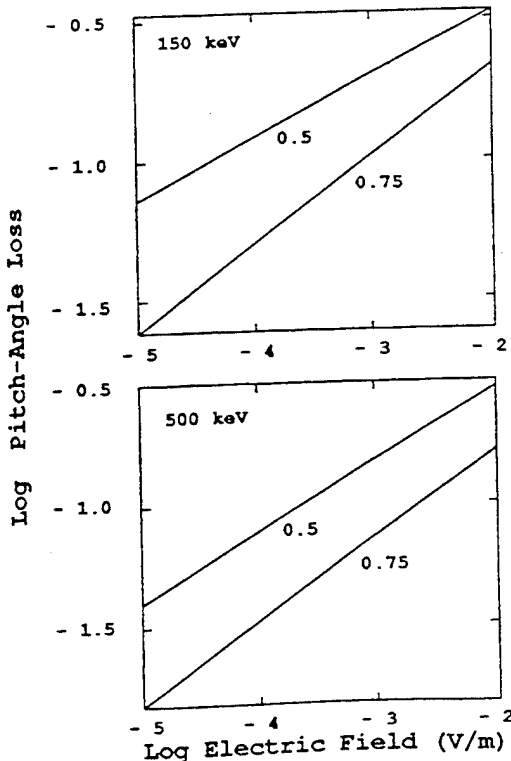


Fig. 8. Logarithm of the change in pitch angle in a quarter of a bounce period, see (52) and (53), versus  $\lg(\mathcal{E})$ , where  $\mathcal{E}$  is given in volts per meter. Physical parameters are as in Figure 7.

These estimate are found from the results in Figure 5, for  $\mathcal{E} = 10^{-4}$  V/m, where the combined contribution of the resonances can be approximated by the areas of two triangles. Adding these areas and considering (53), we arrive at the values of  $C_\chi$ .

Figure 9 shows the logarithm of the net loss in action,  $\lg(I_D)$ , in a quarter of a bounce period versus  $\lg(\mathcal{E})$ . The physical parameters are the same as in Figures 7 and 8. The change in action is obtained by combining the contribution of all the resonances and considering that for all  $\ell \Delta\chi < 0$ , then

$$I_D = \left\{ \sum_{\ell=-\infty}^{\ell_0} - \sum_{\ell=\ell_0}^{\infty} \right\} \frac{|\Delta I|}{W_0} \quad (54)$$

These results are obtained based on

$$\lg(I_D) = C_I \lg(\sqrt{\mathcal{E}(V/m)}) \quad (55)$$

For 150-keV protons,  $C_I \sim 2.05$  and  $2.15$  for  $f_e^{-1} = 0.75$  and  $0.5$ , respectively. For 500-keV protons,  $C_I \sim 2.1$  and  $2.25$  for  $f_e^{-1} = 0.75$  and  $0.5$ , respectively.

A final comment on how our results apply to others  $L$  shells, as  $L$  decreases from  $3.5$  to smaller values, say  $L = 2$ , the equatorial gyrofrequency increases as  $1/L^3$ , and the plasma density as  $1/L^4$ . By assuming that the proton energies remain constant, solving for the resonance condition gives  $f_e^{-1} \sim L^3 \omega$ . Then by decreasing  $L$ ,  $\omega$  must also increase as  $1/L^3$ . Thus our results apply to others  $L$  shells within the plasmasphere, by considering that the wave frequencies must change accordingly as  $\omega \sim 1/L^3$ .

## 9. SUMMARY AND CONCLUSIONS

We have presented a theoretical study of the proton whistler interactions near the equator in the Earth's magnetic field. Whistler waves propagating near the quasi-electrostatic limit, can interact with protons of several hundreds keV energy, travelling in the same directions as the waves along field lines. We assume a wave packet of a finite bandwidth in frequencies  $\omega$ , and propagation angle  $\phi$ , with respect to the geomagnetic field. Near the equator  $\omega \sim \Omega_e(L) \cos \phi$ . Our investigation of the Hamiltonian equations, including multiple harmonics of the proton gyrofrequency for each independent resonance, indicate that

1. The contributions of a large number of negative  $\ell < 0$ , and positive  $\ell \geq 0$  harmonics as defined by the resonance condition (6), are relevant. The Landau resonance takes place off the equator at the geomagnetic latitude  $\Lambda = \Lambda_0$ . Negative harmonics interactions takes place near the equator for  $\Lambda \leq \Lambda_0$ . Positive harmonics cyclotron resonances take place for  $\Lambda \geq \Lambda_0$ .

2. The spacing along magnetic field lines between cyclotron resonances is small. Within a few degrees of the magnetic equator the particles may interact with as many as a hundred harmonics.

3. Protons and waves satisfying the second-order resonance conditions, stay in resonance over relatively long distances along flux tubes. This is because the inhomogeneity of the magnetic field is compensated by the frequency variation of interactions. The wave-frequency

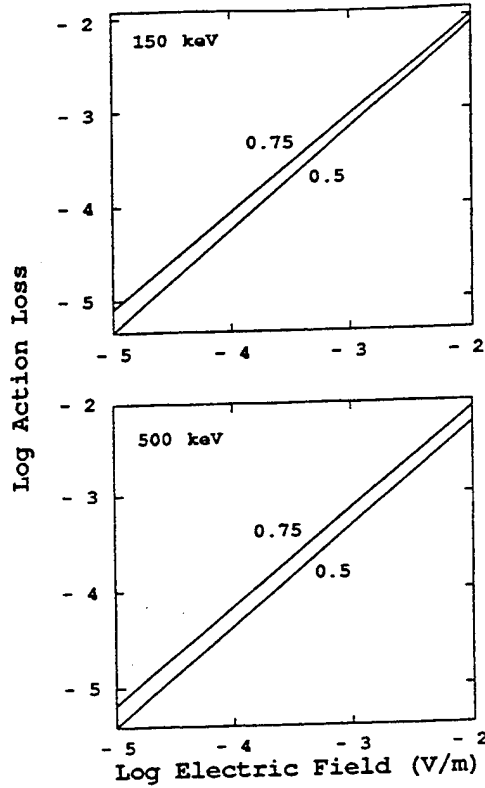


Fig. 9. Logarithm of the change in action in a quarter of a bounce period, see (54) and (55), versus  $\lg(\mathcal{E})$ , where  $\mathcal{E}$  is given in volts per meter. Physical parameters are as in Figure 7.

spectrum needed for second-order resonant interactions is a function of the distance along the flux tube, and the harmonic number.

4. The overlapping criterion for multiple-resonance crossings is derived. In the fields of multiple waves, harmonics overlap in phase space and lead to significant changes in energy and pitch angle.

The numerical calculations applied this theory to parameters relevant to the plasmasphere and control VLF experiments. As an example we have studied the  $L = 3.5$  shell, and particles energies of 150- and 500-keV. The results are as follows:

1. The number of cyclotron-harmonics resonances increases with decreasing frequency, making the interactions more efficient. On the other hand, the distance between resonances also increases with decreasing  $\omega$  which requires a larger bandwidth of waves to overlap those harmonics. As a consequence this investigation is restricted to  $0.5 \leq \omega/\Omega_e(L) < 1$ .

2. Interactions are more efficient for the 150-keV protons than for the 500-keV. Calculations show that for electric fields  $\sim 10^{-4}$  V/m, a proton's pitch angle can decrease one degree or more in a single bounce period.

#### APPENDIX A: DERIVATION OF EQUATION (8)

Near the equator we may expand  $\eta$  as

$$\eta = \eta(L) + \left(\frac{d\eta}{d\Omega_e}\right)_{(L)} (\Omega_e - \Omega_e(L)) \quad (56)$$

where  $(L)$  denotes equatorial values. We also consider

the following ordering in terms of  $m_e/m_p \ll 1$

$$\left(\frac{\Omega_e}{\Omega_e(L)} - 1\right) \sim \frac{\Omega_p}{\omega} \sim \frac{m_e}{m_p} \quad (57)$$

Throughout the calculations, we keep terms only first order in  $m_e/m_p$ . We rewrite (6) as

$$1 - \ell \frac{\Omega_p}{\omega} = \frac{ck_{\parallel}}{\omega} \frac{v_{\parallel}}{c} \quad (58)$$

After taking the square value of (58), the resonance condition approximately reduces to

$$1 - 2\ell \frac{m_e}{m_p} \frac{\Omega_e}{\omega} = \eta^2 \cos^2 \phi \left(\frac{v}{c}\right)^2 \left[1 - \mu \frac{\Omega}{\Omega(L)}\right] \quad (59)$$

Next we substitute  $v/c$  by (7) and  $\eta$  by its expansion in (56), and then show that to first order in  $m_e/m_p$

$$2 \frac{m_e}{m_p} \frac{\Omega_e(L)}{\omega} (\ell + \nu) \simeq \left(1 - \frac{\Omega_e}{\Omega_e(L)}\right) \times \left[2 \left(\frac{d\eta}{d\Omega_e}\right)_{(L)} \left(\frac{\Omega_e}{\eta}\right)_{(L)} - \frac{\mu}{1 - \mu}\right] \quad (60)$$

Next substitute  $\Omega_e/\Omega_e(L)$  by the parabolic profile

$$\frac{\Omega}{\Omega(L)} = 1 + \frac{9}{2} \Lambda^2 \quad (61)$$

Combining (60) and (61), and the value of  $d\eta/d\Omega_e$  as obtained from (2), it can easily be shown that (60) leads to the result in (8).

#### APPENDIX B: THE INTERACTION LENGTH

We consider the behavior of Bessel functions of large order and large arguments. For  $n < x$  and  $|x| \gg 1$  is

$$\mathcal{J}_n(x) \sim \left(\frac{2}{\pi x}\right)^{1/2} \cos\left(x - \frac{\pi}{4} - \frac{n}{2}\pi\right) \quad (62)$$

where  $x = k_{\perp} \rho$ , and  $\rho$  is the Larmor radius. For  $n > x/2$  then

$$\mathcal{J}_n(x) \sim \left(\frac{1}{2\pi n}\right)^{1/2} \left(\frac{e x}{2n}\right)^n \quad (63)$$

and then  $\mathcal{J}_n \rightarrow 0$  [Abramowitz and Stegun, 1964]. The harmonics that effectively contribute to resonant interactions in (15), depends on the behaviors of Bessel functions. Based on our numerical calculations and the results in (62) and (63), we approximate the total number of contributing harmonics  $n >$  and  $< 0$ , by  $\sim k_{\perp} \rho$ . These resonances are located along the field line at latitudes such that  $\Lambda \leq \Delta\Lambda$ . By substituting into (8),  $(\ell + \nu) \sim k_{\perp} \rho$  noticing that this is the largest possible number of contributing harmonics we obtain,

$$\Delta\Lambda \simeq \frac{2}{3} \left[\frac{m_e}{m_p} k_{\perp} \rho\right]^{1/2} \left(f_e - \frac{1}{|\cos \phi|}\right)^{1/2} \quad (64)$$

We call  $\Delta z$  the dimensionless interaction length, which is defined as  $\Delta z = (3/\sqrt{2}) \Delta\Lambda$ .

**Acknowledgments.** We acknowledge helpful conversations with J. Albert, R. Helliwell, H. Koons, and J. Kozyra. We thank G. Ginet for a careful reading of the manuscript. This work has been supported by the U.S. Air Force under contract F19628-89-K-0014 with Northeastern University.

The Editor thanks U. S. Inan, A. Draganov, and H. Karimabadi for their assistance in evaluating this paper.

## REFERENCES

- Abramowitz, M., and I. A. Stegun, *Handbook of Mathematical Functions*, Appl. Math. Ser., vol. 55, National Bureau of Standards, United States Department of Commerce, Washington, D. C., 1964.
- Bell, T. F., The nonlinear gyroresonance interaction between energetic electrons and coherent VLF waves propagating at an arbitrary angle with respect to the Earth's magnetic field, *J. Geophys. Res.*, **89**, 905, 1984.
- Bell, T. F., The wave magnetic field amplitude threshold for nonlinear trapping of energetic gyroresonant and Landau resonant electrons by nonducted VLF waves in the magnetosphere, *J. Geophys. Res.*, **91**, 4365, 1986.
- Bespalov, P. A., and V. Yu. Trakhtengerts, Cyclotron instability of Earth radiation belts, *Rev. Plasma Phys.*, **10**, 88, 1980.
- Carlson, C. R., R. A. Helliwell, and D. L. Carpenter, Variable frequency VLF signals in the magnetosphere: Associated phenomena and plasma diagnostics, *J. Geophys. Res.*, **90**, 1507, 1985.
- Chappell, C. R., K. K. Harris, and G. W. Sharp, A study of the influence of magnetic activity on the location of the plasmopause as measured by OGO 5, *J. Geophys. Res.*, **75**, 50, 1970.
- Chirikov, B. V., A Universal instability of many-dimensional oscillator systems, *Phys. Rep.*, **5**, 263, 1979.
- Dysthe, K. B., Some studies of triggered whistler emissions, *J. Geophys. Res.*, **76**, 6915, 1971.
- Dowden, R. L., A. D. McKay, and L. E. S. Amon, Linear and nonlinear amplification in the magnetosphere during a 6.6 kHz transmission, *J. Geophys. Res.*, **83**, 169, 1978.
- Gendrin, R., Gyroresonant wave particle interactions, *Sol. Terr. Phys.*, part III, *Astrophys. Space Sci. Libr.*, vol 29, Edited by E. R. Dyer, p. 236, Kluwer Academic, Boston, Mass. 1972.
- Ginet, G. P., and M. Heinemann, Test particle acceleration by small amplitude electromagnetic waves in a uniform magnetic field, *Phys. Fluids B*, **2**, 700, 1990.
- Helliwell, R. A., A theory of discrete VLF emissions from the magnetosphere, *J. Geophys. Res.*, **72**, 4773, 1967.
- Helliwell, R. A., VLF wave stimulation experiments in the magnetosphere from Siple station, Antarctica, *J. Geophys. Res.*, **26**, 551, 1988.
- Imhof, W. L., H. D. Voss, J. B. Reagan, D. W. Datlowe, E. E. Gaines, J. Mobilia, and D. S. Evans, Relativistic electron and energetic ion precipitations spikes near the plasmopause, *J. Geophys. Res.*, **91**, 3077, 1986.
- Inan, U. S., Gyroresonant pitch angle scattering by coherent and incoherent whistler mode waves in the magnetosphere, *J. Geophys. Res.*, **92**, 127, 1987.
- Kennel, C. F., and H. E. Petschek, Limit on stably trapped particle fluxes, *J. Geophys. Res.*, **71**, 1, 1966.
- Koons, H. C., Proton precipitation by a whistler-mode wave from a VLF Transmitter, *Geophys. Res. Lett.*, **2**, 281, 1975.
- Koons, H. C., Stimulation of Pc 1 micropulsations by controlled VLF transmissions, *J. Geophys. Res.*, **82**, 1163, 1977.
- Kovrazhkin, R. A., M. M. Mogilevskii, Zh. M. Boske, Yu. I. Gal'perin, N. V. Dzhordzhio, Yu. V. Lisakov, O. A. Molchanov, and A. Rem, *JETP Lett., Engl. Transl.*, **38**, 397, 1983.
- Kovrazhkin, R. A., M. M. Mogilevskii, O. A. Molchanov, Yu. I. Gal'perin, N. V. Dzhordzhio, Zh. M. Boske, and A. Rem, Precipitation of protons from the Earth's magnetosphere stimulated by artificial low-frequency radiation, *JETP Lett., Engl. Transl.*, **39**, 228, 1984.
- Lyons, L. R., and D. J. Williams, *Quantitative aspects of magnetospheric physics*, D. Reidel, Hingham, Mass., 1984.
- Matsumoto, H., Nonlinear whistler-mode interaction and triggered emissions in the magnetosphere: A review, in *Wave Instabilities in Space Plasma*, edited by P. J. Palmadesso and K. Papadopoulos, pp. 163-190, D. Reidel, Dordrecht-Holland, 1979.
- Menyuk, C. R., A. T. Dobrok, K. Papadopoulos, and H. Karimabadi, Stochastic electron acceleration in obliquely propagating electromagnetic waves, *Phys. Rev. Lett.*, **58**, 2071, 1987.
- Morgan, M. G., Some features of parametric (PR) whistlers, *J. Geophys. Res.*, **85**, 130, 1980.
- Nunn, D., A self-consistent theory of triggered VLF emissions, *Planet. Space Sci.*, **22**, 349, 1973.
- Sazhin, S. S., Quasielectrostatic wave propagation in a hot anisotropic plasma, *Planet. Space Sci.*, **34**, 497, 1986.
- Schulz, M., and G. T. Davidson, Limiting energy spectrum of a saturated Radiation Belt, *J. Geophys. Res.*, **93**, 59, 1988.
- Shklyar, D. R., Mechanism for proton precipitation triggered by a VLF wave injected into the magnetosphere, *JETP Lett., Engl. Transl.*, **41**, 448, 1985.
- Shklyar, D. R., Particle interaction with an electrostatic VLF wave in the magnetosphere with an application to proton precipitation, *Planet. Space Sci.*, **34**, 1091, 1986.
- Sudan, R. N., and E. Ott, Theory of triggered VLF emissions, *J. Geophys. Res.*, **76**, 4463, 1971.
- Villalón, E., and W. J. Burke, Relativistic particle acceleration by obliquely propagating electromagnetic fields, *Phys. Fluids*, **30**, 3695, 1987.
- Villalón, E., W. J. Burke, P. L. Rothwell, and M. B. Silvestri, Quasilinear wave particle interactions in the Earth's radiation belts, *J. Geophys. Res.*, **94**, 15243, 1989.
- Villalón, E., and W. J. Burke, Near-equatorial pitch angle diffusion of energetic electrons by oblique whistler waves, *J. Geophys. Res.*, **96**, 9655, 1991.
- Walker, G. H., and J. Ford, Amplitude instability and ergodic behavior for conservative nonlinear oscillator systems, *Phys. Rev.*, **188**, 416, 1969.

W. J. Burke, Geophysics Directorate, PL/GPSG, Hanscom Air Force Base, MA 01731.

E. Villalón, Center for Electromagnetics Research, Northeastern University, Boston, MA 02115.

(Received November 2, 1992;  
revised February 3, 1993;  
accepted March 4, 1993.)

The U.S. Government is authorized to reproduce and sell this report.  
Permission for further reproduction by others must be obtained from  
the copyright owner.

# Diffusion of radiation belt protons by whistler waves

Elena Villalón

Center for Electromagnetics Research, Northeastern University, Boston, Massachusetts

William J. Burke

Phillips Laboratory, Hanscom Air Force Base, Massachusetts

**Abstract.** Whistler waves propagating near the quasi-electrostatic limit can interact with energetic protons ( $\sim 80 - 500$  keV) that are transported into the radiation belts. The waves may be launched from either the ground or generated in the magnetosphere as a result of the resonant interactions with trapped electrons. The wave frequencies are significant fractions of the equatorial electron gyrofrequency, and they propagate obliquely to the geomagnetic field. A finite spectrum of waves compensates for the inhomogeneity of the geomagnetic field allowing the protons to stay in gyroresonance with the waves over long distances along magnetic field lines. The Fokker-Planck equation is integrated along the flux tube considering the contributions of multiple-resonance crossings. The quasi-linear diffusion coefficients in energy, cross energy/ pitch angle, and pitch angle are obtained for second-order resonant interactions. They are shown to be proportional to the electric fields amplitudes. Numerical calculations for the second-order interactions show that diffusion dominates near the edge of the loss cone. For small pitch angles the largest diffusion coefficient is in energy, although the cross energy/ pitch angle term is also important. This may explain the induced proton precipitation observed in active space experiments.

## 1. Introduction

Proton precipitation during controlled VLF transmission experiments occurs over a wide range of plasmaspheric  $L$  shells. Whistler waves transmitted from the ground propagate along the field lines to the magnetic equator where they become quasi-electrostatic [Koons, 1975, 1977; Kovrazhkin *et al.*, 1983, 1984], and interact with the protons in the energy range ( $\sim 80 - 500$  keV). Furthermore, Bell and Ngo [1988] have shown that VLF electromagnetic waves commonly excite high-amplitude electrostatic waves with the same frequencies but with much shorter wavelengths and that have the characteristics necessary to interact with the energetic protons. Lightning discharges [Burgess and Inan, 1990] also generate VLF waves that, after entering the magnetosphere, can become trapped bouncing back and forth between hemispheres. Some of these waves can also interact with energetic protons.

The waves considered here are such that the ratios of the wave frequencies to the equatorial electron gyrofrequencies are  $0.5 < \omega/\Omega_e(L) < 1$ . The argument  $L$  references the electron cyclotron frequency  $\Omega_e$  to its equatorial values. The wave vectors  $\mathbf{k}$ , form an angle  $\phi$  with the background geomagnetic field  $\mathbf{B}_0$ , which is assumed

to be along the  $z$  direction. See Figure 1 for a representation of the geometry of the problem. Thus for most of their trajectories along the field lines  $\omega \ll \Omega_e$ ,  $\phi < 30^\circ$ . Near the equator the waves propagate obliquely to the geomagnetic field with  $0^\circ < \phi < 60^\circ$ .

The frequency range ( $0.5f_{ce} < f < f_{ce}$ ) for the waves we propose to investigate has been observed in a number of experiments [Dowden *et al.*, 1978; Koons, 1977; Kovrazhkin *et al.*, 1984]. For purposes of illustration Plate 1 shows a color wave spectrogram frequency-versus-time, taken using the electric field sweep frequency receiver on the CRRES satellite during the outbound portion of orbit 216 [Gussenhoven *et al.*, 1985]. The color scale represents wave intensities in  $V^2/m^2$  Hz. The white line indicates the electron gyrofrequency. The upper hybrid resonance is above the electron gyrofrequency and has a sharp drop near  $L = 4$ , marking the location of the plasmopause. Note that inside the plasmopause strong emissions were detected in the range  $0.5f_{ce} < f < 0.75f_{ce}$ . The right-hand side of Plate 1 shows the wave-amplitude versus frequency spectrum compiled at 1445:02 UT when CRRES was crossing the magnetic equator, just inside the plasmopause. The wave amplitudes at these frequencies range between  $10^{-5}$  and  $10^{-4}$  V/m. The bandwidths  $\Delta\omega$  over which the wave amplitudes were measured are in the range  $6.5 \text{ Hz} \leq \Delta\omega \leq 3.2 \text{ kHz}$ . In all cases  $\Delta\omega/\omega \ll 1$ ; for  $f \simeq 0.5f_{ce}$  the bandwidth is  $\Delta\omega = 400 \text{ Hz}$ .

For quasi-electrostatic waves the propagation angle  $\phi$  is near the resonance cone angle  $\cos \phi \sim \omega/\Omega_e(L)$ . Owing to the reduced phase and group velocities of

Copyright 1994 by the American Geophysical Union.

Paper number 94JA01480.  
0148-0227/94/94JA-01480\$05.00

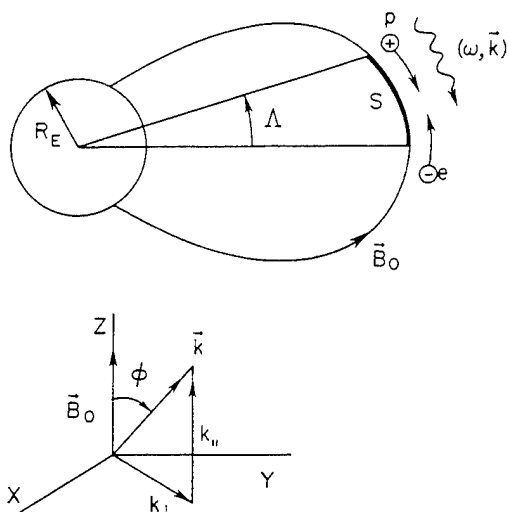


Figure 1. Schematic representation of whistler  $(\omega, \mathbf{k})$ , interacting with electrons and protons near the equator. The Earth's dipole magnetic field is  $\mathbf{B}_0$ , the geomagnetic latitude is  $\Lambda$ , and  $s$  is the coordinate along the flux tube. The coordinate system used in this paper is depicted here.

the waves, resonant interactions occur with slower protons. For proton-whistler interactions the particles' parallel velocities  $v_{\parallel}$  and the wave phase velocities are in the same direction. The characteristic feature of the proton-whistler interactions is the crossing of multiple harmonics of the proton gyrofrequency [Shklyar, 1985, 1986]. Because the waves frequencies are near the equatorial electron gyrofrequency, the resonances are spaced very close to one another, and proton-whistler interactions occur within a few degrees latitude of the magnetic equator.

Interactions in the magnetosphere between the trans-

mitted signals and energetic electrons can lead to the amplification of the original waves [Kennel and Petschek, 1966; Bespalov and Trakhtengerts, 1980] and to frequency spreading [Nunn, 1974; Carlson *et al.*, 1990]. Nonlinear amplification of waves occurs as a result of coherent cyclotron interactions between the VLF waves and resonant electrons. Note that for electron-whistler interactions the parallel velocities  $v_{\parallel}$  of the electrons and the wave phase velocities are oppositely directed. The first harmonic and the Landau resonance play the most important role in the interactions. Triggered emissions sometimes have amplitudes which are larger than the initially transmitted wave [Hellwell, 1967]. They also have narrow bandwidths in frequency and propagation angle that are closely limited to those of the transmitted waves. Having a finite bandwidth of waves is a key element to enhance the efficiency of proton-whistler interactions. Since resonant interactions with energetic electrons are important sources of wave energy, the proton-whistler interaction is a complicated process, involving more than one plasma species.

Finite wave bandwidths allow protons and whistlers to satisfy the conditions for second-order resonances [Dysthe, 1971; Brinca, 1981; Carlson *et al.*, 1985], where inhomogeneities of the magnetic field are compensated by frequency variations. The relative phase between the proton and the wave is  $\xi_e$  as defined below in (13). For resonant particles the spatial derivative of the phase along the field line is such  $d\xi_e/ds = 0$ . In addition, for second order resonances  $d^2\xi_e/ds^2 = 0$ . Thus the waves and particles may remain in resonance for relatively long distances along the magnetic field lines. The resonant wave frequency varies as a function of the distance along the field line, compensating for the variation of the geomagnetic field. In a previous work [Villalón and Burke, 1993], we showed that second-order interactions

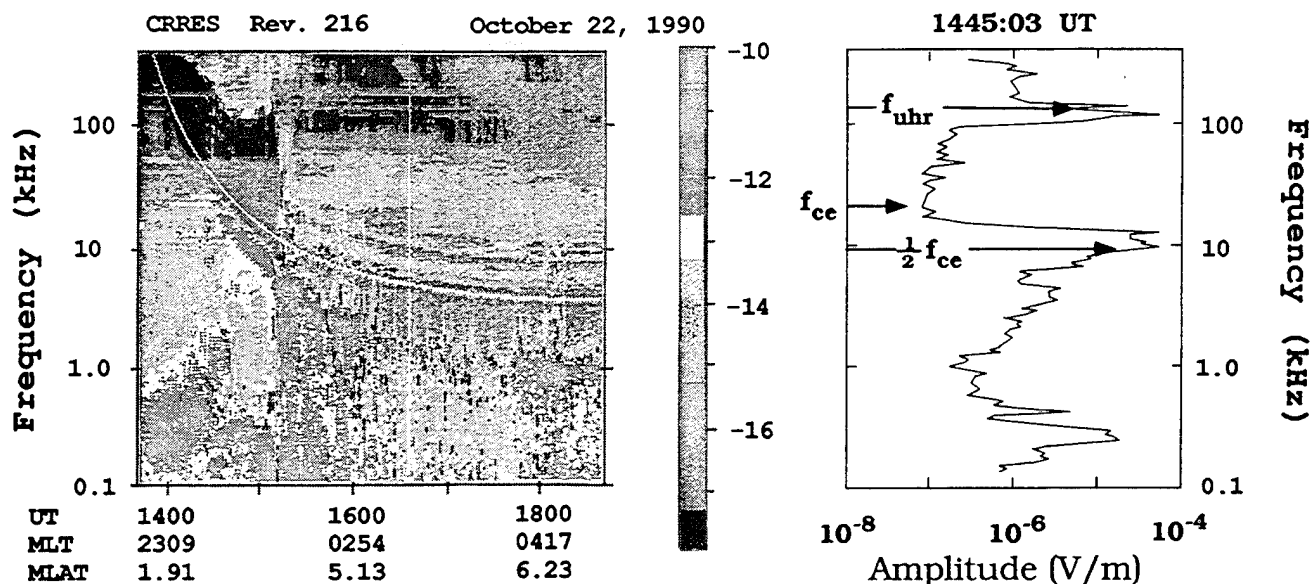


Plate 1. A frequency-versus-time spectrogram obtained by the sweep frequency analyzer on the CRRES satellite. Frequency is given in kilohertz. The color scales are  $\log_{10}$  spectral density in  $\text{V}^2/\text{m}^2 \text{ Hz}$ . The right-hand side gives the wave electric field amplitudes in volts per meter, as function of the wave frequency in kilohertz measured at 1445 UT near the magnetic equator.

resembles those in a homogeneous plasma. Because the resonances can easily overlap in phase space, they lead to significant changes in both the particle energies and pitch angles.

This article extends previous work using a Hamiltonian formulation [Villalón and Burke, 1993] of test-particle interactions with the whistlers which, near the magnetospheric equatorial plane, appear Doppler shifted to some harmonic of the proton gyrofrequency. The affected protons gain energy from the waves and decrease their pitch angles while crossing many resonances. Here we evaluate the diffusion coefficients, for second-order resonant interactions between protons and whistlers based on this Hamiltonian formulation. The diffusion coefficients are shown to be linearly proportional to the waves' electric field amplitudes. These are then used to investigate the behavior of quasilinear, bounce-averaged diffusion equations. Because the number of energetic protons is small, waves gain more energy interacting with the electrons than they lose interacting with the protons. Thus we do not solve the self-consistent problem for the protons, but assume that wave amplitudes remain relatively unchanged during the interactions.

The Fokker-Planck equation has also been investigated by [Kozyra *et al.*, 1994] for the interaction of ring current protons with plasmaspheric hiss. The waves frequencies considered in their article are much smaller than the equatorial electron gyrofrequency. In this case the Doppler shifted harmonic resonances extend for long distances along the flux tube. They only considered first-order resonances. Thus their diffusion coefficients are proportional to the square of the waves' electric field amplitudes. They found that energy diffusion was very important near the edge of the loss cone. Pitch angle diffusion was significant only at large pitch angles, and almost negligible near the loss cone.

The paper is organized as follows. Section 2 describes the resonance condition between the waves and protons at multiple harmonic resonances, for waves propagating in a cold plasma. Section 3 determines the length of the interaction region along the flux tube and the number of possible interacting harmonics as function of the wave-frequency bandwidth. Section 4 briefly reviews the Hamiltonian equations of motion derived by Villalón and Burke [1993]. Section 5 presents the Fokker-Planck equation as function of the equatorial pitch angle and proton energy. In section 6 we integrate the quasilinear diffusion equation along the flux tube by considering the contribution of multiple resonances crossing, for a finite bandwidth of waves. Section 7 considers the case of a weakly inhomogeneous plasma, for second-order resonant interactions, where the inhomogeneity of the magnetic field is compensated by frequency variations. For second-order resonances the energy diffusion equation is studied near the loss cone in Appendix B. Section 8 studies first-order resonant interactions for a strongly inhomogeneous plasma. A comparison of first-order and second-order interactions is given.

Numerical applications are presented in sections 9 for second-order interactions along the magnetic shells  $L = 3.5$  and 2. For the  $L = 3.5$  shell the diffusion

coefficients are large near the loss cone and almost negligible for large pitch angles. For small bandwidths ( $\Delta\omega/\omega \sim 0.005 - 0.01$ ), only protons with energies of  $\sim 100$  keV and pitch angles near the loss cone undergo significant diffusion. Thus one should expect first-order resonant interactions to bring the protons closer to the loss cone. In our theory the scattering of the protons into the loss cone results from second-order interactions. The dominant diffusion coefficient is in energy, though the contribution of the cross energy/pitch angle coefficient is also significant near the edge of the loss cone. We show that diffusion is more effective near  $L = 2$  than near the  $L = 3.5$  shell. In addition, the diffusion coefficients may also become large for large pitch angles. The summary and conclusions are given in section 10.

## 2. Resonant Proton-Whistler Interactions

Consider a whistler wave of frequency  $\omega$  and wave vector  $\mathbf{k}$ , propagating in a field aligned duct. The geomagnetic field  $\mathbf{B}_0$  is along the  $z$  direction and  $\phi$  is the angle between  $\mathbf{k}$  and  $\mathbf{B}_0$  (see Figure 1). The refractive index  $\eta = ck/\omega$  satisfies the dispersion relation

$$\eta^2 = 1 + \frac{(\omega_p/\omega)^2}{(\Omega_e/\omega)|\cos\phi| - 1} \quad (1)$$

where  $\omega_p$  and  $\Omega_e$  are the electron plasma and gyrofrequencies, respectively. The angle  $\phi$  is such that  $\cos\phi_r \leq \cos\phi \leq 1$ . The resonance cone angle  $\phi_r$ , is defined as

$$\cos\phi_r = \frac{\omega}{\Omega_e(L)} \quad (2)$$

where  $(L)$  denotes the equatorial value of the electron gyrofrequency.

The electric field is  $\mathbf{E} = \hat{x} \mathcal{E}_1 \cos\Psi - \hat{y} \mathcal{E}_2 \sin\Psi - \hat{z} \mathcal{E}_3 \cos\Psi$ , where  $\hat{x}$ ,  $\hat{y}$  and  $\hat{z}$  are unit vectors;  $\Psi = k_\perp x + k_\parallel z - \omega t$ , and  $k_\parallel, k_\perp$  are the components along and perpendicular to  $\mathbf{B}_0$  of the wave vector. The ratios of the electric field components are

$$\begin{aligned} \frac{\mathcal{E}_2}{\mathcal{E}_1} &= \frac{1}{\eta^2} \frac{(\omega_p/\omega)^2}{(\Omega_e/\omega) - |\cos\phi|} \\ \frac{\mathcal{E}_1}{\mathcal{E}_3} &= \frac{1 - (\omega_p/\omega)^2 - (\eta \sin\phi)^2}{\eta^2 \sin\phi \cos\phi} \end{aligned} \quad (3)$$

For the case of waves propagating near the resonance cone,  $\omega \sim \Omega_e(L)|\cos\phi|$ , the equatorial refractive index  $\eta^2(L) \gg 1$ . The wave electric field which is linearly polarized, has components  $\mathcal{E}_2/\mathcal{E}_1 \ll 1$ , and  $\mathcal{E}_1/\mathcal{E}_3 \sim -\sin\phi/\cos\phi$ . In this case the wave becomes quasi-electrostatic since  $\mathbf{E}$  is almost in the direction of  $\mathbf{k}$ , and the group velocities  $v_g \sim 1/\eta$  are very small.

Near the equator, we approximate the Earth's magnetic field by a parabolic profile

$$\frac{\Omega}{\Omega(L)} = 1 + \left(\frac{s}{r_L}\right)^2 \quad (4)$$



where  $s \simeq R_E L \Lambda$ ,  $R_E$  is the Earth's radius,  $L$  is the magnetic shell parameter,  $\Lambda$  is the geomagnetic latitude, and  $r_L = (\sqrt{2}/3)R_E L$ . The equatorial gyrofrequency is denoted by  $\Omega(L)$ , and  $\Omega$  stands for the gyrofrequencies either for electrons or protons at a location  $s$  away from the equator along the field line. Equation (4) is obtained from a Taylor expansion of the dipole field and is an excellent representation of the magnetic geometry within  $\pm 20^\circ$  of the equator.

Whistler-proton interactions satisfy the resonance condition

$$\omega - k_{\parallel} v_{\parallel} - \ell \Omega_p = 0 \quad (5)$$

where,  $\ell = 0, \pm 1, \pm 2, \dots$ , is the harmonic number;  $\Omega_p$  is the proton gyrofrequency; and  $v_{\parallel}$  is the parallel components of the particle's velocity. We call  $\mu = \sin^2 \theta_L$ , where  $\theta_L$  is the equatorial pitch angle. Here  $\theta_L > \theta_c$ , where  $\theta_c$  is the pitch angle at the edge of the loss cone, and  $\mu_c$  is the corresponding value of  $\mu$ . As a function of the  $L$  shell, the mirror ratio is  $\sigma = \mu_c^{-1} = L^3 (4 - 3/L)^{1/2}$ . To zero order in the electric field amplitudes, the particle's magnetic moment is conserved. Then we may write for the parallel and perpendicular components of the particle velocity  $v$ :  $v_{\parallel} = v[1 - \mu\Omega/\Omega(L)]^{1/2}$ ,  $v_{\perp} = v[\mu\Omega/\Omega(L)]^{1/2}$ . Note that as the particles and waves move away from the equator, the parallel velocities  $v_{\parallel}$  of particles decrease, while the waves' phase velocities  $\omega/k_{\parallel}$  increase.

Protons of energies less than a few hundred keV, satisfy the resonance condition with waves whose refractive indices  $\eta$  are very large. As the proton energy decreases and the pitch angle increases,  $\eta$  increases. If  $\eta$  becomes very large the dispersion relation in (1) is no longer valid. In this case we must consider thermal corrections for the plasmaspheric electron population that supports the waves as described by *Sazhin* [1993]. These thermal corrections limit the magnitudes of  $\eta_{\parallel} = \eta \omega/\Omega_e(L)$ , to finite values. This means that as  $v_{\parallel} \rightarrow 0$ , resonant interactions described by (5) may not be possible. As the particles energies decreases, the resonant pitch angles must be closer to the loss cone. Interactions for larger pitch angles required larger energies. Thus there could exist a lower value in particle energy, and an upper value in the pitch angle needed to satisfy (5). These values depend on the thermal corrections that defined the possible upper limits of the refractive indices.

### 3. Interaction Region

We assume that a proton interacts at the equator with the harmonic  $\ell = -\nu$ , where  $\nu > 0$ . The geomagnetic latitude  $\Lambda_{\ell}$  of higher-order resonances has been obtained by [Villalón and Burke, 1993] and turn out to be

$$\Lambda_{\ell}^2 = \frac{4}{9} \frac{m_e}{m_p} (\ell + \nu) \frac{1}{|\cos \phi|} \left( \frac{\Omega_e(L)}{\omega} |\cos \phi| - 1 \right) \quad (6)$$

where  $\nu < k_{\perp} \rho$ , and  $\rho = v_{\perp}/\Omega_p$  is the Larmor radius. For reasons explained below the resonant harmonics that effectively contribute to the proton-whistler interactions are such that  $-k_{\perp} \rho < \ell < k_{\perp} \rho$ , where  $k_{\perp} \rho \gg 1$ .

We consider a spectrum of waves that is centered at a certain value of  $\omega$ , and propagates near the resonance cone angle in (2). The widths of this spectrum are  $\Delta\omega (\ll \omega)$ , and  $\Delta\phi (\ll \phi_r)$ . The interaction regions  $\Delta\Omega_e$ , where  $0 < \Omega_e - \Omega_e(L) < \Delta\Omega_e$ , are functions of the waves' frequency bandwidths. The geomagnetic latitudes for resonant interactions,  $\Lambda$ , extend over  $0 \leq \Lambda \leq \Delta\Lambda$ . From (4) we get that  $(\Delta\Lambda)^2 = (2/9) \Delta\Omega_e/\Omega_e(L)$ . Referring to (46) of [Villalón and Burke, 1993], in terms of the waves' frequency bandwidths we show

$$(\Delta\Lambda)^2 = -\frac{2}{9} \frac{\Delta\omega}{\omega} \frac{d\eta_{\parallel}}{d\omega_{\phi}} \left[ \frac{d\eta_{\parallel}}{d\Omega_e} + \eta_{\parallel} \frac{1}{v_{\parallel}} \frac{dv_{\parallel}}{d\Omega_e} \right]^{-1} \quad (7)$$

where  $\eta_{\parallel} = \eta \cos \phi$  and depends on  $\omega$  and  $\phi$  through the variable  $\omega_{\phi} = \omega/\cos \phi$ . Here  $d\eta_{\parallel}/d\Omega_e$ ,  $d\eta_{\parallel}/d\omega_{\phi}$  are obtained from (1), and  $dv_{\parallel}/d\Omega_e = -v_{\perp}^2/[2\Omega_e(L) v_{\parallel}]$ .

The number of possible interacting harmonics covered by this spectrum is  $n$ , where  $-n \leq \ell \leq n$ , is approximated as

$$n = \frac{m_p}{m_e} \frac{\cos \phi}{(\Omega_e(L)/\omega) |\cos \phi| - 1} (\Delta\Lambda)^2 \quad (8)$$

Combining (7) and (8), we find the number of contributing resonant harmonics  $n$  as function of the width of the spectrum  $\Delta\omega/\omega$ .

The interaction region along the field line has a maximum extent in geomagnetic latitude  $\sim \Delta\Lambda_L$ , that is,  $\Delta\Lambda_L \geq \Delta\Lambda$ , for any value of  $\Delta\omega/\omega$ . It is obtained by substituting  $(\ell + \nu)$  by  $\sim 2k_{\perp} \rho$  in (6), which leads to

$$(\Delta\Lambda_L)^2 = \frac{8m_e}{9m_p} k_{\perp} \rho \left( \frac{\Omega_e(L)}{\omega} - \frac{1}{|\cos \phi|} \right) \quad (9)$$

Note that  $\Delta\Lambda_L$  increases with the particle energy and with the pitch angle. By substituting in (7)  $\Delta\Lambda$  by  $\Delta\Lambda_L$ , and solving for the bandwidths yields  $(\Delta\omega/\omega)_L$ .

$$\left( \frac{\Delta\omega}{\omega} \right)_L = \left[ \frac{3\Delta\Lambda_L}{\sqrt{2}} \right]^2 \left[ 1 + \tan^2 \theta_L \left( 1 - \frac{\omega}{\cos \phi \Omega_e(L)} \right) \right] \quad (10)$$

If the widths of the spectrum are equal or larger than  $(\Delta\omega/\omega)_L$ , the entire range of possible resonant harmonics is included in the interactions.

For equatorial interactions that occur near the loss cone, resonant particles must have energies in the range:  $0 < v^2 \leq v_M^2$ . For a finite width spectrum such that  $\phi_r > \phi \geq \phi_r - \Delta\phi$ , we show

$$v_M = \frac{\Omega_e(L)}{\omega_p} \left[ \tan \phi_r \sin \Delta\phi \frac{\sigma}{\sigma - 1} \right]^{1/2} \quad (11)$$

### 4. Equations of Motion

In this section we briefly summarize the Hamiltonian formulation presented by [Villalón and Burke, 1993], to provide the main equations that are relevant to the theory developed here. We normalize the proton  $v$  and canonical  $V$  velocities, by  $c^{-1}$ , length  $s$  by  $r_L^{-1}$ , call  $\tau = t\Omega_p(L)$ , and define  $\kappa = \Omega_p(L) r_L/c \sim 1$ . The dimensionless electric field amplitudes are

$$\epsilon_i = \frac{q\mathcal{E}_i}{m_p c \omega} \quad (12)$$

for  $i = 1, 2, 3$ , and where  $q$  is the proton charge. The relative wave-proton phase angle is

$$\xi_\ell = \ell\lambda + \int_0^s ds' \tau_L k_{\parallel}(s') - \frac{\omega}{\Omega_p(L)} \tau \quad (13)$$

where, in terms of the canonical velocities in the  $y$  and  $x$  directions,  $\lambda = \arctan(V_y/V_x)$ . To zero order in the electric fields amplitudes,  $\lambda = t \Omega_p(L)$ . The canonical action-angle variables are  $I$  and  $\lambda$ , where  $I = (V_{\perp}^2/2) \Omega(L)/\Omega$ .

To first order in the electric field amplitudes  $\epsilon_i$ , the normalized, time-dependent Hamiltonian is a function of the canonical pairs of variables,  $(V_{\parallel}, s)$ , and  $(I, \lambda)$ ,

$$\mathcal{H} = \frac{V_{\parallel}^2}{2} + I \frac{\Omega}{\Omega(L)} - V_{\parallel} \sum_{\ell=-\infty}^{\infty} \sin \xi_\ell \Upsilon_\ell \quad (14)$$

Here

$$\Upsilon_\ell = \frac{V_{\perp}}{2V_{\parallel}} [(\epsilon_1 - \epsilon_2) \mathcal{J}_{\ell+1}(x) + (\epsilon_1 + \epsilon_2) \mathcal{J}_{\ell-1}(x)] - \epsilon_3 \mathcal{J}_\ell(x) \quad (15)$$

where  $\mathcal{J}_\ell$  are Bessel functions, whose argument is  $x = k_{\perp} \rho$ , and  $\rho = V_{\perp}/\Omega_p$ . The behavior of Bessel functions for large arguments is such that if  $\ell < k_{\perp} \rho$ , then [Abramowitz and Stegun, 1964]

$$\mathcal{J}_\ell(z) = \left(\frac{2}{\pi z}\right)^{1/2} \cos\left(z - \frac{1}{2}\ell\pi - \frac{1}{4}\pi\right) \quad (16)$$

if  $\ell > k_{\perp} \rho$  then the contribution of the Bessel functions are negligible. In the numerical calculations we find that near the loss cone, where  $v_{\perp}$  is small, the argument of the Bessel functions is large. Equation (16) may still be used near the loss cone provided the harmonic  $\ell$  is smaller than the argument of the Bessel function.

For a particle crossing an isolated cyclotron resonance we need only consider a single term  $\ell$  in the summation in (14). In this case we find that

$$\frac{dI}{ds} = \ell \cos \xi_\ell \Upsilon_\ell \quad (17)$$

For the phase angle we find

$$\frac{d^2 \xi_\ell}{ds^2} = \alpha + \cos \xi_\ell \frac{(k_{\parallel} r_L)^2}{v_{\parallel}} \Upsilon_\ell \quad (18)$$

The inhomogeneity factor  $\alpha$  depends on the variation of the geomagnetic field, and the frequency spectrum, we show

$$\alpha = \kappa \frac{\omega}{\Omega_p(L)} \left[ \Omega_e(L) \frac{d\eta_{\parallel}}{d\Omega_e} - \eta_{\parallel}(L) \frac{\mu}{2(1-\mu)} \right] + \frac{1}{\Omega(L)} \frac{d\Omega}{ds} + \kappa \frac{\omega}{\Omega_p(L)} \frac{d\eta_{\parallel}}{d\omega_\phi} \frac{d\omega_\phi}{ds} \quad (19)$$

where  $\omega_\phi = \omega/\cos \phi$ ,  $\eta_{\parallel} = \eta \cos \phi$ , and for resonant protons  $d\xi_\ell/ds = 0$ . By using the resonance condition ( $\ell = 0$ ) we estimate that

$$\left[ \frac{1}{\Omega(L)} \frac{d\Omega}{ds} \right]^2 \simeq 8 \frac{\Omega_p(L)}{\omega} \left[ \frac{\mu}{1-\mu} + \frac{|\cos \phi|}{|\cos \phi| - \omega/\Omega_e(L)} \right] \quad (20)$$

The change in particle kinetic energy  $W$  is

$$\frac{dW}{ds} = \frac{\omega}{\ell \Omega_p(L)} \frac{dI}{ds} \quad (21)$$

We define  $\chi = \Omega(L)/\Omega \sin^2 \theta$ , where  $\theta$  is the local pitch angle. The evolution of  $\chi$  as a function of  $s$  is

$$\frac{d\chi}{ds} = \frac{1}{W} \left[ 1 - \mu \frac{\omega}{\ell \Omega_p(L)} \right] \frac{dI}{ds} \quad (22)$$

## 5. Diffusion Equation

Consider the diffusion equation [Lyons and Williams, 1984]:

$$\begin{aligned} \frac{\partial f}{\partial \tau} + \frac{v_{\parallel}}{\kappa} \frac{\partial f}{\partial s} &= \frac{\omega}{\Omega_p(L)} \sum_{\ell=-\infty}^{+\infty} \int \left(\frac{c}{\omega}\right)^3 \frac{d^3 \mathbf{k}}{(2\pi)^3} \\ &\cdot \left[ \hat{G} + \frac{1}{v_{\perp}} (1 - \eta \cos \phi v_{\parallel}) \right] \\ &\cdot \delta(\eta_{\parallel} v_{\parallel} + \ell \frac{\Omega_p}{\omega} - 1) \left( \sqrt{\pi} \frac{v_{\parallel}}{v_{\perp}} \Upsilon_\ell \right)^2 \hat{G} f \end{aligned} \quad (23)$$

where the operators:

$$\hat{G} = 2 \frac{\Omega(L)}{\Omega} \frac{v_{\perp}}{v^2} \left[ \ell \frac{\Omega_p}{\omega} - \left(\frac{v_{\perp}}{v}\right)^2 \right] \frac{\partial}{\partial \mu} + \frac{v_{\perp}}{v} \frac{\partial}{\partial v} \quad (24)$$

$$\hat{G} + \frac{1}{v_{\perp}} (1 - \eta_{\parallel} v_{\parallel}) = \frac{1}{v^2} \frac{\partial}{\partial v} v^2 \sin \theta$$

$$+ 2 \frac{\Omega(L)}{\Omega} \frac{v_{\parallel}}{v} \frac{\partial}{\partial \mu} \left[ \ell \frac{\Omega_p}{\omega} - \left(\frac{v_{\perp}}{v}\right)^2 \right] \frac{v_{\perp}}{v v_{\parallel}}$$

$\mu = \sin^2 \theta_L$ ,  $\theta_L$  is the equatorial pitch angle, and  $v$  is the normalized proton velocity.

We can further rewrite the diffusion equation as

$$\frac{\partial f}{\partial \tau} + \frac{v_{\parallel}}{\kappa} \frac{\partial f}{\partial s} = \sum_{\ell=-\infty}^{+\infty} \int \left(\frac{c}{\omega}\right)^3 \frac{d^3 \mathbf{k}}{2\pi} S_\ell \quad (25)$$

where

$$\begin{aligned} S_\ell &= \frac{v_{\parallel}}{v} \frac{\partial}{\partial \mu} \left\{ \left[ d_{\mu,v} \frac{\partial}{\partial v} + \frac{1}{v} d_{\mu,\mu} \frac{\partial}{\partial \mu} \right] f \right. \\ &\quad \left. + \frac{1}{v^2} \frac{\partial}{\partial v} \left\{ v \left[ v d_{v,v} \frac{\partial}{\partial v} + d_{v,\mu} \frac{\partial}{\partial \mu} \right] \right\} f \right\} \end{aligned} \quad (26)$$

The diffusion coefficients are defined in terms of

$$\Delta_\ell = \left(\frac{\omega}{\Omega_p(L)}\right)^2 \frac{1}{4\pi v_o} \left(\frac{v_{\parallel}}{v_{\perp}}\right)^2 \Upsilon_\ell^2 \delta\left(\frac{d\xi_\ell}{ds}\right), \quad (27)$$

where  $v_o = v_{\parallel}/\kappa$ , and  $\Upsilon_\ell$  is given in (15). Here  $d\xi_\ell/ds = k_{\parallel} r_L + (\ell \Omega_p - \omega)/v_o \Omega_p(L)$ ; and for resonant protons,  $d\xi_\ell/ds = 0$ . Because of the behavior of Bessel functions for large arguments, the number of harmonics that give nonzero contribution to the summation in (25), is such

that  $|\ell|$  is smaller than or of the order of  $k_{\perp}\rho$ . For  $|\ell| > k_{\perp}\rho$  the Bessel functions contribution to  $\Upsilon_{\ell}$  are negligible. We show

$$\begin{aligned} d_{v,v} &= \left(\frac{v_{\perp}}{v}\right)^2 \Delta_{\ell} \\ d_{v,\mu} &= v_{\parallel} d_{\mu,v} = 2\mu^2 \frac{\Omega}{\Omega(L)} \left[\ell \frac{\Omega_p(L)}{\omega \mu} - 1\right] \Delta_{\ell} \\ d_{\mu,\mu} &= 4 \frac{\Omega}{\Omega(L)} \mu^3 \left[\ell \frac{\Omega_p(L)}{\omega \mu} - 1\right]^2 \frac{1}{v_{\parallel}} \Delta_{\ell} \end{aligned} \quad (28)$$

## 6. Integrated Diffusion Equation

To include the effects of the atmospheric loss cone, we introduce the term  $f/\tau_{\text{atm}}$ . Here  $\tau_{\text{atm}} = \tau_B/2$ , if  $\theta_L$  is within the loss cone and  $\tau_{\text{atm}} = \infty$ , if  $\theta_L$  is outside the loss cone. The proton bounce period  $\tau_B$  is the time for a particle to travel from one mirror point to the other and back again. Next integrate along the flux tube by applying the operator:  $\int_{-\infty}^{+\infty} ds/(\tau_B v_o)$  to both sides of (25), which becomes

$$\frac{\partial f}{\partial \tau} + \frac{f}{\tau_{\text{atm}}} = \sum_{\ell=-\infty}^{+\infty} \int_0^{\infty} \eta^2 d\eta \int_{-\pi/2}^{\pi/2} \sin \phi d\phi \frac{1}{v^2} \mathcal{T}_{\ell} \quad (29)$$

where

$$\begin{aligned} \mathcal{T}_{\ell} &= \frac{\partial}{\partial \mu} \left[ v D_{\mu,v} \frac{\partial}{\partial v} + D_{\mu,\mu} \frac{\partial}{\partial \mu} \right] f + \\ &\quad \frac{\partial}{\partial v} \left[ v^2 D_{v,v} \frac{\partial}{\partial v} + v D_{v,\mu} \frac{\partial}{\partial \mu} \right] f \end{aligned} \quad (30)$$

The diffusion coefficients are obtained after integrating along the field lines as follows:

$$D_{v,v} = \left[ \frac{\omega}{\Omega_p(L)} \kappa \right]^2 \frac{1}{4\pi \tau_B v} \frac{\Upsilon_{\ell}^2}{v |d^2 \xi_{\ell}/ds^2|} \quad (31)$$

$$D_{v,\mu} = D_{\mu,v} = 2\mu \left[ \ell \frac{\Omega_p(L)}{\omega \mu} - 1 \right] D_{v,v} \quad (32)$$

$$D_{\mu,\mu} = 4\mu^2 \left[ \ell \frac{\Omega_p(L)}{\omega \mu} - 1 \right]^2 D_{v,v} \quad (33)$$

where  $\Upsilon_{\ell}$  must be evaluated at the resonance and  $\tau_B v \sim 6\sqrt{2}\kappa \times 1.3802$  is independent of  $v$ .

By assuming we have a narrow spectrum of waves we approximate the integrals in (29) as

$$\begin{aligned} \beta &= \int_0^{\infty} \eta^2 d\eta \int_{-\pi/2}^{\pi/2} \sin \phi d\phi \\ &\simeq \eta(L)^2 \left( \frac{d\eta}{d\omega} \right)_{(L)} \Delta\omega \Delta \cos \phi \end{aligned} \quad (34)$$

where  $\Delta\omega$  and  $\Delta \cos \phi$  are the frequency and angular widths of the wave spectrum, such that  $\Delta\omega/\omega$  and  $\Delta \cos \phi / \cos \phi_r \ll 1$ . Thus the integrand is evaluated for  $\eta \sim \eta(L)$  and  $\cos \phi \sim \omega/\Omega_e(L)$ .

We define the diffusion functions

$$\begin{aligned} \mathcal{W}(\mu, v) &= \beta \sum_{\ell=-n}^{+n} D_{v,v} \\ \mathcal{N}(\mu, v) &= \beta \sum_{\ell=-n}^{+n} D_{v,\mu} \\ \mathcal{P}(\mu, v) &= \beta \sum_{\ell=-n}^{+n} D_{\mu,\mu} \end{aligned} \quad (35)$$

The summation extends to all the resonant harmonics. If the interaction region  $\Delta\Lambda$  is such that extends to the entire range of resonant harmonics, that is,  $\Delta\Lambda \rightarrow \Delta\Lambda_L$ , then we may take  $n \rightarrow \infty$ .

Next take  $f = F(\tau_o) G(v, \mu)$ , where  $\tau_o = \tau v$  is independent of  $v$  and  $\mu$ . We define

$$\hat{\tau}_p = -\left[ \frac{1}{F} \frac{dF}{d\tau_o} \right]^{-1} \quad (36)$$

and  $\hat{\tau}_{\text{atm}} = \tau_{\text{atm}} v$ , which is independent of  $v$ . After substituting in (29) and (30), we show that in terms of the proton velocity and pitch angle ( $\mu = \sin^2 \theta_L$ ), the diffusion equation becomes

$$\begin{aligned} \left[ -\frac{1}{\hat{\tau}_p} + \frac{1}{\hat{\tau}_{\text{atm}}} \right] v G &= \frac{1}{v^2} \frac{\partial}{\partial \mu} \left[ v \mathcal{N} \frac{\partial}{\partial v} + \mathcal{P} \frac{\partial}{\partial \mu} \right] G \\ &+ \frac{1}{v^2} \frac{\partial}{\partial v} \left[ v^2 \mathcal{W} \frac{\partial}{\partial v} + v \mathcal{N} \frac{\partial}{\partial \mu} \right] G \end{aligned} \quad (37)$$

## 7. Weakly Inhomogeneous Case

For sufficiently large waves amplitudes and for a wave spectrum such that we can neglect the contribution of  $\alpha$  in the right-hand side of (18), the inhomogeneity of the magnetic field is compensated by the wave spectrum and the solutions of the equations of motion resemble that of a homogeneous plasma. From (18) and (31) we find that the energy diffusion coefficient for second-order resonant protons, is

$$D_{v,v} = \frac{1}{8(\eta \cos \phi)^2} \frac{1}{\tau_B v} \frac{v_{\parallel}}{v} \Upsilon_{\ell} \quad (38)$$

The other coefficients are given in terms of  $D_{v,v}$  by means of (32) and (33). Recall that  $\Upsilon_{\ell}$ , which is a function of  $\mu$ , is defined in (15). We can also derive the diffusion coefficients by using the equations of motion in section 4 (see Appendix A for details).

We consider the following properties of Bessel functions:

$$\begin{aligned} \sum_{\ell=-\infty}^{+\infty} \ell^{\nu} \mathcal{J}_{\ell}(x) &= x^{\nu} \\ \sum_{\ell=-\infty}^{+\infty} \ell^{\nu} \mathcal{J}_{\ell \pm 1}(x) &= (x \mp 1)^{\nu} \end{aligned} \quad (39)$$

where  $\nu = 0, 1, 2$ . For interactions that occur near the loss cone, the argument of the Bessel functions is ap-

proximately obtained by using the resonance condition in (5) as

$$x = k_{\perp} \frac{v_{\perp}}{\Omega_p} \sim \frac{\omega}{\Omega_p(L)} \tan \theta_L \tan \phi_r \gg 1 \quad (40)$$

where  $\phi_r$  is defined in (2).

The diffusion functions  $\mathcal{W}$ ,  $\mathcal{N}$ , and  $\mathcal{P}$ , are given by (35). If the interaction region  $\Delta\Omega_e$  extends to the entire spectrum of resonant harmonics, we may take  $n \rightarrow \infty$ . In this case we can add over all the harmonics, by considering that  $(\Omega_p(L)/\omega\mu) \ll 1$  and (40), we obtain

$$\begin{aligned} \mathcal{W}(\theta_L) &= \frac{\beta}{8(\eta \cos \phi_r)^2} \frac{1}{\tau_B v} [\varepsilon_1 \sin \theta_L - \varepsilon_3 \cos \theta_L] \\ \mathcal{N}(\theta_L) &= 2 \mathcal{W}(\theta_L) [\tan \theta_L \tan \phi_r - \sin^2 \theta_L] \\ \mathcal{P}(\theta_L) &= 4 \mathcal{W}(\theta_L) [\tan \theta_L \tan \phi_r - \sin^2 \theta_L]^2 \end{aligned} \quad (41)$$

where  $\beta$  is defined in (34). For large pitch angles  $\cos \theta_L \rightarrow 0$ , and pitch angle diffusion dominates over energy diffusion. We define  $\zeta = \mu^{1/2} = \sin \theta_L$ , for small pitch angles near the loss cone,  $\zeta \ll 1$  and  $\mathcal{W}(\theta_L) \sim \mathcal{W}_c$ . We show

$$\begin{aligned} \mathcal{W}_c &= \left[ \frac{1}{4 \cos \phi_r} \frac{\Omega_e(L)}{\omega_p} \frac{\Delta\omega}{\omega} \right]^2 \left[ \eta(L) \frac{\omega}{\Omega_e(L)} \right]^3 \\ &\quad \cdot \frac{1}{\tau_B v} \left[ \left( \frac{1}{\sigma - 1} \right)^{1/2} \varepsilon_1 - \varepsilon_3 \right] \end{aligned} \quad (42)$$

$$\begin{aligned} \mathcal{N}(\theta_L) &\sim \nu_1 \zeta + \nu_2 \zeta^2 \\ &= 2 \mathcal{W}_c [\tan \phi_r \sin \theta_L - \sin^2 \theta_L] \\ \mathcal{P}(\theta_L) &\sim p_1 \zeta^2 + p_2 \zeta^3 \\ &= 4 \mathcal{W}_c \tan \phi_r \sin^2 \theta_L [\tan \phi_r - 2 \sin \theta_L] \end{aligned}$$

thus energy diffusion dominates over pitch angle diffusion.

## 8. Strongly Inhomogeneous Case

If the inhomogeneity of the magnetic field and the wave spectrum are such that we can approximate in (18),  $d^2 \xi_e / ds^2 \sim \alpha$ , and if the waves are near the quasi-electrostatic limit then

$$\alpha \simeq -\frac{\kappa}{v_{\parallel}} \left[ 2 \frac{\omega}{\Omega_p(L)} \right]^{1/2} \left\{ \frac{\mu}{1-\mu} + \frac{|\cos \phi|}{|\cos \phi| - \omega/\Omega_e(L)} \right\}^{1/2} \quad (43)$$

The energy diffusion coefficient becomes

$$\mathcal{D}_{v,v} = \left[ \frac{\omega}{2 \Omega_p(L)} \right]^{3/2} \frac{\kappa}{2\pi\tau_B v} \frac{\omega_p}{\Omega_e(L)} v [\Upsilon_{\ell}^2 (1-\mu)] \quad (44)$$

The other coefficients are readily obtained combining (44), (32), and (33). By comparing (38) and (44) we see that for second-order resonant interaction the diffusion coefficient is  $\sim \varepsilon$ , the amplitudes of the electric fields. For first-order interactions  $\sim \varepsilon^2$  and thus the diffusion coefficients for first-order interactions are much smaller than for second-order interactions.

## 9. Numerical Applications

### 9.1. Frequency Bandwidths

We have carried out some numerical calculations based on the model presented in the previous sections for the magnetic shells  $L = 3.5$  and  $L = 2$ . The plasma density in  $\text{cm}^{-3}$  is approximated at the equator as [Chappell *et al.*, 1970]:  $n_e = 3 \times 10^3 (2/L)^4$ . Recall that the dipole magnetic field at the equator is  $B(L) = B_0/L^3$ , where  $B_0 = 0.311$  G. For the  $L = 3.5$  shell the equatorial electron gyrofrequency is  $\Omega_e(L) = 1.28 \times 10^5$  rad/s; the ratio between the electron plasma frequency and the equatorial cyclotron frequency is  $\omega_p/\Omega_e(L) = 7.9$ ; and the width of the equatorial loss cone is  $\theta_c = 6.5^\circ$ . For the  $L = 2$  shell we find  $\Omega_e(L) = 6.8 \times 10^5$  rad/s;  $\omega_p/\Omega_e(L) = 4.5$ ; and  $\theta_c \sim 16^\circ$ . Calculations were conducted for the three frequencies  $\omega/\Omega_e(L) = 0.5, 0.75$ , and  $0.9$ , and for pitch angles at the loss cones and  $20^\circ$  from the loss cones. That is, for  $\theta_L = 6.5^\circ$  and  $20^\circ$  at  $L = 3.5$ , and for  $\theta_L = 16.3^\circ$  and  $35^\circ$  at  $L = 2$ .

For the Landau resonance  $\ell = 0$  the refractive index  $\eta = ck/\omega$  as obtained from the resonance condition in (5), is a function of  $\omega/\Omega_e(L)$ , the particle energy, and the pitch angle. Figure 2 shows  $\eta(L)$  as a function of the proton energy in keV for the shells  $L = 3.5$ , and  $2$ . The three different values of  $\omega$  are indicated by the curves. The pitch angles are also indicated in the figure. Note that as  $\theta_L$  increases so does the refractive index. For a given energy  $> 50$  keV, as  $\theta_L \rightarrow 90^\circ$ ,  $\eta \rightarrow \infty$ . As the refractive index gets very large thermal corrections to (1) due to the plasmaspheric electron population that supports the waves become necessary. This will give the upper limits for the values of  $\eta$ . Thus interactions at large pitch angles may not satisfy the resonance condition in (5), and consequently may not be possible. Note that refractive indices that satisfy the resonance condition in (5) are similar in magnitudes for  $L = 3.5$  and  $2$ .

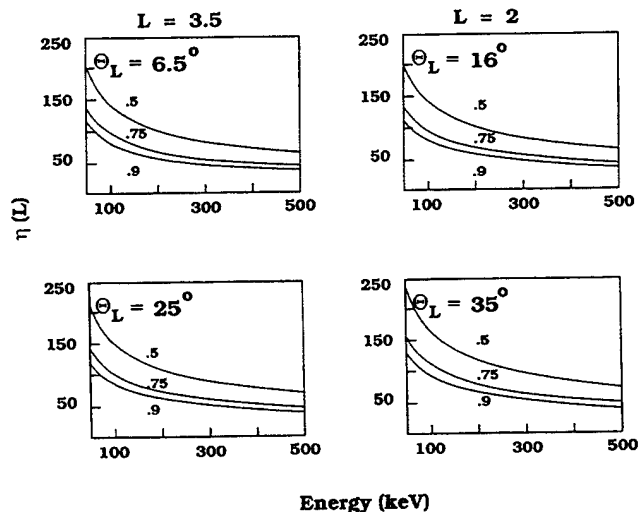


Figure 2. Equatorial refractive index,  $\eta(L)$ , versus the proton energy in keV, for the magnetic shells  $L = 3.5$  and  $2$ . The wave frequencies are  $\omega/\Omega_e(L) = 0.5, 0.75$ , and  $0.9$ . The pitch angles are as indicated in the panels.

This is because, though  $\omega_p/\Omega_e(L)$  decreases with  $L$ , the waves angles  $\phi$  come closer to the resonant cone angle  $\phi_r$  as  $L$  decreases, thus  $\eta(L)$  remains almost constant with  $L$ , for given values of  $\omega/\Omega_e(L)$  and the proton energy.

Combining (5) and (1), we can show that in terms of the normalized particle velocity, the wave normal angle is

$$\cos \phi = \frac{\omega}{\Omega_e(L)} \left\{ \left[ v \frac{\omega_p}{\Omega_e(L)} \cos \theta_L \right]^2 + 1 \right\} \quad (45)$$

Thus as  $\omega_p/\Omega_e(L)$  and  $\cos \theta_L$  decrease with  $L$ ,  $\cos \phi$  becomes closer to  $\cos \phi_r = \omega/\Omega_e(L)$ . Figure 3 plots  $\cos \phi$  versus the proton energy in keV, for the shells  $L = 2$  (solid line), and  $L = 3.5$  (dashed line), and for the three frequencies. At the edge of the loss cones the pitch angles are  $\theta_L = 16.3^\circ$  (solid line), and  $\theta_L = 6.5^\circ$  (dashed line). We see that for  $L = 2$ ,  $\cos \phi$  must stay closer to  $\omega/\Omega_e(L)$  than for  $L = 3.5$ , to satisfy the resonance condition in (5).

Figure 4 shows  $k_\perp \rho$  as function of the energy (keV), for  $L = 3.5$  (left panels) and  $L = 2$  (right panels). The frequencies and physical parameters are the same as in Figure 3. The pitch angles are as indicated in the figure. As we can see,  $k_\perp \rho$  increases with  $\theta_L$  and thus, so does the number of contributing harmonics which are proportional to  $k_\perp \rho$ . Since the loss cone is wider for  $L = 2$  than for  $L = 3.5$ , we find that the arguments of the Bessel functions,  $k_\perp \rho$ , are larger near the loss cone at  $L = 2$  than at  $L = 3.5$ , due to the increasing values of  $\sin \theta_L$ . Thus the numbers of resonant harmonics that contribute to the interactions near the loss cone are larger for the  $L = 2$  than for the  $L = 3.5$  shells. However these harmonics are closer to each other at  $L = 2$  because  $\phi$  is closer to  $\phi_r$ . The extent in geomagnetic latitude remains small at  $L = 2$  even for large pitch angles.

In Figure 5 we show  $\Delta \Lambda_L$  (in degrees) as given in (9) versus the proton energy (in keV), for  $L = 3.5$  and 2, and for the same frequencies and physical parameter as in Figures 4 and 6. The interaction region along the flux tube extends to  $0 \leq \Omega_e - \Omega_e(L) \leq \Delta \Omega_e$ , where  $\Delta \Omega_e/\Omega_e(L) = 4.5(\Delta \Lambda_L)^2$ . Thus the interaction region increases with increasing pitch angle, and with the proton energy. It also increases with decreasing  $\omega$ . The ex-

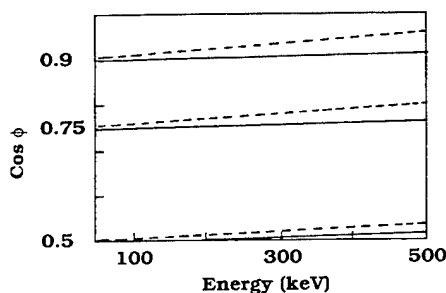


Figure 3. Wave normal angle  $\cos \phi$ , versus proton energy in keV, for  $L = 2$  (solid line) and for  $L = 3.5$  (dashed line). The frequencies are  $\omega/\Omega_e(L) = 0.5, 0.75$ , and  $0.9$ . The pitch angles are  $\theta_L = 16^\circ$  and  $\theta_L = 6.5^\circ$  which correspond to the edge of the loss cones.

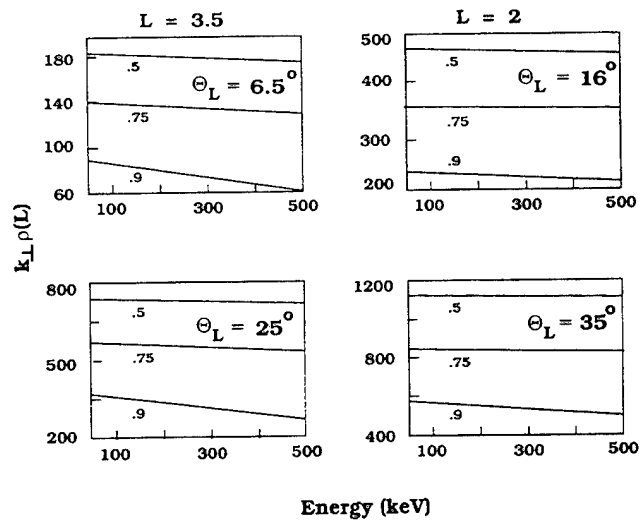


Figure 4. Argument of Bessel functions  $k_\perp \rho$ , versus the proton energy in keV, for  $L = 3.5$  and 2. The frequencies and pitch angles are as in Figure 4.

tent of resonant interactions remains smaller for  $L = 2$  than for  $L = 3.5$  because the proximity of the harmonics decreases with  $L$ .

Figure 6 represents  $(\Delta \omega/\omega)_L$  versus the proton energy as given in (10), for the same parameters as in Figure 6. We see that near the loss cone the wave frequency bandwidths are smaller than for larger pitch angles. The bandwidths increase with increasing energy, and as  $\omega/\Omega_e(L)$  decreases. Because the bandwidths become unrealistically large for large pitch angles and energies, the proton-whistler interactions are more efficient for small energies ( $\sim 100$  keV), and for pitch angles that are near the loss cone.

Next we show some calculations to obtain the diffusion coefficients for second order resonant interactions. The diffusion functions are given in (35), where the number of interacting harmonics  $n$ , is a function of the width of the spectrum  $\Delta \omega/\omega$ , as defined in (8).

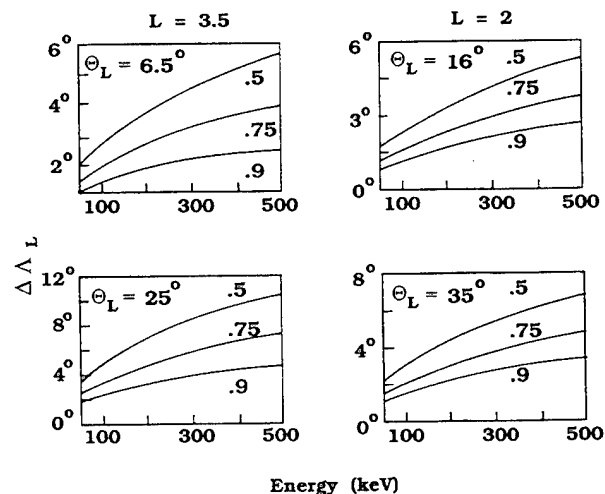


Figure 5. Maximum extent in geomagnetic latitude  $\Delta \Lambda_L$  versus proton energy in keV for  $L = 3.5$  and 2. The frequencies and pitch angles are as in Figures 4 and 6.

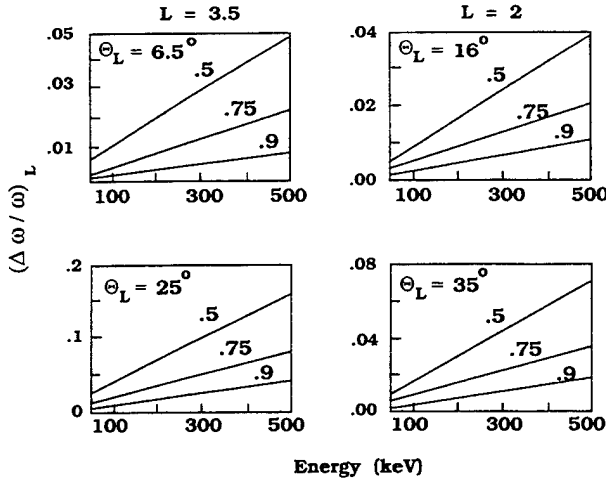


Figure 6. Wave frequency bandwidth,  $(\Delta\omega/\omega)_L$ , versus proton energy in keV, for  $L = 3.5$  and  $2$ . These bandwidths correspond to the resonance lengths as given by  $\Delta\Lambda_L$ , in Figure 7. The frequencies and pitch angles are as in Figures 4 - 7.

They depend on the normalized electric field amplitudes  $\epsilon = 2.5 \times 10^{-6} \times f_e \mathcal{E}$ , where  $f_e = \Omega_e(L)/\omega$ , and  $\mathcal{E}$ , the electric field amplitude, is given in volts per meter. The energy diffusion coefficient is given in (38). The cross pitch angle/energy and pitch angle coefficients are obtained combining (38), (32) and (33).

In all the figures the diffusion functions are normalized to the value that the energy diffusion function  $\mathcal{W}$  takes at the edge of the loss cone which is represented by  $w_c = \mathcal{W}_c/\epsilon_1$ . Here  $\epsilon_1 \sim \epsilon \sin \phi_r$ , and  $\mathcal{W}_c$  is given in (42).

## 9.2. Diffusion Functions for $L = 3.5$

Figure 7 gives the normalized diffusion coefficients versus the  $\sin \theta_L$ , for  $\theta_L > \theta_c = 6.5^\circ$ , for  $\omega/\Omega_e(L) = 0.75$  and for a spectral bandwidth of  $\Delta\omega/\omega = 0.01$ . The proton energy is 100 keV. We see that significant diffusion takes place mostly near the loss cone. The reasons for this have already been explained since near the

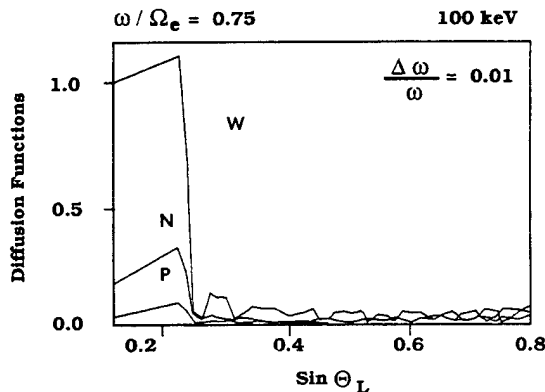


Figure 7. Normalized diffusion functions versus  $\sin \theta_L$ , for  $\theta_L > 6.5^\circ$  and for  $L = 3.5$ . The diffusion functions in all the figures are obtained for second-order resonant protons. The wave frequency is  $\omega/\Omega_e(L) = 0.75$ , and the spectral bandwidth is  $\Delta\omega/\omega = 0.01$ . The proton energy is 100 keV.

loss cone protons and whistlers stay in gyroresonance over the entire resonant length, which extends to all the resonant harmonics that contribute to the interaction. We also observed that the dominant diffusion coefficient is the energy term. However, the contribution of the cross energy/pitch angle coefficient is also significant. We show that  $w_c = 2.5 \times 10^{-3}$ . If the proton energy is 500 keV, and the other physical parameters remain the same, we find that  $w_c = 2. \times 10^{-6}$  which is very small. This is because at large energies, the particles and the waves cannot stay in gyroresonance over the entire interaction length even for small pitch angles. Thus second-order resonant diffusion is more efficient for protons which energies are  $\sim 100$  keV, and whose pitch angles are near the loss cone.

In Figure 8 we represent the normalized diffusion functions versus  $\sin \theta_L$  for  $\theta_L > 6.5^\circ$ , and for  $\omega/\Omega_e(L) = 0.9$ . For the top panel the proton energy is 100 keV, the frequency bandwidth  $\Delta\omega/\omega = 0.005$ , and  $w_c = 7.5 \times 10^{-4}$ . For the lower panel the proton energy is 300 keV,  $\Delta\omega/\omega = 0.01$ , and  $w_c = 5.4 \times 10^{-4}$ . Significant diffusion for small pitch angles are found in both cases. This is because as  $\omega \rightarrow \Omega_e(L)$  the interactions occur very close to the equator and the bandwidths needed to overlap all the harmonics are smaller than for smaller values of  $\omega$ .

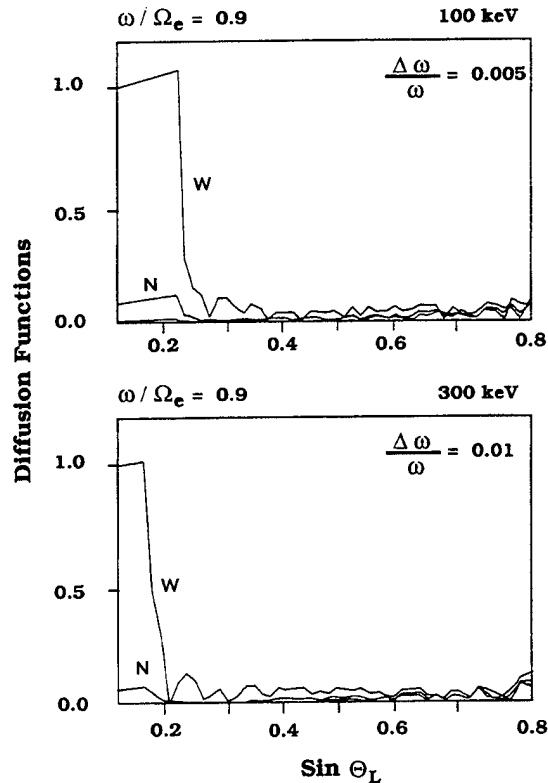


Figure 8. Normalized diffusion functions versus  $\sin \theta_L$ , for  $\theta_L > 6.5^\circ$ , and for  $L = 3.5$ . The wave frequency is  $\omega/\Omega_e(L) = 0.9$ . For the top panel the proton energy is 100 keV, and for the lower panel is 300 keV. The spectral bandwidths for the upper panel is  $\Delta\omega/\omega = 0.005$ , and for the lower panel is  $\Delta\omega/\omega = 0.01$ .

### 9.3. Diffusion Functions for $L = 2$

Figure 9 represents the diffusion functions versus  $\sin \theta_L$ , for  $\theta_L > 16^\circ$ . The proton energy is 100 keV,  $\omega/\Omega_e(L) = 0.5$ , and  $\Delta\omega/\omega = 0.01$ . Because of the large pitch angles, diffusion in energy and pitch angle are almost comparable near the loss cone. The diffusion functions are normalized as in the previous calculations in section 9.2, here  $w_c = 4.27 \times 10^{-3}$ .

The maximum extent of the resonant region  $\Delta\Lambda_L$  is defined in (9). For pitch angles near the loss cone  $k_\perp \rho$  and  $\Delta\Lambda_L$  are small. Given a fixed value of  $\Delta\omega/\omega$ , the actual interaction region extends over  $0 \leq \Lambda \leq \Delta\Lambda_L$ , where  $\Delta\Lambda$  is given in (7). For pitch angles such that  $\sin \theta_L \leq 0.36$ , then  $\Delta\Lambda \geq \Delta\Lambda_L$ . In this case all possible harmonics contribute to the interaction. For  $\sin \theta_L > 0.36$ ,  $\Delta\Lambda < \Delta\Lambda_L$  and the interaction region do not cover the total range of possible contributing harmonics. In this case the number of harmonics  $n$  is defined in (8). As we can see in Figure 9 for small values of  $\sin \theta_L$  all harmonics add up. When  $\sin \theta_L > 0.36$  only a few harmonics contribute and the diffusion coefficients are small.

The frequency ratio  $\omega/\Omega_e(L) = 0.5$  is quite efficient for low  $L$  shells; however, it does not work so well for the  $L = 3.5$  shell. Similar calculations for this frequency and bandwidth at  $L = 3.5$ , show that the number of harmonics that contribute, even for pitch angles near the loss cone, is small and do not cover the whole range of possible harmonics.

Figure 10 shows the diffusion functions versus  $\sin \theta_L$ , for  $\theta_L > 16^\circ$ . The proton energy is 100 keV, and  $\omega/\Omega_e(L) = 0.75$ . For the upper and lower panels the bandwidths are  $\Delta\omega/\omega = 0.005$  and 0.01, respectively. We see that the proton-whistler interactions are more efficient for smaller  $L$  shells. As a matter of fact, calculations at  $L = 3.5$ , for this frequency and energy and a bandwidth of  $\Delta\omega/\omega = 0.005$ , show that the harmonics do not overlap for small pitch angles. For the upper and lower panels we find  $w_c = 8 \times 10^{-4}$  and  $3 \times 10^{-3}$ , respectively. For the bandwidth of 0.01 the harmonics overlap for all values of  $\theta_L$ , and the interactions are very efficient for large pitch angles. However, as explained in

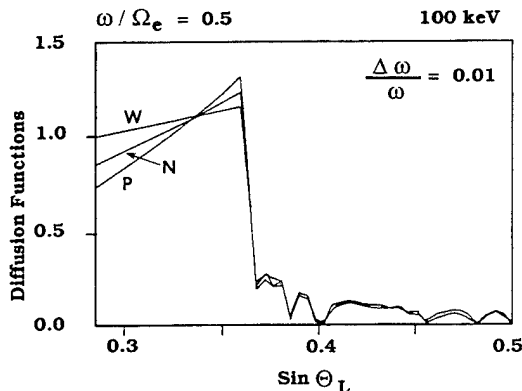


Figure 9. Normalized diffusion functions versus  $\sin \theta_L$ , for  $\theta_L > 16^\circ$ , and for  $L = 2$ . The wave frequency is  $\omega/\Omega_e(L) = 0.5$ , the spectral bandwidth is  $\Delta\omega/\omega = 0.01$ , and the proton energy is 100 keV.

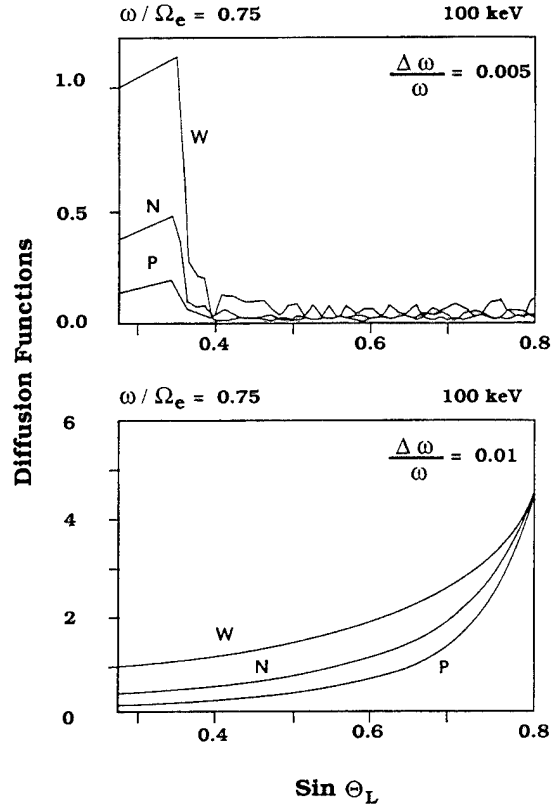


Figure 10. Normalized diffusion functions versus  $\sin \theta_L$ , for  $\theta_L > 16^\circ$ , and for  $L = 2$ . The wave frequency is  $\omega/\Omega_e(L) = 0.75$ , and the proton energy is 100 keV. The bandwidths are for the top and lower panels 0.005 and 0.01, respectively.

section 2, since  $\phi$  is very close to  $\phi_r$ , we may have to calculate the refractive indices using a finite temperature plasma.

Figure 11 shows the diffusion functions versus  $\sin \theta_L$ , for  $\theta_L > 16^\circ$  and  $\omega/\Omega_e(L) = 0.9$ . For the top panel the proton energy is 100 keV,  $\Delta\omega/\omega = 0.003$ , and  $w_c = 3.2 \times 10^{-4}$ . For the lower panel, we have 300 keV,  $\Delta\omega/\omega = 0.01$ , and  $w_c = 6.8 \times 10^{-4}$ . Comparing these results with those in section 9.2, we show that the interactions are more effective for  $L = 2$  than for  $L = 3.5$ . This is mostly due to the fact that as  $L$  and  $\omega_p/\Omega_e(L)$  decrease,  $\phi \rightarrow \phi_r$ , so  $\eta$  is such that the waves and protons can satisfy the resonance condition in (5). As a result, the distances between resonant harmonics as described by (6), are also smaller as  $L$  decreases. Thus the frequency bandwidths required to cover the entire range of possible resonances become also smaller with decreasing  $L$ , which contributes to the efficiency of the interactions.

## 10. Summary and Conclusions

We have investigated the diffusion of protons by oblique whistler waves, which near the magnetic equator, propagate in a quasi-electrostatic mode. We assume a spectrum such that the ratios of the waves frequencies to the equatorial electron gyro-frequencies are  $0.5 < \omega/\Omega_e(L) < 1$ . If the waves appear Doppler shifted to

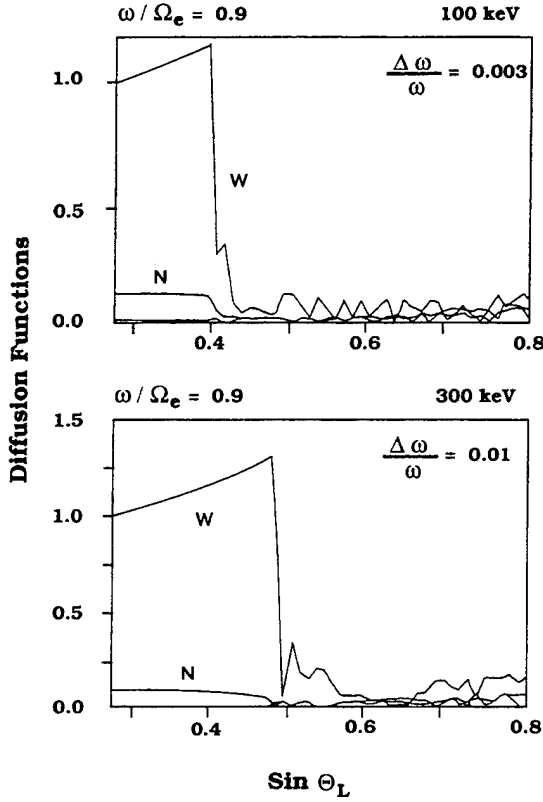


**Figure 11.** Normalized diffusion functions versus  $\sin \theta_L$ , for  $\theta_L > 16^\circ$ , and for  $L = 2$ . The wave frequency is  $\omega/\Omega_e(L) = 0.9$ . For the top and lower panels the proton energies are 100 and 300 keV, respectively. The bandwidths are  $\Delta\omega/\omega = 0.003$  and  $0.01$ , respectively.

some harmonic of the proton gyrofrequency, they can interact strongly with protons whose energies are several hundred keV. The Fokker-Planck equation has been integrated along the flux tube by considering the contribution of multiple harmonics of the proton gyrofrequency. The main results of our theoretical analysis are the following:

1. For second-order resonant interactions the inhomogeneity of the geomagnetic field may be compensated by the resonant-frequency variation along the field line. Thus the interactions resemble those of a homogeneous plasma, and protons and waves can stay in gyroresonance over long distance along the field lines.

2. For second-order resonant interactions the diffusion coefficients in energy, cross energy/pitch angle, and pitch angle are linearly proportional to the amplitudes of the waves' electric fields.

3. The lengths of the regions for resonant interactions along the flux tube, decrease with the protons energies and pitch angles. Thus the wave frequency bandwidths which are required to cover the interaction regions, are small for small energies and pitch angles. The required bandwidths also increase with decreasing  $\omega$ .

Numerical applications of this theory have been carried out for the shells  $L = 3.5$  and  $2$ . The frequencies bandwidths are in the range  $\Delta\omega/\omega \sim 0.005 - 0.01$ . These calculations show the following:

1. The proton-whistler interactions are more effective for small  $L$  shells, due to the fact that as  $L$  decreases the harmonics resonances become closely spaced. They are also quite efficient as  $\omega \rightarrow \Omega_e(L)$ , because then the interactions are also confined very close to the equator. As a matter of fact, for  $L = 2$  the ratio  $\omega/\Omega_e(L) \geq 0.5$  for efficient energy and pitch angle diffusion. For  $L = 3.5$ ,  $\omega/\Omega_e(L) \geq 0.75$  to obtain any significant diffusion.

2. For the  $L = 3.5$  shell we show that the interactions are more efficient for protons of relatively small energies ( $\sim 100$  keV), and whose pitch angles are small. As the pitch angles increase, the diffusion coefficients become very small because the protons and the waves do not stay in gyroresonance over the entire interaction length.

3. The dominant diffusion coefficient is in energy but the cross energy/pitch angle coefficients is also significant for pitch angles which are near the loss cone. For the  $L = 2$  shell and for  $\omega \sim 0.5\Omega_e(L)$ , pitch angle and energy diffusion are comparable. As  $\omega \rightarrow \Omega_e(L)$ , protons diffuse only in energy.

## Appendix A: Diffusion Coefficients

In terms of the equation of motion as defined in section 3 we have

$$\begin{aligned} \mathcal{D}_{v,v} &\sim \frac{(\Delta v)^2}{2\tau_B} \\ \mathcal{D}_{v,\mu} &\sim \frac{v \Delta v \Delta \chi}{2\tau_B} \\ \mathcal{D}_{\mu,\mu} &\sim \frac{(v \Delta \chi)^2}{2\tau_B} \end{aligned} \quad (46)$$

where  $\Delta v = \Delta W/v$ , and  $\Delta W$  is obtained from (21) in terms of  $\Delta I$  as

$$\Delta W = \frac{\omega}{\ell \Omega_p(L)} \Delta I \quad (47)$$

$$\Delta I = \ell \cos \xi_\ell(R) \Upsilon_\ell \delta s$$

For second-order interactions,  $\delta s$  has been given by Villalón and Burke [1993] as

$$(\delta s)^2 = \pi \frac{v_{\parallel}}{(k_{\parallel} r_L)^2} \frac{1}{\cos \xi_\ell(R)} \Upsilon_\ell \quad (48)$$

By substituting  $\cos \xi_\ell(R)$  by  $\pi/8$ , combining (21), (22), and (46) through (48), we arrive at the results in (38) and (32), (33).

## Appendix B: Energy Diffusion Equation

Let us consider second-order resonant protons. Near the loss cone, we may expand  $G(v, \mu)$  in powers of  $\zeta$  as

$$G(v, \zeta) = R(v) + (\zeta - \zeta_c) T(v) \pm (\zeta - \zeta_c)^2 S(v) \quad (49)$$

Here the plus sign is taken when  $\zeta > \zeta_c$ , and the minus when  $\zeta < \zeta_c$ , where  $\zeta_c = \sin \theta_c$ . Near the loss cone,  $\theta_L \sim \theta_c$ , we show

$$-\frac{2v^3}{\tau_B v} \delta(\zeta_c - \zeta) G(v, \zeta) = \frac{p_1}{4} \frac{d^3 G}{d\zeta^3} \quad (50)$$



where  $p_1$  is defined in (42). Integrating (50) from  $\zeta = \zeta_c - \epsilon$  to  $\zeta_c + \epsilon$ , letting  $\epsilon \rightarrow 0$ , substituting  $G$  by its expression in (49) we find

$$S(v) = -\frac{2}{\tau_B v} \frac{v^3}{p_1} R(v) \quad (51)$$

Next we solve (37) for  $0 \leq \zeta - \zeta_c \ll \zeta_c$ , by equating powers of  $\zeta_c$  we find

$$T(v) = -\frac{2\nu_1}{p_1} v \frac{dR(v)}{dv} \quad (52)$$

The function  $R(v)$  satisfies the second-order differential equation

$$v^2 \frac{d^2 R(v)}{dv^2} - v \frac{dR(v)}{dv} + \lambda^2 v^3 R(v) = 0 \quad (53)$$

where

$$\lambda^2 = \frac{1}{\mathcal{W}_c} \left[ \frac{1}{\hat{\tau}_B} \frac{\mu_c}{\mu_m} - \frac{1}{\hat{\tau}_p} \right] \quad (54)$$

where  $\hat{\tau}_B = \tau_B v$ ,  $\mu_m = \sin^2 \theta_m$ , and  $\theta_c < \theta_L < \theta_m$ . The solutions to (53) are Bessel functions. By choosing the solution that goes to zero as  $v \rightarrow 0$  we get

$$R(v) = C \left[ \sqrt{3} A'(-\lambda^{2/3} v) + B'(-\lambda^{2/3} v) \right] \quad (55)$$

where  $C$  is a constant. The functions  $A'$  and  $B'$  are derivatives of the Airy functions.

Consider that  $0 < v \leq v_M$ , where  $v_M$  is given in (11). For energies  $v^2 \leq v_M^2$  the precipitation life times,  $\hat{\tau}_p$ , of protons near the loss cone are obtained from  $(dR/dv) = 0$  at  $v = v_M$ . This leads to  $\lambda v_M^{3/2} \sim 3$ , which solves for  $\hat{\tau}_p$  as function of the velocity  $v_M$ , bounce time  $\hat{\tau}_B$ , and the waves amplitudes through  $\mathcal{W}_c$  as given in (42).

**Acknowledgments.** This work has been supported by the U.S. Air Force under contract with Northeastern University, F19628-89-K-0014, and the Air Force Office of Scientific Research, task 2311PL03.

The Editor thanks J. U. Kozyra and R. A. Helliwell for their assistance in evaluating this paper.

## References

- Abramowitz, M., and I. A. Stegun, *Handbook of Mathematical Functions, Appl. Math. Ser.*, vol. 55, National Bureau of Standards, Gaithersburg, Md., 1964.
- Bell, T. F., and H. D. Ngo, Electrostatic waves stimulated by coherent VLF signals in and near the inner radiation belts, *J. Geophys. Res.*, **93**, 2599, 1988.
- Bespalov, P. A., and V. Yu. Trakhtengerts, Cyclotron instability of Earth radiation belts, *Rev. Plasma Phys.*, **10**, 88, 1980.
- Brinca, A. L., Enhancing whistler wave-electron interaction by the use of specially modulated VLF wave injection, *J. Geophys. Res.*, **86**, 792, 1981.
- Burgess, W. C., and U. S. Inan, Simultaneous disturbance of conjugate ionospheric regions in association with individual lightning flashes, *Geophys. Res. Lett.*, **17**, 259, 1990.
- Carlson, C. R., R. A. Helliwell, and D. L. Carpenter, Variable frequency VLF signals in the magnetosphere: Associated phenomena and plasma diagnostics, *J. Geophys. Res.*, **90**, 1507, 1985.
- Carlson, C. R., R. A. Helliwell, and U. S. Inan, Space-time evolution of whistler mode wave growth in the magnetosphere, *J. Geophys. Res.*, **95**, 15,073, 1990.
- Chappell, C. R., K. K. Harris, and G. W. Sharp, A study of the influence of magnetic activity on the location of the plasmapause as measured by OGO 5, *J. Geophys. Res.*, **75**, 50, 1970.
- Dowden, R. L., A. D. McKay, and L. E. S. Amon, Linear and nonlinear amplification in the magnetosphere during a 6.6 kHz transmission, *J. Geophys. Res.*, **83**, 169, 1978.
- Dysthe, K. B., Some studies of triggered whistler emissions, *J. Geophys. Res.*, **76**, 6915, 1971.
- Gussenhoven, M. S., E. G. Mullen, and R. C. Sagalyn, CRRES/SPACERAD Experiment Descriptions, *Environ. Res. Pap.*, **906**, AFGL-TR-85-0017, Phillips Lab., Hanscom Air Force Base, Mass., 1985.
- Helliwell, R. A., A theory of discrete VLF emissions from the magnetosphere, *J. Geophys. Res.*, **72**, 4773, 1967.
- Kennel, C. F., and H. E. Petschek, Limit on stably trapped particle fluxes, *J. Geophys. Res.*, **71**, 1, 1966.
- Koons, H. C., Proton precipitation by a whistler-mode wave from a VLF transmitter, *Geophys. Res. Lett.*, **2**, 281, 1975.
- Koons, H. C., Stimulation of Pc 1 micropulsations by controlled VLF transmissions, *J. Geophys. Res.*, **82**, 1163, 1977.
- Kovrazhkin, R. A., M. M. Mogilevskii, Zh. M. Boske, Yu. I. Gal'perin, N. V. Dzhordzhio, Yu. V. Lisakov, O. A. Molchanov and A. Rem, Observation of particle precipitation from the ring-current zone stimulated by a powerful ground-base VLF transmitter, *JETP Lett., Eng. Transl.*, **38**, 397, 1983.
- Kovrazhkin, R. A., M. M. Mogilevskii, O. A. Molchanov, Yu. I. Gal'perin, N. V. Dzhordzhio, Zh. M. Boske, and A. Rem, Precipitation of protons from the Earth's magnetosphere stimulated by artificial low-frequency radiation, *JETP Lett., Engl. Transl.*, **39**, 228, 1984.
- Kozyra, J. U., C. E. Rasmussen, and L. R. Lyons, The interaction of ring current and radiation belt protons with ducted plasmaspheric hiss. 1. Diffusion coefficients and timescales, *J. Geophys. Res.*, **99**, 4069, 1994.
- Lyons, L. R., and D. J. Williams, *Quantitative Aspects of Magnetospheric Physics*, D. Reidel, Norwell, Mass., 1984.
- Nunn, D., A self-consistent theory of triggered VLF emissions, *Planet. Space Sci.*, **22**, 349, 1974.
- Sazhin, S. S., *Whistler-Mode Waves in a Hot Plasma*, Cambridge Atmos. and Space Sci. Ser., Cambridge University Press, New York, 1993.
- Shklyar, D. R., Mechanism for proton precipitation triggered by a VLF wave injected into the magnetosphere, *JETP Lett., Engl. Transl.*, **41**, 448, 1985.
- Shklyar, D. R., Particle interaction with an electrostatic VLF wave in the magnetosphere with an application to proton precipitation, *Planet. Space Sci.*, **34**, 1091, 1986.
- Villalón, E., and W. J. Burke, Proton whistler interactions near the equator in the radiation belts, *J. Geophys. Res.*, **98**, 13,509, 1993.
- W. J. Burke, Phillips Laboratory, Hanscom Air Force Base, MA 01731.
- E. Villalón, Center Electromagnetics Research, Northeastern University, Boston, MA 02115. (e-mail: villalon@zircon.phl.af.mil)

(Received November 30, 1993; revised May 31, 1994; accepted May 31, 1994.)

# WHISTLER WAVE INTERACTIONS: SOURCES FOR DIFFUSE AURORA ELECTRON PRECIPITATION ?

Elena Villalón

Center for Electromagnetics Research,  
Northeastern University, Boston MA 02115

William J. Burke

Phillips Laboratory, Hanscom AFB, MA 01731

## ABSTRACT

Resonant electron-whistler interactions in the plasma sheet are investigated as possible explanations of the nearly isotropic fluxes of low-energy electrons observed above the diffuse aurora. Whistler-mode waves, propagating obliquely to the geomagnetic field with frequencies near or larger than half the equatorial electron cyclotron frequency, can interact with the low-energy electrons found in the plasma sheet. A Hamiltonian formulation is developed for test particles interacting with a coherent, chorus-emission spectra. We consider the second-order resonance condition which requires that inhomogeneities in the Earth's magnetic field be compensated by a finite bandwidth of wave frequencies to maintain resonance for extended distances along field lines. Numerical calculations are presented for the magnetic shell  $L = 5.5$  for wave amplitudes of  $\sim 10^{-6}$  V/m, using different frequency and magnetospheric conditions.

## I. INTRODUCTION

The diffuse aurora is formed by nearly isotropic fluxes of electrons, mostly with energies  $< 10$  keV, that precipitate from the plasma sheet [1, 2]. A number of studies have attempted to explain the diffuse aurora by the interaction of the electrons with electrostatic electron cyclotron harmonic (ECH) waves. However, it does not appear that the amplitudes of ECH waves are large enough to account for the observed electron precipitation [3]. Ref. [4] proposed that the  $< 10$  keV electrons that form the diffuse aurora, are precipitated by whistler-mode waves that propagate along the magnetic field with frequencies  $\omega \rightarrow \Omega_e$ . They successfully explained how the resonant energy of the electrons could be well below the characteristic energy or magnetic energy per particle  $E_c$ . Normalized to the electron rest energy  $E_c = (\Omega_e/\omega_p)^2$ , where  $\Omega_e$  and  $\omega_p$  are the electron gyro and plasma frequencies respectively.

Refs. [2], and [5], have interactions between low energy electrons and obliquely propagating chorus emissions. They consider first-order resonant

interactions with upper-band chorus, where the wave frequencies are  $> 0.5 \Omega_e$ . The wave magnetic field amplitudes for chorus were reported to be in the 1–100 pT. If these waves propagate near the resonance cone they become quasi-electrostatic. In this way they can even interact with suprathermal electrons and efficiently precipitate low-energy electrons into the atmosphere, leading to the morningside diffuse aurora.

Figure 3 of Ref. [6] gives an example of waves in this frequency band, observed by the CRRES satellite while passed through the inner plasma sheet during a period of magnetic quieting. Near apogee, where CRRES encountered nearly isotropic plasma sheet electrons it also measured waves covering the band between  $0.5\Omega_e$  and  $\Omega_e$ . In the case shown in Ref. [6] electric field amplitudes of  $\sim 10^{-6} \text{ V m}^{-1}$  appear in the frequency band of interest and, during disturbed times, the intensities of these waves may be several orders of magnitude stronger. Here we wish to demonstrate that even the low amplitudes are sufficient to explain diffuse auroral electron precipitation.

Chorus and triggered emissions are characterized by coherent wave spectra. Triggered emissions are artificially stimulated inside the plasmasphere by ground based transmitters [7]. VLF chorus is frequently associated to microbursts of electron precipitation [8, 9]. The non-linear interactions between energetic electrons and the waves also produce almost monochromatic wavelets which generate chorus elements in a manner similar to that of artificially stimulated emissions [10]. Because of the phase coherence of these emissions, the electrons may stay in gyroresonance for long distances along the field lines, leading to second-order resonant interactions [11].

Here we consider waves with  $0.45 \leq \frac{\omega}{\Omega_e} < 1$  that propagate obliquely to the background geomagnetic field. In contrast with the work in Ref. [2], we consider second-order interactions for a broad spectrum of VLF chorus. The paper is organized as follows: Section II presents the resonance condition for electron interacting with whistler-mode-waves. Section III describes the Hamiltonian theory for second-order interactions. Numerical calculations for low energy ( $< 10 \text{ keV}$ ) plasmasheet electrons are given in Section IV. The amplitude of the waves are  $\approx 10^{-6} \text{ V m}^{-1}$ . Section V contains the conclusions.

## II. RESONANT ELECTRON WHISTLER INTERACTIONS

Figure 1 represents the geometry of wave-particle interactions with a whistler-mode wave of frequency  $\omega$  and wave vector  $\mathbf{k}$ , propagating in a field-aligned duct. The geomagnetic field  $\mathbf{B}_0$  is along the  $z$  direction and  $\phi$  is the angle between  $\mathbf{k}$  and  $\mathbf{B}_0$ . Near the equator, we approximate the Earth's dipole magnetic field as having a parabolic profile. If we define  $h$  as

the ratio between the electron gyrofrequency at a location  $z$  along the field line  $\Omega_e(z)$ , and the equatorial value of the gyrofrequency  $\Omega_e(L)$ , we show

$$h = \frac{\Omega_e(z)}{\Omega_e(L)} = 1 + \left(\frac{z}{r_L}\right)^2 \quad (1)$$

where  $z \simeq R_E L \Lambda$ ,  $R_E$  is the Earth's radius,  $L$  is the magnetic shell parameter,  $\Lambda$  is the geomagnetic latitude, and  $r_L = (\frac{\sqrt{2}}{3}) R_E L$ .

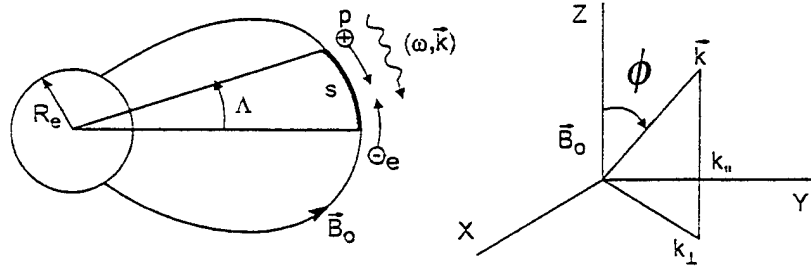


Figure 1. Schematic representation of whistler electrons interactions. The coordinate system is depicted here.

The refractive index  $\eta = \frac{ck}{\omega}$  satisfies the dispersion relation

$$\eta^2 = 1 + \frac{(\omega_p/\omega)^2}{(\Omega_e/\omega) |\cos \phi| - 1} \quad (2)$$

The angle  $\phi$  is such that  $\cos \phi_r \leq \cos \phi \leq 1$ . The resonance cone angle  $\phi_r$ , is defined as  $\cos \phi_r = \frac{\omega}{\Omega_e}$ .

Here we consider relativistic electrons, normalize their energies to  $(m_e c^2)^{-1}$ , their velocities to  $c^{-1}$ , and their momenta  $p$  to  $(m_e c)^{-1}$ . The relativistic factor is  $\gamma_R = [1 - v^2]^{-\frac{1}{2}}$ , where  $v$  is the particle velocity. Resonant whistler-electron interactions must satisfy the condition

$$1 - \eta_{||} v_{||} - \ell \frac{\Omega_e}{\omega} \frac{1}{\gamma_R} = 0 \quad (3)$$

where,  $\ell = 0, \pm 1, \pm 2, \dots$  is the harmonic number. Here  $v_{||}$  and  $\eta_{||} = \eta \cos \phi$ , are the parallel components of the particle's velocity and refractive index, respectively. In terms of the local pitch angle  $v_{||} = v \cos \theta$ . Here  $\theta$  is the angle between  $B_0$  and  $v$ . We call  $\mu = \sin^2 \theta(L)$ , where  $\theta(L)$  is the equatorial pitch angle. Here  $\theta(L) > \theta_c$ , where  $\theta_c$  is the pitch angle at the edge of the loss cone, and  $\mu_c$  is the corresponding value of  $\mu$ . In addition, we require

that  $\theta(L) < \theta_M$ , thus the range of resonant equatorial pitch angles is:  $\mu_c < \mu < \mu_M$ .

If the waves propagate near the equator in the region  $1 \leq h \leq h_M$ , where  $h$  is defined in Eq. (1), then there exists a mapping between  $h$  and  $\mu$ . From Eq. (3) we obtain the following relation between  $\mu_M$  and  $h_M$  as function of the resonant energy  $\gamma_R$  and  $\theta_c$ ,

$$\sqrt{1 - \mu_M} = \sqrt{1 - \mu_c h_M} \left[ \frac{1 + f_L \gamma_R}{-h_M + f_L \gamma_R} \right] \quad (4)$$

where we define  $f_L = \frac{\omega}{\Omega_e(L)}$ . The waves exist near the equator and their extend along the field lines is such that  $h \leq h_M$ , where  $h$  is defined in Eq. (1). Because interactions take place near equatorial regions, then  $h_M$  is close to one. The upper limit on the resonant equatorial pitch angles  $\theta_M$ , is obtained from Eq. (4) and depends on the extend of the interaction region as given by  $h_M$ .

### III. HAMILTONIAN THEORY

We normalize length  $s$  by  $r_L^{-1}$ , call  $\tau = t\Omega_e(L)$ , and define  $\kappa = \frac{c}{\Omega_e(L)r_L} \ll 1$ . The dimensionless electric field amplitudes are  $\varepsilon_i = \frac{|q|\mathcal{E}_i}{m_e c \omega}$ , for  $i = 1, 2, 3$ , where  $\mathcal{E}_i$  are the components of the wave electric field. The relative phase angle between the wave and the electron is:

$$\xi_\ell = \ell\lambda + r_L \int_0^s k_{||} ds' - \frac{\omega}{\Omega_e(L)} \tau \quad (5)$$

where  $\lambda = \arctan(\frac{P_y}{P_x})$ ,  $P_{x,y}$  are components of the canonical momentum. For resonant electrons  $\frac{d\xi_\ell}{ds} = 0$ , which leads to the resonance condition in Eq. (3).

To first order in wave electric field amplitudes, the time-dependent Hamiltonian [12] is:

$$\mathcal{H} = \gamma_o - \frac{P}{\gamma_o} \sum_{\ell=-\infty}^{+\infty} \Upsilon_\ell(I, P_{||}, s) \sin \xi_\ell \quad (6)$$

where  $P = \sqrt{\gamma_o^2 - 1}$ , and  $P_{||}$  is the parallel component of the canonical momentum. Here

$$\begin{aligned} \Upsilon_\ell &= -\frac{1}{2P} \sqrt{2I \frac{\Omega}{\Omega(L)}} [(\varepsilon_1 + \varepsilon_2) \mathcal{J}_{\ell-1}(k_\perp \rho) + (\varepsilon_1 - \varepsilon_2) \mathcal{J}_{\ell+1}(k_\perp \rho)] \\ &+ \varepsilon_3 \frac{P_{||}}{P} \mathcal{J}_\ell(k_\perp \rho) \end{aligned} \quad (7)$$

where the  $J$ 's are Bessel functions and  $\rho = \left(\frac{e}{\Omega_e}\right) \left[\frac{2I\Omega}{\Omega(L)}\right]^{\frac{1}{2}}$ , is the Larmor radius. In terms of  $P_{\perp}$ , the perpendicular component of the canonical momentum, the canonical action is  $I = \frac{\Omega(L)}{2\Omega} P_{\perp}^2$ .

After differentiating Eq. (5) twice with respect to  $s$ , we show

$$\frac{d^2 \xi_{\ell}}{ds^2} = \xi_{\ell}^{(2)} = \alpha_{\ell} + \frac{p}{(\kappa p_{\parallel})^2} (\eta_{\parallel}^2 - 1) \left[\frac{\omega}{\Omega_e(L)}\right]^2 \Upsilon_{\ell} \quad (8)$$

where the constant  $\alpha_{\ell}$  depends on the magnetic field inhomogeneities and the wave frequency. For second-order resonances the inhomogeneity of the magnetic field is compensated by variation of the resonant frequency along the field lines [13]. In this case  $\alpha_{\ell} = 0$ , which leads to the frequency variation along the field line

$$\frac{1}{\omega} \frac{d\omega}{ds} = \frac{\gamma_R}{\ell h} \sqrt{\frac{h-1}{1-\mu h}} \left[ \frac{2\ell}{\gamma_R} \sqrt{1-\mu h} - \Lambda(L, v) \mu \right] \quad (9)$$

where  $\Lambda(L, v) = \frac{\eta_{\parallel} v \omega}{\Omega_e(L)}$ .

After solving for the equations of motion the change in action, energy and pitch angle are

$$\Delta I = \frac{\ell}{\kappa} \frac{p}{p_{\parallel}} \sqrt{\frac{\pi}{|\xi_{\ell}^{(2)}|}} \Upsilon_{\ell} \quad (10)$$

$$\Delta \gamma_R = \frac{\omega}{\ell \Omega_e(L)} \Delta I \quad (11)$$

$$\Delta \mu = \frac{2}{\gamma_R^2 - 1} \left[ \frac{\ell \Omega_e}{\omega} - \gamma_R \mu \right] \Delta \gamma_R \quad (12)$$

where  $\xi_{\ell}^{(2)}$  is defined in Eq. (8). Note that for second-order resonances,  $\alpha_{\ell} = 0$ , and then the changes in the physical variables are proportional to  $\varepsilon_i^{1/2}$ . This is to be contrasted to first-order interactions where these changes are linear with the electric field amplitudes.

#### IV. NUMERICAL APPLICATIONS

We have conducted some numerical calculations based on this model for the magnetic shell  $L = 5.5$ . The equatorial electron gyrofrequency is  $\Omega_e(L) = 0.33 \times 10^5 \text{ s}^{-1}$ . The ratio between the electron plasma and the equatorial cyclotron frequencies, is  $\frac{\omega_p}{\Omega_e(L)} = 3$ . The width of the loss cone is  $\theta_c = 3.25^\circ$ . Calculations were conducted for the frequencies  $\frac{\omega}{\Omega_e(L)} = 0.55$ , and 0.75. We assume that the waves have a coherent spectrum of finite frequency bandwidth, as occurs in the chorus and triggered emissions.

Figure 2 plots the energies of resonant electrons in keV versus  $\cos \phi$ , where  $\phi$  is the angle between the wave vector and the geomagnetic field. The electron energies represent solutions for the resonance condition at the equator, for a maximum geomagnetic latitude of  $5^\circ$ . For panel A,  $\frac{\omega}{\Omega_e(L)} = 0.55$ , and we represent the harmonics  $\ell = 0, 1$  as indicated next to the curves. For panel B,  $\frac{\omega}{\Omega_e(L)} = 0.75$  and we only represent the first harmonic  $\ell = 1$ . We also observe that for waves to interact with electrons of energy  $< 1$  keV, their angles of propagation  $\phi$  must get closer to the resonance angle  $\phi_r$ . Also, if  $\omega \rightarrow \Omega_e(L)$  then the electron energy decreases below 1 keV.

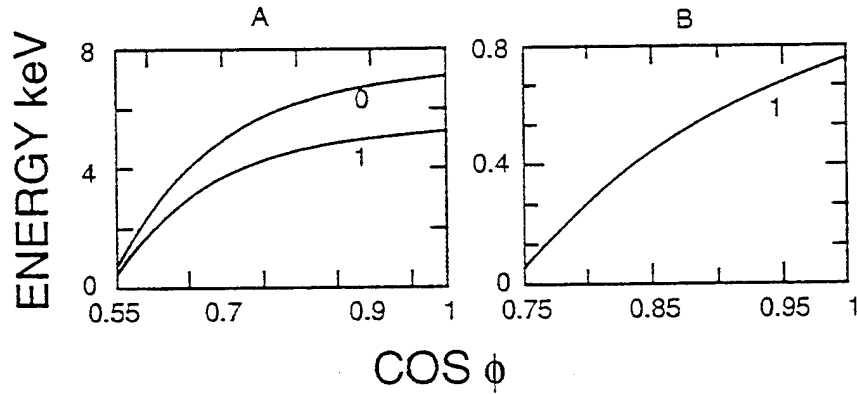


Figure 2. Electron energy in keV versus  $\cos \phi$ . For panel A, and B,  $\frac{\omega}{\Omega_e(L)} = 0.55$ , and  $0.75$ , respectively.

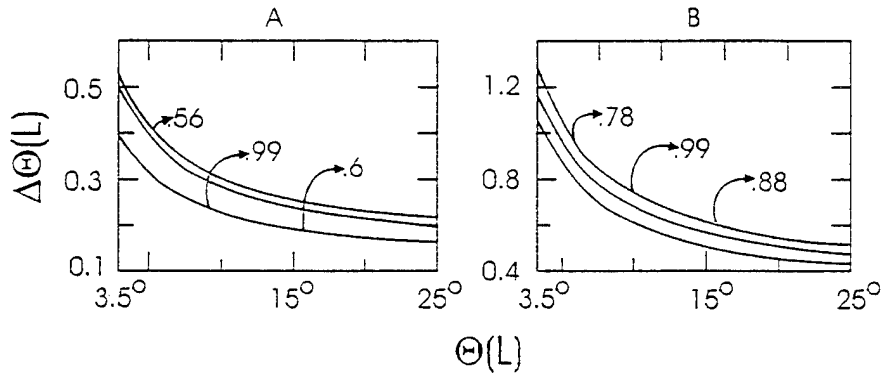


Figure 3. Change in pitch angle  $\Delta\theta(L)$  versus  $\theta(L)$  for  $\ell = 1$  harmonic.

Figure 3 represents the change in equatorial pitch-angle  $\Delta\theta_L$  versus the pitch-angle in degrees for second-order resonances, and for interactions for the first  $\ell = 1$  gyroharmonic. The change in pitch-angle is obtained by

combining Eqs. (8) through (12). Panel A represents the frequency ratio  $\frac{\omega}{\Omega_e(L)} = 0.55$  at three propagation angles  $\cos \phi = 0.56, 0.6$ , and  $0.99$  as indicated next to the curves; the corresponding resonant energies are  $0.4, 1.75$ , and  $5.5$  keV. Panel B represents the frequency ratio  $\frac{\omega}{\Omega_e(L)} = 0.75$  at three propagation angles  $\cos \phi = 0.78, 0.88$ , and  $0.99$ ; the corresponding resonant energies are  $140, 470$  and  $700$  eV.

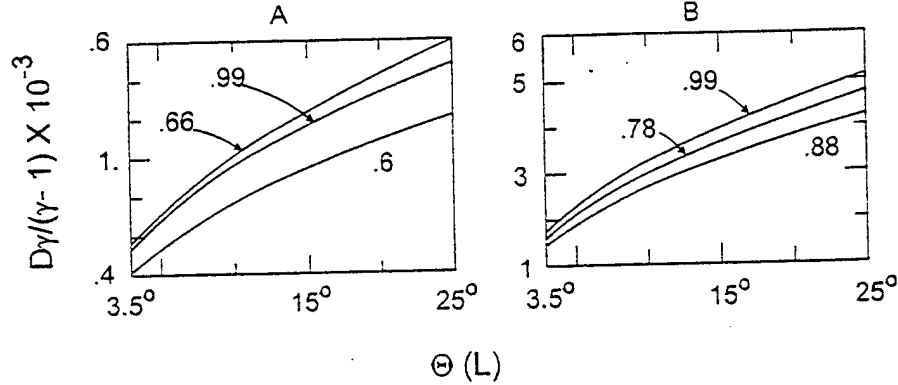


Figure 4. Change in electron resonant energy  $\frac{\Delta\gamma_R}{\gamma_R-1}$  versus  $\theta(L)$ , for  $\ell = 1$  harmonic.

Figure 4 shows the normalized changes in energy as  $\frac{\Delta\gamma_R}{\gamma_R-1}$ , versus resonant equatorial pitch angles. The panels correspond to the same examples as presented in Figure 3. The changes in energy are obtained as in Eq. (11), by assuming that the second-order resonance condition is satisfied with the first gyroharmonic. Note that as  $\omega \rightarrow \Omega_e(L)$  larger changes in energies are calculated than for smaller values of the ratio  $\frac{\omega}{\Omega_e(L)}$ .

## VI. CONCLUSIONS

We have presented a test-particle, Hamiltonian theory for the interactions of whistler-mode waves and low energy ( $< 10$  keV) electrons near the equatorial plasma sheet. The main results are:

(1) Efficient whistler-electrons interactions require that the ratios  $\frac{\omega}{\Omega_e(L)} \geq 0.5$ . For waves propagating near the resonance cone and for  $\omega \rightarrow \Omega_e(L)$ , resonant energies are  $< 1$  keV.

(2) Second-order resonant interactions require a coherent spectrum of multiple-frequency waves such as found in chorus. In this case the inhomogeneities of the magnetic field are compensated by variations of the resonant wave frequency. Thus the electrons and the waves stay in gyroresonance long



distances along the field lines, which render the interactions very efficient.

(3) Numerical calculations have been conducted for the  $L = 5.5$  shell. As an example we considered wave amplitudes of  $10^{-6} \text{ V m}^{-1}$ , consistent with observations from the CRRES satellite. Changes in pitch-angle can be  $> 1^\circ$  for electrons with pitch-angles near the edge of the loss cone. Thus, whistler-electron interactions are viable explanations of the nearly isotropic precipitation of low-energy electrons from the plasma sheet to form the diffuse aurora.

### ACKNOWLEDGEMENTS

This work has been supported in part by the U. S. Air Force contract with Northeastern University, F19628-92-K-0007. We are grateful to Dr. David Hardy of the Phillips Laboratory for suggesting this problem.

### REFERENCES

- [1] A. D. Johnstone, *Ann. Geophys.*, **1**, 4, 397 (1983).
- [2] U. S. Inan, Y. T. Chiu and G. T. Davidson, *Geophys. Res. Lett.*, **19**, 653 (1992).
- [3] J. L. Roeder, and H. C. Koons, *J. Geophys. Res.*, **94**, 2529 (1989).
- [4] A. D. Johnstone, D. M. Walton, R. Liu, and D. A. Hardy, *J. Geophys. Res.*, **98**, 5959 (1993).
- [5] U. S. Inan, and T. F. Bell, *Geophys. Res. Lett.*, **18**, 49 (1991).
- [6] W. J. Burke, A. G. Rubin, D. A. Hardy and E. G. Holeman, *J. Geophys. Res.*, **100**, in press (1995).
- [7] W. J. Burtis, and R. A. Helliwell, *J. Geophys. Res.*, **80**, 1007 (1976).
- [8] D. A. Hardy, W. J. Burke, and E. Villalón, *J. Geophys. Res.*, **95**, 6451 (1990).
- [9] G. T. Davidson, and Y. T. Chiu, *Geophys. Res. Lett.*, **14**, 1166 (1987).
- [10] S. S. Sazhin, and M. Hayakawa, *Planet. Space Sci.* **40**, 681 (1992).
- [11] K. B. Dysthe, *J. Geophys. Res.* **76**, 6915 (1971).
- [12] G. P. Ginat, and M. Heinemann, *Phys. Fluids B*, **2**, 700 (1990).
- [13] E. Villalón, and W. J. Burke, *J. Geophys. Res.*, **98**, 13,509 (1993).

# Pitch angle scattering of diffuse auroral electrons by whistler mode waves

Elena Villalón

Center for Electromagnetics Research, Northeastern University, Boston, Massachusetts

William J. Burke

Space Science Division, Phillips Laboratory, Hanscom Air Force Base, Massachusetts

**Abstract.** Resonant electron-whistler interactions in the plasma sheet are investigated as possible explanations of the nearly isotropic fluxes of low-energy electrons observed above the diffuse aurora. Whistler mode waves, propagating near the resonance cone with frequencies near or larger than half the equatorial electron cyclotron frequency, can interact with low-energy plasma sheet electrons. A Hamiltonian formulation is developed for test particles interacting with the coherent chorus emission spectra. We consider the second-order resonance condition which requires that inhomogeneities in the Earth's magnetic field be compensated by a finite bandwidth of wave frequencies to maintain resonance for extended distances along field lines. These second-order interactions are very efficient in scattering the electrons toward the atmospheric loss cone. Numerical calculations are presented for the magnetic shell  $L = 5.5$  for wave amplitudes of  $\sim 10^{-6}$  V/m, using different frequency and magnetospheric conditions.

## 1. Introduction

The pitch angle scattering of energetic electrons by whistler waves in the Earth's radiation belts is a long-standing research problem [Lyons and Williams, 1984, and references therein]. Whistler waves are responsible for the precipitation of electrons in both the plasmasphere and the plasma sheet [Bell, 1984]. As electrons scatter toward smaller pitch angles, they give up small quantities of energy, amplifying the waves to the point where the interaction becomes self-sustaining. The limit for stably trapped particle fluxes was first investigated by Kennel and Petschek [1966], and later in self-consistent quasi-linear diffusion models by Bespalov and Trakhtengerts [1986], Villalón et al. [1989], and Villalón and Burke [1991].

Past studies have considered whistler waves for which the ratio between the wave and the electron cyclotron frequencies is  $\omega/\Omega_e \ll 1$ . In this case, only electrons whose energies are larger than or of the order of the magnetic energy per particle  $E_c$ , may interact with the waves. Normalized to the electron rest energy,  $E_c = (\Omega_e/\omega_p)^2$ . Here,  $\Omega_e$  and  $\omega_p$  are the electron cyclotron and the plasma frequencies, respectively. As pointed out by Johnstone et al. [1993], in the outer plasma sheet the threshold energy for resonant interactions is estimated to be  $> 10$  keV. In this paper we investigate

the possibility of resonant interactions of whistler mode waves with electrons with energies well below 10 keV. For these interactions to take place, the wave frequency must be close to  $\Omega_e$ .

The diffuse aurora is formed by nearly isotropic fluxes of electrons, mostly with energies of  $< 10$  keV, that precipitate from the plasma sheet [Johnstone, 1983; Inan et al., 1992]. A number of studies have attempted to explain the diffuse aurora by the interaction of the electrons with electrostatic electron cyclotron harmonic (ECH) waves [Swift, 1981]. However, it does not appear that the amplitudes of ECH waves are large enough to account for the electron precipitation [Belmont et al., 1983; Roeder and Koons, 1989]. Johnstone et al. [1993] proposed that the  $< 10$  keV electrons that form the diffuse aurora may be precipitated by whistler mode waves that propagate along the magnetic field with frequencies such that  $\omega \rightarrow \Omega_e$ . They successfully explained how the resonant energy of the electrons could be well below  $E_c$ .

We note that Figure 3 of Burke et al. [1995] gives an example of waves in this frequency band, observed by the CRRES satellite while it passed through the inner plasma sheet during a period of magnetic quieting. Near apogee, where CRRES encountered nearly isotropic plasma sheet electrons, it also measured waves covering the band between  $0.5\Omega_e$  and  $\Omega_e$ . Our experience is that these frequencies are detected by the CRRES plasma wave experiment only in the presence of central plasma sheet electrons. In the case shown by Burke et al. [1995], electric field amplitudes of  $\sim 10^{-6}$  V m $^{-1}$  appear in the frequency band of interest. Dur-

ing disturbed times the intensities of these waves may be several orders of magnitude stronger than in the case presented. Here we wish to demonstrate that even the low amplitudes are sufficient to explain diffuse auroral electron precipitation.

Inan *et al.* [1992] and Inan and Bell [1991] have studied interactions between low-energy electrons and obliquely propagating chorus emissions. They consider first-order resonant interactions with upper band chorus, where the wave frequencies are  $> 0.5\Omega_e$ . The wave magnetic field amplitudes for chorus were reported to be in the range of 1–100 pT. Inan *et al.* [1992] used wave magnetic amplitudes of 1 pT in their calculations. If these waves propagate near the resonance cone, they become quasi-electrostatic. In this way they can even interact with suprathermal electrons [Jasna *et al.*, 1992] and efficiently precipitate low-energy electrons into the atmosphere, leading to the morningside diffuse aurora.

Chorus and triggered emissions are characterized by coherent wave spectra. Triggered emissions are artificially stimulated inside the plasmasphere by ground-based transmitters [Burtis and Helliwell, 1976; Helliwell, 1993]. VLF chorus is frequently associated with microbursts of electron precipitation [Rosenberg *et al.*, 1981; Parks, 1978]. It is believed that chorus is generated through a cyclotron instability which is produced by anisotropic warm electrons in the equatorial plasma sheet [Hashimoto and Kimura, 1981; Ohmi and Hayakawa, 1986]. The nonlinear interactions produce impulsive precipitation of the electrons [Hardy *et al.*, 1990] due to the filling of the loss cone as described by Davidson and Chiu [1987]. The nonlinear interactions between energetic electrons and the waves also produce almost monochromatic wavelets, which generate chorus elements in a manner similar to that of artificially stimulated emissions [Sazhin and Hayakawa, 1992]. Because of the phase coherence of these emissions, the electrons may stay in gyroresonance for long distances along the field lines, leading to second-order resonant interactions [Dysthe, 1971; Nunn, 1974].

Here we consider waves with  $0.45 \leq \omega/\Omega_e < 1$  that propagate obliquely to the background geomagnetic field. These waves may be generated by the linear cyclotron instability of warm electrons interacting with the waves as described by Kennel and Petschek [1966] and Johnstone [1983]. For linear interactions the diffusion of the electrons into the loss cone is weak, and the precipitation does not occur in an impulsive way as in the microbursts [Davidson, 1986a and 1986b]. If wave amplitudes grow to some critical levels, nonlinear effects allow for second-order interactions to take place. Second-order interactions require that the wave amplitudes be large and have a finite frequency spectral spread to compensate for the magnetic field inhomogeneities [Villalón and Burke, 1993]. Second-order interactions are defined in terms of the variation of the relative phase angle between the waves and the electrons, which leads to a specific change of the wave frequency along the field line, as given in section 5. In contrast with the work by Inan *et al.* [1992], we consider second-order interactions for a broad spectrum of VLF chorus.

The wave amplitudes required for efficient electron precipitation are smaller with the second-order resonant interactions than those used by Inan *et al.* [1992]. We assume electric field amplitudes of  $\approx 10^{-6}$  V m $^{-1}$ . For a refractive index  $\eta \leq 30$  this corresponds to wave magnetic field amplitudes of  $\leq 0.1$  pT.

The paper is organized as follows. Section 2 presents the basic equations that describe whistler mode waves propagating in a cold magnetized plasma. Section 3 considers electron-whistler resonant interactions in the Earth's inhomogeneous magnetic field. We establish a mapping between the location of the interactions along the field line and the equatorial pitch angles of electrons resonant at the first cyclotron harmonic. Section 4 contains the basic equations of a test particle Hamiltonian theory. In section 5 we integrate these equations along magnetic field lines. Conditions for second-order resonances are also given. Section 6 contains numerical applications for plasma sheet electrons. We consider second-order resonant interactions of test particles with multiple-frequency waves. The changes in pitch angle and energy are calculated. For wave amplitudes of  $\sim 10^{-6}$  V m $^{-1}$ , we show that the changes in pitch angle may be  $\geq 1^\circ$  for electrons near the edge of the loss cone.

## 2. Whistler Mode Waves

Figure 1 represents the geometry of wave-particle interactions with a whistler mode wave of frequency  $\omega$  and wave vector  $\mathbf{k}$ , propagating in a field-aligned duct. The geomagnetic field  $\mathbf{B}_0$  is along the  $z$  direction, and  $\phi$  is the angle between  $\mathbf{k}$  and  $\mathbf{B}_0$ . For waves propagating near the resonance cone,  $\cos \phi \sim \omega/\Omega_e$ , the refractive indices are very large, and the waves become quasi-electrostatic [Sazhin, 1993]. In terms of  $X = (\omega_p/\omega)^2$ , the refractive index  $\eta = ck/\omega$  satisfies the dispersion relation

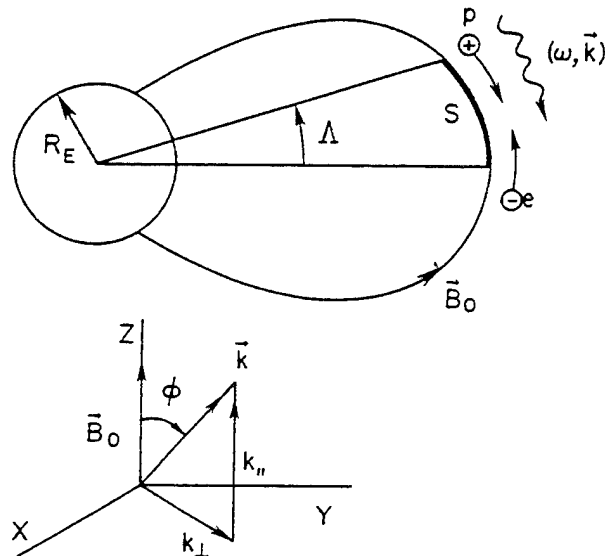


Figure 1. Schematic representation of a whistler mode wave of frequency  $(\omega, \mathbf{k})$ , interacting with electrons and protons. The Earth's dipole magnetic field is  $\mathbf{B}_0$ , the geomagnetic latitude is  $\Lambda$ , and  $s$  is the coordinate along the flux tube.

$$\eta^2 = 1 + \frac{X}{\delta} \quad (1)$$

$$\delta = \frac{\Omega_e}{\omega} |\cos \phi| - 1$$

Near the equator, the angle  $\phi$  is such that  $\cos \phi_r \leq \cos \phi \leq 1$ . The resonance cone angle,  $\phi_r$ , is defined as

$$\cos \phi_r = \frac{\omega}{\Omega_e(L)} \quad (2)$$

We use the argument ( $L$ ) to denote equatorial values of physical quantities. If we call  $\delta(L)$  the value of  $\delta$  at the magnetic equator, we show that when  $\phi = \phi_r$ , then  $\delta(L) = 0$ .

The group velocity in the parallel direction can readily be obtained from (1) considering  $v_{g,\parallel} = d\omega/dk_{\parallel}$ . Normalizing  $v_{g,\parallel}$  to  $c^{-1}$ , we find that

$$v_{g,\parallel} = \frac{1}{\eta_{\parallel}} t(\delta, \phi) \quad (3)$$

$$t(\delta, \phi) = 1 + \cos^2 \phi \left(1 - \frac{2}{\delta + 1}\right)$$

where  $\eta_{\parallel} = \eta \cos \phi$ . Note that as  $\delta \rightarrow 0$ ,  $t(\delta, \phi) \rightarrow \sin^2 \phi$ .

The electric field,  $\mathbf{E}$ , of the wave is represented by

$$\mathbf{E} = \hat{x} \mathcal{E}_1 \cos \Psi - \hat{y} \mathcal{E}_2 \sin \Psi - \hat{z} \mathcal{E}_3 \cos \Psi \quad (4)$$

where  $\hat{x}$ ,  $\hat{y}$ , and  $\hat{z}$  are unit vectors,  $\Psi = k_{\perp} x + k_{\parallel} z - \omega t$ , and  $k_{\parallel}$ ,  $k_{\perp}$  are the components of the wave vector along and perpendicular to  $\mathbf{B}_0$ . The ratios of the electric field components are

$$\frac{\mathcal{E}_2}{\mathcal{E}_1} = \frac{1}{\eta^2} \frac{X}{\left(\frac{\Omega_e}{\omega}\right) - |\cos \phi|} \quad (5)$$

$$\frac{\mathcal{E}_3}{\mathcal{E}_1} = \frac{1 - X - (\eta \sin \phi)^2}{\eta^2 \sin \phi \cos \phi}$$

For the case of waves propagating near the resonance cone,  $\omega \sim \Omega_e(L) |\cos \phi|$ , the equatorial refractive index  $\eta^2(L) \gg 1$ . Its electric field is linearly polarized, having components  $|\mathcal{E}_2/\mathcal{E}_1| \ll 1$  and  $|\mathcal{E}_1/\mathcal{E}_3| \sim -(\sin \phi / \cos \phi)$ . In this case the wave becomes quasi-electrostatic, since  $\mathbf{E}$  is almost in the direction of  $\mathbf{k}$ , and the group velocities  $v_g \sim \eta^{-1}$  are very small.

Near the equator, we approximate the Earth's dipole magnetic field as having a parabolic profile

$$h = \frac{\Omega}{\Omega(L)} = 1 + \left(\frac{z}{\tau_L}\right)^2 \quad (6)$$

where  $z \simeq R_E L \Lambda$ ,  $R_E$  is the Earth's radius,  $L$  is the magnetic shell parameter,  $\Lambda$  is the geomagnetic latitude, and  $\tau_L = (2^{1/2}/3) R_E L$ . The equatorial gyrofrequency is  $\Omega(L)$ , and  $\Omega$  represents the gyrofrequencies of either electrons or protons at locations  $s$  away from the equator along the field line. Equation (6) is obtained

from a Taylor expansion of the dipole field and is an excellent representation of the magnetic geometry within  $\pm 20^\circ$  of the equator.

### 3. Resonant Electron-Whistler Interactions

Here we consider relativistic electrons and normalize their energies to  $(m_e c^2)^{-1}$ , their velocities to  $c^{-1}$ , and their momenta  $p$  to  $(m_e c)^{-1}$ . In what follows we only refer to these normalized quantities. The relativistic factor is  $\gamma_R = [1 - v^2]^{-1/2}$ , where  $v$  is the particle velocity. Resonant whistler-electron interactions must satisfy the condition

$$1 - \eta_{\parallel} v_{\parallel} - \ell \frac{\Omega_e}{\omega} \frac{1}{\gamma_R} = 0 \quad (7)$$

where  $\ell = 0, \pm 1, \pm 2, \dots$  is the harmonic number, and  $\Omega_e = |q| B_0 / m_e c$  is the electron gyrofrequency. Here,  $v_{\parallel}$  and  $\eta_{\parallel} = \eta \cos \phi$  are the parallel components of the particle's velocity and refractive index, respectively.

In terms of the local pitch angle,  $v_{\parallel} = v \cos \theta$ . Here,  $\theta$  is the angle between  $\mathbf{B}_0$  and  $\mathbf{v}$ . We call  $\mu = \sin^2 \theta(L)$ , where  $\theta(L)$  is the equatorial pitch angle. Here,  $\theta(L) > \theta_c$ , where  $\theta_c$  is the pitch angle at the edge of the loss cone, and  $\mu_c$  is the corresponding value of  $\mu$ . In addition, we require that  $\theta(L) < \theta_M$ ; thus the range of resonant equatorial pitch angles is  $\mu_c < \mu < \mu_M$ . The upper limit  $\theta_M$  depends on the extent of the resonant region along the field line, as we shall explain below. As a function of  $L$  shell, the mirror ratio is  $\sigma = \mu_c^{-1} = L^3 (4 - 3/L)^{1/2}$ . To zero order in the electric field amplitudes, a particle's magnetic moment is conserved. Then we may write for the parallel and perpendicular components of the particle velocity  $v$ ,  $v_{\parallel} = v[1 - \mu \Omega / \Omega(L)]^{1/2}$ ,  $v_{\perp} = v[\mu \Omega / \Omega(L)]^{1/2}$ .

As the particles move away from the equator, their parallel velocities  $v_{\parallel}$  decrease. We assume, however, that the waves' phase velocities  $\omega/k_{\parallel}$  remain constant. That is, variations in  $\Omega_e$ ,  $\omega$ , and  $\cos \phi$  are such that  $\eta_{\parallel}$  is constant along the near-equatorial parts of field lines. Given a resonant energy for the  $\ell$  the harmonic,  $\gamma_R = (1 + p_{\ell}^2)^{1/2}$ , interactions take place at geomagnetic latitudes such that  $1 \leq h \leq h_M$ , where  $h$  is defined in (6). For  $h = 1$  we take  $\theta(L) = \theta_M$ , and for  $h = h_M$  then  $\theta(L) = \theta_c$ . Thus there exists a mapping between  $h$  and  $\mu$ , which may be obtained by solving for the resonance condition in (7).

In terms of the resonant parallel momentum  $p_{\ell\parallel}$ , where  $p_{\ell\parallel} = p_{\ell} [1 - \mu \Omega / \Omega(L)]^{1/2}$ , (7) becomes

$$p_{\ell\parallel} = \frac{1}{\eta_{\parallel}} \left[ -\frac{\ell \Omega_e}{\omega} + \sqrt{1 + p_{\ell}^2} \right] \quad (8)$$

The equatorial parallel velocity is obtained from  $v_{\ell\parallel}^2 = p_{\ell\parallel}^2 (1 + p_{\ell}^2)^{-1}$ .

To find the resonant energy, we consider interactions that take place at the equator  $h = 1$ , such that the resonant pitch angle is  $\theta(L) = \theta_M$ . Next we define

$$\begin{aligned}
A_o &= \eta_{\parallel}^2 \cos^2 \theta_M - 1 \\
D_o &= 2 \frac{\ell \Omega_e(L)}{\omega} \eta_{\parallel} \cos \theta_M \\
C_o &= \left[ \frac{\ell \Omega_e(L)}{\omega} \right]^2 - 1
\end{aligned} \quad (9)$$

Then we show

$$p_{\ell} = -\frac{D_o}{2A_o} \pm \left[ \left( \frac{D_o}{2A_o} \right)^2 - \frac{C_o}{A_o} \right]^{1/2} \quad (10)$$

which solves for the electron momentum. The plus sign must be taken for  $\ell \geq 0$ , and the minus sign for  $\ell < 0$ . Note that for  $\ell > 0$ ,  $\cos \theta(L) < 0$ , and for  $\ell \leq 0$ , then  $\cos \theta(L) > 0$ , so that in all cases  $D_o \leq 0$ . Also note that as  $\cos \phi \rightarrow \cos \phi_r$ ,  $\delta(L) \rightarrow 0$ ,  $\eta_{\parallel} \rightarrow \infty$ , and  $p_{\ell} \rightarrow 0$ , and thus the energy of the resonant electron is very small (i.e.,  $< 1$  keV). When the frequency of the waves  $\omega \rightarrow \Omega_e(L)$ , then  $\cos \phi_r \rightarrow 1$ , and again we have  $\delta(L) \rightarrow 0$ ,  $\eta_{\parallel} \rightarrow \infty$ , and  $p_{\ell} \rightarrow 0$ .

In addition, we also consider interactions that occur at  $h = h_M$  and for pitch angles at the edge of the loss cone  $\theta(L) = \theta_c$ . From (8) we obtain the following relation between  $\mu_M$  and  $h_M$  as a function of the resonant energy  $\gamma_R$  and  $\theta_c$ :

$$\sqrt{1 - \mu_M} = \sqrt{1 - \mu_c} h_M \left[ \frac{1 + f_L \gamma_R}{-h_M + f_L \gamma_R} \right] \quad (11)$$

where we define  $f_L = \omega / \ell \Omega_e(L)$ . The waves exist near the equator, and their extent along the field lines is such that  $h \leq h_M$ , where  $h$  is defined in (6). Because interactions take place near equatorial regions,  $h_M$  is close to one. The upper limit on the resonant equatorial pitch angles  $\theta_M$  is obtained from (11) and depends on the extent of the interaction region as given by  $h_M$ .

Solving (7) for  $h_{\ell}$  as a function of  $\mu$ , we show that for  $\ell \neq 0$ ,

$$h_{\ell} = b_{\ell} + [b_{\ell}^2 + (f_L \eta_{\parallel} p)^2 - \gamma_R^2 f_L^2]^{1/2} \quad (12)$$

$$b_{\ell} = \gamma_R f_L - \frac{\mu}{2} (f_L \eta_{\parallel} p)^2$$

where  $\eta_{\parallel} p f_L = (-1 + \gamma_R f_L) (1 - \mu_M)^{-1/2}$ . For the Landau resonance ( $\ell = 0$ ),

$$h_o = \frac{1}{\mu} \left[ 1 - \frac{1}{(\eta_{\parallel} v)^2} \right] \quad (13)$$

For a given value of the electron energy  $\gamma_R$ , (11) to (13) establish a one-to-one correspondence between the resonant equatorial pitch angles  $\theta(L)$  and the geomagnetic latitudes  $\Lambda$  at which the interactions are taking place.

#### 4. Hamiltonian Theory

The dimensionless electric field amplitudes are

$$\epsilon_i = \frac{|q| E_i}{m_e c \omega} \quad (14)$$

We introduce the normalized time  $\tau = t \Omega_e(L)$  and length  $s = z / \tau_L$ , and define the canonical momenta and action:

$$\begin{aligned}
P_{\parallel} &= p_{\parallel} + \epsilon_3 \sin \Psi \\
P_x &= p_x - \epsilon_1 \sin \Psi
\end{aligned} \quad (15)$$

$$P_y = p_y - \epsilon_2 \cos \Psi - \frac{\Omega_e(s) x}{c}$$

$$I = \frac{1}{2} \frac{\Omega(L)}{\Omega(s)} \left[ P_x^2 + \left( P_y + \frac{\Omega_e(s) x}{c} \right)^2 \right] \quad (16)$$

and call

$$\gamma_o = \left[ 1 + P_{\parallel}^2 + 2I \frac{\Omega(s)}{\Omega(L)} \right]^{1/2} \quad (17)$$

The relative phase angle between the wave and the electron is

$$\xi_{\ell} = \ell \lambda + \tau_L \int_0^s k_{\parallel} ds' - \frac{\omega}{\Omega_e(L)} \tau \quad (18)$$

$$\lambda = \arctan \left( \frac{P_y + \Omega_e(s) x / c}{P_x} \right)$$

To first order in wave electric field amplitudes, the time-dependent Hamiltonian is [Ginet and Heinemann, 1990; Albert, 1993; Villalón and Burke, 1993]

$$\mathcal{H} = \gamma_o - \frac{P}{\gamma_o} \sum_{\ell=-\infty}^{+\infty} \Upsilon_{\ell}(I, P_{\parallel}, s) \sin \xi_{\ell} \quad (19)$$

where  $P = (\gamma_o^2 - 1)^{1/2}$ , and

$$\begin{aligned}
\Upsilon_{\ell} &= \epsilon_3 \frac{P_{\parallel}}{P} \mathcal{J}_{\ell}(a) - \frac{1}{2P} \sqrt{2I \frac{\Omega}{\Omega(L)}} \\
&\quad \cdot [(\epsilon_1 + \epsilon_2) \mathcal{J}_{\ell-1}(a) + (\epsilon_1 - \epsilon_2) \mathcal{J}_{\ell+1}(a)] \quad (20)
\end{aligned}$$

where the  $\mathcal{J}$  values are Bessel functions of argument  $a = k_{\perp} \rho$  and  $\rho = (c / \Omega_e) [2I \Omega / \Omega(L)]^{1/2}$  is the Larmor radius. A constant of motion is

$$C_{\ell} = \mathcal{H} - \left[ \frac{\omega}{\Omega_e(L)} \right] I \quad (21)$$

Next we solve for the equations of motion for a single isolated resonance. To zero order in the electric fields  $ds/d\tau = \kappa P_{\parallel} / \gamma_o$ , where  $\kappa = c / \tau_L \Omega_e(L) \ll 1$ . For example, at  $L = 5$  we show that  $\kappa = 4.5 \times 10^{-4}$ . Differentiating (18) with respect to  $s$ , the length along the field line, to zero order in the electric field amplitudes, we show

$$\frac{d\xi_{\ell}}{ds} = \tau_L k_{\parallel} + \frac{\ell \Omega_e - \omega \gamma_o}{\Omega_e(L) \kappa P_{\parallel}} \quad (22)$$

For resonant electrons,  $d\xi_{\ell}/ds = 0$ . Then the equations of motion for the canonical variables reduce to those of the physical variables at the resonance. Referring to the physical action and parallel momentum, in term of the

length  $s$  along the field line, we find that to first order in the electric fields,

$$\frac{dI}{ds} = \frac{\ell}{\kappa} \frac{p}{p_{\parallel}} \Upsilon_{\ell}(I, p_{\parallel}, s) \cos \xi_{\ell} \quad (23)$$

$$\frac{dp_{\parallel}}{ds} = \frac{\kappa r_L k_{\parallel}}{\ell} \frac{dI}{ds} - \frac{I}{p_{\parallel}} \frac{1}{\Omega(L)} \frac{d\Omega}{ds} \quad (24)$$

The evolution of the electron resonant energy  $\gamma_R$ , and the equatorial pitch angle  $\mu = \sin^2 \theta_L$ , is

$$\frac{d\gamma_R}{ds} = \frac{\omega}{\ell \Omega_e(L)} \frac{dI}{ds} \quad (25)$$

$$\frac{d\mu}{ds} = \frac{2}{\gamma_R^2 - 1} \left[ \frac{\ell \Omega_e}{\omega} - \gamma_R \mu \right] \frac{d\gamma_R}{ds} \quad (26)$$

Differentiating (22) with respect to  $s$  and assuming that  $d\xi_{\ell}/ds = 0$  yields

$$\frac{d^2 \xi_{\ell}}{ds^2} = \alpha_{\ell} + \beta_{\ell} \left[ \frac{1}{\ell} \frac{dI}{ds} \right] \quad (27)$$

Here,

$$\alpha_{\ell} = r_L \frac{dk_{\parallel}}{ds} - \frac{\gamma_R}{\kappa p_{\parallel} \Omega_e(L)} \frac{d\omega}{ds} + \frac{\gamma_R}{\kappa p_{\parallel}} \sqrt{\frac{h-1}{1-\mu h}} \left[ \frac{2\ell}{\gamma_R} \sqrt{1-\mu h} - \Lambda(L, v) \mu \right] \quad (28)$$

$$\beta_{\ell} = \frac{1}{\kappa p_{\parallel}} (\eta_{\parallel}^2 - 1) \left[ \frac{\omega}{\Omega_e(L)} \right]^2 \quad (29)$$

where  $\Lambda(L, v) = \eta_{\parallel} v \omega / \Omega_e(L)$ ; all other variable are defined throughout the paper. For second-order resonant electrons the inhomogeneity of the magnetic field is compensated by the frequency variation, and then  $\alpha_{\ell} = 0$ . In addition, if  $\eta_{\parallel} = 1$ , then  $\beta_{\ell} = 0$ ; this is the case of infinite acceleration studied by Roberts and Buchsbaum [1964].

Combining equations (24) and (25), we obtain

$$\frac{d\gamma_R}{ds} - \frac{1}{\eta_{\parallel}} \left[ \frac{dp_{\parallel}}{ds} + \frac{I}{p_{\parallel}} \frac{1}{\Omega(L)} \frac{d\Omega}{ds} \right] = 0 \quad (30)$$

The diffusion curves, or single-wave characteristics, are obtained by integrating (30) along  $s$ . These are the curves along which the representative point of a particle in the  $p_{\parallel}, p_{\perp}$  plane will move. If we neglect magnetic inhomogeneities, we obtain the diffusion curves for homogeneous, relativistic plasmas  $[1 + p_{\parallel}^2 + p_{\perp}^2]^{1/2} - p_{\parallel} / \eta_{\parallel} = \text{const.}$

### 5. Equations of Motion Near Resonance

At the resonance the parallel component of the momentum,  $p_{\ell\parallel}(R)$ , is given by solving for (8). The physical action is obtained from

$$I_{\ell}(R) = \frac{p_{\ell\parallel}^2(R)}{2} \frac{\mu}{1 - \mu h_{\ell}} \quad (31)$$

where  $h_{\ell}$  is given in (12) and (13).

At the resonance we also obtain  $s_{\ell} = (h_{\ell} - 1)^{1/2}$ . Using a Taylor expansion around  $s = s_{\ell}$ , we obtain for the phase angle [Villalón and Burke, 1993]

$$\xi_{\ell} = \xi_{\ell}(R) + \xi_{\ell}^{(1)}(s - s_{\ell}) + \frac{1}{2} \xi_{\ell}^{(2)}(s - s_{\ell})^2 \quad (32)$$

Here,  $\xi_{\ell}^{(1)} = 0$ , and

$$\xi_{\ell}^{(2)} = \alpha_{\ell}(R) + \beta_{\ell}(R) \left[ \frac{1}{\ell} \frac{dI}{ds} \right]_{(R)} \quad (33)$$

where the subscript  $(R)$  denotes values taken at the resonance, for  $I_{\ell} = I(R)$  and  $p_{\parallel} = p_{\ell\parallel}$ .

We define the length of resonant interaction as

$$\delta s_{\ell} = \int_{-\infty}^{+\infty} \cos \xi_{\ell} ds = \sqrt{\frac{2}{|\xi_{\ell}^{(2)}|}} \Gamma\left(\frac{1}{2}\right) \cos \left( \xi_{\ell}(R) + \frac{\xi_{\ell}^{(2)}}{|\xi_{\ell}^{(2)}|} \frac{\pi}{4} \right) \quad (34)$$

Near resonance the change in action, energy, and pitch angle is given by

$$\Delta I = \left[ \frac{dI}{ds} \right]_{(R)} \delta s_{\ell} \quad (35)$$

$$\Delta \gamma_R = \frac{\omega}{\ell \Omega_e(L)} \Delta I \quad (36)$$

$$\Delta \mu = \frac{2}{\gamma_R^2 - 1} \left[ \frac{\ell \Omega_e}{\omega} - \gamma_R \mu \right] \Delta \gamma_R \quad (37)$$

Here,

$$\left[ \frac{dI}{ds} \right]_{(R)} = \frac{\ell}{\kappa} \frac{p}{p_{\ell\parallel}} \Upsilon_{\ell} [I_{\ell}(R), p_{\ell\parallel}(R), s] \quad (38)$$

where  $\Upsilon_{\ell}$  is defined in (20) for the resonant values of  $I$  and  $p_{\parallel}$ .

If the electric field amplitudes are small compared to the inhomogeneity of the plasma, then we may approximate  $\xi_{\ell}^{(2)} \simeq \alpha_{\ell}(R)$ . For this case the changes in action, energy, and pitch angle are proportional to  $\epsilon_i$ , the electric field amplitudes. In contrast, for second-order resonances,  $\beta_{\ell} [(1/\ell) (dI/ds)]_{(R)} \gg \alpha_{\ell}$ , and then  $\xi_{\ell}^{(2)} \simeq \beta_{\ell}(R) [(1/\ell) (dI/ds)]_{(R)}$ . For second-order interactions the changes in action, energy and pitch angle are proportional to  $\epsilon_i^{1/2}$ .

Second-order resonances require that the inhomogeneity of the magnetic field be compensated by wave frequency variations along the field line [Dysthe, 1971; Nunn, 1974]. By considering (27) and (28), we require that for second-order interactions,  $\alpha_{\ell} \rightarrow 0$ , which leads to the frequency variation along the field line as

$$\frac{1}{\omega} \frac{d\omega}{ds} = \frac{\gamma_R}{\ell h} \sqrt{\frac{h-1}{1-\mu h}} \left[ \frac{2\ell}{\gamma_R} \sqrt{1-\mu h} - \Lambda(L, v) \mu \right] \quad (39)$$

where  $\Lambda(L, v)$  is defined after (29), and we have taken  $d\eta_{||}/ds = 0$ .

## 6. Numerical Calculations

### 6.1. Resonance Condition

In this section we present some applications of the test particle theory to plasma sheet electrons in the geomagnetic shell  $L = 5.5$ . The dipole magnetic field at the equator is  $B(L) = B_o L^{-3}$ , where  $B_o = 3.1 \times 10^4$  nT, and the equatorial electron gyrofrequency is  $\Omega_e(L) = 0.33 \times 10^5$  s $^{-1}$ . We take two values for the ratio between the electron plasma and the equatorial cyclotron frequencies,  $\omega_p/\Omega_e(L) = 3$  and 1.5. The width of the resonant cone is  $\theta_c = 3.25^\circ$ . Calculations were conducted for the four frequencies  $\omega/\Omega_e(L) = 0.45, 0.55, 0.75$ , and 0.85. We assume that the waves have a coherent spectrum of finite frequency bandwidth, as occurs in the chorus and triggered emissions [Helliwell, 1967].

Figure 2 plots the energies of resonant electrons in keV versus  $\cos \phi$ , where  $\phi$  is the angle between the wave vector and the geomagnetic field. We take four values for  $\omega/\Omega_e(L)$  as indicated in Figures 2A–2D, and  $\omega_p/\Omega_e(L) = 3$ . The maximum geomagnetic latitude is  $5^\circ$ , which corresponds to  $h_M = 1.035$ . The electron energies represent solutions for the resonance condition as given in (10). The value for  $\theta_M$  is obtained from  $\cos \theta_M = (1 - \mu_c h_M)^{1/2} (1 + f_L) (-h_M + f_L)^{-1}$ . For the frequencies  $\omega/\Omega_e(L) = 0.45$  and 0.55, we consider the two harmonics  $\ell = 0$  and 1; for the frequencies  $\omega/\Omega_e(L) = 0.75$  and 0.85, we represent only the first harmonic,  $\ell = 1$ . We see that for  $\omega/\Omega_e(L) < 0.5$ , the Landau resonance  $\ell = 0$  interacts with lower-energy particles than the first harmonic  $\ell = 1$ . For  $\omega/\Omega_e(L) > 0.5$  the first harmonic reaches lower-energy electrons than the Landau resonance. However, as we

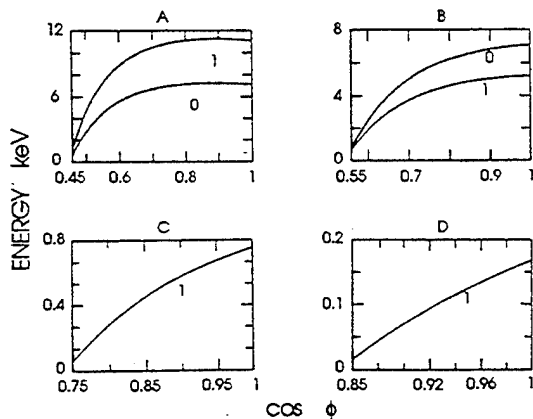


Figure 2. Electron energy in keV versus  $\cos \phi$ , using the ratio  $\omega_p/\Omega_e(L) = 3$ . The frequency ratios  $\omega/\Omega_e(L)$  is equal to (A) 0.45, (B) 0.55, (C) 0.75, and (D) 0.85. Figures 2A and 2B describe the cyclotron harmonics  $\ell = 0$  and 1, as indicated next to the curves. Figures 2C and 2D use only the first harmonic  $\ell = 1$ .

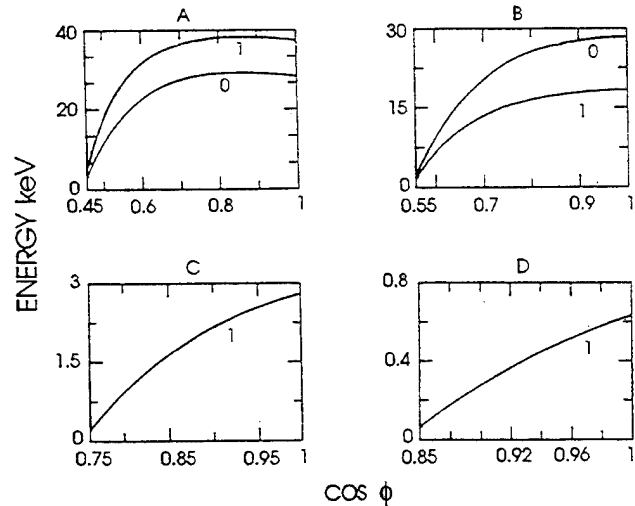


Figure 3. Electron energy in keV versus  $\cos \phi$ , using the ratio  $\omega_p/\Omega_e(L) = 1.5$ . The frequency ratios  $\omega/\Omega_e(L)$  is equal to (A) 0.45, (B) 0.55, (C) 0.75, and (D) 0.85. Figures 3A and 3B describe the cyclotron harmonics  $\ell = 0$  and 1, as indicated next to the curves. Figures 3C and 3D use only the first harmonic  $\ell = 1$ .

show below, only the first harmonic couples efficiently with low energy electrons. We also observe that for waves to interact with electrons of energy of  $< 1$  keV, their angles of propagation  $\phi$  must get closer to the resonance angle  $\phi_r$ . Also, if  $\omega \rightarrow \Omega_e(L)$ , then the electron energy decreases below 1 keV.

Figure 3 shows similar calculations considering that  $\omega_p/\Omega_e(L) = 1.5$ . Other parameters do not change. We observe that for all the panels the electron energy is much larger than in the case shown in Figure 2. This is because as  $\omega_p/\Omega_e(L)$  decreases,  $\eta$  also does as given in (1), which leads to larger values of the electron energies.

Next let us consider (11). Given  $\theta_M$ , we solve (11) for  $h_M$  as a function of the electron energy  $\gamma_R$  and the loss cone angle  $\mu_c = \sin^2 \theta_c$ . For the  $\ell = 1$  harmonic we obtain

$$h_M = \alpha_M + \left\{ \alpha_M^2 - \hat{f}_L^2 + \frac{(\hat{f}_L - 1)^2}{1 - \mu_M} \right\}^{1/2} \quad (40)$$

$$\alpha_M = \hat{f}_L - \frac{\mu_c}{2(1 - \mu_M)} (\hat{f}_L - 1)^2$$

where  $\hat{f}_L = f_L \gamma_R$  and  $f_L = \omega/\Omega_e(L)$ . This is the same as (12), but now  $\mu = \mu_c$ . Equation (40) defines the range of geomagnetic latitudes at which the electron-whistler interactions take place,  $1 \leq h \leq h_M$ , as a function of the resonant equatorial pitch angles whose extension is  $\mu_c \leq \mu \leq \mu_M$ . Note that as  $\hat{f}_L \rightarrow 1$ , then  $h_M \rightarrow \hat{f}_L$ . Thus, as the wave frequency approaches  $\Omega_e$ , the electrons and waves interact very near the equator for all values of  $\mu_M$ .

Figure 4 shows the geomagnetic latitude  $\Lambda$  versus resonant equatorial pitch angles  $\theta_M$ . The latitudes are obtained by solving (40) and taking  $\Lambda = (9/2)^{1/2} (h_M -$

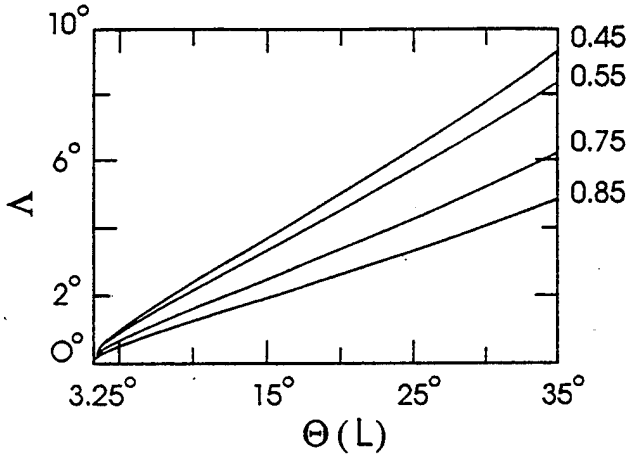


Figure 4. Geomagnetic latitudes  $\Delta$  versus equatorial pitch angles  $\theta(L)$  in degrees. The four curves correspond to the indicated frequency ratios  $\omega/\Omega_e(L)$ .

$1)^{1/2}$ . Because the electron energies are small, we assume that  $\gamma_R = 1$ . We present the four cases  $\omega/\Omega_e(L) = 0.45, 0.55, 0.75$ , and  $0.85$ . As  $\omega \rightarrow \Omega_e(L)$ , the interactions get closer to the equator, and  $h_M \rightarrow 1$ . Figure 4 also shows that for interactions occurring within  $1^\circ$  of the magnetic equator, the range in equatorial pitch angles starting at the loss cone angle is  $\sim 3^\circ$ . Then  $\Delta s = (h_M - 1)^{1/2} = 0.037$ , and the frequency variation as obtained from (39) is small. Note that as  $h \rightarrow 1$ ,  $d\omega/ds \rightarrow 0$ .

## 6.2. Hamiltonian Equations

We now present numerical calculations based on sections 4 and 5 for the geomagnetic shell  $L = 5.5$ . Consider the case  $\omega_p/\Omega_e(L) = 3$ , which gives lower resonant-energy results than if  $\omega_p/\Omega_e(L) = 1.5$ . We again use the four frequencies  $\omega/\Omega_e(L) = 0.45, 0.55, 0.75$ , and  $0.85$ . A wave amplitude of  $10^{-6} \text{ V m}^{-1}$  applies to all examples.

Figure 5 represents the change in equatorial pitch angle  $\Delta\theta_L$  versus the pitch angle in degrees for second-order interactions. The change in pitch angle is obtained by combining (34) through (38), where in (37)  $\Delta\mu = \sin(2\theta_L) \Delta\theta_L$ . We assume that the wave frequency changes along the field line according to (39). Figures 5A–5D correspond to the four frequency ratios. In each panel we represent three values for  $\cos\phi$  as indicated.

Figure 5A, shows the frequency ratio  $\omega/\Omega_e(L) = 0.45$  for the three propagation angles  $\cos\phi = 0.46, 0.5$ , and  $0.999$ ; the corresponding energies of the resonant electrons are 1, 5, and 11 keV. Figure 5B represents the frequency ratio  $\omega/\Omega_e(L) = 0.55$  at three propagation angles  $\cos\phi = 0.56, 0.6$ , and  $0.999$ ; the corresponding resonant energies are 0.4, 1.75, and 5.5 keV. Figure 5C represents the frequency ratio  $\omega/\Omega_e(L) = 0.75$  at three propagation angles  $\cos\phi = 0.78, 0.88$ , and  $0.999$ ; the corresponding resonant energies are 140, 470, and 700 eV. Figure 5D represents the frequency ratio  $\omega/\Omega_e(L) = 0.85$  at three propagation angles  $\cos\phi = 0.86, 0.88$ , and  $0.999$ ; the corresponding resonant energies are 13,

36, and 135 eV. The extensions of the resonant regions along the field line are  $\Delta = 6.3^\circ, 5.7^\circ, 4.3^\circ$ , and  $3.3^\circ$  in Figures 5A, 5B, 5C, and 5D, respectively.

Second-order interactions require frequency variations along the field line given by (39). Thus, for very monochromatic waves the resonance region may extend  $< 1^\circ$  from the magnetic equator. As a matter of fact, if waves are to interact with electrons whose resonant pitch angles are such that  $\theta_c (= 3.25^\circ) \leq \theta_L \leq 6.5^\circ$ , then the interaction region along the field line extends for  $1.4^\circ, 1.25^\circ, 1.0^\circ$ , and  $0.75^\circ$ , corresponding to the frequency ratios  $\omega/\Omega_e(L) = 0.45, 0.55, 0.75$ , and  $0.85$ , respectively.

Calculations have also been conducted for  $\omega_p/\Omega_e(L) = 1.5$ . The changes in pitch angles for all cases are about 30% less efficient than those presented in Figure 5. We have also made calculations for the Landau resonance  $\ell = 0$ , assuming that near the equator  $d\eta_{||}/ds = 0$  to obtain from (28)

$$\alpha_o = -\frac{\gamma_R}{\kappa p_{||}} \sqrt{\frac{h-1}{1-\mu h}} \Lambda(L, v) \mu \quad (41)$$

The magnetic inhomogeneity is uncompensated by frequency variations. In addition, because  $\ell = 0$ ,  $\Delta\mu = -2\gamma_R(\gamma_R^2 - 1)^{-1} \mu \Delta\gamma_R$ . Near the loss cone,  $\mu \sim \mu_c$ , and  $\Delta\mu$  is small.

Figure 6 shows the normalized changes in energy as  $\Delta\gamma_R(\gamma_R - 1)^{-1}$  versus resonant equatorial pitch angles. Figures 6A, 6B, 6C, and 6D correspond to the four different frequency ratios indicated. Each panel of Figure 6 shows same three propagation angles as in Figure 5. The corresponding energies for each panel and for each propagation angle are defined in Figure 5. The changes in energy are obtained as in (36), by assuming that the

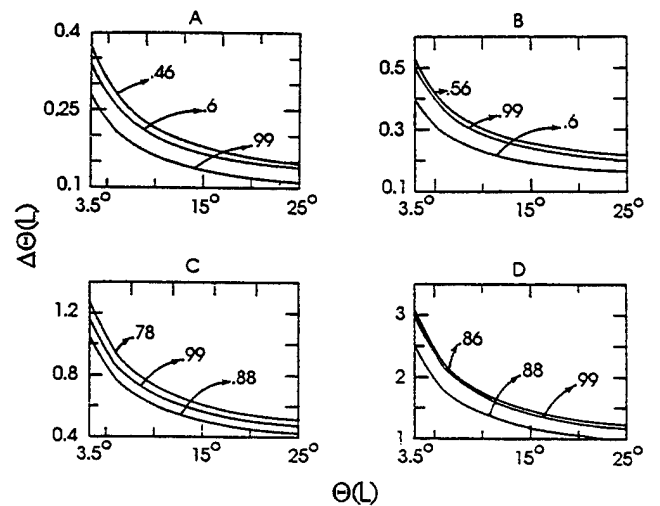


Figure 5. Change in pitch angle  $\Delta\theta(L)$  versus  $\theta(L)$  due to second-order resonant interactions at the first cyclotron harmonic, with  $\omega_p/\Omega_e(L) = 3$ . The frequency ratios  $\omega/\Omega_e(L)$  is equal to (A) 0.45, (B) 0.55, (C) 0.75, and (D) 0.85. Numbers next to the curves correspond to values of  $\cos\phi$ . The resonant energies as functions of  $\cos\phi$  and the frequency ratio are discussed in the text.



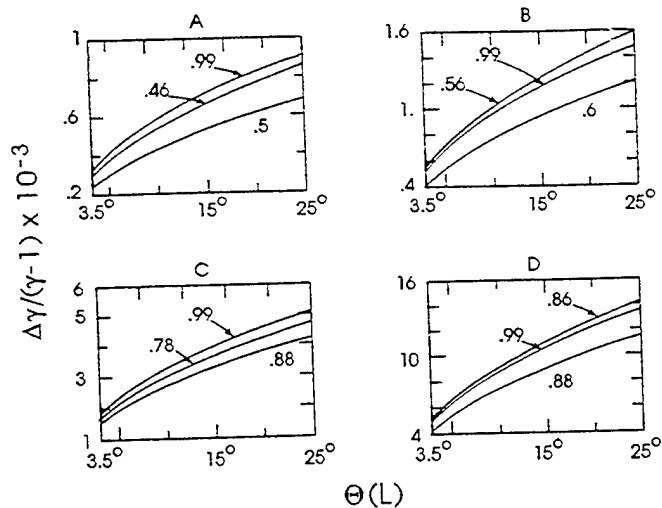


Figure 6. Normalized change in the electron resonant energy  $\Delta\gamma_R (\gamma_R - 1)^{-1}$  versus  $\theta(L)$  for second-order resonant interactions at the first cyclotron harmonic, with  $\omega_p/\Omega_e(L) = 3$ . The ratio  $\omega/\Omega_e(L)$  is equal to (A) 0.45, (B) 0.55, (C) 0.75, and (D) 0.85. Numbers next to the curves refer to different values of  $\cos \phi$ . Resonant energies are given in the text.

second-order resonance condition is satisfied and that the frequency variation along the field line is as given in (39). Note that as  $\omega \rightarrow \Omega_e(L)$ , larger changes in energies are calculated than for smaller values of the ratio  $\omega/\Omega_e(L)$ . For example, for  $\omega/\Omega_e(L) = 0.45$  and  $\Delta\gamma_R (\gamma_R - 1)^{-1} = 10^{-3}$ , there is an energy change of 1 eV for every 1 keV of the electron's initial energy. If  $\omega/\Omega_e(L) = 0.85$  and  $\Delta\gamma_R (\gamma_R - 1)^{-1} = 16 \times 10^{-3}$ , we obtain a change of 16 eV for every 1 keV.

The electrons maintain resonance with the waves over a certain time interval,  $\Delta t$ , over which the phase change of the resonant electron with respect to the wave remains less than, say,  $\pi/2$ . By integrating (27) twice for second-order resonant electrons we obtain,

$$\Delta t = \frac{\pi}{\omega} \left| \gamma_R - \frac{\Omega_e(L)}{\omega} \right| \frac{1}{\eta_{\parallel}^2 - 1} \frac{\gamma_r - 1}{\Delta\gamma_R} \frac{1}{p^2} \quad (42)$$

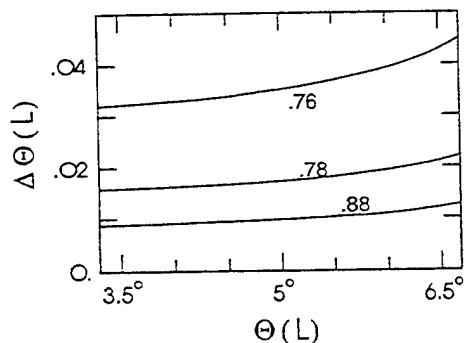


Figure 7. Change in pitch angles  $\Delta\theta(L)$  versus equatorial pitch angles  $\theta(L)$  due to first-order interactions at the first cyclotron harmonic. We use  $\omega/\Omega_e(L) = 0.75$ . Numbers next to the curves refer to values of  $\cos \phi$ .

The time duration as obtained from (42) is consistent with resonance lengths that correspond to  $1^\circ$  to  $3^\circ$  latitude from the equator.

Figure 7 shows the change in pitch angle versus initial pitch angle for first-order resonant electrons. The wave frequency remains constant along the field line. Thus  $\alpha_L$  is finite but at the equator where  $h = 1$ ,  $\alpha_L = 0$ . The changes in pitch angle and energy are linear with the electric field amplitudes. We take the example  $\omega/\Omega_e(L) = 0.75$ . The three angles of propagation are  $\cos \phi = 0.76, 0.78, 0.88$ , and the corresponding resonant energies are 165 eV, 466 eV and 1.5 keV, respectively. The wave amplitude is  $10^{-6} \text{ V m}^{-1}$ . We see that first-order resonant interactions do not give electron scattering as strong as when second-order resonance conditions prevail.

## 7. Summary and Conclusions

We have presented a test particle theory for the interactions of whistler mode waves with  $< 10$ -keV electrons near the equatorial plasma sheet. A Hamiltonian formulation has been developed for interactions with a coherent spectrum of multiple-frequency waves such as those found in the natural chorus emissions. The main results are as follows:

1. Efficient whistler-electron interactions require that the ratios between the wave and the equatorial electron frequencies be such that  $\omega/\Omega_e(L) \geq 0.5$ . For waves propagating near the resonance cone and for  $\omega \rightarrow \Omega_e(L)$ , resonant energies are  $< 1$  keV.

2. We establish a mapping between the resonant, equatorial pitch angles and the geomagnetic latitudes where the resonances take place. For interactions that occur within  $1^\circ$  of the magnetic equator, the range of resonant pitch angles extends about  $3^\circ$  from the edge of the loss cone.

3. Second-order resonant interactions require that inhomogeneities of the magnetic field be compensated by wave frequency variations. In this way, electrons and waves stay in gyroresonance for relatively long distances along the field line. Within a few degrees of the magnetic equator the required frequency variations are small, and the wave spectrum is relatively narrow.

4. Numerical calculations have been conducted for the  $L = 5.5$  shell. As an example we considered wave amplitudes of  $10^{-6} \text{ V m}^{-1}$ , consistent with observations from the CRRES satellite. Changes in pitch angle can be  $> 1^\circ$  for electrons with pitch angles near the edge of the loss cone. This means that the waves can scatter electrons into the atmospheric loss cone very efficiently. Thus whistler-electron interactions are viable explanations of the nearly isotropic precipitation of low-energy electrons from the plasma sheet to form the diffuse aurora.

**Acknowledgments.** This work has been supported by the U.S. Air Force under contract with Northeastern University, F19628-92-K-0007, and the Air Force Office of Scientific Research, task 2311PL03. We are grateful to David A.

Hardy of the Phillips Laboratory, for suggesting this problem.

The Editor thanks D. W. Swift and R. Skoug for their assistance in evaluating this paper.

## References

- Albert, J. M., Cyclotron resonance in an inhomogeneous magnetic field, *Phys. Fluids B*, 5, 2744, 1993.
- Bell, T. F., The nonlinear gyroresonance interaction between energetic electrons and coherent VLF waves propagating at an arbitrary angle with respect to the Earth's magnetic field, *J. Geophys. Res.*, 89, 905, 1984.
- Belmont, G., D. Fontaine, and P. Canu, Are equatorial electron cyclotron waves responsible for diffuse auroral electron precipitation?, *J. Geophys. Res.*, 88, 9163, 1983.
- Bespalov, P. A., and V. Y. Trakhtengerts, Cyclotron instability of Earth radiation belts, *Rev. Plasma Phys.*, 10, 155, 1986.
- Burke, W. J., A. G. Rubin, D. A. Hardy, and E. G. Holeman, Banded electron structures in the plasmasphere, *J. Geophys. Res.*, in press, 1995.
- Burtis, W. J., and R. A. Helliwell, Magnetospheric chorus: Occurrence patterns and normalized frequency, *J. Geophys. Res.*, 80, 1007, 1976.
- Davidson, G. T., Pitch angle diffusion in morningside aurorae, 1, The role of the loss cone in the formation of impulsive bursts precipitation, *J. Geophys. Res.*, 91, 4413, 1986a.
- Davidson, G. T., Pitch angle diffusion in morningside aurorae, 2, The formation of repetitive auroral pulsations, precipitation, *J. Geophys. Res.*, 91, 4429, 1986b.
- Davidson, G. T., and Y. T. Chiu, A nonlinear model of wave-particle interactions in the trapped radiation belts: Auroral pulsation solutions, *Geophys. Res. Lett.*, 14, 1166, 1987.
- Dysthe, K. B., Some studies of triggered whistler emissions, *J. Geophys. Res.*, 76, 6915, 1971.
- Ginet, G. P., and M. Heinemann, Test particle acceleration by small amplitude electromagnetic waves in a uniform magnetic field, *Phys. Fluids B*, 2, 700, 1990.
- Hardy, D. A., W. J. Burke, and E. Villalón, Electron dispersion events in the morningside auroral zone and their relationship with VLF emissions, *J. Geophys. Res.*, 95, 6451, 1990.
- Hashimoto, K., and I. Kimura, A generation mechanism of narrow-band hiss emissions above one half the electron cyclotron frequency in the outer magnetosphere, *J. Geophys. Res.*, 86, 11,148, 1981.
- Helliwell, R. A., A theory of discrete VLF emissions from the magnetosphere, *J. Geophys. Res.*, 72, 4773, 1967.
- Helliwell, R. A., 40 years of whistlers, *Mod. Radio Sci.*, 189, 1993.
- Inan, U. S., and T. F. Bell, Pitch angle scattering of energetic particles by oblique whistler waves, *Geophys. Res. Lett.*, 18, 49, 1991.
- Inan, U. S., Y. T. Chiu, and G. T. Davidson, Whistler-mode chorus and morningside aurorae, *Geophys. Res. Lett.*, 19, 653, 1992.
- Jasna, D., U. S. Inan, and T. F. Bell, Precipitation of suprathermal electrons by oblique whistler waves, *Geophys. Res. Lett.*, 19, 1639, 1992.
- Johnstone, A. D., The mechanism of pulsating aurora, *Ann. Geophys.*, 1, 4, 397, 1983.
- Johnstone, A. D., D. M. Walton, R. Liu, and D. A. Hardy, Pitch angle diffusion of low-energy electrons by whistler-mode waves, *J. Geophys. Res.*, 98, 5959, 1993.
- Kennel, C. F., and H. E. Petschek, Limit on stably trapped particle fluxes, *J. Geophys. Res.*, 71, 1, 1966.
- Lyons, L. R., and D. J. Williams, *Quantitative Aspects of Magnetospheric Physics*, D. Reidel, Norwell, Mass., 1984.
- Nunn, D., A self-consistent theory of triggered VLF emissions, *Planet. Space Sci.*, 22, 349, 1974.
- Ohmi, N., and M. Hayakawa, On the generation of quasi-electrostatic half-electron-gyrofrequency VLF emissions in the magnetosphere, *J. Plasma Phys.*, 35, 351, 1986.
- Parks, G. K., Microburst precipitation phenomena, *J. Geomagn. Geoelectr.*, 30, 327, 1978.
- Roberts, C. S., and S. J. Buchsbaum, Motion of a charged particle in a constant magnetic field and a transverse electromagnetic wave propagating along a field, *Phys. Rev. A*, 135, 381, 1964.
- Roeder, J. L., and H. C. Koons, A survey of electron cyclotron waves in the magnetosphere and the diffuse auroral electron precipitation, *J. Geophys. Res.*, 94, 2529, 1989.
- Rosenberg, T. J., J. C. Siren, D. L. Matthews, K. Marthinsen, J. A. Holtet, A. Egeland, D. L. Carpenter, and R. A. Helliwell, Conjugacy of electron microbursts and VLF chorus, *J. Geophys. Res.*, 86, 5819, 1981.
- Sazhin, S. S., *Whistler-Mode Waves in a Hot Plasma*, Cambridge Atmos. and Space Sci. Ser., Cambridge Univ. Press, New York, 1993.
- Sazhin, S. S., and M. Hayakawa, Magnetospheric chorus emissions: A Review, *Planet. Space Sci.*, 40, 681, 1992.
- Swift, D. W., Mechanism for auroral precipitation: A review, *Rev. Geophys.*, 19, 185, 1981.
- Villalón, E., and W. J. Burke, Near-equatorial pitch angle diffusion of energetic electrons by oblique whistler waves, *J. Geophys. Res.*, 96, 9655, 1991.
- Villalón, E., and W. J. Burke, Proton whistler interactions near the equator in the radiation belts, *J. Geophys. Res.*, 98, 13,509, 1993.
- Villalón, E., W. J. Burke, P. L. Rothwell, and M. B. Silevitch, Quasi-linear wave particle interactions in the Earth's radiation belts, *J. Geophys. Res.*, 94, 15,243, 1989.

W. J. Burke, Space Science Division, Phillips Laboratory/ GPSG, Hanscom Air Force Base, MA 01731. (e-mail: burke@zircon.plh.af.mil)

E. Villalón, Center for Electromagnetics Research, Northeastern University, Boston, MA 02115. (e-mail: villalon@zircon.plh.af.mil)

(Received January 27, 1995; revised April 3, 1995; accepted April 4, 1995.)

The U.S. Government is authorized to reproduce and sell this report.  
Permission for further reproduction by others must be obtained from  
the copyright owner.

# Interaction of ring current and radiation belt protons with ducted plasmaspheric hiss

## 2. Time evolution of the distribution function

J. U. Kozyra, C. E. Rasmussen, and R. H. Miller

Space Physics Research Laboratory, Atmospheric, Oceanic and Space Sciences Department, University of Michigan, Ann Arbor

E. Villalon

Center of Electromagnetic Research, Northeastern University, Boston, Massachusetts

**Abstract.** The evolution of the bounce-averaged ring current/radiation belt proton distribution is simulated during resonant interactions with ducted plasmaspheric hiss. The plasmaspheric hiss is assumed to be generated by ring current electrons and to be damped by the energetic protons. Thus energy is transferred between energetic electrons and protons using the plasmaspheric hiss as a intermediary. The problem is not solved self-consistently. During the simulation period, interactions with ring current electrons (not represented in the model) are assumed to maintain the wave amplitudes in the presence of damping by the energetic protons, allowing the wave spectrum to be held fixed. Diffusion coefficients in pitch angle, cross pitch angle/energy, and energy were previously calculated by Kozyra et al. (1994) and are adopted for the present study. The simulation treats the energy range,  $E \geq 80$  keV, within which the wave diffusion operates on a shorter timescale than other proton loss processes (i.e., Coulomb drag and charge exchange). These other loss processes are not included in the simulation. An interesting result of the simulation is that energy diffusion maximizes at moderate pitch angles near the edge of the atmospheric loss cone. Over the simulation period, diffusion in energy creates an order of magnitude enhancement in the bounce-averaged proton distribution function at moderate pitch angles. The loss cone is nearly empty because scattering of particles at small pitch angles is weak. The bounce-averaged flux distribution, mapped to ionospheric heights, results in elevated locally mirroring proton fluxes. OGO 5 observed order of magnitude enhancements in locally mirroring energetic protons at altitudes between 350 and 1300 km and invariant latitudes between  $50^\circ$  and  $60^\circ$  (Lundblad and Soraas, 1978). The proton distributions were highly anisotropic in pitch angle with nearly empty loss cones. The similarity between the observed distributions and those resulting from this simulation raises the possibility that interactions with plasmaspheric hiss play a role in forming and maintaining the characteristic zones of anisotropic proton precipitation in the subauroral ionosphere. Further assessment of the importance of this process depends on knowledge of the distribution in space and time of ducted plasmaspheric hiss in the inner magnetosphere.

## 1. Introduction

OGO 5 observed enhancements in locally mirroring protons at altitudes between 350 and 1300 km on field lines associated with stable auroral red (SAR) arcs in the subauroral ionosphere [Lundblad and Soraas, 1978]. Pitch angle distributions, observed by the OGO 5 spacecraft, were highly anisotropic in the sense that fluxes at small pitch angles were orders of magnitude less than locally mirroring ones. Protons that are locally mirroring at these altitudes map to the equator near the edge of the atmospheric loss cone. The observed incomplete filling of the loss cone was assumed to indicate weak pitch angle scattering near the equatorial plane. Resonance with ion cyclotron waves was proposed as the source of this weak pitch angle scattering [Cornwall et al., 1971; Lundblad and Soraas, 1978]. The ion cyclotron waves were thought to be amplified

during this interaction with the energetic protons and then damped by thermal electrons during the course of their propagation through the inhomogeneous magnetospheric environment [Cornwall et al., 1971]. The energy transferred to the thermal electron gas in the process leads to increased temperatures at the foot of these field lines and to an associated enhancement in 6300 Å emissions characteristic of SAR arcs. However, in the ensuing time period, ion cyclotron waves have been observed only rarely in the outer plasmasphere. During a recent survey of Pc 1 waves in the inner magnetosphere [Anderson et al., 1992], an occurrence frequency of 1% was found at  $L$  values less than 5 for ion cyclotron waves with frequencies between 0.1 and 4 Hz and amplitudes greater than 0.8 gammas. In contrast, the zones of proton precipitation, described by Lundblad and Soraas [1978] and Voss and Smith [1980] are a characteristic feature of the subauroral ionosphere, as are the temperature enhancements associated with SAR arcs.

The present work assumes no direct relationship between SAR arcs and the enhanced locally mirroring proton fluxes on the same field lines but makes use of reported observations by

Copyright 1995 by the American Geophysical Union.

Paper number 95JA01556.  
0148-0227/95/95JA-01556\$05.00

the Dynamics Explorer (DE) satellite pair at high and low altitudes on SAR arc field lines [Kozyra, 1986; Kozyra *et al.*, 1987a] to propose an alternative explanation for the collocation of these phenomena. The DE spacecraft were in coplanar polar orbits and thus were occasionally in the position to observe the magnetospheric source and ionospheric sink regions on SAR arc field lines nearly simultaneously. Magnetically conjugate DE 1 and 2 data sets revealed the presence of large-scale density structures and associated regions of enhanced plasmaspheric hiss amplitudes at high altitudes on field lines that thread SAR arcs in the ionosphere. Theoretical models using these and other data sets, in combination with ground-based photometric observations of 6300 Å emission, demonstrated that Coulomb drag transfers sufficient energy from the ring current to the thermal electron gas to maintain the observed ionospheric electron temperatures and associated SAR arc emissions [Kozyra *et al.*, 1987b, 1993] without the need for wave damping. The possible role of waves in enhancing the transport of energy from the plasmaspheric thermal electron populations into the underlying ionosphere is still under debate [Thorne and Horne, 1992]. Coulomb drag as a mechanism for the energy transfer was first proposed by Cole [1965]. However, the importance of ring current oxygen ions as a dominant energy source for the thermal electrons only became clear during the DE mission [Kozyra *et al.*, 1987b].

The unique nature of the DE data sets also allowed a detailed comparison between the thermal plasma characteristics at high and low altitudes. Structures in the electron temperature signatures and associated SAR arc emissions at ionospheric heights (i.e., structured temperature peaks, multiple temperature peaks, etc.) map along field lines to single or multiple, large-scale density structures in the outer plasmasphere [Horwitz *et al.*, 1986; Kozyra, 1986; Kozyra *et al.*, 1987a]. This relationship is not surprising. The Coulomb collision frequency is proportional to both the energetic ring current ion flux and the thermal plasma density. Therefore elevated collision frequencies, energy transfer rates and ionospheric electron temperatures are expected to occur on field lines associated with thermal plasma density enhancements in the outer plasmasphere.

Apart from their role in structuring Coulomb energy transfer rates, large-scale density enhancements can directly affect the propagation of plasmaspheric hiss through ducting. Plasmaspheric hiss is a right-hand-polarized, whistler mode emission that fills the plasmasphere almost continuously [Thorne *et al.*, 1973]. Ducting, which maintains small wave normal angles along the ray path, occurs in the presence of gradients in the thermal plasma. Such gradients can be found in association with detached plasma regions, the plasmopause and density structures (ledges, double plasmapauses, etc.) in the outer plasmasphere and dusk bulge region. Hayakawa *et al.* [1986a] derived hiss wave normal directions of less than 25° in detached plasma regions near the equatorial plane. They also presented evidence which reasonably suggests that signatures of the detached plasma regions extend into the topside ionosphere and that the hiss may be ducted down to these altitudes. As mentioned previously, Kozyra *et al.* [1987a] presented observations of intense hiss emissions within large-scale density structures at plasmaspheric altitudes on SAR-arc field lines. Though a direct experimental determination of the wave-normal directions of the enhanced hiss emissions was not possible, it is very likely that the waves were ducted. The

evidence for this is indirect. Nearly simultaneous observations by DE 1 and 2 [Kozyra, 1986] at high and low altitudes on the same field lines indicate enhanced wave electric fields over the frequency interval 100 Hz to several kHz. Enhanced wave amplitudes over the same range of  $L$  values at low altitudes imply that these waves are ducted. Ducting maintains small wave normal angles and allows the waves to reach low altitudes. In contrast, during unducted propagation, hiss emissions will most likely reflect at the lower hybrid frequency and never reach the ground [Church and Thorne, 1983; Huang and Goertz, 1983].

Observations confirm that the plasmopause density gradient is also capable of ducting plasmaspheric hiss. Small wave normal angles were observed just inside the plasmopause near the equatorial plane by Hayakawa *et al.* [1986b]; however, two different groups of wave normal angles, one moderate and one large, were observed deeper in the plasmasphere. In all cases studied by these authors at high geomagnetic latitudes, two different groups of wave normal angles were seen, both large. In fact, recent observational evidence suggests that hiss wave normal angles are quite oblique throughout much of the plasmasphere [Storey *et al.*, 1991; Sonwalker and Inan, 1988]. The present work does not deal with these regions of oblique hiss but focuses on hiss emissions generated within detached plasma regions or large-scale density structures in the outer plasmasphere.

Wave amplification via cyclotron resonance with ring current electrons is maximized in the presence of small wave-normal angles and occurs over a larger fraction of the flux tube. The observed order of magnitude increase in the hiss amplitudes within the plasmaspheric density structures is interpreted to result from the favorable effects of ducting on wave amplification. An interesting consequence of ducting in the context of the present theory is that maintaining small wave-normal angles decreases resonant proton energies to values of the order of ring current and radiation belt energies. Past studies have ignored proton resonances with whistler mode waves, assumed to be propagating at highly oblique wave-normal angles, because the required proton energies for the resonant interaction reach MeV energies.

The association between large hiss amplitudes and thermal density enhancements has been pointed out by a number of authors [Angerami, 1970; Carpenter *et al.*, 1981; Chan and Holzer, 1976; Chan *et al.*, 1974; Scarf and Chappell, 1973] in relation to detached plasma regions. More recently, Koons [1989] observed intense hiss in association with whistler ducts in the outer plasmasphere (4 to 7  $R_E$ ). The density enhancements (up to 190%) associated with the ducts were much larger than values (<40%) reported for ducts at larger radial distances in the studies referenced above. Hiss emissions within the detached plasma structures and whistler ducts were an order of magnitude stronger than hiss emissions on adjacent field lines. The relative enhancement of the hiss within these regions agrees very well with observations in the outer plasmasphere ( $L \leq 4$ ) reported by Kozyra *et al.* [1987a].

The significance to ring current dynamics of resonant proton interactions with strong ducted hiss emissions depends on the amount of time that protons spend traveling through regions containing these emissions. A major assumption in the present work is that ring current electrons are able to resonate with and amplify hiss under conditions present in the outer plasmasphere. When the hiss is maintained at small wave normal angles (e.g., by ducting along density gradients),

protons at ring current energies are able to resonate with and damp the waves. A fundamental question is what portion of the time do energetic ion orbits intersect with density enhancements in the outer plasmasphere. During the initial phase of ring current injection there is probably no interaction with the plasmasphere, because the same electric fields which cause the injection of energetic ions into the inner magnetosphere will evacuate the plasmasphere in the midnight region filled by the newly injected ring current. However, as the energetic ions drift clockwise around the Earth, they will first likely encounter detached plasmaspheric regions in the dusk sector and then the main body of the plasmasphere drifting sunward in the dayside in response to the increased dawn-to-dusk electric fields. As the enhanced electric fields subside, the plasmasphere will begin to refill and the energetic ion orbits will intersect with an increasing greater region of the plasmasphere.

Information on the spatial extent, duration and frequency of occurrence of regions of ducted hiss would allow an estimation of their cumulative effect on the proton distribution. A complete characterization of these density structures has not yet been achieved but some information is available. Recent studies indicate that large-scale density irregularities, similar to the ducts discussed above, extend well into the outer plasmasphere [Carpenter *et al.*, 1993; Horwitz *et al.*, 1990]. These studies do not examine the hiss emissions associated with the density irregularities. Density irregularities in the outer plasmasphere were reported as far back as the mid 1970s. Chappell [1974] described the difficulty in defining detached plasma regions that occur very near the plasmopause as different from the density irregularities inside the plasmasphere. Horwitz *et al.* [1990] performed a statistical study of the plasmopause location and structure using DE 1 satellite data. They found that a double-ledge structure was the most common plasmopause shape on the eveningside, occurring some 50% of the time. Other more complicated large-scale density structures also occurred in this local time sector. Carpenter *et al.* [1993] carried out a study of the outer plasmasphere and dusk bulge region using thermal density data inferred from whistler observations by ground stations and measured in situ by the DE 1, ISEE 1 and GEOS 2 satellites. They observed density irregularities (with factor of 2 to 10 enhancement factors) routinely near the plasmopause in the postdusk sector following magnetic storms. These density irregularities were inferred to be a consequence of the physical processes involved in the erosion of the plasmasphere and formation of the sharp plasmopause boundary. They persist during an extended period of calm following the storm perturbations. Large-scale density gradients associated with these structures should be effective at guiding whistler mode emissions. Since density irregularities in a range of scale sizes are a common feature in the outer plasmasphere, ducted plasmaspheric hiss must also be a frequent occurrence in the evening local time sector.

To determine the effects of ducted plasmaspheric hiss on the ring current proton distribution, Kozyra *et al.* [1994] calculated diffusion coefficients, averaged over a bounce orbit, for protons in resonance with right-hand polarized whistler mode waves. A wave distribution spanning frequencies 100 - 1100 Hz characteristic of plasmaspheric hiss in the outer plasmasphere, with reasonable amplitudes ( $5 \times 10^{-5} \gamma^2/\text{Hz}$ ), and a distribution of wave-normal angles between  $0^\circ$  and  $45^\circ$  was adopted. During the wave-proton interaction, the proton

experiences multiple resonances with the hiss band due both to the finite frequency bandwidth of the waves and the longitudinal inhomogeneity in the magnetic field. The inhomogeneity in the magnetic field produces a constant variation in the pitch angle (and parallel velocity) of the proton as it bounces between mirror points and a resulting transition between resonances. The crossing of multiple resonances greatly enhances the diffusion experienced by the proton during the interaction. The important enhancement in proton diffusion due to the crossing of multiple resonances was pointed out in a different context by Villalon and Burke [1992, 1994]. They examined the interaction between radiation belt protons and whistler mode waves at frequencies between  $0.5 f_{ce}$  and  $1.0 f_{ce}$ , where  $f_{ce}$  is the proton gyrofrequency. These are considerably higher frequencies than are treated in the present study. Significant diffusion into the loss cone was achieved during second-order resonance with the whistler mode waves. In the present study, only first order resonance was treated. The diffusion coefficients were summed over resonances between  $n=100$  and  $n=-100$ . Pitch angle diffusion dominates for large wave-normal angles; energy diffusion becomes important for small pitch angles, near the edge of the atmospheric loss cone. The filling of the loss cone is minimal. Lifetimes for diffusion in energy were estimated to be of the order of a few days at pitch angles near  $\sim 25^\circ$ - $30^\circ$ . These lifetimes are comparable to Coulomb energy loss and charge exchange lifetimes for protons with energies  $\geq 80$  keV.

In the present work, the time-dependent bounce-averaged diffusion equation is solved, including pitch angle and energy diffusion, and the evolution of the proton distribution function is examined during resonant interactions with ducted plasmaspheric hiss. The problem is not solved self-consistently. The wave characteristics are fixed during the simulation period. The plasmaspheric hiss is assumed to have been generated using the free energy contained in the ring current electron distribution (not represented in the simulation) and to be damped by high-energy ring current and radiation belt protons. This constitutes an energy exchange between medium-energy (tens of keV) electrons and high-energy ( $> 80$  -  $100$  keV) protons using the plasmaspheric hiss as a intermediary. The high-energy ( $> 100$  keV) proton population decays over very long timescales due to Coulomb drag and charge exchange losses [cf. Fok *et al.*, 1991], responding adiabatically to changes in the magnetic field produced by the lower-energy ( $1$  -  $80$  keV) ring current ion injections associated with magnetic storms. The damping of the plasmaspheric hiss by protons in the high-energy tail of the distribution is expected to be much smaller than the amplification of the hiss by the tens of keV ring current electrons. Diffusion coefficients, used in the present study, are those given by Kozyra *et al.* [1994] but scaled to more-conservative wave amplitudes of  $1.3 \times 10^{-5} \gamma^2/\text{Hz}$ . It will be shown that energy diffusion at equatorial pitch angles near  $25^\circ$  is capable of producing enhancements in the locally mirroring high-energy proton flux at low altitudes that are confined to field lines threading regions of enhanced hiss amplitudes in the outer plasmasphere. The model proton distributions are consistent with observations of energetic proton fluxes in the topside ionosphere.

## 2. Diffusion Model

In the present treatment, the time-dependent bounce-averaged diffusion equation is solved numerically. This

equation was derived in spherical coordinates by Lyons [1974a] as

$$\begin{aligned} \frac{\partial f_o^\ell}{\partial t} &= \frac{1}{\tau_o s(\alpha_o)} \int_0^{\tau_o} \frac{\partial f^\ell}{\partial t} dt \\ &= \frac{1}{s(\alpha_o) v \cos \alpha_o \sin \alpha_o} \frac{\partial}{\partial \alpha_o} s(\alpha_o) \cos \alpha_o \sin \alpha_o \\ &\quad \left( \left\langle D_{\alpha\alpha} \right\rangle \frac{1}{v} \frac{\partial f_o^\ell}{\partial \alpha_o} + \left\langle D_{\alpha v} \right\rangle \frac{\partial f_o^\ell}{\partial v} \right) \\ &\quad + \frac{1}{v^2} \frac{\partial}{\partial v} v^2 \left( \left\langle D_{v\alpha} \right\rangle \frac{1}{v} \frac{\partial f_o^\ell}{\partial \alpha_o} + \left\langle D_{vv} \right\rangle \frac{\partial f_o^\ell}{\partial v} \right) \end{aligned} \quad (1)$$

where the time-averaged values of the diffusion coefficients are given below;

$$\begin{aligned} \langle D_{\alpha\alpha} \rangle &= \frac{1}{s(\alpha_o)} \int_0^{\lambda_M} D_{\alpha\alpha} \frac{\cos \alpha}{\cos^2 \alpha_o} \cos^7 \lambda d\lambda \\ \langle D_{\alpha v} \rangle = \langle D_{v\alpha} \rangle &= \frac{1}{s(\alpha_o)} \int_0^{\lambda_M} D_{\alpha v} \frac{\sin \alpha}{\cos \alpha_o \sin \alpha_o} \cos^7 \lambda d\lambda \\ \langle D_{vv} \rangle &= \frac{1}{s(\alpha_o)} \int_0^{\lambda_M} D_{vv} \frac{\sin^2 \alpha}{\cos \alpha \sin^2 \alpha_o} \cos^7 \lambda d\lambda \end{aligned}$$

where  $f^\ell$  is the distribution function of species  $\ell$ ,  $f_o^\ell$  is the distribution function of species  $\ell$  averaged over a bounce period,  $\alpha$  is the particle pitch angle, and  $\alpha_o$  is the particle pitch angle at the equator. The bounce period,  $\tau_B = \tau_o s(\alpha_o)$ , is the travel time from one mirror point to the conjugate mirror point and back again, where  $\tau_o = 4LR_E/v$ ; while  $L$  is the equatorial crossing distance of a field line in units of Earth radii ( $R_E$ ),  $s(\alpha_o)$  gives the small variation of  $\tau_B$  with equatorial pitch angle  $\alpha_o$ ,  $\lambda$  is magnetic latitude, and  $\lambda_M$  denotes the magnetic latitude of the mirror point.

The diffusion coefficients, time-averaged over a bounce orbit, were calculated by Kozyra *et al.* [1994] using the theoretical formulation of Lyons [1974b]. The present model assumes that the plasmaspheric hiss is generated during resonance with ring current electrons and maintained against proton damping during the time interval of the simulation. Therefore the wave spectrum is held constant during the simulation. This assumption is examined here. Plasmaspheric hiss, once generated, damps out very slowly due to a scarcity of resonating populations in the plasmasphere [Church and Thorne, 1983; Huang and Goertz, 1983]. While this is true relative to the timescale for wave growth, much longer timescales (approximately tens of days) are involved in the proton damping. During this time period, numerous ring current electron injections are likely to occur and wave amplitudes vary over the range  $10^4$  to  $10^7 \gamma^2/\text{Hz}$  [Smith *et al.*, 1974]. These frequent ring current electron injections will maintain the hiss spectrum against losses due to proton damping. A further complication is introduced by the time variation in the thermal density enhancements responsible for ducting the plasmaspheric hiss and maintaining the necessary small wave-normal angles. These ducts may exist only some fraction of the time and only over some percentage of the particles drift orbit. The details of the background ducted hiss spectrum must be worked out on the basis of satellite observations. At the present time, ducts are assumed to exist during the entire simulation period over the full proton drift

orbit. The hiss power spectral density versus frequency was described by a Gaussian distribution between 100 and 1100 Hz with half width of 400 Hz and peak value at 600 Hz of  $5 \times 10^{-5} \gamma^2/\text{Hz}$  in the work by Kozyra *et al.* [1994]. For the present study, peak power spectral density, seen by the proton, is assumed to average to  $1.3 \times 10^{-5} \gamma^2/\text{Hz}$  over the simulation period and the diffusion coefficients were scaled to this value. The wave-normal angle distribution was taken to be a Gaussian centered at  $0^\circ$  with maximum angle of  $45^\circ$ . Figure 1 is a contour plot of  $\langle D_{\alpha\alpha} \rangle$ ,  $\langle D_{\alpha v} \rangle (= \langle D_{v\alpha} \rangle)$ , and  $\langle D_{vv} \rangle$  versus the energy and pitch angle of the resonating proton at an  $L$  value of 4 with a background thermal density of  $500 \text{ cm}^{-3}$ . Pitch angle scattering is important at large pitch angles but becomes increasingly negligible as pitch angles approach the atmospheric loss cone. Diffusion of protons into the loss cone as a result of pitch angle scattering is relatively ineffective. However, energy diffusion maximizes at pitch angles near the edge of the atmospheric loss cone. The fact that the magnitude of the energy diffusion coefficient depends on pitch angle means that the energy diffusion near the loss cone will create flux gradients in pitch angle as well as energy space. These gradients at small pitch angles will accelerate the rate of proton diffusion into the atmospheric loss cone.

This initial model does not include the effects of Coulomb scattering or charge exchange losses on the distribution function. In the energy range below approximately 80 keV, charge exchange losses will dominate the evolution of the proton distribution. For proton energies near 80 keV, charge exchange lifetimes, Coulomb loss lifetimes and wave-particle energy diffusion lifetimes are all comparable [see Kozyra *et al.*, 1993, Figure 11]. The present study seeks to examine the

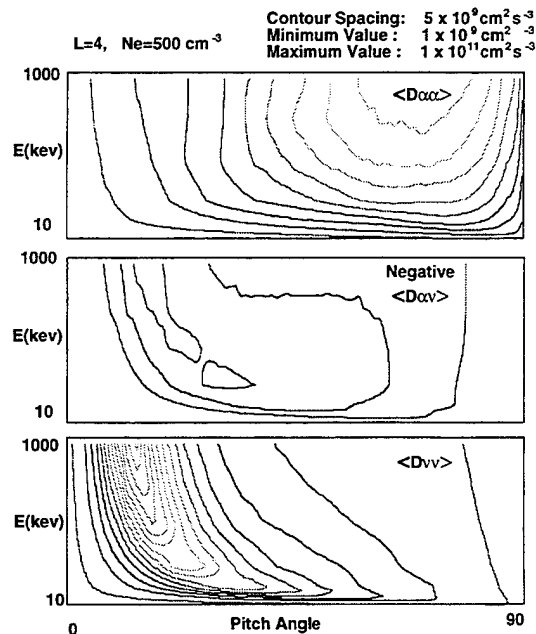


**Figure 1.** Contour plots of (upper)  $\langle D_{\alpha\alpha} \rangle$  (middle)  $\langle D_{\alpha v} \rangle = \langle D_{v\alpha} \rangle$  and (lower)  $\langle D_{vv} \rangle$  versus energy and equatorial pitch angle. The wave distribution was assumed to be (1) a Gaussian distribution in frequency over the range 100 to 1100 Hz with half width of 400 Hz and peak value at 600 Hz of  $1.3 \times 10^{-5} \gamma^2/\text{Hz}$  and (2) a Gaussian distribution in wave-normal angle over the range  $0^\circ$  to  $45^\circ$  with peak value at  $0^\circ$  wave-normal angle.

effects of resonance with plasmaspheric hiss on protons with energies above ~80 keV. In this energy range, resonance with plasmaspheric hiss will have a significant effect on the evolution of the proton distribution function; other loss processes will be neglected.

### 3. Numerical Technique

The bounce-averaged diffusion equation can be conveniently solved in conservative form. Thus (1) is rewritten as

$$\frac{\partial \tilde{f}_o}{\partial t} = \nabla \cdot \left[ \left( \langle \mathbf{D} \rangle \cdot \nabla \right) (\tilde{f}_o) - (\tilde{f}_o) \frac{(\langle \mathbf{D} \rangle \cdot \nabla) a}{a} \right] \quad (2)$$

where  $a = s(\alpha_o) \cos \alpha_o$ , and  $\tilde{f}_o = a f_o$ . The quantity  $s(\alpha_o)$ , which gives the small variation in the bounce period with equatorial pitch angle, is approximately  $s(\alpha_o) = 1.38 - 0.32(\sin \alpha_o + \sqrt{\sin \alpha_o})$  [Lyons, 1974b]. Note that the normalized distribution function  $\tilde{f}_o$  is the conserved quantity, rather than  $f_o$ , due to the temporal averaging of Boltzmann's equation over one bounce period. As particles with a given energy bounce back and forth between mirror points, they fill a certain volume in configuration space. This volume depends on the location of the mirror points. Thus, as the mirror points change, the particle distribution at any point along the field line must also vary, in order to maintain a constant number of particles within the changing volume in configuration space.

Equation (2) was solved by a finite volume technique. In this numerical method, the volume-average change in  $\tilde{f}$ , during a time step  $\delta t$ , is proportional to the sum of the fluxes  $F_i$  leaving each face of the volume element, times the interface area  $A_i$ :

$$\delta \tilde{f} = \frac{\delta t}{V} \sum F_i A_i \quad (3)$$

where  $V$  is the volume of the element. The fluxes in the two coordinate directions,  $v$  and  $\alpha$ , are given by

$$F_v = \langle D_{vv} \rangle \frac{\partial \tilde{f}}{\partial v} + \frac{\langle D_{v\alpha} \rangle}{v} \frac{\partial \tilde{f}}{\partial \alpha} - \frac{\tilde{f} \langle D_{v\alpha} \rangle}{av} \frac{\partial a}{\partial \alpha} \quad (4)$$

$$F_\alpha = \langle D_{\alpha\alpha} \rangle \frac{\partial \tilde{f}}{\partial \alpha} + \frac{\langle D_{\alpha v} \rangle}{v} \frac{\partial \tilde{f}}{\partial v} - \frac{\tilde{f} \langle D_{\alpha v} \rangle}{av} \frac{\partial a}{\partial v}$$

The partial derivatives in (4) were calculated numerically at each face with a second-order central difference scheme. It should be noted that the transformation  $x = \log_{10}(E = mv^2/2)$  was actually used in the numerical solution (leading to a slightly altered form of (4)). This was done so that high resolution could be maintained at low energies in  $E$  while still maintaining a relatively large overall range in energy. Energies ranged from 10 keV to 1000 keV, while pitch angles ranged from 0 to  $\pi$ . Constant cell widths  $\Delta \alpha$  and  $\Delta x$  were employed, with 45 steps in  $\alpha$  and 51 in  $x$ , giving a total of 2295 volume elements. Boundary conditions were chosen so that no flux could enter or leave the computational domain, except through the lower-energy boundary. At this boundary,  $E = 10$  keV, the flux entering the computational domain was chosen to maintain a constant value for  $f$ .

A two-step Runge-Kutta method was selected to advance the numerical solution in time. This method leads to second-order accuracy in time, accompanying the second-order accuracy of the spatial discretization. The numerical method was found to be stable as long as the time step was sufficiently small,  $\Delta t \leq 2$  hours. Several other numerical methods, such as Lax-Wendroff,

were found to be unstable. The major stability problem was caused by the combined hyperbolic and diffusive nature of (2).

The effects of a loss cone were artificially added by including a loss term for pitch angles less than or equal to 9 deg. Loss timescales were chosen to be slower than naturally occurring precipitation timescales in order to speed up the numerical solution and to maintain a stable solution near the loss cone. In the present solution, the edge of the loss cone is under resolved and artificially broad, leading to an underestimation of transport into the loss cone. However, the net effect on transport in the interior of the simulation domain, away from the loss cone, is negligible.

### 4. Time Evolution of the Proton Distribution Function

The initial conditions for the simulation were taken from Williams *et al.* [1976], who present observations of ring current ions, assumed to be protons, in the energy range of a few to several hundred keV. These observations were made on field lines approximately associated with SAR arc emissions in the ionosphere. The distribution function versus energy was represented by the sum of three different analytical fits over specified energy intervals as follows:

$$\begin{aligned} f(E) &= 1.94 \times 10^7 E^{-0.699} & 1.2 \text{ keV} \leq E < 9 \text{ keV} \\ f(E) &= 4.50 \times 10^6 E^0 & 9 \text{ keV} \leq E < 28 \text{ keV} \\ f(E) &= 1.63 \times 10^{10} E^{-2.539} & 28 \text{ keV} \leq E \leq 280 \text{ keV} \end{aligned} \quad (5)$$

The pitch angle distribution was taken to be isotropic independent of the proton energy with the exception of an artificially introduced loss cone. Contours of the initial distribution function versus pitch angle and energy are presented in Plate 1a.

The evolution of the proton distribution function is followed during resonance with the ducted plasmaspheric hiss spectrum described in section 2. Plates 1b and 1c are snapshots of the distribution function after 20 and 40 days, respectively. After 40 days time, the pitch angle distribution has changed dramatically from the isotropic initial condition to exhibit a distinct maximum at pitch angles near the edge of the atmospheric loss-cone. The peak shifts to larger pitch angles with decreasing proton energy. Significant energization of the protons occurs at the location of the peak. The peak in the distribution function at modest pitch angles is a result of energy diffusion that depends on pitch angle and maximizes near 25°. Energy diffusion near the edge of the loss cone will create a steep gradient in the distribution function and enhance pitch angle diffusion into the loss cone. However, even in the presence of this steep gradient, pitch angle diffusion is weak.

Figure 2 is a plot of the distribution function versus pitch angle at a fixed proton energy of 250 keV at selected times during the simulation. Protons with moderate pitch angles damp wave energy and diffuse from lower to higher energies during the simulation time interval producing a buildup in the distribution function. The reason for the buildup in the distribution function at moderate pitch angles is clearly illustrated in Figure 3. Energy diffusion lifetimes reach a minimum value at pitch angles near 27°. Diffusion in energy occurs most rapidly in a band of pitch angles centered about the lifetime minimum. As a consequence fluxes build up at these moderate pitch angles as shown in Figure 2. At larger pitch angles energy diffusion is too slow to produce significant



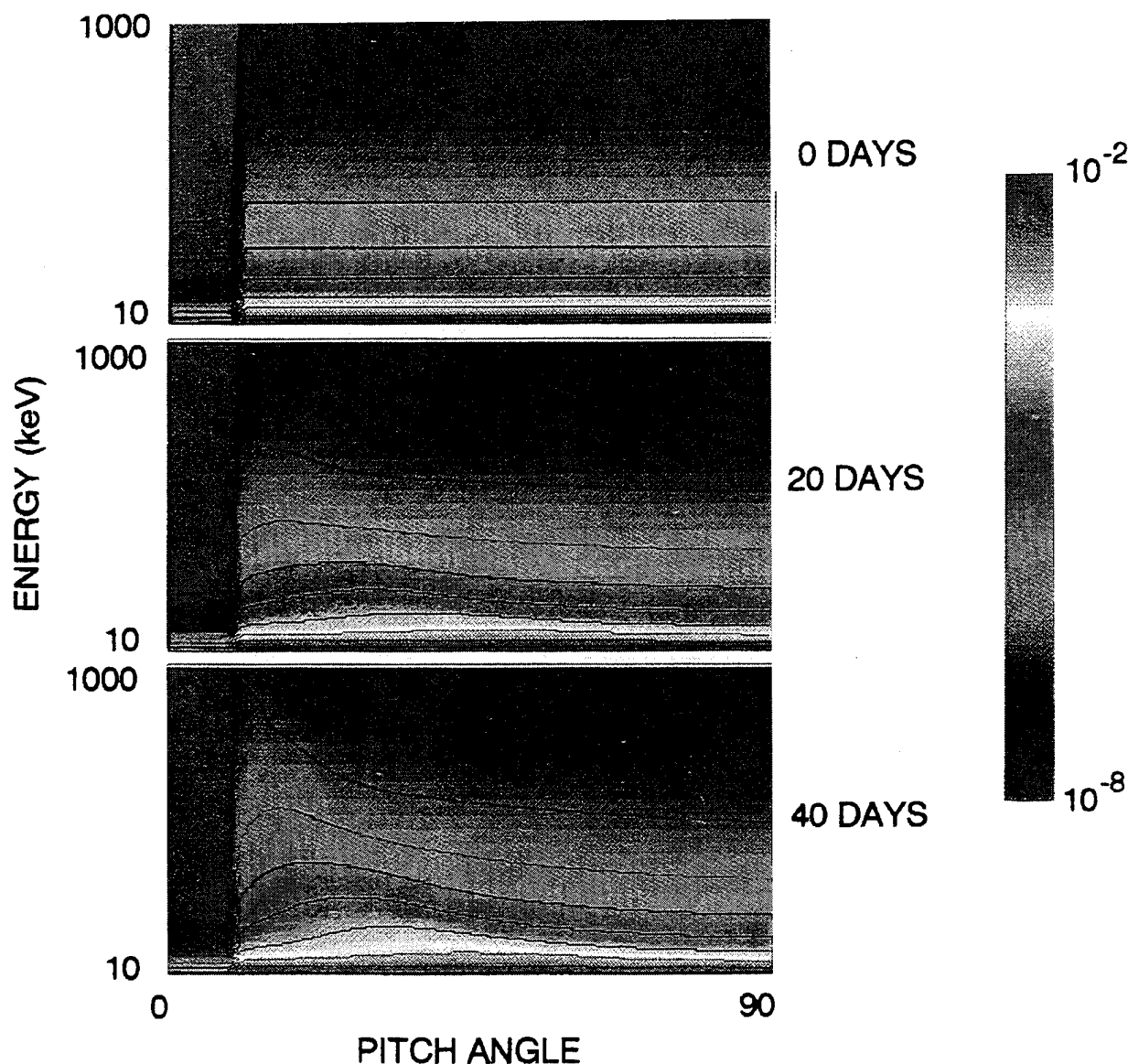


Plate 1. Contour plots of the equatorial proton distribution function versus energy and pitch angle at (a) 0, (b) 20, and (c) 40 days elapsed time during the simulation.

changes in the distribution function over the time interval displayed.

The energy dependence of the diffusive buildup of flux in velocity space is illustrated in Figure 4. In this figure, the distribution function is plotted versus energy at  $27^\circ$  pitch angle. The distribution function increases at all energies from 60 to 600 keV with the maximum relative increase between 200 and 250 keV. Particles in the distribution shown in Figure 4, diffuse in time from lower energies to higher energies. This increase in the distribution of particles with energies higher than 60 keV is balanced by a loss in the distribution of particles with energies less than 60 keV. Because of the log scale, this balance is difficult to see. However, numerical tests indicate that mass is conserved to 5 decimal places of accuracy (single precision) during the simulation period.

## 5. Discussion

It is instructive to examine the energy increase in the ring current protons and compare this to the energy available in the

plasmaspheric hiss and in the ring current electrons that are assumed to be the energy source for the plasmaspheric hiss emissions. The energy density of the initial equatorial distribution of ring current protons is  $237.6 \text{ keV cm}^{-3}$ . After interacting with the plasmaspheric hiss for a simulation period of 24 hours, the proton energy density rose to  $238.2 \text{ keV cm}^{-3}$  and after 240 hours to  $244.7 \text{ keV cm}^{-3}$ . The rate of increase of the energy density of the protons amounts to  $\sim 8 \times 10^{-3} \text{ eV cm}^{-3} \text{ s}^{-1}$  or  $\sim 0.7 \text{ keV cm}^{-3} \text{ d}^{-1}$ . This should be compared to the energy density,  $\sim 0.06 \text{ eV cm}^{-3}$ , of plasmaspheric hiss assuming an amplitude of  $\sim 1.3 \times 10^{-5} \gamma^2 \text{ Hz}^{-1}$  and small wave-normal angles in the outer plasmasphere. The implication of the numbers quoted above is that the timescale for depleting the hiss in the above plasma system is approximately 7 s. It is critical that the electron ring current replenish the hiss on timescales short in comparison with this time period.

A crude estimate of the energy density of ring current electrons can be made. Electrons are generally believed to account for about 20% of the ring current energy density; the bulk of the ring current energy is carried by the ion



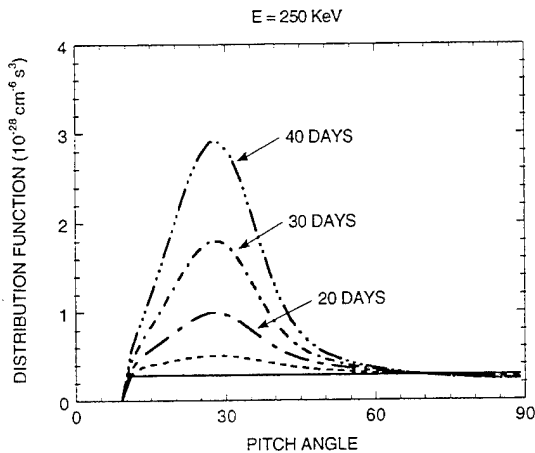


**Figure 2.** Equatorial distribution function versus pitch angle for 250 keV protons at 0, 10, 20, 30, and 40 days elapsed time during the simulation.

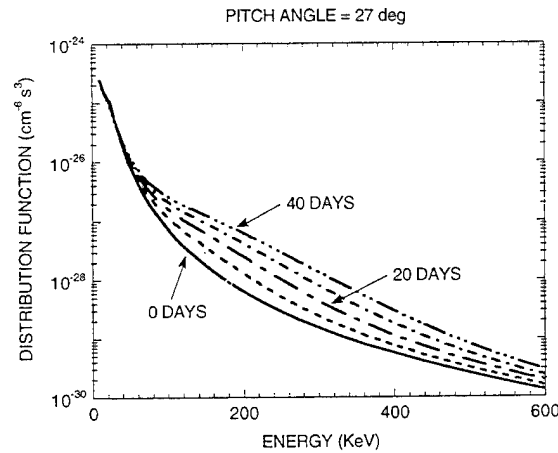


**Figure 4.** Equatorial distribution function versus energy for protons with an equatorial pitch angle of 27° at 0, 10, 20, 30, and 40 days elapsed time during the simulation.

components [cf. Frank, 1967]. Hamilton *et al.* [1988] observed ring current energy densities in the range 500-1300  $\text{keV cm}^{-3}$  at low  $L$  value ( $L \sim 2-3$ ) during the main phase of a great magnetic storm. The energy density of the initial spectrum, used in the present study, is more typical of moderate to high magnetic activity. Typical ring current ion distributions during a moderate storm imply an electron distribution with energy density in the range of many tens of  $\text{keV cm}^{-3}$  which is assumed to be replenished by injections multiple times during the simulation period. As was expected, the energy contained in the ring current electrons is much greater than the energy contained in the plasmaspheric hiss. The hiss amplitudes and associated energy densities, adopted in the study, are not inconsistent with the available ring current electron energy density for moderate to high-activity levels.

Cornilleau-Wehrin *et al.* [1985] examined the interaction between energetic electrons and whistler mode waves (0.2-2 kHz) experimentally within the framework of quasi-linear theory using GEOS 1 and 2 observations. The wave amplitudes in their study ranged from  $3.2 \times 10^{-6} \gamma^2/\text{Hz}$  to  $5 \times 10^{-7} \gamma^2/\text{Hz}$ . They estimate the timescale to be 5 ms to 0.1 s for the linear phase during which the wave amplitudes grow exponentially prior to saturation. Therefore the timescale to replenish the waves is about 2 orders of magnitude shorter than the timescale for the protons to damp out the wave energy. It is reasonable

to assume that, with multiple ring current injections, the electrons will be able to maintain the hiss amplitudes in the presence of the much slower damping of the hiss by the ring current protons. However, more careful studies of the coupled system must be carried out to establish the importance of this mechanism to the energetics of the protons.

An interesting result of the simulation is that energy diffusion maximizes at moderate pitch angles near the edge of the atmospheric loss cone and, over these pitch angles, creates an order of magnitude enhancement in the bounce-averaged proton distribution function, viewed at the equator. Scattering of particles into the loss cone is weak resulting in a nearly empty loss cone. An enhancement in the equatorial distribution function, at pitch angles near the edge of the loss cone, is seen in the ionosphere as an increase in the locally mirroring proton flux. Order of magnitude enhancements in locally mirroring energetic protons were observed by OGO 5 at altitudes between 350 and 1300 km and invariant latitudes between 50° and 60° [Lundblad and Soraas, 1978]. In addition, proton distributions observed at these altitudes were highly anisotropic in pitch angle with nearly empty loss cones. The observed characteristics are consistent with the main features of the proton distribution function, that evolved during interaction with ducted plasmaspheric hiss within the simulation period. This raises the possibility that interactions with plasmaspheric hiss play a role in forming and maintaining the characteristic zones of anisotropic proton precipitation in the subauroral ionosphere. Future assessment of the importance of this process depends on the distribution in space and time of ducted plasmaspheric hiss in the inner magnetosphere.

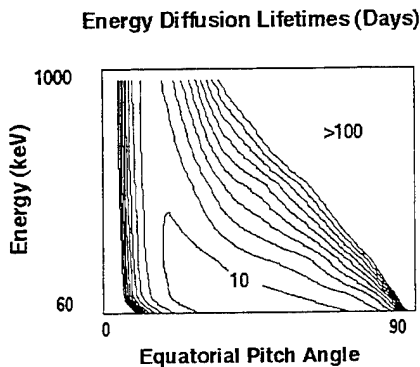


**Figure 3.** Bounce-averaged energy diffusion lifetimes in arbitrary units versus proton energy and equatorial pitch angle for the conditions of the simulation. These lifetimes are taken from Kozyra *et al.* [1994].

## 6. Summary and Conclusion

A numerical solution to the time-dependent bounce-averaged diffusion equation has been undertaken to examine the evolution of the proton distribution function during resonance with ducted plasmaspheric hiss. Diffusion coefficients in energy, cross energy-pitch angle and pitch angle were taken from Kozyra *et al.* [1994] but scaled to represent peak power spectral density in the hiss distribution of  $1.3 \times 10^{-5} \gamma^2/\text{Hz}$ . For these wave amplitudes, energy diffusion lifetimes reach minimum values of a few to tens of days. These lifetimes are

comparable to charge exchange loss and Coulomb drag lifetimes for proton energies in the range  $\geq 80$  keV so the simulation is valid only above 80 keV. The wave power spectral density distribution is held constant during the simulation period and is represented as (1) a Gaussian distribution in frequency over the range of 100–1100 Hz, with half width of 400 Hz, and peak value at 600 Hz; and (2) a Gaussian distribution in wave-normal angle over the range  $\pm 45^\circ$  with peak value at  $0^\circ$ . The problem is not solved self-consistently. This wave distribution is produced by the free energy in the ring current electrons (not treated in the simulation model) and is assumed to be maintained by resonance with this population during the simulation period. An initial proton distribution, observed by Explorer 45 on field lines associated with a SAR arc [Williams *et al.*, 1976] during a moderate magnetic storm, is adopted at  $t=0$ . The pitch angle distribution was assumed to be isotropic with the exception of an arbitrarily imposed loss cone at  $\leq 9^\circ$  equatorial pitch angle. Major results of the simulation are as follows:

1. Pitch angle diffusion maximizes for large equatorial pitch angles and rapidly decreases as the proton pitch angle decreases. As a result, diffusion of protons into the atmospheric loss cone is weak. Highly anisotropic pitch angle distributions are maintained.

2. Energy diffusion maximizes at small to moderate pitch angles just outside of the atmospheric loss cone. This diffusion creates an order of magnitude enhancement in the distribution function at pitch angles near  $27^\circ$  by the end of the simulation period ( $\Delta t = 40$  days) for 250 keV protons and smaller but still substantial enhancements for protons in the energy range of  $\sim 80$  to 600 keV.

3. The large enhancement in the distribution function just outside of the atmospheric loss cone creates a steep slope in the distribution function for small pitch angles and enhances the filling of the atmospheric loss cone. However, even with this steepened gradient, the diffusion into the loss cone is weak.

4. The changes in the distribution function, when mapped to low-altitude Earth orbit, appear as an order of magnitude increase in locally mirroring protons with very negligible filling of the atmospheric loss cone. This increase in the locally mirroring flux is confined to field lines that thread large-scale ducted hiss regions in the outer plasmasphere and associated thermal density structures. SAR arcs also appear at the foot of field lines that map to the large-scale thermal density structures, but have no association with the proton precipitation in this scenario. Kozyra *et al.* [1987b] have shown that Coulomb collisions between ring current  $O^+$  and thermal electrons can supply sufficient energy to maintain a SAR arc in the ionosphere. The energy deposition rate via this process is directly proportional to the thermal plasma density and thus also maximizes in association with these large-scale density structures in the outer plasmasphere.

**Acknowledgments.** The authors wish to thank the referees for interesting and helpful comments. Several authors wish to express appreciation to NASA for support to the University of Michigan under grants NAGW-1619 and National Science Foundation for support under grant numbers ATM-9114409, ATM-9412363 and ATM-9116858. One author wishes to acknowledge support under U.S. Airforce grant F19628-92-K-0007 to Northeastern University.

The Editor thanks U. S. Inan, V. S. Sonwalkar, and J. L. Horwitz for their assistance in evaluating this paper.

## References

- Anderson, B.J., R.E. Erlandson, and L.J. Zanetti, A statistical study of Pc1-2 magnetic pulsations in the equatorial magnetosphere, 1. Equatorial occurrence distributions, *J. Geophys. Res.*, **97**, 3075, 1992.
- Angerami, J.J., Whistler duct properties deduced from VLF observations made with the OGO 3 satellite near the magnetic equator, *J. Geophys. Res.*, **75**, 6115, 1970.
- Carpenter, D.L., R.R. Anderson, T.F. Bell, and T.R. Miller, A comparison of equatorial electron densities measured by whistlers and by a satellite radio technique, *Geophys. Res. Lett.*, **8**, 1107, 1981.
- Carpenter, D.L., B.L. Giles, C.R. Chappell, P.M.E. Decreau, R.R. Anderson, A.M. Persoon, A.J. Smith, Y. Corcuff, and P. Canu, Plasmaspheric dynamics in the duskside bulge region: A new look at an old topic, *J. Geophys. Res.*, **98**, 19243, 1993.
- Chan, K.W., and R.E. Holzer, ELF hiss associated with plasma density enhancements in the outer magnetosphere, *J. Geophys. Res.*, **81**, 2267, 1976.
- Chan, K.W., R.E. Holzer, and E.J. Smith, A relation between ELF hiss amplitude and plasma density in the outer plasmasphere, *J. Geophys. Res.*, **79**, 1989, 1974.
- Chappell, C.R., Detached plasma regions in the magnetosphere, *J. Geophys. Res.*, **79**, 1861, 1974.
- Church, S.R., and R.M. Thorne, On the origin of plasmaspheric hiss: Ray path integrated amplification, *J. Geophys. Res.*, **88**, 7941, 1983.
- Cole, K.D., Stable auroral red arc, sinks for energy of *Dst* main phase, *J. Geophys. Res.*, **70**, 1689, 1965.
- Cornilleau-Wehrlin, N., J. Solomon, A. Korth, and G. Kremser, Experimental study of the relationship between energetic electrons and ELF waves observed on board GEOS: A support to quasi-linear theory, *J. Geophys. Res.*, **90**, 4141, 1985.
- Comwall, J.M., F.V. Coroniti, and R.M. Thorne, Unified theory of SAR-arc formation at the plasmopause, *J. Geophys. Res.*, **76**, 4428, 1971.
- Fok, M.-C., J. U. Kozyra, A. F. Nagy and T. E. Cravens, Lifetime of ring current particles due to Coulomb collisions in the plasmasphere, *J. Geophys. Res.*, **96**, 7861, 1991.
- Frank, L. A., On the extraterrestrial ring current during geomagnetic storms, *J. Geophys. Res.*, **72**, 3753, 1967.
- Hamilton, D. C., G. Gloeckler, F. M. Ipavich, W. Studemann, B. Wilken, and G. Kremser, Ring current development during the great geomagnetic storm of February 1986, *J. Geophys. Res.*, **93**, 14,343, 1988.
- Hayakawa, M., N. Ohmi, M. Parrot, and F. Lefevre, Direction finding of ELF Hiss emissions in a detached plasma region of the magnetosphere, *J. Geophys. Res.*, **91**, 135, 1986a.
- Hayakawa, M., M. Parrot, and F. Lefevre, The wave normals of ELF hiss emissions observed onboard GEOS1 at the equatorial and off-equatorial regions of the plasmasphere, *J. Geophys. Res.*, **91**, 7989, 1986b.
- Horwitz, J. L., L. H. Brace, R. H. Comfort, and C. R. Chappell, Dual spacecraft measurements of plasmasphere-ionosphere coupling, *J. Geophys. Res.*, **91**, 11203, 1986.
- Horwitz, J.L., R.H. Comfort, and C.R. Chappell, A statistical characterization of plasmasphere density structures and boundary locations, *J. Geophys. Res.*, **95**, 7937, 1990.
- Huang, C.Y., and C.K. Goertz, Ray-tracing studies and path-integrated gain of ELF unducted whistler mode waves in the Earth's magnetosphere, *J. Geophys. Res.*, **88**, 6181, 1983.
- Koons, H.C., Observations of large-amplitude, whistler-mode wave ducts in the outer plasmasphere, *J. Geophys. Res.*, **94**, 15393, 1989.
- Kozyra, J.U., Observational and theoretical investigation of stable auroral red arcs and their magnetospheric energy source, Ph.D. thesis, Univ. of Mich., Ann Arbor, 1986.
- Kozyra, J.U., et al., Satellite observations of new particle and field signatures associated with SAR arc field lines at magnetospheric heights, *Adv. Space Res.*, **7**, 3, 1987a.
- Kozyra, J.U., E.G. Shelly, R.H. Comfort, L.H. Brace, T.E. Cravens, and A.F. Nagy, The role of ring current  $O^+$  in the formation of stable red arcs, *J. Geophys. Res.*, **92**, 7487, 1987b.

- Kozyra, J. U., M. O. Chandler, D. C. Hamilton, W. K. Peterson, D. M. Klumpp, D. W. Slater, M. J. Buonsanto, and H. C. Carlson, The role of ring current nose events in producing stable auroral red arc intensifications during the main phase: Observations during the September 19-24, 1984, equinox transition study, *J. Geophys. Res.*, **98**, 9267, 1993.
- Kozyra, J.U., C.E. Rasmussen, R.H. Miller, and L.R. Lyons, The interaction of ring current and radiation belt protons with ducted plasmaspheric hiss. 1. Diffusion coefficients and timescales, *J. Geophys. Res.*, **99**, 4069, 1994.
- Lundblad, J.A., and F. Soraas, Proton observations supporting the ion cyclotron wave heating theory of SAR arc formation, *Planet. Space Sci.*, **26**, 245, 1978.
- Lyons, L.R., General relations for resonant particle diffusion in pitch angle and energy, *J. Plasma Phys.*, **12**, 45, 1974a.
- Lyons, L.R., Pitch angle and energy diffusion coefficients from resonant interactions with ion-cyclotron and whistler waves, *J. Plasma Phys.*, **12**, 417, 1974b.
- Scarf, F.L., and C.R. Chappell, An association of magnetospheric whistler dispersion characteristics with changes in local plasma density, *J. Geophys. Res.*, **78**, 1597, 1973.
- Smith, E.J., A.M.A. Frandsen, B.T. Tsurutani, R.M. Thorne, and K.W. Chan, Plasmaspheric hiss intensity variations during magnetic storms, *J. Geophys. Res.*, **79**, 2507, 1974.
- Sonwalker, V.S., and U. S. Inan, Wave normal direction and spectral properties of whistler mode hiss observed on the DE 1 satellite, *J. Geophys. Res.*, **93**, 7493, 1988.
- Storey, L. R. O., F. Lefevre, M. Parrot, L. Cairo, and R. R. Anderson, Initial survey of the wave distribution functions for plasmaspheric hiss observed by ISEE 1, *J. Geophys. Res.*, **86**, 19,469, 1991.
- Thorne, R.M., and R. B. Horne, The contribution of ion-cyclotron waves to electron heating and SAR-arc excitation near the storm-time plasmapause, *Geophys. Res. Lett.*, **19**, 417, 1992.
- Thorne, R.M., E.J. Smith, R.K. Burton, and R.E. Holzer, Plasmaspheric hiss, *J. Geophys. Res.*, **78**, 1581, 1973.
- Villalon, E., and W. J. Burke, Whistler interactions with energetic protons, in *Physics of Space Plasmas (1991)*, p. 473, SPI Conf. Proc. Reprint Ser. no. 11, edited by T. Change, G. B. Crew and J. R. Jasperse, Scientific, Cambridge, Mass., 1992.
- Villalon, E., and W. J. Burke, Diffusion of radiation belt protons by whistler waves, *J. Geophys. Res.*, **99**, 21,329, 1994.
- Voss, H.D., and L.G. Smith, Global zones of energetic particle precipitation, *J. Atmos. Terr. Phys.*, **42**, 227, 1980.
- Williams, D.J., G. Hernandez, and L.R. Lyons, Simultaneous observations of the proton ring current and stable auroral red arcs, *J. Geophys. Res.*, **81**, 608, 1976.

---

J. U. Kozyra, R. H. Miller, and C. E. Rasmussen, Space Physics Research Laboratory, Atmospheric, Oceanic and Space Sciences Department, University of Michigan, Ann Arbor, MI 489109-2143.  
 E. Villalon, Center for Electromagnetic Research, Northeastern University, Boston, MA 02115.

(Received April 28, 1994; revised May 12, 1995;  
 accepted May 16, 1995.)